HOLOGRAPHIC MICROWAVE IMAGING FOR LESION DETECTION

Lulu Wang

PhD

2013

Auckland, New Zealand

Holographic Microwave Imaging for Lesion Detection

Lulu Wang

A thesis submitted to Auckland University of Technology

in fulfilment of the requirements for the degree of

Doctor of Philosophy (PhD)

June, 2013

Faculty of Design & Creative Technologies

School of Engineering

Auckland University of Technology

Auckland, New Zealand

Primary Supervisor : Professor Ahmed Al-Jumaily

Secondary Supervisor : Dr. Ray Simpkin

Declarations

I hereby declare that this submission is my own work and that, to the best of my knowledge and belief, it contains no material previously published or written by another person nor material which to a substantial extent has been accepted for the award of any other degree or diploma of a university or other institution of higher learning, except where due acknowledgement is made in the acknowledgements.

Signature Date 30/05/2013

Lulu Wang

I further authorise the Auckland University of Technology to reproduce this thesis by photocopying or by other means, in total or in part, at the request of other institutions or individuals for the sole purpose of scholarly research.

Signature Date 30/05/2013

Lulu Wang

Borrowers Page

The Auckland University of Technology requires the signatures of all people using or photocopying this thesis. Accordingly, all borrowers are required to fill out this page.

Date	Name	Address	Signature

Acknowledgements

I would like to acknowledge all those gave me the possibility to complete this thesis.

First and foremost, I am extremely grateful for the guidance and encouragement from my amazing and wonderful primary supervisor Professor Ahmed Al-Jumaily, Director of Institute of Biomedical Technologies (IBTec), Auckland University of Technology. I first met Prof. Ahmed Al-Jumaily in early 2008 when I was in IBTec for a Master's degree. Since then, he has showed me the meaning of being a responsible educator, passion being a hard worker, how to take life seriously, and management and communication skills. I am grateful to Prof. Ahmed Al-Jumaily for providing the opportunity to work on such great project, encouraging me to take experimental work, supporting me every time when I was in trouble and guiding me to finish this thesis. The professional skills and personal lessons that I learned from him will be invaluable in my life. Without his contributions and support, there was no hope for me to complete this research within 3 years.

I would like to express my thanks and gratitude to my great supervisor Dr. Ray Simpkin, who joined the supervisory team in March 2012, from Medical Device Technology, Callaghan Innovation. Dr. Ray is professional and a very patient and hard-working supervisor. I am very grateful to Dr. Ray for his continuous guidance, invaluable help, discussion and support, which make this project work possible.

I would like to thank Assoc Prof. Slava Kitaeff, School of Physics, the University of Western Australia, for introducing me to this field and interesting discussion.

I gratefully acknowledge the support of the Institute of Biomedical Technologies (IBTec), at the Auckland University of Technology (AUT). I also would like to thank all my lovely colleagues at IBtec, thanks for sharing your time with me and providing me such great working environment.

I gratefully acknowledge the Callaghan Innovation, Auckland, for providing the equipment and laboratory to let me complete all my experiments. My special thanks go

to Mr Terry Palmer and Mr Tim Wyatt for manufacturing the cables, switch assembly and waveguides for the experimental set-up.

I would like to acknowledge the AUT scholarship office, School of Engineering, Engineering Research Institute (ERI) and Universities New Zealand for providing the following scholarships: Doctoral enrolment fees waiver scholarship, SoE doctor scholarship, ERIC Grant stipend, AUT Laptop Scholarship, and the Claude McCarthy Fellowship: Category A.

I gratefully acknowledge the support of School of Engineering, particularly thanks to Head of Research and Doctoral Studies Prof. Zhan Chen, Head of Department Prof. Tek Tjing Lie and School Manager Mrs Kath Mills.

I would like to extend my special thanks to my brilliant friends Mr Arrian Prince-Pike and Mr Jonathan Currie at School of Engineering, for always providing fast and meticulous proofreading, computer technical support and friendship.

Finally and most importantly, I would like to thank my wonderful parents, Mr Fengye Wang and Mrs Wenxia Zhai, for their endless supporting and unconditional love through all these years.

Abstract

This thesis presents the preliminary analysis and development of a novel technique to detect inclusion in a dielectric object that is based on holographic microwave imaging array (HMIA) and aperture synthesis far-field imaging techniques. This new microwave based approach may have a potential to become an imaging tool for breast lesion detection in the future. The two dimensional (2D) and three dimensional (3D) computer simulation models have been developed using MATLAB to demonstrate the 2D and 3D HMIA image reconstruction algorithms. A suitable antenna for experimental implementation using HMIA techniques is designed, and the spiral and random antenna array configurations are developed to significantly improve the quality of the images. The proposed technique has been validated through simulation and measurements on multiple dielectric objects (breast phantoms). Results have demonstrated the feasibility and superiority of detecting small inclusions (lesions) in the breast model using the HMIA imaging algorithms. The achieved simulation and experimental images using different antenna array configurations have been evaluated using visual inspection and quantitative analysis methods. Results show that the spiral and random antenna array configurations have the ability to produce better quality images compare to the most widely used regularly spaced array.

Finally, the 2D HMIA technique has been applied on 2D and 3D head models for brain stroke detection. The Method of Moments (MoM) and Born approximation approaches are employed to solve the scattering electric field of 2D and 3D head models respectively. The simulation results indicate that the HMIA technique has a potential for other medical imaging applications, such as brain stroke detection.

Publications

The work carried out during this PhD study is described in this thesis and in the papers found at the very end of the thesis. At the time of Writing, these papers have all either been published or accepted for publication. I am the main author of six conference papers [CP1]~[CP6] and two journal papers [JP1]~[JP2].

The six published or accepted conference papers, of which I am the main author, are included at the end of this thesis.

[CP1] Wang, L., Simpkin, R. and Al-Jumaily, A.M. (2012, November). Holography microwave imaging array for early breast cancer detection. *Proceedings of 2012 ASME International Mechanical Engineering Congress & Exposition, Houston, Texas, United States*. Paper number: IMECE2012-85910.

[CP2] Wang, L., Simpkin, R., & Al-Jumaily, A. M. (2012, November). 3D breast cancer imaging using holographic microwave interferometry. *Proceedings of the 27th Conference on Image and Vision Computing New Zealand*, pp.180-185.

[CP3] Wang, L., Simpkin, R., & Al-Jumaily, A. M. (2013, August) Holographic Microwave Imaging: Experimental Investigation of Breast Tumour Detection. *Proceedings of 2013 IEEE International Workshop on Electromagnetics: Applications and Student Innovation Competition (iWEM 2013), Hong Kong, China,* pp.61-64.

[CP4] Wang, L., Simpkin, R., & Al-Jumaily, A. M. (2013). Three-Dimensional Holographic Microwave Imaging Array: Experimental Investigation of Tumour Detection in Breast Phantom. *Accepted by 2013 ASME International Mechanical Engineering Congress & Exposition, November 15-21, 2013, San Diego, CA, United States.* Paper number: IMECE2013-63132.

[CP5] Wang, L., Simpkin, R., & Al-Jumaily, A. M. (2013, August). Open-ended Waveguide Antenna for Microwave Breast Cancer Detection. *Proceedings of 2013 IEEE International Workshop on Electromagnetics:*

Applications and Student Innovation Competition (iWEM 2013), Hong Kong, China, pp.65-68.

[CP6] Wang, L., Simpkin, R., & Al-Jumaily, A. M. (2013, July). Microwave Imaging for Brain Stroke Detection. *Proceedings of Shanghai International Conference on Applied Science and Engineering*, pp.65-71.

The two published journal papers, of which I am the main author, are listed below.

[JP1] Wang, L., Al-Jumaily, A. M., & Simpkin, R. (August 2013). Holographic Microwave Imaging Array for Brain Stroke Detection. *Journal of Signal and Information Processing, Vol 4, No. 3B,* pp.96-101.

[JP2] Wang, L., Simpkin, R., & Al-Jumaily, A. M. (2013). Holographic Microwave Imaging for Medical Applications. *Journal of Biomedical Science and Engineering, Vol 6, No.8,* pp. 823-833.

Table of Contents

List of Figures

List of Tables

List of Abbreviations

Abbreviation	Definition
AAC	Antenna Array Configuration
CTT	Computed Thermo-acoustic Tomography
CMI	Confocal Microwave Imaging
DCIS	Ductal Carcinoma in Situ
EM	Electromagnetic
EMI	Electromagnetic Interference
FFT	Fast Fourier Transform
HMIA	Holographic Microwave Imaging Array
IFFT	Inversion Fast Fourier Transform
IHM	Indirect holography microwave
LCIS	Lobular Carcinoma in Situ
MGC	Machinable Glass Ceramic
MI	Microwave Imaging
MoM	Method of Moments
MRI	Magnetic Resonance Imaging
MIST	Imaging Via Space Time
PAT	Physical Anomaly Tomography
PET	Position Emission Tomography
PNA	Vector Network Analyser
STT	Scanning Thermo-acoustic Tomography
SAR	Sensing Adaptive Radar
SFM	Screen Film Mammography
TSAR	Tissue Sensing Adaptive Radar
2D	Two dimensional
3D	Three dimensional
USVA	Ultrasound Simulated Vibro-acoustic Imaging

List of Symbols

Symbol	Definition
A	Broad aperture dimension of antenna aperture
B	Narrow aperture dimension of antenna aperture
c	The light speed in free space
$\underline{E}_{tot}$	Total electric field
$\underline{E}_0$	Wave amplitude of TE_{10} mode at within waveguide aperture
$\underline{E}_{inc}$	Incident electric field
$\underline{E}_{scat}$	Back-scattered electric field
f_0	The centre frequency
$h(\theta, \phi)$	Radiation pattern function
j	$\sqrt{-1}$
k_0	Propagation constant in free space
k_b	Propagation constant in host medium
$\underline{P}(\theta, \phi)$	Polarisation vector
R_0	Position vector from a point in the breast to the transmitting antenna
$\hat{R}$	Unit vector parallel to the vector R
R	Position vector from a point in the lesion to the receiving antenna
$R = \lvert\underline{R}\rvert$	Distance from a point in the breast to the receiving antenna
(θ, ϕ)	Incident angle
ε	Complex relative permittivity distribution of object
ε_b	Complex relative permittivity of host medium
ε_r	Relative permittivity
σ	Conductivity

Chapter 1 Introduction

1.1 Background and Motivation

Cancer is a group of diseases characterized by uncontrolled growth and spread of abnormal cells [1]. It is a leading cause of death and accounted for 7.6 million deaths (approximately 13% of all deaths) in 2008 [2]. According to a report by the American Cancer Society in 2012 [1], just under than 50% of men and a little more than 33% of women will develop cancer in their lifetime in the US. In 2011 [3]-[4], there were 7,441,886 people living with cancer and 4,939,810 deaths caused by this illness. The estimated number of new cases each year is expected to rise from 10 million in 2002 to 15 million by 2025. This number will increase to 21.4 million by 2030 and 13.3 million deaths will occur during this time, which is 72% more than that in 2008 [1], [4]. In the United States, the three most common cancers in men are prostate cancer, lung cancer and colon cancer, while the three most common cancers in women are breast cancer, colon cancer and lung cancer [5].

Breast cancer is a major killer of women worldwide and also in New Zealand [5]- [10]. In fact, 1 in 8 women would get or have had breast cancer if they lived beyond the age of 70 [3]. Approximately 50% of the breast cancer cases and 60% of the deaths are estimated to occur in economically developing countries. Approximately, 226,870 new cases of invasive breast cancer will be diagnosed among women and about 2,190 new cases are expected in men in the United State in 2012 [1]. Approximately, 2800 new cases of breast cancer are diagnosed and more than 650 women lose their life every year in New Zealand [6]. Despite epidemiological evidence of many possible risk factors for

breast cancer, at this stage there are no clear opportunities for prevention [9]. Studies show that only early detection (when the lesion less than 5 mm) and timely treatment can significantly increase the survival rate [10]. Early detection has gained more attention due to advances in imaging algorithms, models, experimental systems and computational power [10].

Mammography techniques are currently the gold standard for the detection of breast lesions and use X-rays [11]. However, X-ray mammography has a number of limitations. For example, approximately 10%-30% of breast cancers may be missed at mammography [11], discomfort and unpleasant pain to the patient as the breast is highly compressed during operation [13]-[14]. A further disadvantage of X-ray mammography is the difficulty in imaging of radio graphically dense glandular tissue especially common amongst younger women who have high risk factors [15]. Moreover, the ionizing properties of X-rays restrict the frequency of screening [16]. These limitations of X-Ray mammography motivate the development of new alternate imaging modalities.

Microwave imaging has been considered as one of the most promising alternatives to X-ray mammography for early breast cancer detection and has received significant attention in recent years. The physical basis for microwave imaging is tissue dependent microwave scattering and absorption in the breast due to the contrast in the dielectric properties between the malignant and normal breast tissues. Using electromagnetic waves in the radio frequency range for non-invasive diagnostics and imaging of human organs and tissue has been researched extensively [17]-[25]. Recently the majority contribution comes from the two research groups Meaney *et al.* [26]-[34] and Hagness *et al*. [36]-[41]. Microwave imaging exploits the dielectric contrast between normal and

malignant breast tissue at microwave frequencies and has attracted the interest of a number of research groups [42]-[86]. Compared to other medical applications, microwave based imaging techniques have benefits such as no risk to the human body due to the lack of ionizing radiation, it is more comfortable for patients during operation and relatively low cost. However, there are various weaknesses in current microwave imaging techniques. In recent extensive measurements on the dielectric properties of different types of breast tissues discovered that the dielectric contrast varies widely from individual to individual, with age and other biological factors [17]-[25]. The limited resolution comes from the fact that the heterogeneous structure of the breast causes multiple scatterings and reflections of the microwave signal while penetrating inside the different types of tissues [87].

Holographic interferometer (HI) is one of the possible ways to overcome the current challenges of microwave imaging and detection. A microwave holographic based technique does not require expensive ultra-high speed electronics, as narrow-band signals can be converted to the baseband for digitalization at a slower rate, thereby enabling real-time imaging at significantly lower cost [83]. It also offers high contrast between healthy and malignant tissues and assists in forming an image of the location and the extent of the malignant tissue. This technique exploits the advantages of holography without requiring the direct measurement of vector quantities, which requires an expensive network analyser [79]. The application of microwave holography imaging and tissue sensing has been reported in [76]-[86] recently.

1.2 Research Objectives

This research aims at exploring the possibility of using the holographic microwave imaging technique and aperture synthesis technique to detect inclusion in a dielectric object, potential application would be breast lesion detection.

Unlike the work discovered in [76]-[86], this research investigates a new far-field holographic microwave imaging array (HMIA) technique for breast lesion detection by using a single microwave frequency and utilising holographic microwave and aperture synthesis imaging techniques. The main objectives of this research are:

- Develop a 2D imaging algorithm to form a 2D breast image for breast lesion detection, this approach should has benefits of easy to use, more comfortable during operation compare to the currently available breast lesion detection technologies (see Chapter 3 for details)
- Construct a 2D computer model to demonstrate the proposed 2D imaging algorithm
- Develop a 3D imaging algorithm to generate a 3D breast image that should solve the problem that not all lesions can be identified in 2D image if two lesions are located in the same x-y planes but different z-plane (see Chapter 4 for details)
- Construct a 3D computer model to demonstrate the proposed 3D imaging algorithm
- Develop a suitable antenna for breast lesion detection using the proposed technique and investigate the antenna array configurations to generate a high quality breast image (see Chapter 5 for details)
- Design a small antenna that suits for the proposed technique for breast phantom detection (see Chapter 6 for details)

- Validate the proposed imaging algorithms by designing and building an experimental system (see Chapter 6 for details)

1.3 Thesis Overview and Outline

In this chapter, the motivation for this work and the objectives were explained. The remaining chapters of this thesis are arranged in the following order:

Chapter 2 presents an overview of the currently available breast imaging techniques, and with introduces of microwave breast imaging. A review of electrical properties of normal and malignant tissues is reported. An introduction of microwave imaging and several approaches of microwave imaging techniques are given.

Chapter 3 introduces a new 2D HMIA technique. 2D imaging system design, data collection method and imaging algorithm, simulation set-up, as well as simulation results are presented in this chapter.

Chapter 4 describes the development of the novel 3D HMIA technique. 3D imaging system design, data collection method, imaging algorithm, simulation set-up, as well as simulation results are detailed in this chapter.

Chapter 5 details the design of the most suitable antenna and antenna array configurations for implementation of the HMIA technique. Simulation results using various antenna array configurations are compared in this chapter.

Chapter 6 demonstrates an experimental system set-up to validate the proposed HMIA techniques for breast lesion detection. The hardware component is discussed in detail, as its shape and material were both considered carefully before manufacturing. Simplified experimental system set-ups for 2D and 3D HMIA techniques are presented and experimental results are reported.

Chapter 7 discusses the simulation and experimental results of the proposed HMIA technique. Comparison of published microwave imaging results with HMIA technique and an example of other applications of HMIA techniques are presented.

Chapter 8 summarizes and concludes of this thesis. Contributions and future work are detailed in this chapter.

Chapter 2 Literature Review

2.1 Introduction

In this chapter the most important clinically established breast imaging methods are introduced. The effectiveness of the currently available breast lesion detection technologies and alternative breast imaging methods are summarized. Microwave imaging for breast lesion detection has made considerable progress during the past few decades. It relies on the dielectric properties difference between the normal and malignant tissues in the breast. Recent research showed that microwave breast imaging has the potential to replace mammography and become a clinical implementation in the future. The electrical properties of breast tissues are reviewed, with emphasis on studies examining breast tissues and malignancies. Several different approaches to microwave breast imaging are explored and methods are described in section 2.3.

2.2 Breast Imaging Techniques and Limitations

Medical imaging techniques are used to view the human body in order to diagnose, monitor or treat medical conditions [88]-[89]. Breast imaging techniques are used to detect small, nonpalpable breast abnormalities, evaluate clinical findings, and guide diagnostic procedures [90]. There are several widely used imaging techniques for breast lesion detection [91], including mammography, ultrasound and magnetic resonance imaging (MRI). Generally, mammography or screen-film mammography (SFM) is the most common form of breast imaging.

2.2.1 Mammography

Mammography is an X-ray based imaging modality, which is widely used as a screening tool to detect breast lesion in women. It can also be used to detect and diagnose breast disease in women experiencing symptoms such as a lump, pain or nipple discharge. Imaging with X-rays involves exposing parts of the body to a small dose of ionizing radiation to produce pictures of the inside of the body. X-rays are high energy photons generated in X-ray tubes by bombarding a heavy metal anode with a stream of electrons. The emitter is shielded to allow only a directional beam to exit the device. The X-ray beam is aimed through the volume of interest towards an X-ray detector and as it passes through various different tissues the beam energy is attenuated due to both absorption and scattering. Figure 2.1 shows the breast is pressed between two plastic plates during a mammogram.

Figure 2.1 X-ray Mammography [91]

Although X-ray mammography is the current most available effective technology for early-stage screening [11], the limitations of X-ray mammography are well known, especially in radiologically dense glandular tissue [12]. X-ray mammography also has a relatively high false negative rate (4%~34%) [92] and high false positive rate (70%) [93], particularly with patients having dense breast tissue [94]. In younger women in particular, breast tissue typically presents a higher dense-to-fatty tissue ratio and lesions

occurring in dense-tissue breasts are statistically more likely to be missed by X-ray mammography [95]. Breast compression is required to reduce image blurring and to create uniform tissue density, and this causes discomfort and pain for the patients. Recent research [96] found that X-ray mammography appears to have reduced cancer death rates by only 0.4 deaths per 1000 women, which means it is not only unsafe but also not saving women's lives as was commonly thought. Past research has also shown that adding an annual mammogram to a careful physical examination of the breasts does not improve breast cancer survival rates over physical examination alone.

2.2.2 Ultrasound

Ultrasound imaging, also called ultrasound scanning or sonography is an attractive supplement to mammography because it is widely available, relatively inexpensive and well-tolerated by patients [97]-[98]. It involves the use of a small transducer (probe) and ultrasound gel to expose the body and produces pictures of the inside of the body using high-frequency sound waves [99]-[100]. Because ultrasound images are captured in real-time, they can show the structure and movement of the body's internal organs as well as blood flowing through blood vessels. In the breast, ultrasound is able to differentiate skin, fat, glandular tissue and muscle. Ultrasound can be offered as a breast screening tool for women who are pregnant or at high risk for breast cancer and unable to undergo a mammography examination [100].

In 1998, researchers at the Mayo clinic introduced ultrasound-stimulated vibro-acoustic imaging (USVA) which is based on the radiation force of ultrasound [101]. Vibro-acoustography [102], an imaging modality based on ultrasound-simulated acoustic emission, has been used to image calcifications in human arteries, micro-calcifications in breast tissue and calcified arteries in the breast [103]-[104].

Ultrasound imaging can determine a breast cancer is just a cyst or a lump, or a cyst with a lump inside, but is less efficient than breast X-ray inspection for the detection of early-stage cancer. A major limitation of ultrasound is that breast fat and most cancer cells have similar acoustic properties, and this makes detecting many lesions impossible with ultrasound. Also, it is important to recognize that the vast majority of ultrasound procedures are performed using hand-held devices, making the imaging results highly operator-dependent [100].

2.2.3 Magnetic Resonance Imaging (MRI)

Magnetic resonance imaging (MRI) (see Figure 2.2) creates an image based on the alignment change of hydrogen nuclei, which is caused by a magnetic field (generally 1.0–1.5 T) and radio waves [105]. Detailed MRI images allow physicians to evaluate various parts of the body and determine the presence of certain diseases. MRI has the ability to show dynamic functionality of the breast through the use of contrast agent injections. The main magnet, the gradient coils and the radio frequency coil are the three major components of an MRI system. The sensitivity of MRI in visualizing invasive cancer is 94% to 100%, yet specificity values vary [106]-[107]. Multiple studies demonstrated that breast lesions were successfully detected by MRI while they were unsuccessful detected by mammogram, ultrasound, and a clinical breast exam [108]-[109]. Recent research results [107], [110] found that breast MRI increases the ability to detect small breast cancers in high-risk women compared to mammography and ultrasound.

Currently, there is no study of the impact of MRI on breast cancer recurrence or mortality, an analyses of the cost-effectiveness of MRI, optimize the application and

performance of breast MRI, as well as clarify optimal acquisition protocols are significant works that need to be done [108].

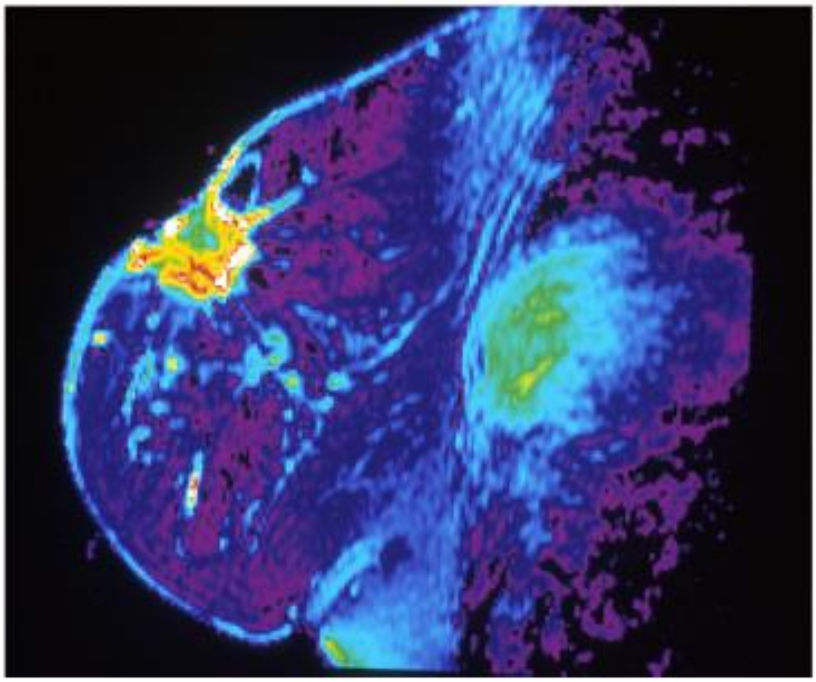

Figure 2.2 Colour Enhanced MRI Image of the Breast [97]

Table 2-1 compares the main features of X-ray mammography, MRI and Ultrasound. Although X-ray mammography remains the most commonly used technique, it can be inaccurate, requires the uncomfortable compression of the breast, can provoke cancer due to ionizing radiation, is unusable during surgery and is relatively expensive. Ultrasound and MRI play an important role in breast cancer detection, however, these techniques are either not yet sensitive enough, have low contrast resolution (small lesion are not detectable), less effective, too operator dependent, or too expensive for screening purpose. These limitations means that there is an urgent need to find a new safe, low-cost, reliable method to compliment X-ray mammography with high image contrast and resolution for early breast cancer detection. One of the most promising emerging imaging technologies for breast cancer detection is microwave imaging.

Table 2-1 Comparison of X-ray mammography, MRI and Ultrasound

Parameter	X-ray mammography	MRI	Ultrasound
Physical property	Tissue density	Hydrogen distribution and binding in tissues	Tissue density
Information provided	Structural, including micro-calcifications	Structural and functional (with CE)	Structural
Spatial resolution	High	Low	Low
Acquisition time	Seconds	Minutes	Minutes
3D information	Limited to 2D views	2D, 3D	2D, 3D
Anatomical distortion	Compression	Gravity	Compression
Specific application	Reconstruction of multiple slices	Lesions lack a characteristic signature, so uptake of a contrast enhancement agent is monitored	
Issues	• Development of effective image processing • Computer aided detection methods easily applied images • Increased radiation exposure	• Breast coils and appropriate imaging sequence required • Expensive method • Proposed for staging of cancer and imaging women with implants	• Less effective • Too operator dependent • Low contrast resolution

2.3 Microwave Imaging

Microwave imaging has gained the attention of an increasing number of research groups over the last couple of decades [42]-[86]. Compared to X-ray mammography, microwave imaging can potentially offer an earlier detection of breast cancer due to the fact that microwaves detect dielectric property changes while X-rays detect structural changes and importantly dielectric properties changes occur before structural changes in tissue cells [79]. Other advantages include it is non-ionizing, does not require breast compression, is less invasive than X-rays and is potentially low cost [97].

Using electromagnetic waves of radio range for non-invasive diagnostics and imaging of human organs and tissue has been tried by a number of research groups [42]-[86]. Recent investigations [78]-[86] have demonstrated that microwaves could offer a new low cost non-ionising technique for the detection and imaging of breast cancer lesions.

Microwave imaging is based on the fact that an inhomogeneity in the constitutive electromagnetic parameters (permittivity and conductivity) of a material will cause an incident electromagnetic field to scatter [111]. Figure 2.3 shows a schematic of a microwave imaging system.

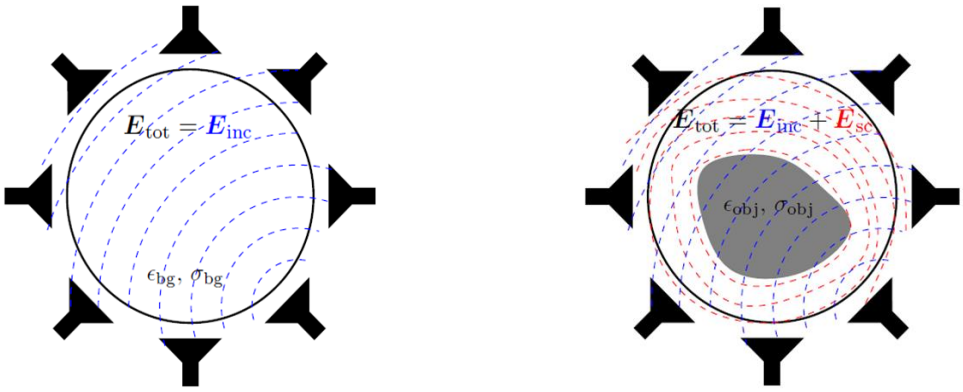

(a) (b)

Figure 2.3 Schematic of a microwave imaging system (a) Empty system (b) Object inserted in system [111]

Figure 2.3 (a) shows a background medium (fat tissue) in which the microwave imaging system is embedded. It is characterized by the permittivity, ε_{bg} , the conductivity, σ_{bg}, and the circular area in the centre of the antenna group represents the imaging domain. This domain is irradiated by a transmitter and the response is measured by one or more antennas positioned outside the domain. When an object (lesion) with contrast in the constitutive parameters, ε_{obj}, and conductivity, σ_{obj}, is positioned inside the imaging domain, a scattered field will arise (see Figure 2.3 (b)). The total field is defined as:

$$E_{tot} = E_{inc} + E_{scat} \tag{2-1}$$

Where E_{inc} is the incident field and E_{scat} is the backscattered field.

2.3.1 Breast Anatomy and Breast Cancer

The breast anatomy as shown in Figure 2.4, is comprised of the chest wall, muscles, lobules, skin areola, nipple, duct and fat tissue. Normally, a breast has between 15 to 20

lobes arranged in a circular fashion and each lobe is comprised of many smaller lobules, each lobule, in turn, contains several sac-shaped glands [112]. A healthy breast consists mainly of fat tissue surrounding glandular structures that include both the lobules and the ducts that connect the lobules to the nipple. Ducts connect the lobes, lobules and glands in nursing women and milk is delivered through ducts to the nipple [113]. Embedded in the fatty breast tissue there are also lymph nodes and small organs that store white blood cells.

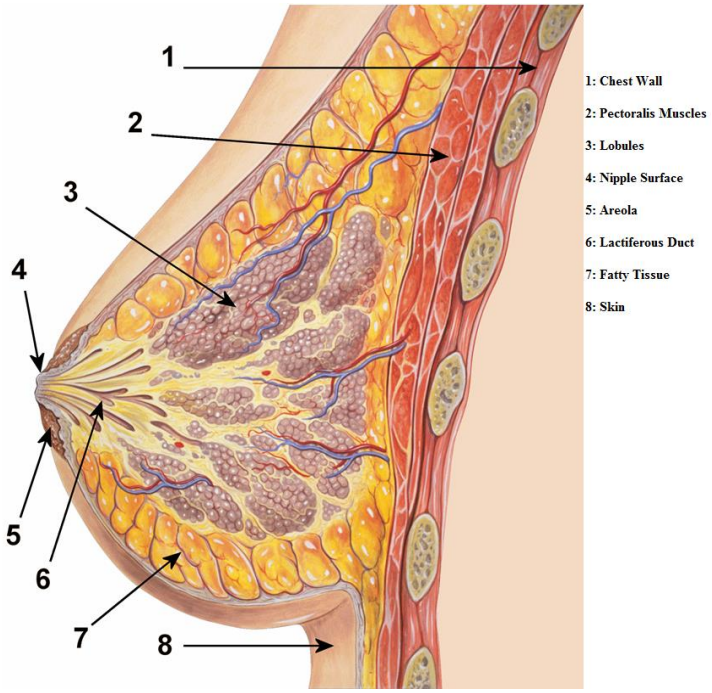

Figure 2.4 Anatomy of the breast [113]

Breast cancer is an unusually fast cell growth within the breast tissue, often in the epithelium of the lobules and ducts [113]. Cancer cells normally clump together to form tumours, which then spread into surrounding tissue and will make the person very ill and possibly die if a cancerous lesion is not identified and treated promptly [112]. Cancers can be divided into two groups: non-invasive and invasive. Non-invasive cancer normally grows in a small area that has not metastasized into surrounding tissue. Invasive cancer is more dangerous and harder to treat because it has already metastasized into nearby tissue [112]. It should also be noted that breast cancer can also

occur in men and many risk factors can increase the chance of developing breast cancer, such as, age, family history, personal history, alcohol consumption and whether the person is overweight [114].

There are several types [114] of non-invasive breast cancer, such as ductal carcinoma in situ (DCIS) [starts inside the milk ducts], lobular carcinoma in situ (LCIS) [is caused by cancer cells growing in the lobules] and Paget's disease [cancer cells develop in the ducts just below the nipple and progress to invade the nipple].

There are three common types [114] of invasive breast cancer, invasive ductal carcinoma (IDC) [the most common type of breast cancer, about 80% of all breast cancers are IDC], invasive lobular carcinoma (ILC) [about 10% of all the breast cancers are ILC] and inflammatory breast cancer (IBC) [about 5% of all the breast cancers are IBC]. It is important to note that IBC is the most dangerous invasive breast cancer as it is a rare and aggressive form of breast cancer [112].

2.3.2 Electrical Properties of Breast Tissue

The fundamental basis for microwave breast imaging is the high contrast between the permittivity and conductivity of healthy and malignant breast tissue in the microwave radio spectrum. A variety of studies of the dielectric properties of malignant and healthy breast tissues at microwave frequencies have been documented [17]-[25]. This section will review several published dielectric properties of various breast tissues at microwave frequencies, as well as the measurement techniques and challenges associated with them.

Permittivity is actually a complex number and the complex permittivity of a material, ε^*, in general is defined as [115]:

$$\varepsilon^* = \varepsilon' - j\varepsilon'' \tag{2-2}$$

Where $j = \sqrt{-1}$, ε' is the real part of the dielectric constant, ε'' is the imaginary part of the dielectric loss factor that characterizes the material's ability to absorb energy and to attenuate it.

The loss factor can also be represented by conductivity σ:

$$\sigma = \omega\varepsilon_0\varepsilon'' \tag{2-3}$$

Where the angular frequency $\omega = 2\pi f$, f is the frequency and ε_0 is the permittivity of free space ($\varepsilon_0 = 1$).

The relative permittivity ε_r is defined as:

$$\varepsilon_r = \frac{\varepsilon'}{\varepsilon_0} \tag{2-4}$$

The total dielectric loss tangent, $tan\,\delta$, can be used to express losses in the material and it is defined as [115]:

$$tan\,\delta = \frac{\varepsilon''}{\varepsilon'} \tag{2-5}$$

2.3.2.1 Model of the Electrical Properties of Breast Tissue

In biological tissues, both the dielectric permittivity and conductivity are strongly non-linear functions of frequency [116]. There are different models used to study the effect of an incident field in a body and Debye and Cole-Cole models are the two most used models in microwave imaging for breast cancer detection [117].

The Debye model sufficiently models the frequency dependence of the complex permittivity of the tissues, and this model is defined as follow [116]:

$$\varepsilon_r = \varepsilon_\infty + \frac{\varepsilon_s + \varepsilon_\infty}{1 + j\omega\tau} - j\frac{\sigma}{\omega\varepsilon_0} \tag{2-6}$$

Where ε_∞ is the permittivity and its value depends on the water content of the tissue, ε_s is the static permittivity, and τ is the characteristic relaxation time of the medium.

The Cole-Cole model [117] was introduced by K. S. Cole and R. H. Cole that gives an alternative to the Debye model:

$$\varepsilon^*(\omega) = \varepsilon_\infty + \frac{\varepsilon_s - \varepsilon_\infty}{1 + (j\omega\tau)^{1-\alpha}} \tag{2-7}$$

Where ε^* is the complex dielectric constant, ε_s and ε_∞ are static and infinite frequency dielectric constants, ω is the angular frequency and τ is a time constant. The exponent parameter α, which takes a value between 0 and 1 describes different spectral shapes. When $\alpha = 0$, the Cole-Cole model reduces to the Debye model. When $\alpha > 0$, the relaxation is stretched.

In 1996, Gabriel *et al*. [20] measured the dielectric properties of biological tissues based on the following equation:

$$\varepsilon^*(\omega) = \varepsilon_\infty + \frac{\varepsilon_s - \varepsilon_\infty}{1 + (j\omega\tau)^{1-\alpha}} + j\frac{\sigma}{\omega\varepsilon_0} \tag{2-8}$$

In 2007, Lazebnik *et al*. [24]-[25] studied the dielectric properties of normal breast tissue and cancerous tissue based on the Cole-Cole equation:

$$\varepsilon^*(\omega) = \varepsilon_\infty + \sum_n \frac{\varepsilon_s - \varepsilon_\infty}{1 + (j\omega\tau)^{1-\alpha}} + \frac{\sigma}{j\omega\varepsilon_0} \tag{2-9}$$

2.3.2.2 Measurement Techniques of Electrical Properties of Breast Tissue

The dielectric properties of breast carcinoma and normal tissues at frequencies from 3 MHz to 3 GHz (using frequency and time domain dielectric spectroscopy) have been studied by Chaudhary *et al.* in 1984 [86]. The sample was placed in a chamber at the centre of a parallel plate capacitor between 3 MHz and 100 MHz, and the measurements were obtained with an impedance meter that was corrected for lead inductance. The time-domain method was used to perform the measurements from between 100 MHz and 3 GHz. This study examined 15 patients and their normal and malignant tissues were investigated. The result showed that the electrical properties of malignant tissues are increased compared to normal tissues. The permittivity and conductivity increasing by at least a factor of 4 at 3 GHz.

In 1988, Surowiec *et al.* [18] measured the dielectric properties of infiltrating breast carcinoma and selected surrounding non-malignant tissue at frequencies from 20 kHz to 100 MHz. Samples of excised human tissues were obtained from the centre of the lesions, the margins of the lesions and from normal breast tissues. In this study, lesion specimens from 7 patients were used and 28 samples were studied in total. The samples were examined within 4 hours of excision and cut from the excised tissue in the form of thin disks (6 mm in diameter and 1 mm thick). The input reflection coefficient at 101 frequencies from 100 KHz to 100 MHz was measured by using an automatic network analyser and an end-of-line coaxial sensor. The measurements were performed at 37 degree Celsius and each sample measured 10 to 15 times and the results were fitted to Cole-Cole dielectric relaxation models.

Table 2-2 shows the measurements of the three different ranges of the dielectric constant, where the permittivity and conductivity ranges are determined at 100 KHz, while the conductivity increment is the difference in conductivity between 100 KHz and 100 MHz. This study found that significantly higher permittivity values for the central part of the lesion and the infiltrating margins compared to tissue taken from the periphery of the lesion. They suggested that the high permittivity associated with the infiltrating margins of the lesion was due to lesion cell proliferation and could result in a large microwave scattering, allowing for the identification and localisation of small lesions using UWB radar.

Table 2-2 Measurement of breast tissues [18]

Tissue	$\boldsymbol{\varepsilon_r}$	$\boldsymbol{\sigma}$ **(S/m)**	$\boldsymbol{\sigma}$ **increment (S/m)**
Bulk lesion	2000 to 6000	0.2 to 0.4	0.4 to 0.5
Lesion margins	2500 to 8000	0.4 to 0.7	0.5 to 0.7
Normal breast tissue	<500	0.1	<0.05

In 1994 Joines *et al.* [19] measured the dielectric properties of freshly excised tissues from several organs, including breasts, at frequencies ranging from 50 MHz to 900 MHz. A flat-ended coaxial probe was used to measure freshly excised tissues, and each sample was measured 3 times at different positions. The results showed that breast tissue had the largest contrast between normal and malignant tissues of the investigated tissue types that included colon, kidney, liver, lung, breast and muscle. They observed the greatest dielectric contrast between normal and malignant tissue for the mammary gland, with an average difference in relative permittivity and conductivity of 6.4:1 and 3.8:1 respectively, which is in general agreement with the measurements of Chaudhary *et al* [86].

Figure 2.5 shows a summary of measurements from the previous three studies based on the single-pole Debye equation and a comparison of the permittivity and conductivity between normal and malignant tissue over microwave frequency range.

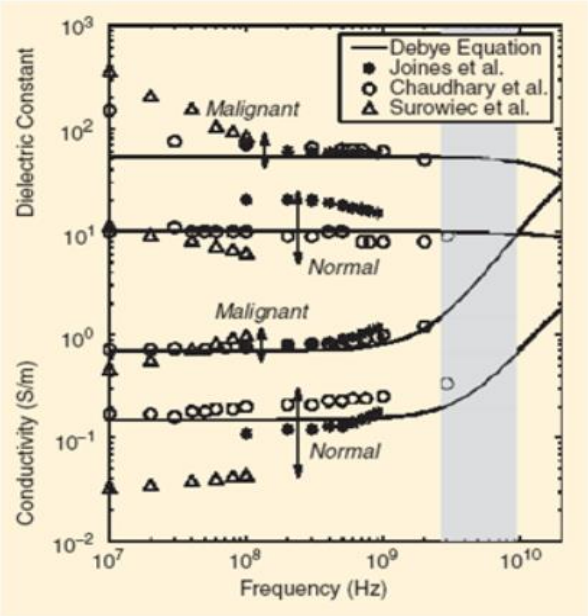

Figure 2.5 Measured baseline dielectric-properties data for normal and malignant breast tissue at radio and microwave frequencies [25]

Gabriel *et al*. [20] published the measurement results of the dielectric properties of biological tissues in the frequency range 10 Hz to 20 GHz in 1996. Three material sources including excised animal tissue, human autopsy materials, human skin and tongue were used in this study. An automatic swept-frequency network and impendence analyzer were used to perform the dielectric measurements and open-ended coaxial probes were used to interface the measuring equipment with the samples in all cases. The investigation indicated that electrode polarization errors affect the results below 1 KHz and became significant below 100 Hz in the case of tissue samples. At 6 GHz, dielectric properties of normal breast tissue are about $\varepsilon_{r-breast} = 9$ for the permittivity and $\sigma_{breast} = 7$ S/m for the conductivity, which are similar to those of fat. The dielectric properties of a malignant lesion are $\varepsilon_{r-lesion} = 50$ for the permittivity and $\sigma_{lesion} = 7$ S/m for the conductivity, which are similar to those of muscle. This

dielectric contrast causes malignant lesions to have significantly larger microwave backscattering cross sections relative to normal tissues of comparable size and geometry. The permittivity $\varepsilon_{r-skin} = 36$ and the conductivity $\sigma_{skin} = 7$ S/m were found for breast skin tissue.

A recent study of the dielectric properties of normal breast tissue and cancerous tissue from 0.5 GHz to 20 GHz using a precision open-ended coaxial probe was performed by Lazebnik *et al.* in 2007 [24]-[25]. The tissue composition within the probe's sensing region was quantified in terms of percentages of adipose, fibroconnective and glandular tissues. This study involved 93 patients and over 400 benign tissue samples were collected. Results showed that the dielectric heterogeneity of the breast tissues was larger than previous studies. Figure 2.6 shows the dielectric properties of normal breast tissues have a wide range of values depending on tissue type. The solid lines show dielectric properties of 85% to 100% adipose tissues, while the top lines show 0% to 30% and 31% to 84% adipose tissues. Results illustrated that both the dielectric constant and conductivity tend to decrease as the adipose content increases, and conversely as the percentage of glandular and/or fibroconnective tissue increases, both the dielectric constant and conductivity increase [11]. This study determined that the dielectric properties of breast tissue are primarily determined by the adipose content of each tissue sample. Patient age, tissue temperature and time between excision and measurement had only negligible effects on the observed dielectric properties and there was no statistically significant difference between the within-patient and between-patient variability in the dielectric constant and effective conductivity.

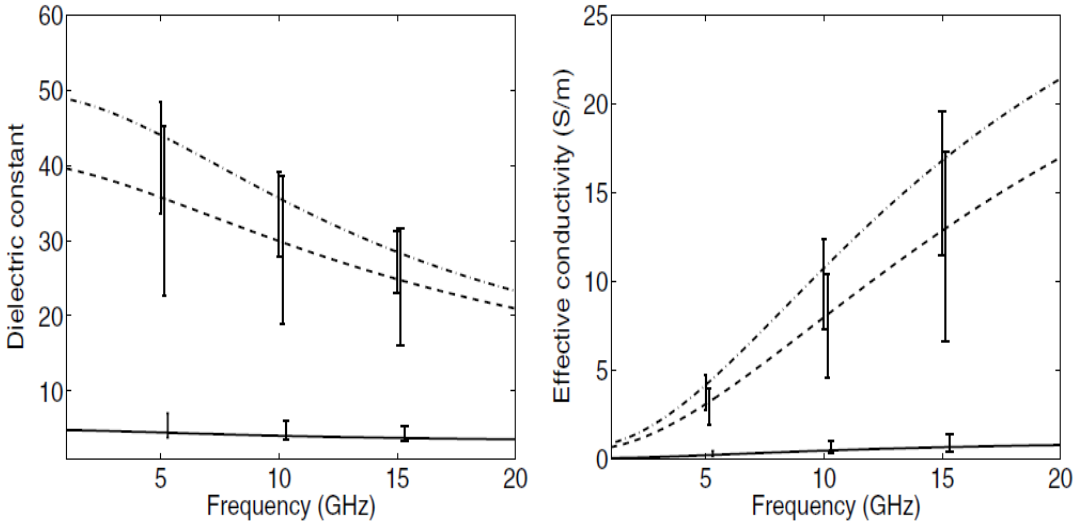

Figure 2.6 Measured dielectric properties of the three tissue groups defined by percentage adipose tissue present in the sample. The variability bars show the 25th–75th percentiles of the fitted values. Dash-dot line: group 1 (0%~30% adipose), dashed line: group 2 (31%~84% adipose), solid line: group 3 (85%~100% adipose) [25]

Lazebnik *et al*. [25] compared their results with the results of previous studies [18]-[20] and found only a 10% difference between the conductivity of normal tissue and malignant tissue, and approximately an 8% difference in permittivity at 5 GHz by adjusting for adipose content. However after adjusting for adipose and fibroconnective tissue, their results showed no statistical differences between normal glandular and malignant glandular tissues in the breast. This presents a much more difficult imaging scenario than previously assumed [18]-[20].

2.4 Microwave Imaging Techniques

Microwave imaging techniques for medical applications have been investigated by many groups [51]-[86] over the last few decades. Microwave imaging techniques can be divided into three approaches: hybrid, passive and active microwave imaging as illustrated in Figure 2.7 [118].

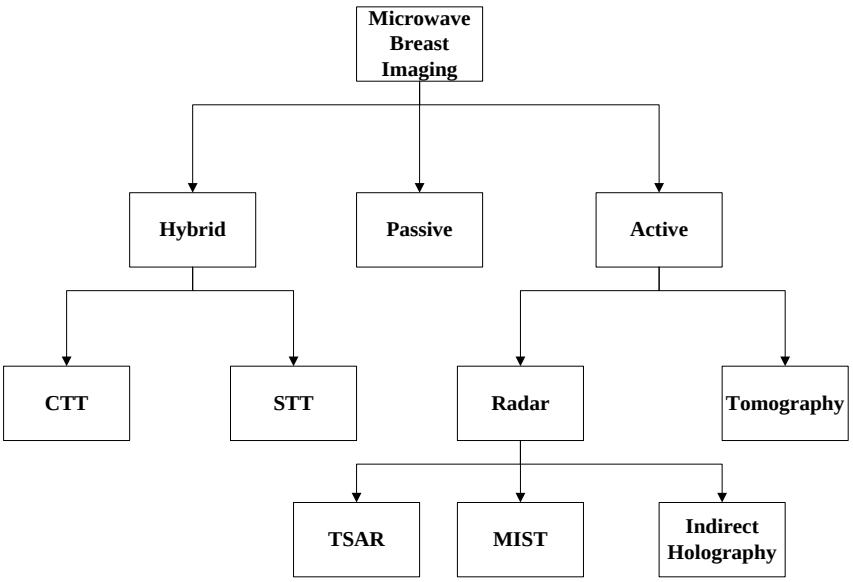

Figure 2.7 Microwave imaging techniques [118]

2.4.1 Hybrid Microwave Imaging

Hybrid approaches involve heating the tissue with microwaves and detecting the pressure waves generated by the mechanical expansion of the tissue. The basis of lesion detection is differential heating of the lesion compared to normal breast tissue. Computed thermoacoustic tomography (CTT) and scanning thermoacoustic tomography (STT) are two approaches of a hybrid microwave-acoustic imaging system.

In CTT, ultrasound transducers are used to record the signals and a filtered back-project algorithm adapted from X-ray computed tomography is used to form an image. In the proposed system [119]-[120], the breast was placed in a water-bath and illuminated with $0.5\,\mu s$ pulses and 434 MHz signals using waveguides were used to generate acoustic waves in the medical region. 64 ultrasound transducers with a peak frequency of 1 MHz were arranged in a spiral pattern in a hemispherical stainless steel bowl. The results showed that this system has the ability to detect lesions of 1 cm to 2 cm in diameters. STT is much simpler as it uses a focused ultrasound transducer that was first developed by L. Wang [121]. Images of breast phantoms have been successfully obtained and

numerous improvements on imaging algorithms for the STT approach have been published [115], [122]. The time response recorded at the transducer was shown to represent the variations in the material along the transducer axis. Images were formed by scanning the transducer along the sample and recording traces at each position. A short microwave pulse and wideband ultrasound transducer achieved axial resolution, while the lateral resolution was related to the transducer aperture and sample-transducer distance.

2.4.2 Passive Microwave Imaging

Passive microwave imaging measures the temperature of the breast by radiometric techniques and compares the formed thermical map images of the target area with corresponding healthy breast area that is obtained at microwave frequencies. Passive microwave radiometry [123] exploits temperature differences between malignant and normal breast tissue.

2.4.3 Active Microwave Imaging

The principle of active microwave imaging illuminates the breast with lower-power microwave signals and detects the reflections by employing a set of receivers or by recording the reflections at the transmitter antenna [118]. The breast will show changes in electrical properties that will cause a variation in the detected energy at the receivers and the transmitters. Images are formed using information contained in the detected energy [118]. In general, active microwave imaging can be categorized into two different techniques: radar-based imaging and tomography.

2.4.3.1 Radar-Based Imaging

Different research groups have conducted radar-based microwave techniques, which can be divided into three major groups: microwave imaging via space time (MIST) [36]-[39], [59], [63], [66], tissue sensing adaptive radar (TSAR) system [39], [59], [54], [65], [67] and indirect holographic technique [76]-[83].

In 1998, Hagness *et al.* [34] introduced a novel active microwave system for breast cancer detection called confocal microwave imaging (CMI). This radar-based imaging approach aims to identify the presence and location of strong scattered reflections based on the significant contrast between the lesion and healthy breast tissue. This technology could provide both the necessary imaging resolution and adequate penetration depth in the breast. During operation, the patient to be scanned lies in a supine position. Seventeen receivers were used to record the reflections, and a spherical lesion of 5 mm diameter that was located 3 cm beneath the array was detected successfully. In their 3D study [35], a resistively loaded 8 cm long bowtie antenna was used as a sensor and a circular lesion of 1.76 cm diameter located 5 cm below the antenna was detected. However, this approach does not compensate for frequency-dependent propagation effects and has limited ability to discriminate against artifacts and noise.

In 2003 the MIST system was introduced for detecting early stage breast cancer [38]. The beam former spatially focuses the backscattered signals to discriminate against clutter and noise while compensating for frequency-dependent propagation effects. In the MIST system, the patient lies in a supine (face-up) position on the examination table with the antennas scanned over the naturally flattened breast. Their simulation results showed that a 2 mm lesion in a 2D breast model derived from magnetic resonance

imaging could be detected [38]. They also developed a method to remove skin-breast interface that produced artifacts in the image prior to performing lesion detection. In 2004 [41] they presented an experimental set-up consisting of a breast phantom simulated as a container filled with a liquid mimicking normal breast tissue, a small synthetic lesion suspended in the liquid and a thin layer of material representing the skin layer.

Tissue Sensing Adaptive Radar (TSAR) was proposed for breast imaging by Fear *et al.* [64]-[65]. This algorithm contains three steps: tissue sensing to locate the breast in the tank, the skin reflections are estimated and subtracted and finally the breast image is formed from the reflection signals without skin reflections. In the TSAR system, the patient lying in the prone (face-down) position on the examination table with her breast extending through a hole in the examination table and the antennas are scanned around the breast. Results showed that this technique has the ability for detecting and localizing lesions (>4 mm diameter). Difficulties of this technique include large reflections of the radio pulse from the skin and very high cost of ultra-high speed digital electronics required for real-time imaging [118].

Indirect holography microwave (IHM) uses the application of Fourier transforms and direct back transformation onto the measured interference pattern at microwave frequencies. This technique involves recording of a holographic intensity pattern and reconstructing the image by using Fourier transformation from the 2D holographic intensity pattern produced [77]. Compared with the TSAR technique, IHM does not require expensive ultra-high speed electronics, as narrow-band signals can be converted to the baseband for digitisation at a slower rate, thereby enabling real-time imaging at significantly lower cost [78]. It also offers high contrast between healthy and malignant

tissues and assists in forming an image of the location and extent of the malignant tissue.

2.4.3.2 Microwave Tomography

Microwave tomography for applications in medicine has been investigated for many years [26]-[30], [124]. Meaney *et. al* [29]-[30] conducted clinical trials with a tomography prototype system which has produced some promising results. During the procedure, the woman lies face-down on the examination table with her breast extending through a hole in the examination table. Numerous antennas are located surrounding the breast, which is immersed in liquid for minimizing the contrast with the body [118]. The tomography-based approach reconstructs the spatial distribution of the dielectric properties of the whole breast. This is usually done iteratively and thus requires significantly more computational power than the radar-based approaches.

Different tomographic techniques [125]-[129] have been suggested for imaging of the breast, such as single-frequency, multi-frequency, and time-domain tomography. These algorithms have different requirements to the hardware of the imaging system as well as the computational power needed to create the images.

2.4.4 Microwave Imaging Systems

Several experimental microwave imaging systems have been developed in several countries over the last decade as shown in Table 2-3. Few of them have been applied in clinical trials, while others have been exploited for laboratory research. In most of these systems a bath with a coupling liquid was required for better matching of antennas with

the imaging object (human breast or other parts of the body). This requirement significantly increased the system cost and difficulty of practical implementation.

Table 2-3 Experimental Microwave Imaging Systems

System	Antenna	Frequency	Breast Phantom	Immersion medium	Image	Clinical trial
Dartmouth College (USA) [30]-[34]	Circular array of 16 (Tx/Rx) monopoles	0.5~3 GHz	Real patients	0.9% saline ($\varepsilon_r = 76.6$, $\sigma = 2.48$ S/m)	2D, 3D	Yes
Keele University (UK) [42]-[44]	Circular array of 24 Tx/Rx ceramic filled opened waveguides	1.0~2.3 GHz	Soft animals tissues, like pig's extremities	Metallic bath with the coupling liquid	2D	No
Univerity of Bristol (UK) [45]-[47]	Two spherical arrays that consists of 31 and 60 UWB antennas	4~8 GHz	Real breast	Matching ceramic inserts	3D	Yes
University of Manitoba (Canada) [48]-[50]	Circular array of doubled layers Vivaldy antennas	3~6 GHz	Different dielectric objects	No matching medium, air only	2D	No
Chalmers University of Technology (Sweden) [51]	Circular array with 20 short monopoles	0.5~4.5 GHz	Multistatic scattering matrix	Metallic bath containing the coupling liquid	2D	No
Electronics and Telecommunications Research Institute (Korean) [52]	Circular array with 16 monopoles	500~3000 MHz	Different dielectric objects ($\varepsilon_r = 40, \sigma = 0.2$ S/m)	Plastic bath with the coupling liquid ($\varepsilon_r = 20, \sigma = 1.3$ S/m)	3D	No

2.5 Holographic Interferometry in Breast Imaging

Denis Gabor first developed the theory of holography in 1948 [130]. This process includes writing and reading the hologram. Figure 2.8 shows Gabor's experimental set-up for writing the hologram that involves recording on film the amplitude and phase

information. A point source of monochromatic light is collimated by a lens and the resulting collimated beam illuminates the semi-transparent object. An intensity distribution of an object is generated by the interference when the light source passes through a semi-transparent object [131]:

$$I(x,y) = |U_0 + U_1(x,y)|^2 \\ = |U_0|^2 + |U_1(x,y)|^2 + U_0 U_1^*(x,y) + U_0^* U_1(x,y) \quad (2\text{-}10)$$

Where U_1 is the scattered field and U_0 is the unscattered field.

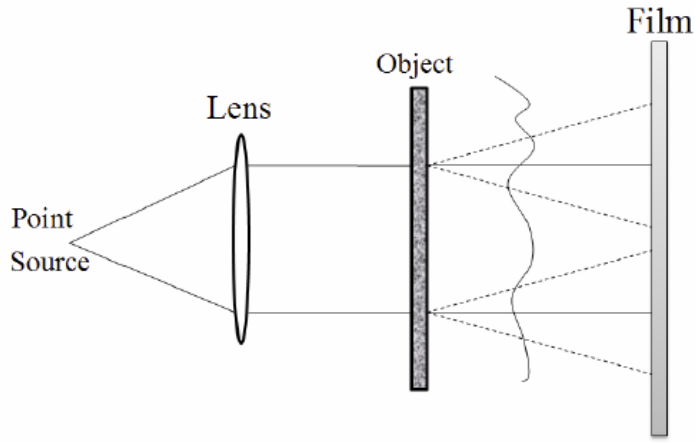

Figure 2.8 Inline optical set-up for writing an hologram [131]

The transmission function is formed when assuming a linear response to intensity associated with the photographic film [131]:

$$t(x,y) = a + bI(x,y) \quad (2\text{-}11)$$

Where a and b are constants, $I(x,y)$ is the intensity of the incident light at the photographic plate.

Figure 2.9 demonstrates reading an inline hologram. The field scattered from the hologram is the product between the illuminating plane wave (assumed to be U_0) and the transmission function [131]:

$$U(x,y) = U_0 t(x,y) \\ = U_0(a + b|U_0|)^2 + bU_0|U_1(x,y)|^2 + b|U_0|^2 U_1(x,y) \\ + bU_0^2 U_1^*(x,y) \quad (2\text{-}12)$$

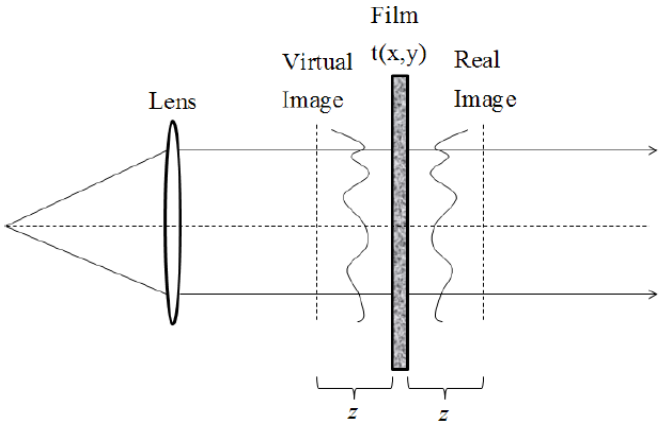

Figure 2.9 Reading an in-line hologram [131]

Leith and Upatnieks pioneered the off-axis hologram technique for the recording of optical wave-fronts in 1962 [132], who greatly boosted the development of holography. This technique consists two stages: recording of the hologram and image reconstruction. Figure 2.10 shows the recording of an off-axis hologram. A separate coherent reference wave that is assumed to be a collimated beam of uniform intensity, is allowed to fall on the hologram plate at an offset angle θ to the beam from the object. The intensity at the photographic plate is defined as [133]:

$$I(x,y) = |R(x,y) + O(x,y)|^2 \\ = |R(x,y)|^2 + |O(x,y)|^2 + R|O(x,y)|e^{-j\phi(x,y)}e^{-j2\pi\alpha x} \\ + R|O(x,y)|e^{-j\phi(x,y)}e^{-j2\pi\alpha y} \\ = |R|^2 + |O(x,y)|^2 + 2RO(x,y)\,cos(2\pi\alpha y - \phi(x,y)) \quad (2\text{-}13)$$

Where the amplitude of the object $O(x,y) = |O(x,y)|e^{-j\phi(x,y)}$, the reference beam $R(x,y) = Re^{-j2\pi\alpha y}$, $\alpha = \sin\theta/\lambda$ is the spatial frequency, λ is the wavelength.

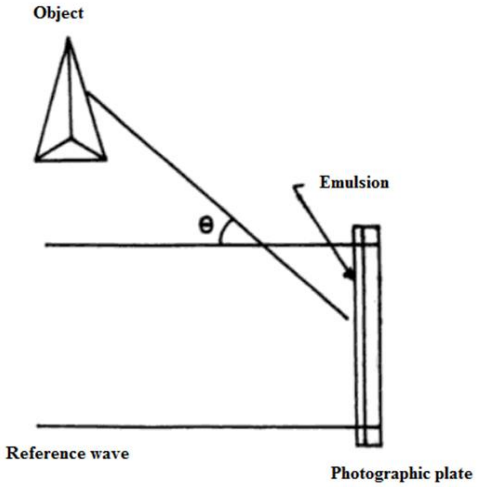

Figure 2.10 Recording of an off-axis hologram [133]

The amplitude and phase of the object beam are encoded respectively as amplitude and phase modulation of a set of interference fringes equivalent to a spatial carrier wave with a spatial frequency. The exposed plate is developed by normal photographic procedures. If the amplitude transmittance $t_A(x,y)$ of the plate after development is proportional to the exposure then:

$$t_A(x,y) = t_b + \beta\{|O(x,y)|^2 + R|O(x,y)|e^{-j\phi(x,y)}e^{-j2\pi\alpha y} + R|O(x,y)|e^{j\phi(x,y)}e^{-j2\pi\alpha y}\} \quad (2\text{-}14)$$

Where β is the slope of t_A versus exposure response characteristic of the photographic material and t_b is a constant background transmittance.

Figure 2.11 displays the reconstruction process of an off-axis hologram. The hologram is illuminated, for example by a plane wave of uniform amplitude B. The amplitude $U(x,y)$ of the transmitted wave is [133]:

$$U(x,y) = U_1(x,y) + U_2(x,y) + U_3(x,y) + U_4(x,y) \quad (2\text{-}15)$$

Where $U_1(x,y) = Bt_b$, $U_2(x,y) = B\beta|O(x,y)|^2$,

$U_3(x,y) = B\beta R|O(x,y)|e^{-j\phi(x,y)}e^{j2\pi\alpha y}$,

$U_4(x,y) = B\beta R|O(x,y)|e^{j\phi(x,y)}e^{-j2\pi\alpha y}$.

The reconstruction process consists of four terms, which $U_1(x,y)$ is merely a plane wave of uniform amplitude travelling along the axis, $U_2(x,y)$ corresponds to a halo around the direct beam. If the spatial frequency content of the object is not too large, the angular spread due to the second term is small. The third term $U_3(x,y)$ is proportional to object wavefront $O(x,y)$ multiplied by a linear exponential factor. Proportionality indicates the generation of a virtual image of the object at the same distance from the hologram. $U_4(x,y)$ gives rise to the conjugate image, identical to the object wavefront except that is of opposite curvature [133].

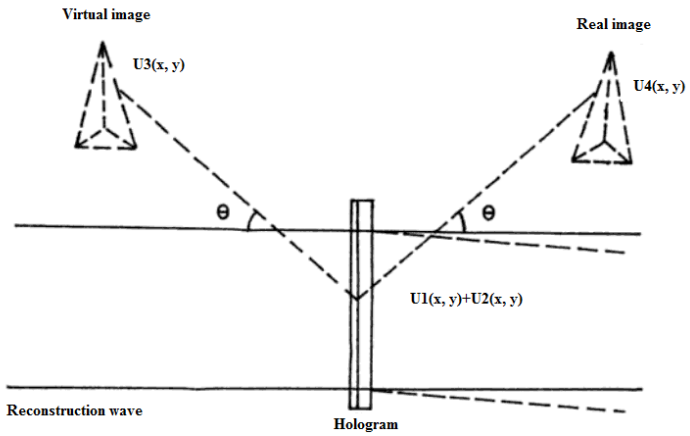

Figure 2.11 Reconstruction of an off-axis hologram [133]

Holographic interferometer (HI) has been established as a non-destructive method for detection of defects within composite materials [134]. This process uses mild or moderate physical stressing, such as changes in environmental pressures, sound waves or mechanical vibration to cause a surface displacement on the object being tested [134]. A holographic technique with a moving transmitter-receiver interferometer, as used to examine surfaces of parabolic antenna was proposed for breast cancer detection in 1993 [135]. The adoption of the off-axis hologram technique at microwave frequencies for breast cancer has been described [81]-[83]. An electronically

synthesised reference signal replaced the radiated reference wave in this proposed system and an outline of the system as shown in Figure 2.12.

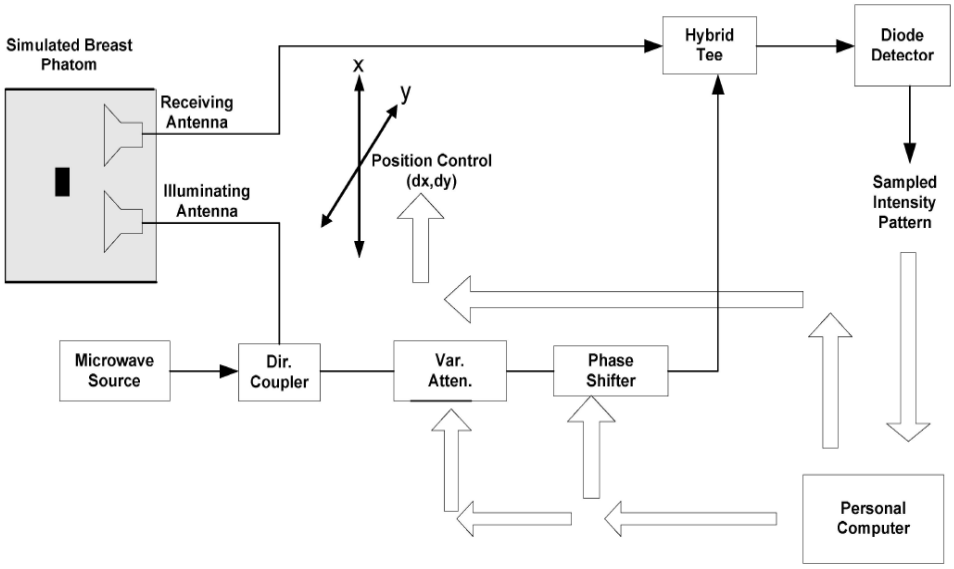

Figure 2.12 Experimental arrangement for intensity pattern measurements [81]

This technique consists of two steps: the first stage is the recording of a sampled intensity pattern $I(x,y)$ by combining the scattered signal from the object $E(x,y)$, with a reference signal $R(x,y)$:

$$\begin{aligned} I(x,y) &= |E(x,y) + R(x,y)|^2 \\ &= |E(x,y)|^2 + |R(x,y)|^2 + E(x,y)R^*(x,y) \\ &\quad + E^*(x,y)R(x,y) \end{aligned} \tag{2-16}$$

The second stage is the reconstruction of the complex field of the antenna $E(x,y)$, from the hologram by the Fourier transform of the intensity pattern of equation (2-16):

$$\begin{aligned} F\{I(x,y)\} &= F\{|E(x,y)|^2\} + F\{|R|^2\} + F\{E(x,y)\} \otimes F\{R^*(x,y)\} \\ &\quad + F\{E^*(x,y)\} \otimes F\{R(x,y)\} \end{aligned} \tag{2-17}$$

Where $\otimes$ denotes convolution.

2.6 Finite Difference Time Domain (FDTD) Method

All microwave imaging approaches that have been described earlier require accurate numerical breast phantoms to model the propagation and scattering of microwave signals within the breast [136]. The finite-difference-time domain method (FDTD) is the most commonly used numerical modelling techniques to model the propagation of electromagnetic (EM) waves in biological tissue. An accurate FDTD model must account for the physical geometry of the breast, the heterogeneity and the dispersive nature of normal breast tissue. The design of an FDTD model of the breast depends on the imaging approach taken. The planar configuration [38] and the cylindrical configuration [76] have been considered as the most widely used existing imaging configurations.

Figure 2.13 shows the 2D FDTD model of the breast that was developed by Hagness *et al.* [38].

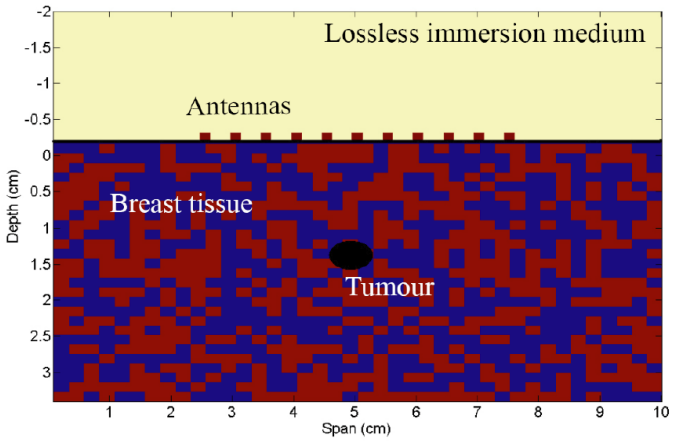

Figure 2.13 The 2D FDTD model as developed by Hagness et al. [38]

This model is based on the planar configuration, which consists of a naturally flattened breast made of normal breast tissue, malignant breast tissue, glandular tissue and veins. The typical depth of a normal non-lactating breast is 5 cm. A planar array of antenna is

placed across the naturally flattened breast and the dielectric of the normal breast is varied by $\pm 10\%$ in a checkerboard pattern. The dielectric properties of the normal breast used in Hagness's model are based on the dielectric properties measured by Joines *et al.* [19] and Chaudhary *et al.* [86] and extrapolated to higher frequencies by Foster and Schwan [137] using the Debye model [116].

A cylindrical configuration based FDTD breast model was developed by Fear *et al.* [76] with the patient positioned in the prone position and the breast extending naturally through a hole in the examination table. The breast itself is modelled as a 6.8 cm diameter cylinder, with a 2 mm layer of skin. Figure 2.14 displays the homogeneous and heterogeneous tissue model as developed by Fear *et al.* [76].

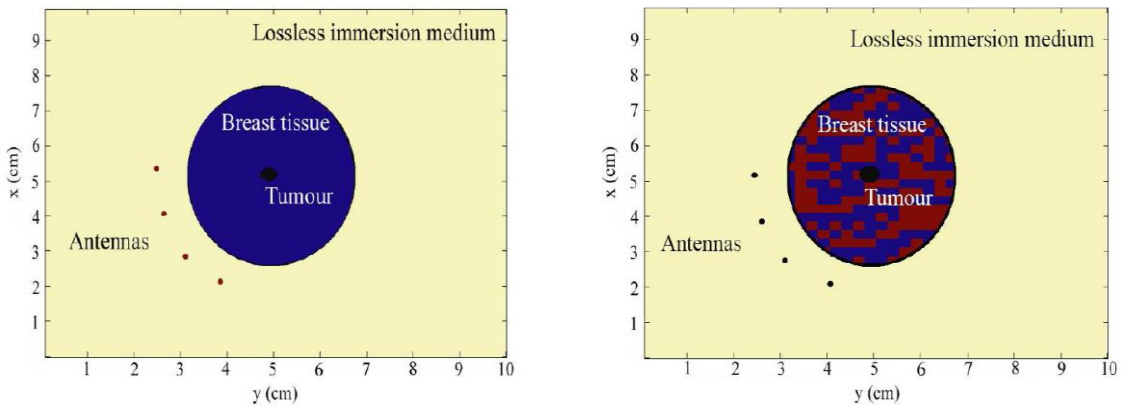

(a) (b)

Figure 2.14 (a) The homogenous cylindrical model (b) the heterogenous model as developed by Fear *et al.* [76]

This model is similar to Hagness's model in that the heterogeneity of breast tissue was incorporated by varying the dielectric properties by $\pm 10\%$ around the nominal values, in line with data from Joines *et al.* [19] and Chaudhary *et al.* [86]. Important differences from Hagness's model are: no Debye or any other method to model the dispersive nature of breast tissue was included in Fear's model because she assumed that dispersive or pulse broadening effects of the breast tissue was negligible for the confocal microwave imaging (CMI) approach. It should be noted that in contrast to

Hagness's model where the antenna were placed across the surface of the breast, in Fear's model the antennas were placed at a distance of either 1 cm or 2 cm from the surface of the skin.

Figure 2.15 shows the 2D MRI based FDTD model developed by Li *et al.*[138]. A planar array of antennas is placed across the naturally flattened breast. The distribution of adipose and fibroglandular tissue within the breast is clearly displayed in this modified MRI scan. In this model, a high resolution MRI of the breast was taken with the patient in the prone position, and a second low resolution MRI was taken with the patient oriented in the supine position. The low resolution MRI of the patient in the supine position was used to horizontally expand and vertically compress the high resolution scan, so the overall shape of the high resolution scan matched that of the low-resolution scan. The MRI artifacts were removed from the image and a linear interpolation scheme was used to map the MRI image to the FDTD grid. The Debye model also was used in Li's model to simulate the dispersive nature of breast tissue. A tolerance of $\pm 10\%$ around the nominal value was used since it represented the upper bound of breast tissue variability as reported by Joines *et al.* [19] and Chaudhary *et al.* [86].

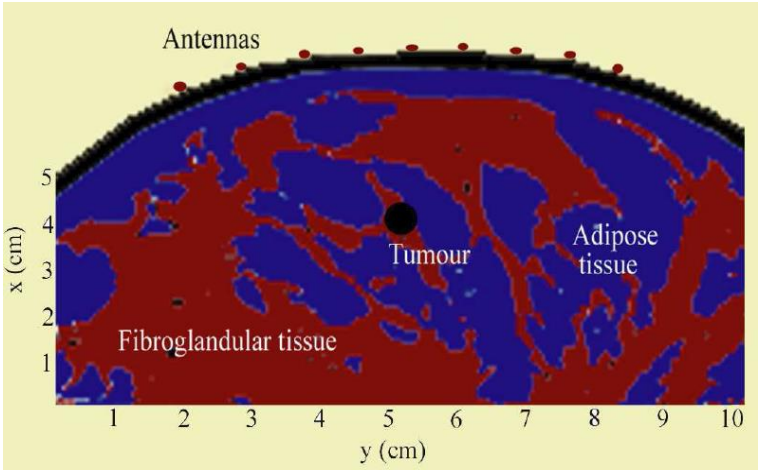

Figure 2.15 The 2D FDTD model as developed by Li *et al.*[138]

2.7 The Proposed Technique

The currently available medical breast imaging and microwave imaging technologies have a number of shortcomings, which are summarized in Table 2-4. The developments of new approaches to overcome the current challenges of imaging techniques for breast lesion detection are needed.

This research aimed to investigate a new microwave imaging approach called Holographic Microwave Imaging Array (HMIA) technique for imaging of dielectric objects, should has the potential to contribute significantly to detection of the breast lesion. The proposed HMIA technique is based on holographic microwave and aperture synthesis imaging techniques. This technique involves two stages: data collection and image reconstruction. In the first stage, a fixed transmitter illuminates microwave waves to a 3D dielectric object, and the backscattered signals from the object are measured by an array of small microwave antennas that are optimally distributed on a flat plane at a far field from the object. In the second stage, a complex visibility data of any two antennas is obtained from the measured data, and then an image is reconstructed from the measured visibility data using the HMIA image processing algorithms.

The applications of the HMIA techniques may help in interpreting the features and improving the diagnosis of breast lesions. Compare to other microwave imaging techniques, this approach is expected to offer the significant benefits in terms of providing a complementary, safe and high-resolution breast image.

Table 2-4 Breast imaging technologies

Technology	**X-ray mammography**	**MRI**	**Ultrasound**	**Computed thermoacoustic tomography**	**Microwave imaging**
Description	The standard X-ray technique	Forms images using radio emissions from nuclear spins	Forms images by reflection of megahertz frequency sound waves	Generates short sound pulses within breast using RF energy and constructs a 3D image from them	Views breast using scattered microwaves
Physical property	Tissue density	Hydrogen distribution and binding in tissues	Tissue density	Electrical property distributions	Electrical property distributions
Used routinely	Screening & diagnosis	Screening & diagnosis	Diagnosis	Diagnosis	Screening & diagnosis
Used infrequently	~	Diagnosis	~	~	~
Clinical data suggests a role	Screening & diagnosis	Screening & diagnosis	Screening	~	~
Data not available yet	~	~	~	Screening & diagnosis	Screening & diagnosis
Advantages	Currently the stand detection method	• No radiation • High-resolution 3D image • Suits for high-risk women with dense breasts	• No radiation • Low cost	• Non-ionizing • Non-invasive medical imaging	• No radiation • More sensitive • Significantly low cost • More comfortable • Suits for high-risk women with dense breasts
Disadvantages	• Ionizing radiation • High rate of missed detections • Unsuitable for pregnant and breast feeding women • Very painful	Expensive	• Less effective • Too operator dependent • Low contrast resolution	• Linear detector is that the lines are not aligned to the object • Measuring the integrated pressure over laser beams around the object does not provide a simple and compact experimental build-up	Discussed in section 2.4

2.8 Closure

In this chapter, various breast imaging technologies and their limitations were discussed and the potential for microwave breast imaging was introduced. Breast structure and electric properties of breast tissue were reviewed. Several approaches to microwave breast imaging and prototype system were described. The holographic microwave imaging of dielectric objects introduced, the application of the proposed technique to breast lesion was envisaged.

The next chapter details the designed 2D HMIA technique for breast lesion detection.

Chapter 3 Two Dimensional Holographic Microwave Imaging Array System Design

3.1 Introduction

The currently available microwave imaging techniques include two dimensional (2D) and three-dimensional (3D) model systems. To successfully investigate microwave imaging for breast lesion detection, it is necessary to develop a realistic 3D breast model. However, a 3D computer model normally requires high computational cost for data acquisition and long image reconstruction time that can be up to eight hours. It also requires a supercomputer to compute and store the large scattering field of a 3D object.

This project presents the initial analysis and development of holographic microwave imaging array (HMIA) technique for breast lesion detection. This study starts with developing a 2D imaging model in a 3D geometry system in order to save computation time and easily investigate the HMIA technique. This chapter presents the basic principles of the 2D HMIA and its suitability for breast lesion detection. The most significant parts of this work are presented in details conference paper 1 [CP1].

In section 3.1 and section 3.2 the 2D HMIA system and the theory of the image reconstruction algorithm are detailed. In section 3.3 the forward model that includes the antenna model, breast model and antenna array configuration used for simulations are presented. In section 3.4 the simulation images of the breast model are presented. In section 3.5 a short summary describing the limitations of the 2D HMIA system are given.

3.2 2D Holographic Microwave Imaging Array (HMIA) Technique

The idea of the HMIA technique for early breast lesion detection is based on the holographic and aperture synthesis far-field imaging technique similar to the one widely used in radio astronomy [139]. The process involves transmitting microwave sources to a dielectric object by a single transmitting antenna and measuring the backscattered electric field from a dielectric object by an array of antennas and using image processing algorithms on the measured data to reconstruct an image.

3.2.1 Imaging System Design

The HMIA technique acquires a set of microwave radiation data, analyses the acquired data and then displays information and images to decipher the existence, size and position of a breast lesion. It has the following two parts: the acquisition of microwave radiation data from breast and the visualization and analysis of the acquired data.

Figure 3.1 shows one of the possible practical implementations of the HMIA technique. The patient lies in a prone position on an examination bed with a hole allowing her breast to extend through and the breast is naturally flattened against the examination bed. The breast hole is made of a material with a dielectric constant close to that of normal average breast tissue. The system consists of an array of 16 small microwave antennas with one of the elements being a transmitting antenna and the others are receiving antennas. The antenna array is located under the examination bed in the far-field. No additional impedance matching medium is necessary between the examination bed and the antenna array, only air, which will greatly simplify the practical implementation of such a system.

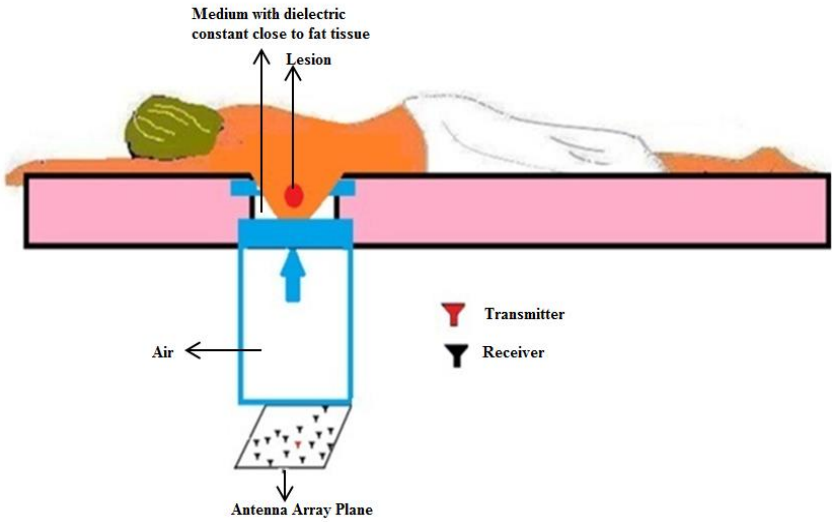

Figure 3.1 HMIA implementation configuration

3.2.2 2D HMIA Imaging Algorithm

Figure 3.2 shows the block diagram of the 2D HMIA technique. During operation, one port of the vector network analyzer (PNA) generates a single frequency microwave signal to the transmitting antenna and the transmitting antenna transmits the electromagnetic wave into the breast through the air where it is scattered in different directions. The backscattered electric field from the breast is received by each receiving antenna that is connected to the remaining port of the PNA in turn via a multi-position switch. Microwave measurements are obtained using the PNA and the measured data is then processed using the HMIA image reconstruction algorithm.

The phase and magnitude of the measured signal at each antenna is used to calculate the complex visibility function for each possible pair of antennas. A 2D breast intensity distribution is reconstructed using an Inverse Fast Fourier Transform (IFFT) on the complex visibility. A 2D projection image on the 2D antenna array plane of a 3D breast image can be obtained from the breast intensity distribution. Details of the imaging algorithm are described in the following section.

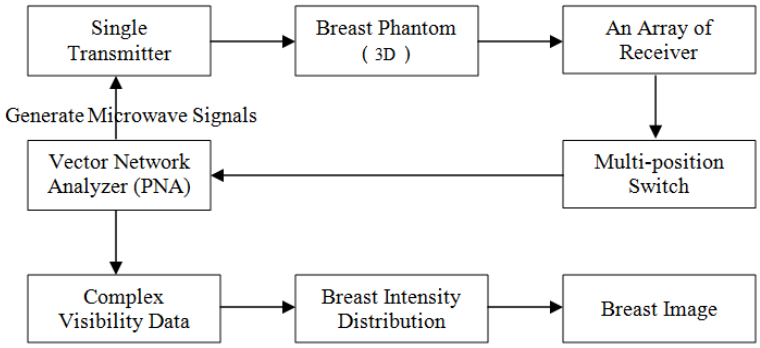

Figure 3.2 The block diagram of the 2D HMIA technique

3.2.2.1 Complex Visibility Function in Far-field

Figure 3.3 shows the 3D geometry relevant to the HMIA technique, where x, y and z represent antenna locations in the array plane. If a point $P(x', y', z')$ is assumed in the breast, under far-field conditions the visibility function of the backscattered electric field $\underline{E}_{scat}$ for any two antennas located at $\underline{r}_1$ and $\underline{r}_2$ is defined as:

$$G(\underline{r}_1, \underline{r}_2) = < \underline{E}_{scat}\left(\underline{r}_1\right) \cdot \underline{E}^*_{scat}(\underline{r}_2) > \tag{3-1}$$

Where the asterisk denotes the complex conjugate and <> stands for the expected value (time average).

It is well known that the scattered electric field can be represented as an integral over the volume of the scatterer involving the induced polarisation currents that arise from the complex permittivity contrast with the host medium [140]. In the far-field of the antenna, the scattered field can then be written as follows:

$$\underline{E}_{scat}(\underline{r}) = \left(\frac{k_0^2}{4\pi}\right) \int_V \left(\varepsilon(\underline{s}) - \varepsilon_b\right) \underline{E}_T(\underline{s}) \frac{e^{-jk_b|\underline{s}-\underline{r}|}}{|\underline{s}-\underline{r}|} dV \tag{3-2}$$

Where $j = \sqrt{-1}$,

$k_0 = 2\pi/\lambda_0$,

$k_b = 2\pi/\lambda_b$,

λ_0=Wavelength in free space,

λ_b=Wavelength in host medium,

$\varepsilon(\underline{s})$=Complex relative permittivity distribution of object,

ε_b=Complex relative permittivity of host medium,

$\underline{r}$=Position vector from a point in the breast to the receiving antenna,

$\underline{E_T}(\underline{s})$=Total electric field (incident plus scattered) at a point inside the breast with position vector $\underline{s}$.

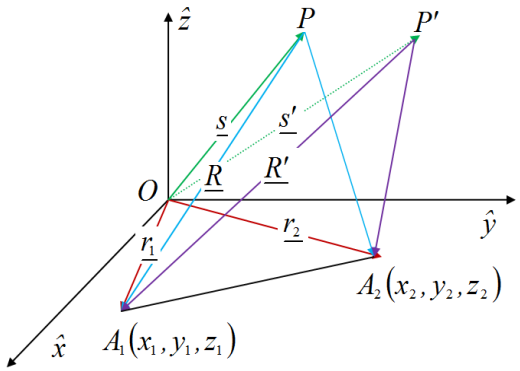

Figure 3.3 Geometry of HMIA measurements by a pair of antennas

Substituting for the scattered fields in (3-1) using (3-2) gives the following six-fold integral for the complex visibility function:

$$G(\underline{r_1}, \underline{r_2}) = \left(\frac{k_0^2}{4\pi}\right)^2 \iiint_V \iiint_{V'} (\varepsilon(\underline{s}) - \varepsilon_b)(\varepsilon(\underline{s'}) - \varepsilon_b)^* \underline{E_{T(s)}} \cdot \underline{E_T^*}(\underline{s'}) \frac{e^{-jk_b(R-R')}}{RR'} dV dV' \tag{3-3}$$

Where $R = \left|\underline{r_1} - \underline{s}\right|$ and $R' = \left|\underline{r_1} - \underline{s'}\right|$.

If the distance from a point P to the receiving antenna A_1 is very large compared to the size of antenna array plane, that is $R \gg \left|\underline{r_1}\right|$ then:

$$R = |\underline{R}| = \sqrt{\left(\underline{r_1} - \underline{s}\right) \cdot \left(\underline{r_1} - \underline{s}\right)} = \sqrt{r_1^2 + s^2 - 2\underline{r_1} \cdot \underline{s}} \cong s - \frac{\underline{r_1} \cdot \underline{s}}{s} = s - \underline{r_1} \cdot \hat{\underline{s}} \tag{3-4}$$

Where the "dot" denotes the scalar product and $\hat{\underline{s}}$ is a unit vector. Similarly, the distance from another point P' within the breast to the receiving antenna A_2 can be calculated as:

$$R' = \left|\underline{R'}\right| = s' - \underline{r_2} \cdot \widehat{\underline{s'}} \tag{3-5}$$

Then

$$\frac{e^{-jk_b(R-R')}}{RR'} \approx \frac{1}{ss'} e^{-jk_b(s-s')} e^{jk_b(\underline{r_2} \cdot \underline{\hat{s}'} - \underline{r_1} \cdot \underline{\hat{s}})} \tag{3-6}$$

The six-fold integral of (3-3) can be simplified by noting that the phase factor $e^{-jk_b(s-s')}$ oscillates rapidly as the operator scan over all possible pairs of points (P, P') within the domain of integration. Consequently, the only significant contribution to the value of the integral in (3-3) arises from points for which the phase varies slowly. This situation corresponds to the case for which the points (P, P') coincide. Therefore, $\underline{s} - \underline{s'} \to 0$ is allowed, so that $s = s'$. The visibility function where the integration is over the volume of the breast can be obtained:

$$G\left(\underline{r_1}, \underline{r_2}\right) = \left(\frac{k_0^2}{4\pi}\right)^2 \iiint_V \left(\left|\varepsilon(\underline{s}) - \varepsilon_b\right|^2\right) \underline{E}_{T(\underline{s})} \cdot \underline{E_T^*}(\underline{s}) \frac{e^{-jk_b\left(\underline{r_1} - \underline{r_2'}\right) \cdot \hat{\underline{s}}}}{s^2} dV \tag{3-7}$$

Defining the breast intensity function at the position $\underline{s}$ as:

$$I(\underline{s}) = \left(\frac{k_0^2}{4\pi}\right)^2 \left|\varepsilon(\underline{s}) - \varepsilon_b\right|^2 \underline{E_T}(\underline{s}) \cdot \underline{E_T^*}(\underline{s}) \tag{3-8}$$

And defining the baseline vector as:

$$\underline{D} = (\underline{r_1} - \underline{r_2})/\lambda_b \tag{3-9}$$

Equation (3-7) can be rewritten as:

$$G(\underline{D}) = \iiint_V I(\underline{s}) \frac{e^{-j2\pi \underline{D}\cdot\hat{\underline{s}}}}{s^2} dV \tag{3-10}$$

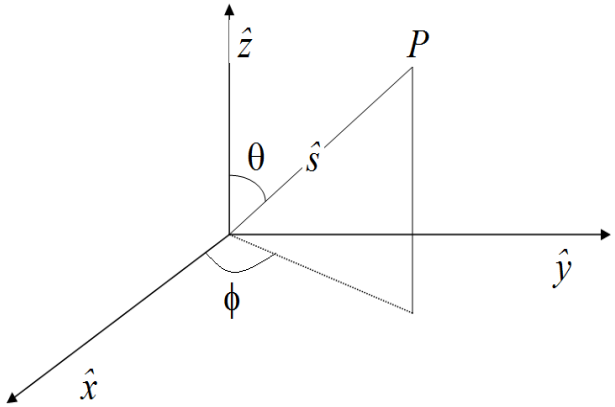

Figure 3.4 Spherical polar coordinate system

Let the Cartesian components of the unit vector $\hat{\underline{s}}$ be expressed in spherical polar coordinates (θ, ϕ) as follows (see Figure 3.4):

$$\hat{s} = sin\,\theta\, cos\,\phi\, \hat{\underline{x}} + sin\,\theta\, sin\,\phi\, \hat{\underline{y}} + cos\,\theta\, \hat{\underline{z}} \tag{3-11}$$

The volume element dV becomes:

$$dV = s^2\, sin\,\theta\, d\theta d\phi ds \tag{3-12}$$

Defining new variables (l, m, n) as:

$$\begin{aligned} l &= sin\,\theta\, cos\,\phi \\ m &= sin\,\theta\, sin\,\phi \\ n &= cos\,\theta = \sqrt{1 - l^2 - m^2} \end{aligned} \tag{3-13}$$

The element dV can be written as:

$$dV = s^2 dldmds/n \tag{3-14}$$

Substituting (3-14) into (3-10), a more useful form is obtained as follows:

$$G(\underline{D}) = \iiint_V I(\underline{s}) \frac{e^{-j2\pi \underline{D}\cdot\underline{\hat{s}}}}{n} dldmds \tag{3-15}$$

Writing the Cartesian components of the baseline vector $\underline{D}$ as (u, v, w) such that:

$$\begin{aligned} u &= (x_2 - x_1)/\lambda_b \\ v &= (y_2 - y_1)/\lambda_b \\ w &= (z_2 - z_1)/\lambda_b \end{aligned} \tag{3-16}$$

The visibility function then becomes:

$$G(u, v, w) = \int_l \int_m \int_s \frac{I(s, l, m)}{\sqrt{1 - l^2 - m^2}} e^{-j2\pi\Phi} dldmds \tag{3-17}$$

Where $\Phi = \underline{D} \cdot \underline{\hat{s}} = ul + vm + wn$

3.2.2.2 Breast Intensity Distribution

If all antennas are assumed to be located on a 2D plane then it follows that $w = 0$. A line integral along the radial coordinate s is defined as:

$$\tilde{I}(l, m) = \int_s \frac{I(s, l, m)}{\sqrt{1 - l^2 - m^2}} ds \tag{3-18}$$

Using (3-18) leads to the following 2D integral over the variables (l, m) for the visibility function:

$$G(u, v, 0) = \iint \tilde{I}(l, m) e^{-j2\pi(ul+vm)} dldm \tag{3-19}$$

It is evident that the visibility function in (3-19) is the 2D Fourier transform of the 2D intensity function $\tilde{I}(l,m)$, which is consistent with the Van Cittert-Zernike theorem [141]. Therefore, the 2D intensity function is obtained by inverse Fourier transform:

$$\tilde{I}(l,m) = \iint G(u,v,0)e^{j2\pi(ul+vm)}\,dudv \tag{3-20}$$

Equation (3-20) shows that if measurements of the visibility function $G(u,v)$ that span the space (u,v) are available then a 2D image can be determined by inverse Fourier transform. The 2D image is the intensity function $\tilde{I}(l,m)$ which is defined by the line integral in (3-18) and represents the scattering intensity in the breast integrated along each radial vector.

3.3 Forward Models

After studying and comparing the wide frequency spectrum from 10 GHz to 20 GHz, for simplicity, the single frequency of 12.6 GHz was selected as the system operation frequency. In practice, the relative permittivity of the lesion could be somewhat larger than that of the fat tissue. Values for the real part of the relative permittivity of lesion can be as high as 50 [20]. The use of a small permittivity contrast greatly simplifies the forward model for the scattered field without sacrificing the underlying physics of the HMIA technique.

3.3.1 Antenna Model

A small open-ended rectangular wave-guide was assumed to be a transmitting antenna. The broad and narrow wall dimensions of the antenna are 15.788 mm and 7.5 mm. The radiated far-field from such an antenna is well represented by the following expression:

$$\underline{E}_{inc}(R_0,\theta,\phi) = \frac{-jk_b}{2\pi^2}\underline{E}_0\frac{e^{-jk_bR_0}}{R_0}ABh(\theta,\phi)\underline{P}(\theta,\phi) \quad (3\text{-}21)$$

Where $\underline{E}_0$=Wave amplitude of TE_0 mode within wave-guide aperture,

R_0=Distance from a point in the breast to the transmitting antenna,

A=Broad aperture dimension of antenna aperture,

B=Narrow aperture dimension of antenna aperture,

$h(\theta,\phi)$=Antenna far-field radiation pattern,

$\underline{P}(\theta,\phi)$=Polarisation vector.

The backscattered electric field from the breast can be found by applying the Stratton & Chu formulation [140] which gives the following integral over the volume of the breast:

$$\underline{E}_{scat} = \frac{k_0^2}{4\pi}\int_V \left(\varepsilon(\underline{s}) - \varepsilon_\mathrm{b}\right)[a\underline{E}_T + b(\underline{E}_T\cdot\hat{\underline{R}})\hat{\underline{R}}]\frac{e^{-jk_\mathrm{b}\mathrm{R}}}{\mathrm{R}}dV \quad (3\text{-}22)$$

Where $a = 1 - \frac{j}{k_bR} - \frac{1}{(k_bR)^2}$,

$b = -1 + \frac{3j}{k_bR} + \frac{3}{(k_bR)^2}$,

$\hat{\underline{R}}$=Unit vector parallel to the vector $\underline{\mathrm{R}}$,

R=Distance from a point in the breast to the receiving antenna,

$\underline{\mathrm{R}}$=Position vector from a point in the breast to the receiving antenna.

When $k_bR \gg 1$, the above factors can be approximated by $a \approx 1$ and $b \approx -1$. For the purposes of demonstrating the HMIA technique, it is computationally advantageous to consider a small permittivity contrast between the breast and host medium that is $\left(\varepsilon(\underline{s}) - \varepsilon_b\right)$ is assumed to be small. The backscattered far-field can be readily

determined using the Born Approximation, which allows the total electric field $\underline{E_T}$ to be approximated by the incident field $\underline{E_{inc}}$:

$$\underline{E_{scat}} = \frac{k_0^2}{4\pi}\int_V \big(\varepsilon(\underline{s}) - \varepsilon_b\big)[\underline{E_{inc}} + (\underline{E_{inc}} \cdot \hat{\underline{R}})\hat{\underline{R}}]\frac{e^{-jk_bR}}{R}dV \qquad (3\text{-}23)$$

Also, in the far-field $\underline{E_{inc}} \cdot \hat{\underline{R}} \approx 0$ is assumed, therefore the backscattered electric field $\underline{E_{scat}}$ can be expressed:

$$\underline{E_{scat}} = \frac{k_0^2}{4\pi}\int_V \big(\varepsilon(\underline{s}) - \varepsilon_b\big)\underline{E_{inc}}\frac{e^{-jk_bR}}{R}dV \qquad (3\text{-}24)$$

3.3.2 Antenna Array Configurations

Several antenna array configurations have been investigated to produce a high-resolution breast image and this study will be discussed in Chapter 5. Figure 3.5 shows a one of the most suitable 16-element antenna array configurations for breast lesion detection based on the HMIA technique. With 15 receiving antennas, there are 15(15-1) unique pairs of antennas in the array, hence 210 signals were collected. The HMIA image reconstruction algorithm (detailed in section 3.2) was applied for reconstructing the breast image using the collected data.

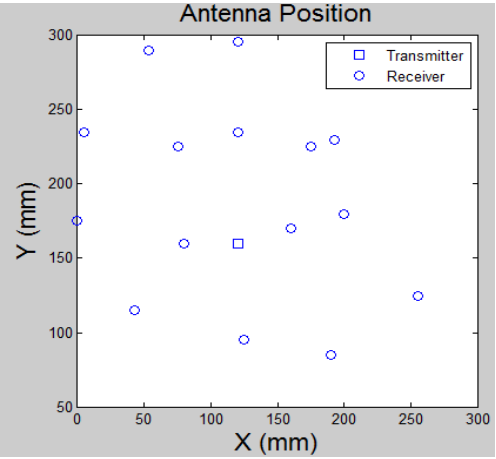

Figure 3.5 2D spiral antenna array configuration

3.3.3 Breast Model

The hemispherical shaped breast model has a radius of 70 mm was used in simulations. A 2 mm thick skin layer surrounded the breast fat tissue. Various lesions with different shape and size were simulated. The space between the breast and antenna array was assumed to be filled with air ($\varepsilon_r = 1, \sigma = 0$ S/m).

Figure 3.6 shows the 2D and 3D views of a simplified breast model that contains skin, fat tissue and malignant tissue. Colour bar plots the dielectric properties of breast model and the dielectric properties of breast used in the simulation model are summarized in Table 3-1.

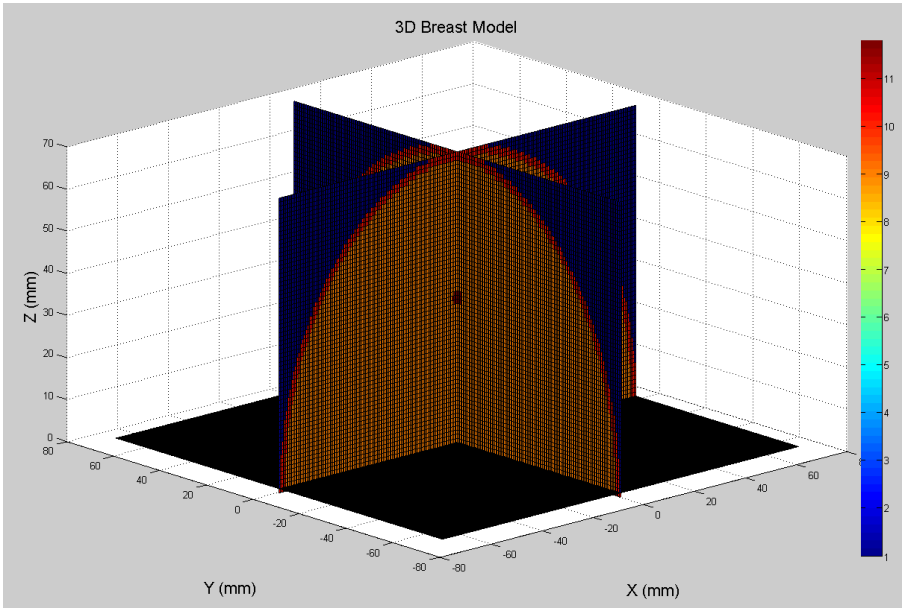

(a)

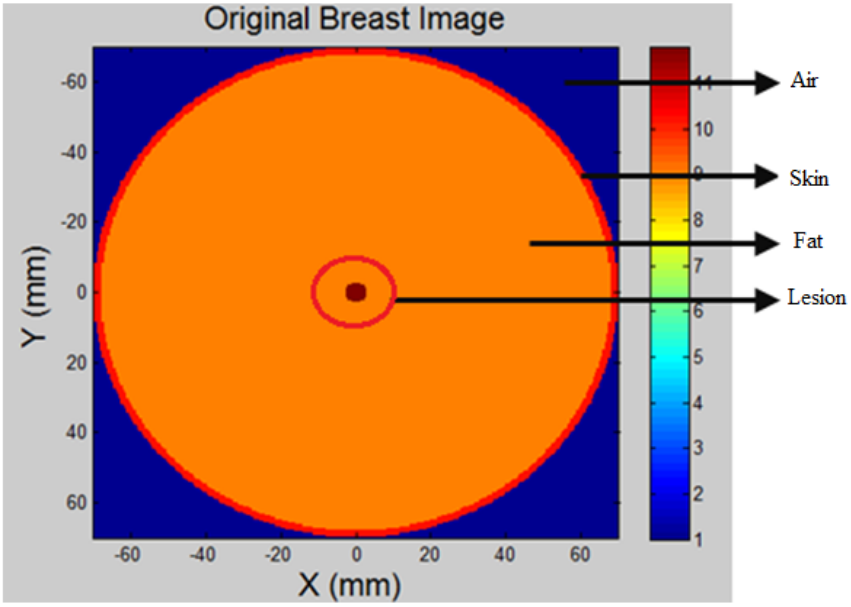

(b)

Figure 3.6 Orignial 3D breast model with one lesion (a) 3D view (b) 2D view

Table 3-1 Dielectric properties of breast

Region	**Thickness (mm)**	**Dielectric properties**
Air	~	1 [142]
Skin	2	9.3-4j
Fat	~	9-0.4j
Lesion	2~6	9.5-7j

A 2D computer simulation model was developed using MATLAB by combining the results of (3-24) in (3-1) to simulate the complex visibility function and the Fourier relationship of (3-20) was then used to form a 2D image. Figure 3.7 demonstrates the flowchart of the 2D HMIA technique simulation set-up and the MATLAB code of 2D HMIA imaging algorithms to generate a 2D breast image are detailed in Appendix A.

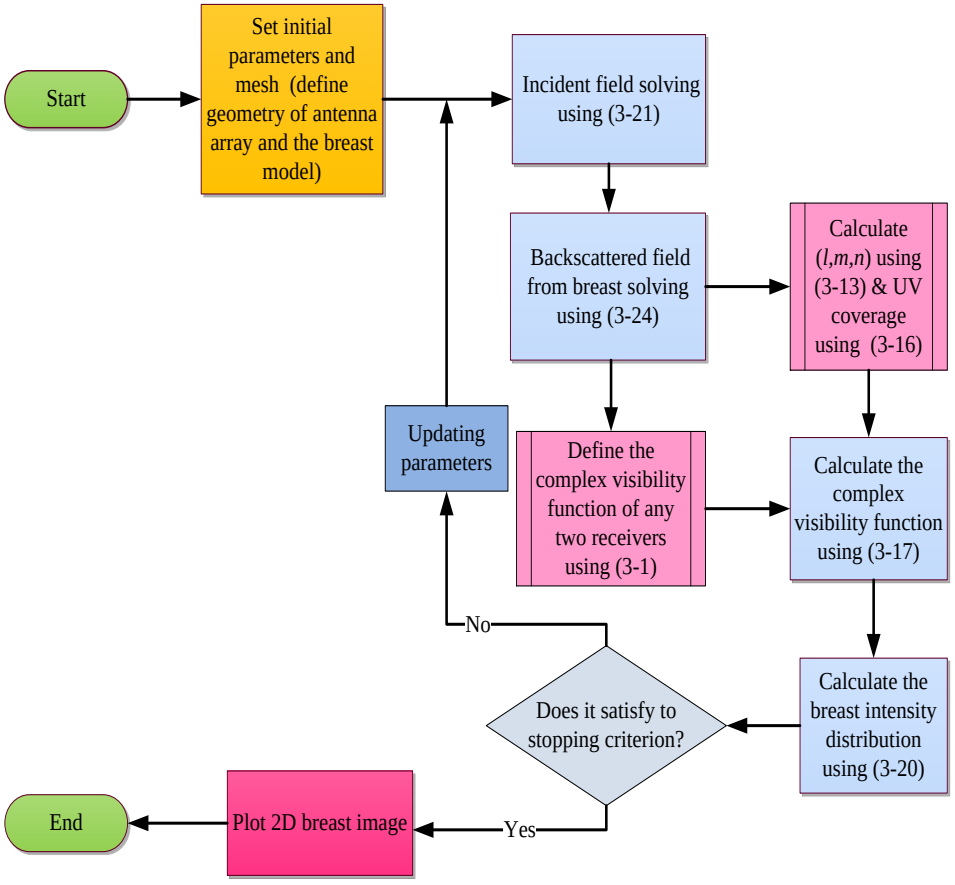

Figure 3.7 Flowchart of 2D HMIA technique simulation set-up

3.4 Simulation Results

In simulations, the breast model was placed at $z = 0$ mm and the antenna array plane was placed at $z = -450$ mm respectively. The explanation of the measurement distance between the antenna array and the breast model can be found in Chapter 5. The 140 mm x 140 mm square image region containing the dielectric object (breast) and the background medium (air $\varepsilon_r = 1$, $\sigma = 0$ S/m) is uniformly subdivided into 281 x 281 elementary square cells. Figure 3.8 displays the 2D view of the original and reconstructed breast images without lesion.

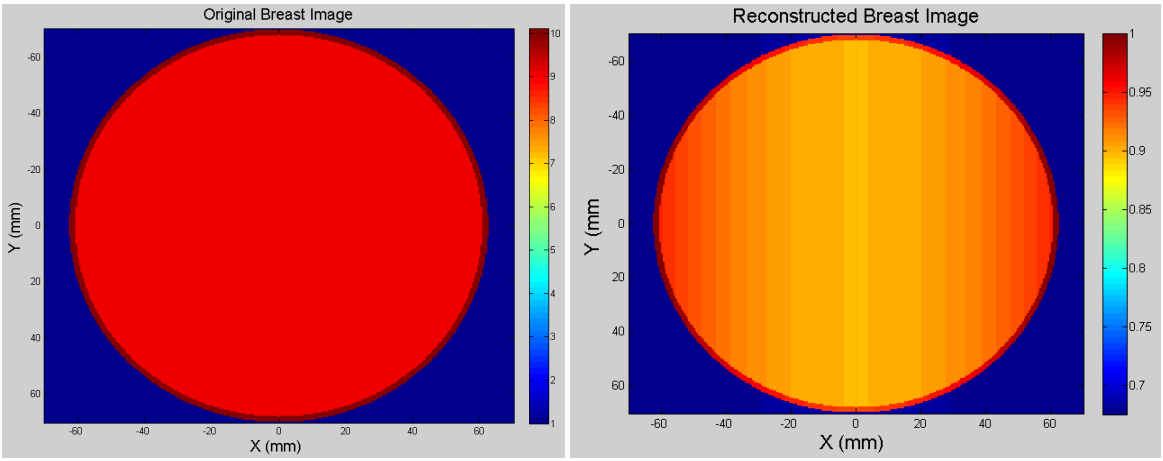

(a) (b)

Figure 3.8 (a) 2D view of 3D original breast model: skin and fat only (b) 2D reconstructed breast image with the antenna array plane was placed at $z = -450$ mm

Figure 3.9 illustrates the original breast model and reconstructed breast image of five spherical lesions (circled in black). The location and size of five spherical shaped lesions within the breast model are listed in Table 3-2.

Table 3-2 Location and size of five spherical shaped lesions

Number	**Position**			**Size (mm)**		
	X **(mm)**	Y **(mm)**	Z **(mm)**	σ_x	σ_y	σ_z
1	0	-40	35	2	2	2
2	0	-20	35	3	3	3
3	0	0	35	4	4	4
4	0	20	35	5	5	5
5	0	40	35	6	6	6

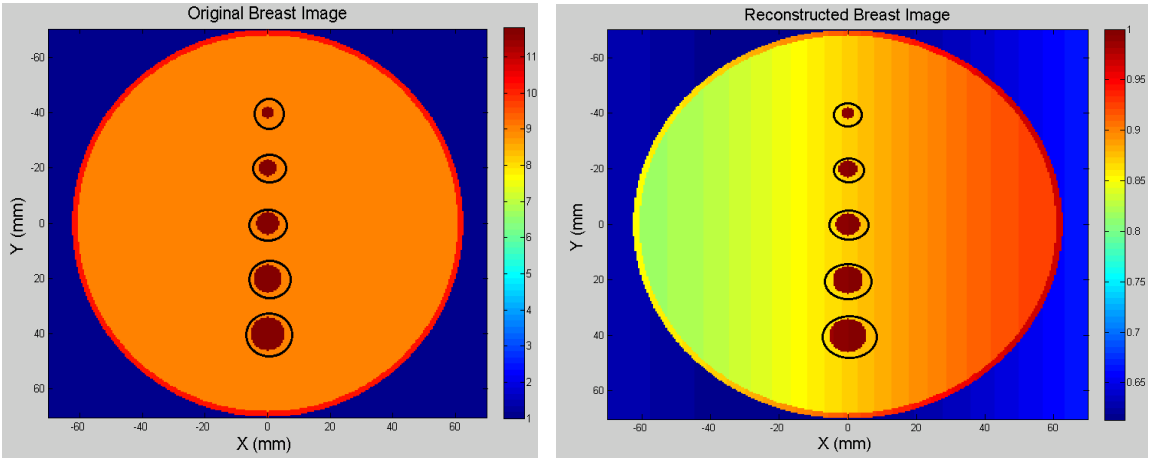

(a) (b)

Figure 3.9 (a) Breast model (b) 2D reconstructed breast image of five lesions

Figure 3.10 shows the 2D view of the original 3D breast model and the reconstructed breast image of four spherical lesions (2 mm in diameter, circled in black). Table 3-3 shows the location and size of four spherical shaped lesions within the breast model.

Table 3-3 Location and size of four spherical shaped lesions

Number	**Position**			**Size (mm)**		
	X **(mm)**	Y **(mm)**	Z **(mm)**	σ_x	σ_y	σ_z
1	0	0	5	2	2	2
2	10	10	10	2	2	2
3	20	20	15	2	2	2
4	30	30	20	2	2	2

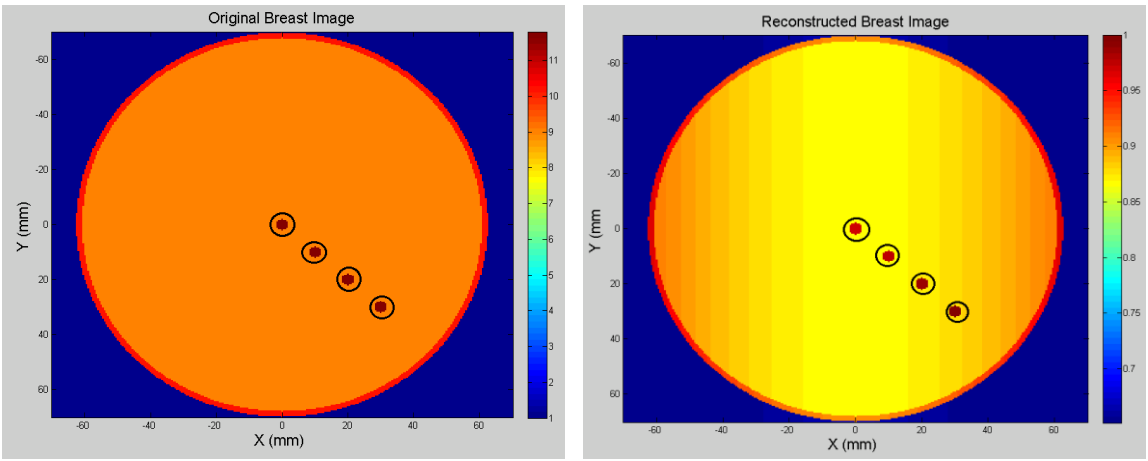

(a) (b)

Figure 3.10 (a) Breast model (b) 2D reconstructed breast of four lesions

Figure 3.11 displays the original and the 2D reconstructed images of a 3D breast model including skin, fat and two lesions. The location and size of two elliptical shaped lesions are summarized in Table 3-4.

Table 3-4 Location and size of two elliptical shaped lesions

Number	**Position**			**Size (mm)**		
	***X* (mm)**	***Y* (mm)**	***Z* (mm)**	σ_x	σ_y	σ_z
1	0	0	5	2	4	2
2	0	0	10	2	4	2

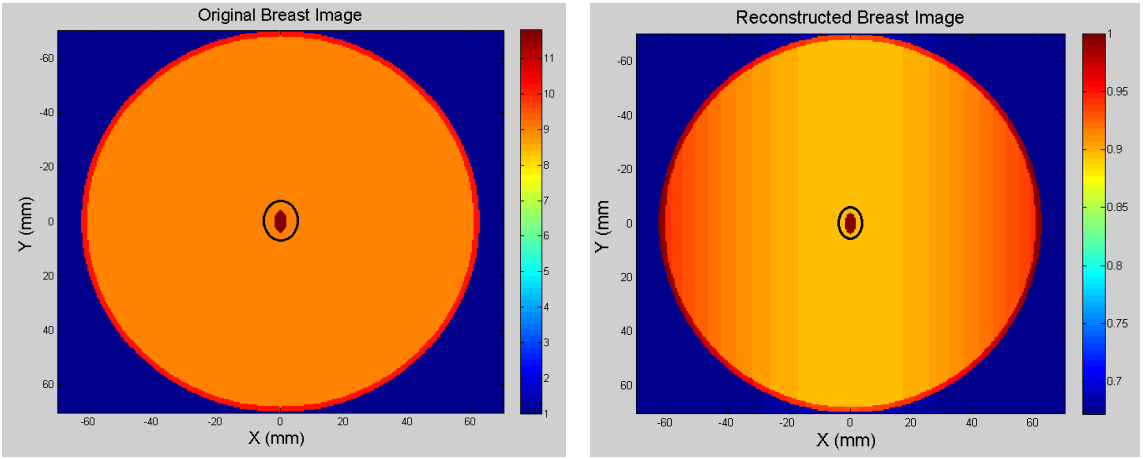

(a) (b)

Figure 3.11 (a) 2D view of original 3D breast model (b) 2D reconstructed breast model containing two lesions (circled in black)

Figure 3.12 shows the 2D reconstructed breast image that including skin, fat and two lesions located at different z-planes within the breast model. The location and size of two spherical shaped lesions are summarized in Table 3-5.

Table 3-5 Location and size of two spherical shaped lesions

Number	**Position**			**Size (mm)**		
	***X* (mm)**	***Y* (mm)**	***Z* (mm)**	σ_x	σ_y	σ_z
1	50	0	25	3	3	3
2	50	0	35	3	3	3

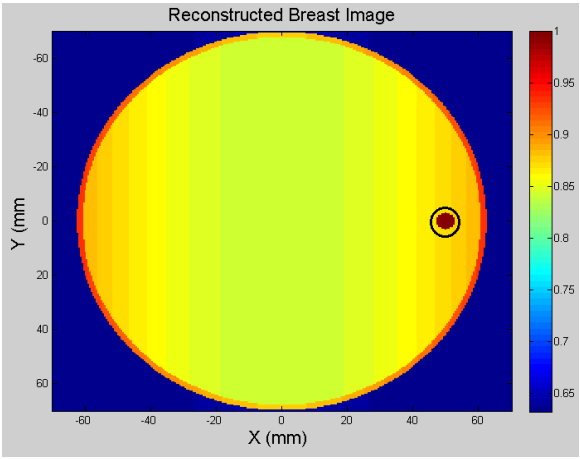

Figure 3.12 2D reconstructed breast model containing two lesions (circled in black), but only one lesion displayed within the image

Colour bars in the original breast images (Figure 3.8 (a), Figure 3.9 (a), Figure 3.10 (a), Figure 3.11 (a)) plot the dielectric properties of breast models, and colour bars in reconstructed breast images (Figure 3.8 (b), Figure 3.9 (b), Figure 3.10 (b), Figure 3.11 (b) and Figure 3.12) plot signal energy on a linear scale, normalised to the maximum in the breast volume.

3.5 Closure

In this chapter, a new HMIA technique for early breast lesion detection was presented. A computer simulation model was developed to demonstrate the proposed HMIA image algorithms.

In evaluating the HMIA technique, several breast models were simulated using a 16-element spiral array. The dielectric properties of skin and malignant tissue were deliberately chosen to be of low-contrast in the forward model described to simplify the simulated scattered field data to facilitate an investigation of the image algorithm, rather than modelling realistic values of skin and malignant tissue properties. The simulation results demonstrated that lesions of various locations and sizes within the breast model

could be successfully detected against the background (see Figure 3.8 to Figure 3.10). However, two lesions located different z-planes will not be imaged as separate lesions (see Figure 3.11 and Figure 3.12).

The simulation results confirmed that the lower dielectric contrast imposes additional challenges for microwave imaging modalities. The major limitation of the 2D HMIA technique is the developed 2D image reconstruction algorithm produces a 2D image only corresponding to the projection of the scattering intensity along radial lines emanating from the coordinate origin. Only one lesion could be detected if more than one lesion located at the same x, y coordinates but in different z-planes.

The next chapter provides a novel 3D HMIA technique to overcome the current limitations of the 2D image reconstruction algorithm.

Chapter 4 Three Dimensional Holographic Microwave Imaging Array System Design

4.1 Introduction

This chapter presents a novel 3D HMIA technique for breast imaging, which overcomes the limitation of the developed 2D HMIA technique. The most significant parts of this work are presented in details of conference paper 2 [CP2]. Section 4.1 overviews of the 3D HMIA system, section 4.2 details the 3D image reconstruction algorithm, section 4.3 presents the simulation system set-up including forward models, section 4.4 displays the simulation results of 3D HMIA approach and section 4.5 summaries this chapter.

4.2 3D Holographic Microwave Imaging Array (HMIA) Technique

Due to the critical need for complementary and or alternative modalities to current X-ray mammography for breast imaging, a 3D HMIA technique has been developed. A 3D computer simulation model was developed to demonstrate that the proposed 3D HMIA technique has the ability to produces high quality 3D breast images.

4.2.1 Data Collection Method and System Design

Figure 4.1 shows the block diagram of a 3D HMIA technique. Similar to the 2D HMIA system, the 3D HMIA system contains one transmitter and an array of 15 receivers located under the breast model in far-field. However, the receiving antenna array is designed to be movable. The breast phantom is placed at $z = 0$ mm and an array of 16 antennas is placed under the breast which is movable from $z = H_1$ mm to $z = H_n$ mm in equal M steps.

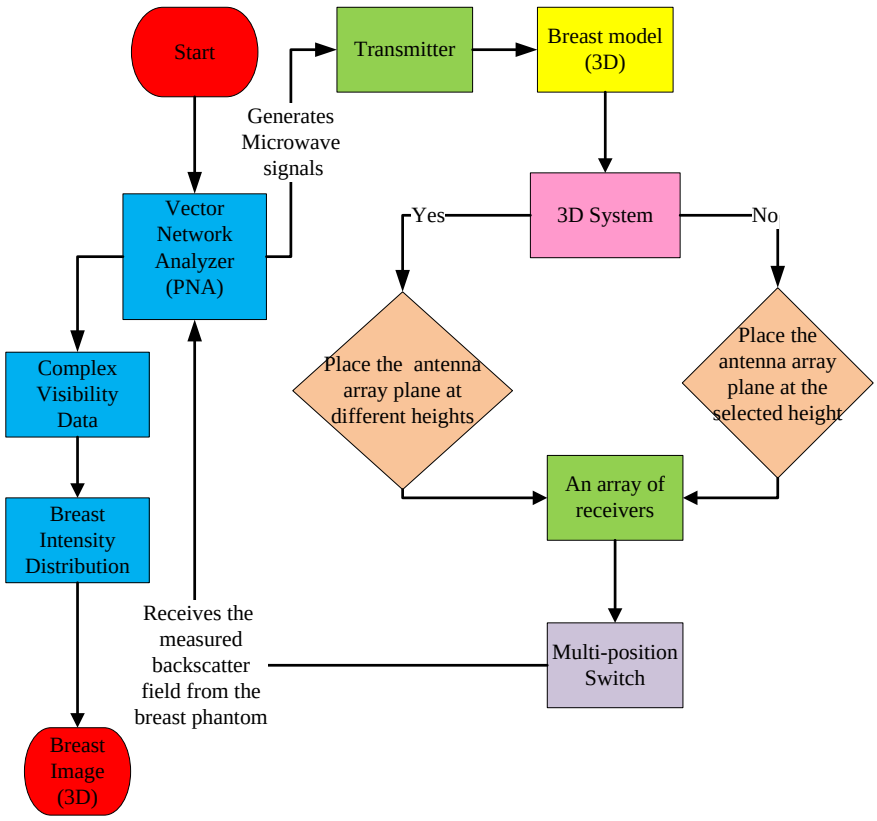

Figure 4.1 The block diagram of 3D HMIA technique set-up

The two-port PNA generates a single frequency microwave signal to the single transmitting antenna that transmits the EM wave into the breast through the air where it is scattered in different directions. Each receiving antenna receives the backscattered electric field from the breast. These measurements were repeated every time when the antenna array is moved to a new position (change the measurement heights between the breast phantom and the antenna array plane). Microwave measurements that contain the phase and magnitude of the reflection coefficient information are obtained using a PNA. The complex visibility function is calculated using the measured data, and the 2D breast intensity distribution is formed by applying an Inverse Fast Fourier Transform (IFFT) to the complex visibility data. A 2D projection image of a 3D breast model is then formed from the breast intensity distribution. Then a 3D breast image is reconstructed by using

the 3D HMIA image reconstruction algorithm with the antenna array plane placed at different heights.

4.2.2 3D HMIA Imaging Algorithm

Equation (3-20) in Chapter 3 represents a 2D projection of the 3D breast intensity function onto a 2D plane in (l, m) space. To obtain a 3D image, the 3D breast model as designed contains multi-layers as shown in Figure 4.2.

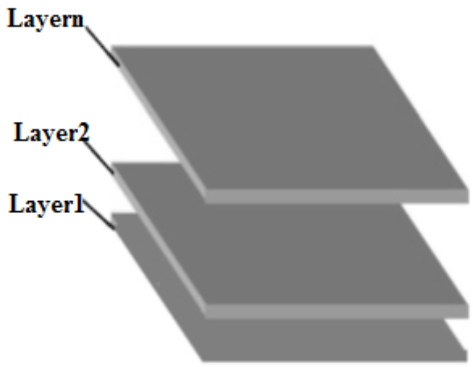

Figure 4.2 3D imaging of breast layers

During operation, the antenna array plane is designed to be moveable from H_1 (mm) to H_n (mm) in equal M steps, where H is the distance between antenna array plane and breast model (see Figure 4.3). Then the lesion at the breast depth location z_n within the same breast model is defined as:

$$z_n = s_n cos(\theta_n) \tag{4-1}$$

Where θ_n is the transmitting or receiving angle of the same antenna on the antenna array plane to the detected object at the position s_n with the antenna array plane to breast model at the distance H_n. Thus ds in (3-18) becomes:

$$ds = \frac{dz}{cos(\theta_n)} = \frac{dz}{\sqrt{1 - l^2 - m^2}} \tag{4-2}$$

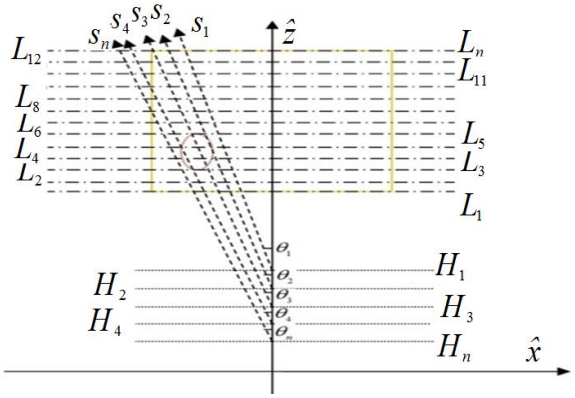

Figure 4.3 Block diagram showing the scattering characterization scheme from different receiving height H_n

By differentiating (3-18), the 3D image of the breast intensity function at a selected height $H = H_n$, can be obtained as (see Figure 4.3).

$$I(H = z_n, l, m) = \frac{d\tilde{I}(l,m) \cdot (1 - l^2 - m^2)}{dz} \tag{4-3}$$

The derivative in (4-3) can be approximated by the following forward difference expression:

$$\frac{d\tilde{I}}{dz} = \frac{\tilde{I}_{z_n} - \tilde{I}_{z_{n-1}}}{z_n - z_{n-1}} \tag{4-4}$$

A reconstructed 3D image of the breast intensity function is then computed using (4-3) and (4-4) by placing the antenna array plane at difference heights.

To quantitatively assess imaging results, a zooming function can be applied to enhance the image contrast:

$$\tilde{I}_m(H, l, m) = [\tilde{I}(H, l, m)]^Q \tag{4-5}$$

Equation (4-5) performs a Q: 1 zoom on an image of the breast.

4.3 Forward Models

Like the 2D HMIA system, the 3D HMIA system operated on a single frequency of 12.6 GHz, and the same 16 small open-ended rectangular wave-guides were chosen, one acting as transmitting antenna and the remaining acting as receiving antennas. Antennas were randomly located on a 2D array plane (300 mm x 300 mm) as shown in Figure 4.4, which was placed under the breast phantom that was varied between $z = -450$ mm and $z = -460$ mm in 10 equal steps.

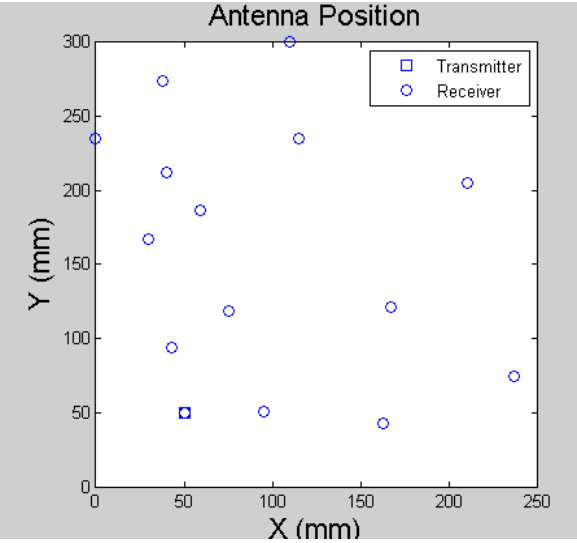

Figure 4.4 Antenn array plane

The hemispherical shaped breast model (radius of 70 mm) contains skin, fat and lesion was used in 3D HMIA simulations. A small permittivity contrast greatly simplifies the forward model for the scattered field without sacrificing the underlying physics of the HMIA method. A lesion ($\varepsilon_r = 9.5,\ \sigma = 7$ S/m) was assumed to be located inside normal breast tissue ($\varepsilon_r = 9,\ \sigma = 0.4$ S/m). Skin layer ($\varepsilon_r = 9.3,\ \sigma = 4$ S/m) was modelled as 2 mm thick and placed surrounding breast fat tissue while the space between the breast and antenna array was assumed to be filled with air ($\varepsilon_r = 1, \sigma = 0$ S/m).

4.4 Simulation Set-up

A 3D computer model was developed using MATLAB software by combining (3-24) and (3-1) to simulate the complex visibility function that is detailed in Chapter 3. Equation (4-5) was used to generate a 3D breast image. Figure 4.5 demonstrates the flowchart of the 3D HMIA system simulation set-up. The MATLAB code of the 3D HMIA imaging algorithms to generate a 3D image is detailed in Appendix B.

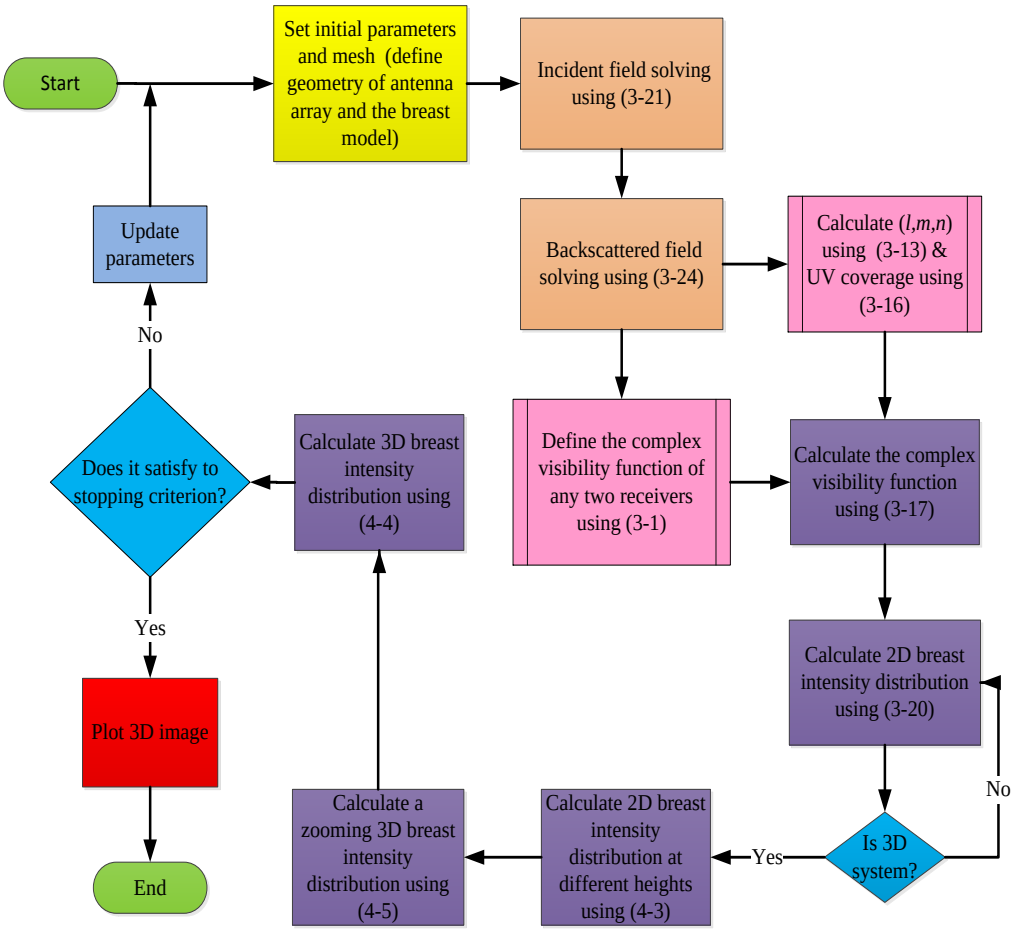

Figure 4.5 Flow chart of 3D HMIA system simulation set-up

4.5 Simulation Results

The 140 mm x 140 x 70 mm cube image region containing the object (breast) and the background medium (air $\varepsilon_r = 1$, $\sigma = 0$ S/m) is uniformly subdivided into 141x141x71 elementary cells.

Figure 4.6 shows the original 3D breast model with five spherical lesions (3 mm in diameter) located in different z-planes (see Table 4-1) and the colour bar shows the dielectric properties of the breast.

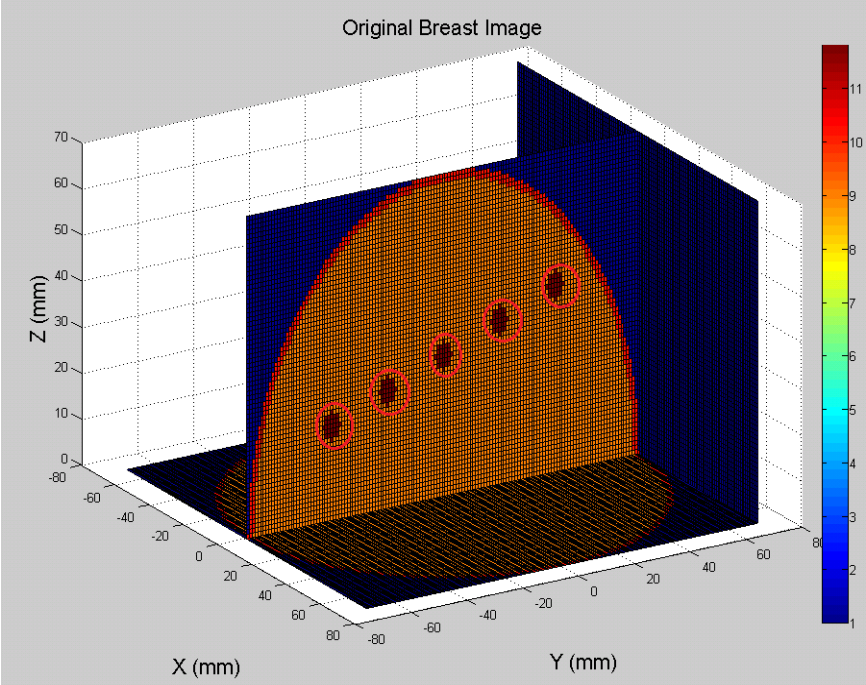

Figure 4.6 Original 3D breast model contains skin, fat and five lesions

Table 4-1 Location and size of five spherical shaped lesion

Number	**Position (mm)**			**Size (mm)**		
	x	y	z	σ_x	σ_y	σ_z
1	0	-40	20	3	3	3
2	0	-20	25	3	3	3
3	0	0	30	3	3	3
4	0	20	35	3	3	3
5	0	40	40	3	3	3

Figure 4.7 clearly shows the skin layer, fat and five simulated spherical lesions (circled in red) within the reconstructed 3D breast image and colour bar plots signal energy on a linear scale, normalised to maximum in the breast volume.

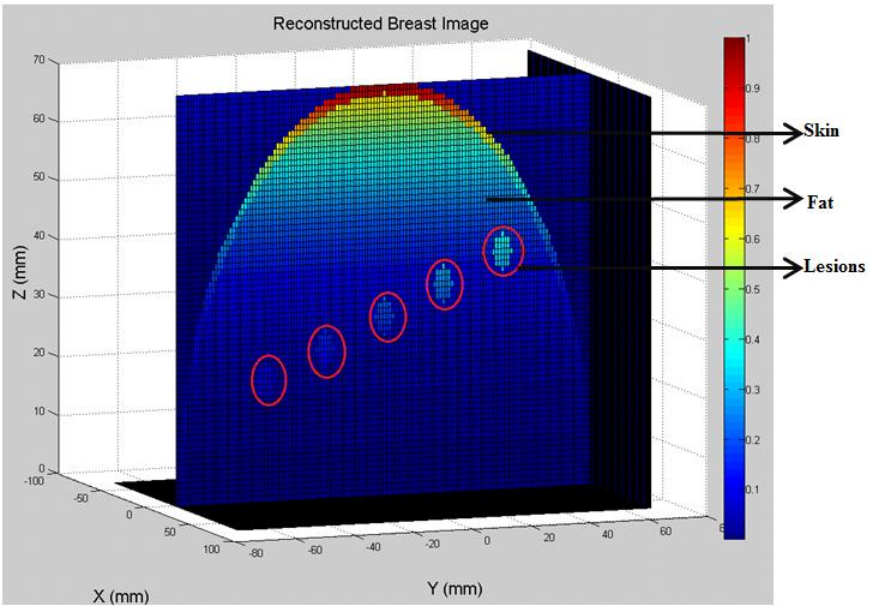

Figure 4.7 Side view of 3D reconstructed image of skin, fat and five lesions (circled in red)

Figure 4.8 illustrates the original 3D breast model of two lesions in random shape and size (see Table 4-2), colour bar plots the dielectric properties of the breast.

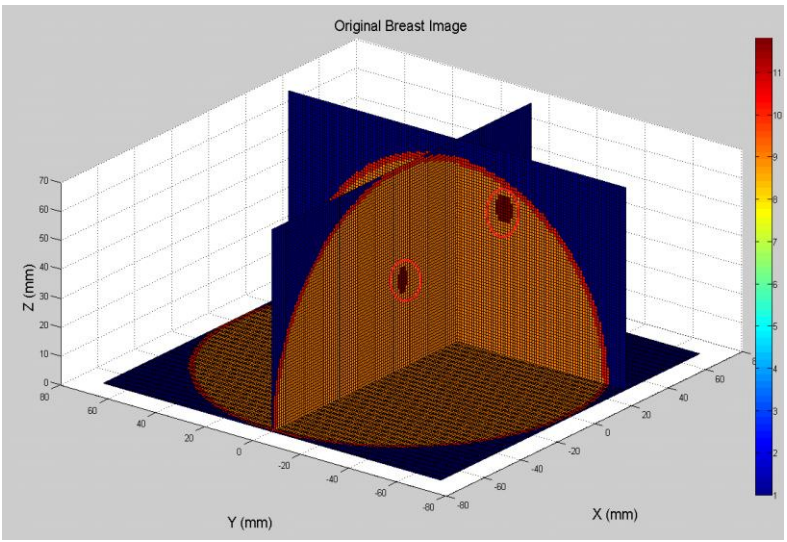

Figure 4.8 Original 3D breast model of two lesions

Table 4-2 Location and size of two randomly shaped lesions

Number	**Position (mm)**			**Size (mm)**		
	x	y	z	σ_x	σ_y	σ_z
1	0	0	30	2.3992	4.1727	4.9086
2	30	-20	50	1.2332	3.4964	4.8925

Figure 4.9 clearly shows the skin layer, fat and two simulated lesions (circled in red) within the reconstructed 3D image of the breast model. Colour bar plots the signal energy on a linear scale, normalised to the maximum in the breast volume.

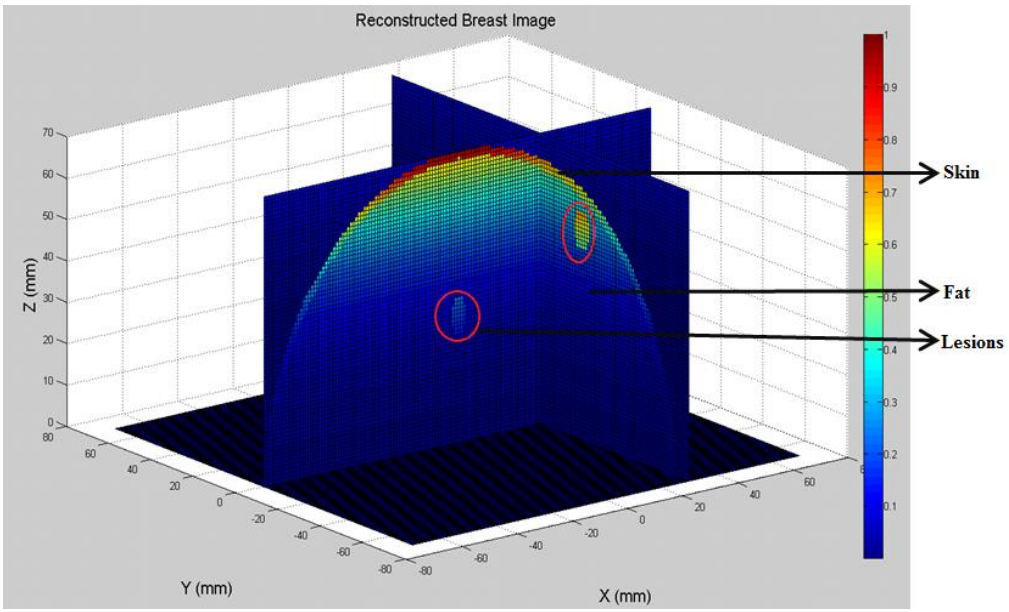

Figure 4.9 3D reconstructed image with two lesions (circled in red)

4.6 Closure

In this chapter the development of a novel 3D HMIA image reconstruction algorithm to detect breast lesions is described that is based on the 2D HMIA system (as detailed in Chapter 3). The 3D simulation model was developed using MATLAB to demonstrate the proposed 3D HMIA technique. It exploits breast tissue physical properties unique to the microwave spectrum, namely the translucent nature of normal breast tissues (without lesions) and the low dielectric contrast between malignant lesions and the surrounding normal breast tissues.

The original and reconstructed 3D breast images were displayed and compared in Figure 4.6 to Figure 4.9. Results observed that lesions of different sizes, shapes and

locations were successfully detected and clearly identified against the background even when they are in random shape and location.

Lesions located at different layers (three dimensional) within the breast model were also fully detected, this proved that the 3D HMIA system has an ability to solve the limitation of the 2D HMIA system which cannot identify lesions as separate lesions if they are located in different layers (z-plane) but at the same x and y coordinates.

The next chapter presents the development of a suitable antenna for HMIA technique and the concept of using spiral and random antenna array configurations to produce high-resolution breast images.

Chapter 5 Antenna and Antenna Array Configuration

5.1 Introduction

This chapter presents a new antenna design suitable for breast lesion detection and introduces the concept of using random and spiral antenna array configurations to generate a high-resolution breast image using the HMIA technique. The significant parts of this work have also been described in the conference paper 5 [CP5]. Section 5.2 describes the open-ended rectangular waveguide antenna, section 5.3 reviews of existing configurations and section 5.4 presents the proposed antenna array configurations, section 5.5 details the simulation system set-up, section 5.6 presents the simulation results and section 5.7 concludes this work.

5.2 Open-ended Rectangular Waveguide Antenna

To design an antenna suitable for breast lesion detection using the HMIA technique, the following factors need to be considered:

- The antenna should be able to radiate the wave into the sample and to receive the backscattered field from the target
- The antenna should be compact enough to be located on to a scanning arrangement
- The antenna should be easy to move and able to be relocated on the array plane to study the performance of the antenna array
- The antenna should be cost effective and widely available

Figure 5.1 shows the schematic of a small flanged open-ended rectangular waveguide antenna (ORWA). The excitation port P was placed at 9 mm from the end of waveguide

and the dimensions are listed in Table 5-1. This design was selected for HMIA experiments because of its low-cost and ease of manufacture. The small size also allowed for the positioning of many antennas close to the imaging domain.

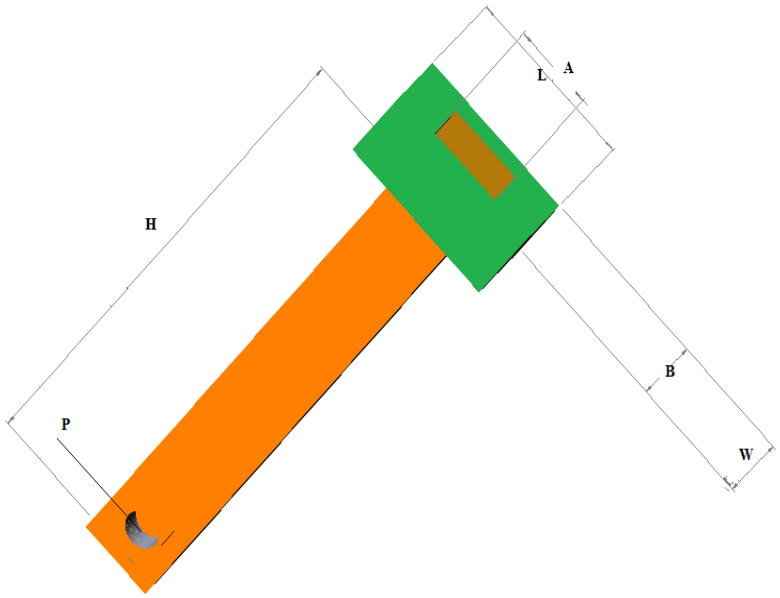

Figure 5.1 Configuration of flanged open-ended rectangular waveguide antenna

Table 5-1 Dimensions of flanged ORWA

Parameter	**Dimension (mm)**
Width of waveguide (A)	15.8
Length of waveguide (B)	7.9
Height of waveguide (H)	120
Thickness of the waveguide walls	1
Length of flange (L)	38
Width of flange (W)	2
Thickness of the flange (T)	6
Length of excitation port from the end of waveguide (P)	9

The cut-off frequency of a rectangular cross-sectioned waveguide is given by:

$$f_c = \frac{1}{2A\sqrt{\mu\varepsilon}} = \frac{c}{A} \tag{5-1}$$

Where A=Broad aperture dimension of antenna,

μ=The permeability of the material that fills the waveguide,

ε=The permittivity of the material that fills in the waveguide,

c=The speed of light in free space within the waveguide.

5.3 Existing Antenna Array Configurations in Microwave Imaging and Radio Astronomy

The performance of producing high-resolution microwave breast images have been investigated by several researchers [37], [143]-[144], which includes antenna model design, antenna array configuration and image reconstruction algorithms. The most widely used two antenna array configurations in microwave imaging for breast lesion detection are the planar configuration developed by Hagness *et al*. [38] and the cylindrical configuration developed by Fear *et al*. [76]. Both of them are regularly spaced antenna array configurations.

The planar configuration uses a 2D array of antennas placed on the naturally flattened breast with the patient lying in the supine position. In data measurement, each antenna in the array sequentially illuminates the breast with an ultra-wideband pulse and that antenna alone records the backscatter. Conversely, the circular configuration involves the patient lying in the prone position with the breast surrounded by a circular array of antennas. In data collection, each antenna in the array once again sequentially illuminates the breast but this time the backscattered signals are recorded at all of the antenna array elements located at different positions around the breast.

The results [42] showed that circular configuration is more suitable for clinical testing because the circular configuration acquires many more reflections from the breast compared to planar configuration ($(N-1)^2/2$ signals VS N signals). It also provides much greater spatial diversity in the propagation paths of the reflected signals, allowing

any dielectric scatter to be more precisely localized [147]. Results also demonstrated that using more antennas would provide better and reliable images especially for identifying small lesions. However, the cost of a microwave imaging system will significantly increase with use of more antennas and the required operation time can be up to eight hours [148].

It is important to study existing array configurations in radio astronomy in this project as the aperture synthesis technique has been widely used in radio astronomy [139]. During the past few years, the array configurations in radio astronomy have undergone significant evolution [149]. It is useful to consider how radio astronomy array configurations are determined as the astronomy community has a long history of designing and using arrays with large numbers of antennas.

The goal of most future array configuration studies is to produce (u, v) sampling with a truncated Gaussian density distribution and thus synthesize beams with a nearly Gaussian profile. Previous research [150] showed several general results: regularly spaced arrays produce poor aperture plane coverage leading to high side-lobe levels; very compact configurations produce too many short projected baselines and too much shadowing between antennas; and extended configurations are more difficult to keep phase stable and can result in long (and expensive) fiber optic runs to the antennas. Logarithmic spiral array configurations are favoured for imaging because they provide dense sampling of the aperture plane over a wide range of projected baseline lengths [149]. This is important for high dynamic range imaging of radio sources that contain structure on many different spatial scales.

5.4 Proposed Antenna Array Configurations

To design a suitable antenna array configuration to detect lesions at their early stage using the proposed HMIA techniques, the following factors need to be considered:

- The antenna array should contain as few antennas as possible
- The antenna array should be able to provide dense sampling of the aperture (uv coverage) over a wide range of projected baseline values
- The antenna array should be able to offer the best possibility of detecting lesions anywhere within the breast

In this chapter, a spiral array and random array configurations are proposed and compared with a widely used regularly spaced antenna array configuration. A computer simulation model was developed to demonstrate that the proposed antenna array configurations have the ability to produce a better quality breast image using HMIA technique.

All antennas are assumed to be located on a 2D plane in this work, then the antenna location of a spiral array in x-y plane is defined as:

$$x = \frac{L(t\,cos(t) + min\|t\,cos(t)\|)}{max\|t\,cos(t)\| + min\|t\,cos(t)\|}$$
$$y = \frac{W(t\,sin(t) + min\|t\,sin(t)\|)}{max\|t\,sin(t)\| + min\|t\,sin(t)\|} \quad (5\text{-}2)$$

Where $t = linespace(a\pi, \frac{\pi}{b}, N)$,

a=Anticlockwise rotation angle,

b=Clockwise rotation angle,

N=Antenna number,

L=Antenna array plane length,

W=Antenna plane width.

Then the antenna location of a random array in the x-y plane can be computed using the MATLAB random function:

$$(x, y) = rand(N, 2) \tag{5-3}$$

Where N=Receiving antenna number,

L=Antenna array plane length.

The uv coverage of the antenna array for a given pair of antennas $A_1(x_1, y_1)$ and $A_2(x_2, y_2)$ is defined as:

$$\begin{aligned} u &= (x_2 - x_1)/\lambda_b \\ v &= (y_2 - y_1)/\lambda_b \end{aligned} \tag{5-4}$$

Sixteen small ORWAs were selected to be located on a flat plane (300 mm x 300 mm) with one acting as a transmitting antenna and the remaining devices acting as receiving antennas.

Figure 5.2 shows the regularly spaced, spiral and random antenna array configurations and the obtained uv coverage using the selected antenna arrays respectively. It is can be seen in Figure 5.2 that the spiral and random antenna array configurations produce more dense sampling of the aperture (uv coverage) compared to the regularly spaced array. The random array provides the highest density sampling over the uv plane. Therefore, the spiral and random antenna array configurations should produce a better quality breast image compared to the current widely used regularly spaced array.

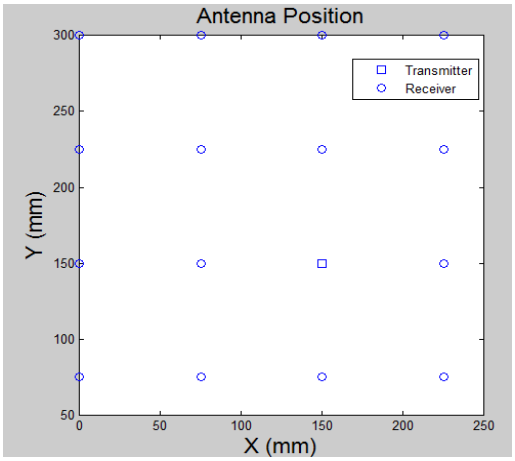

(a)

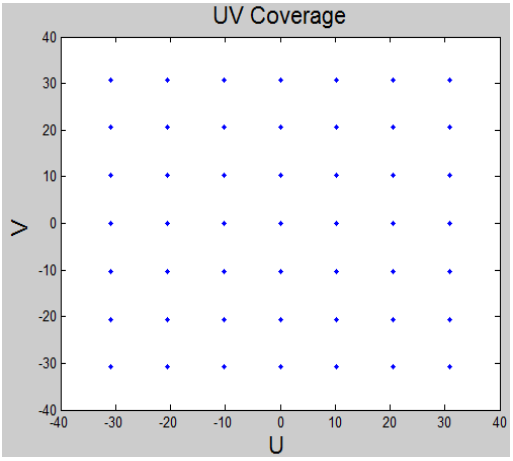

(b)

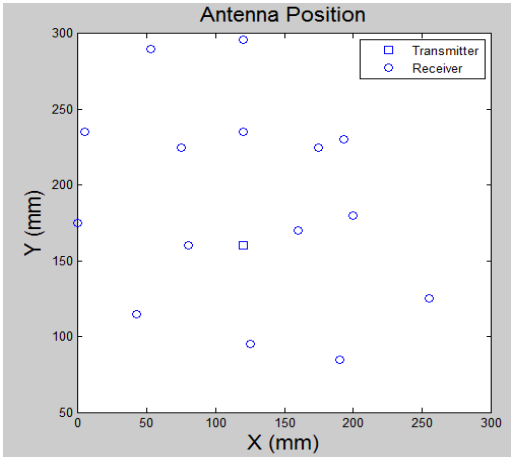

(c)

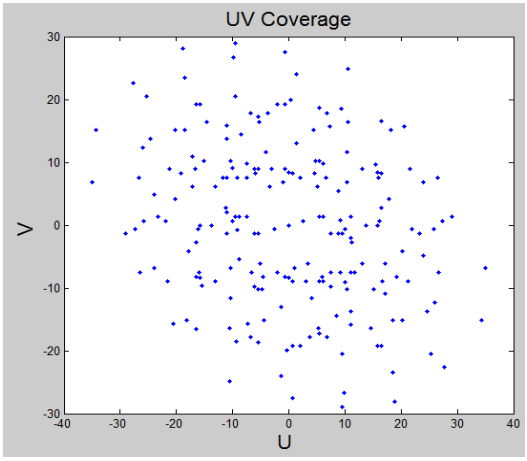

(d)

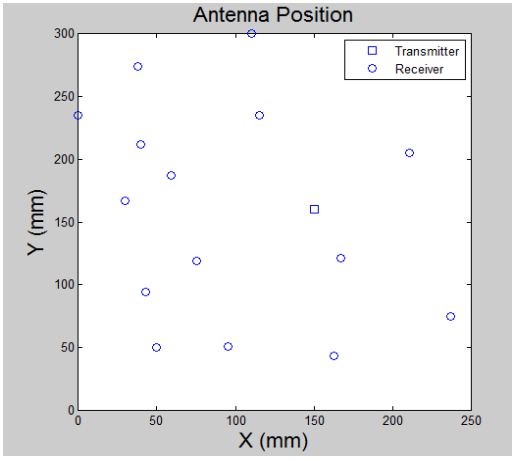

(e)

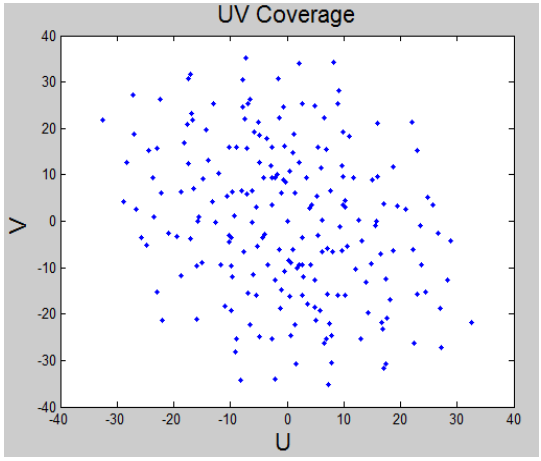

(f)

Figure 5.2 (a) Regularly spaced array configuration (b) uv coverage of regularly spaced array (c) Spiral array configuration (d) uv coverage of spiral spaced array (e) Random array configuration (f) uv coverage of random array

5.5 Simulation Set-up

A mathematical computer model was developed using MATLAB, and simulations using various antenna arrays were performed to evaluate the proposed antenna configurations. Figure 5.3 demonstrates the flowchart of the HMIA technique simulation set-up using different antenna array configurations.

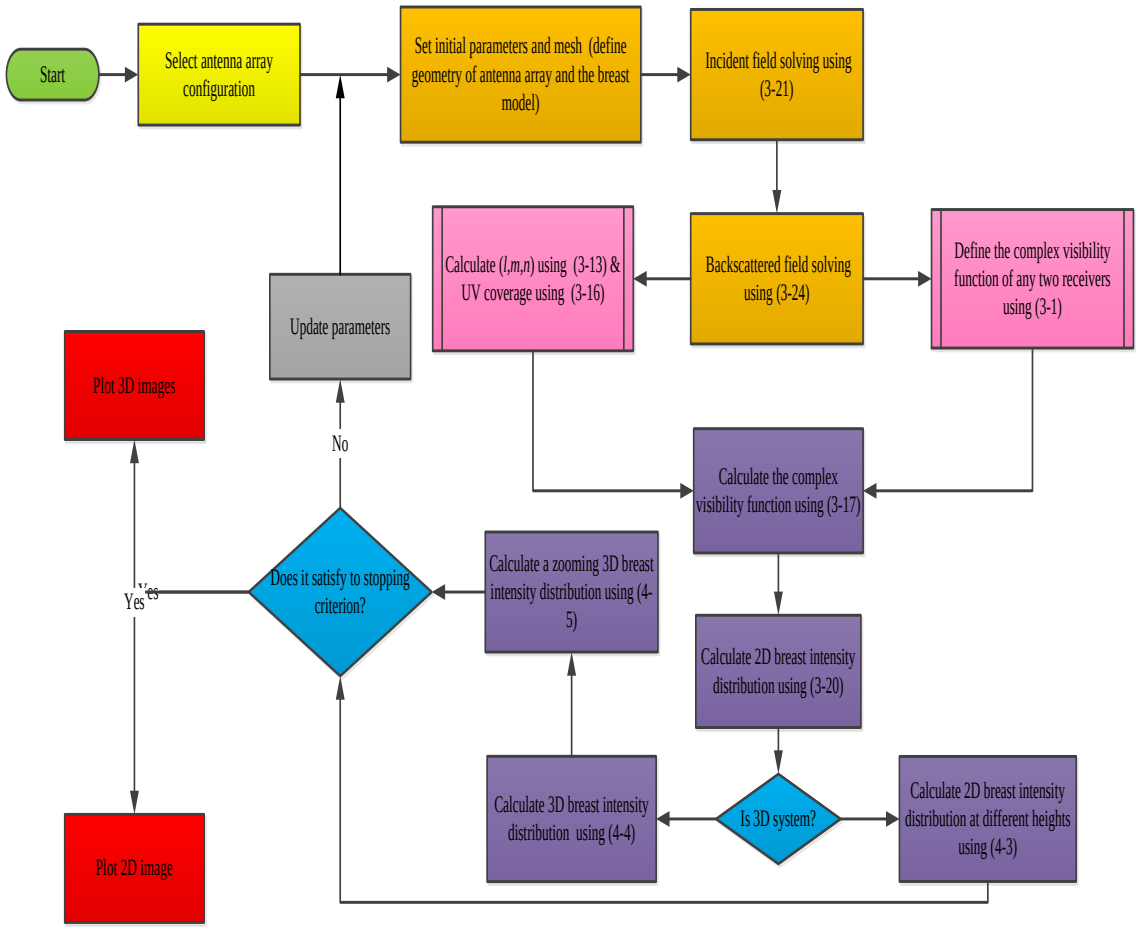

Figure 5.3 Flowchart of the simulation set-up using different array configurations

5.6 Simulation Results

Figure 5.4 shows the 2D view of the original 3D breast model with two spherical lesions located at the same layer within the breast (see Table 5-2). The breast model was located at $z = 0$ mm. Colour bar shows the complex relative permittivity of the breast.

Colour bars in the reconstructed images indicate the backscattered electric field from the breast.

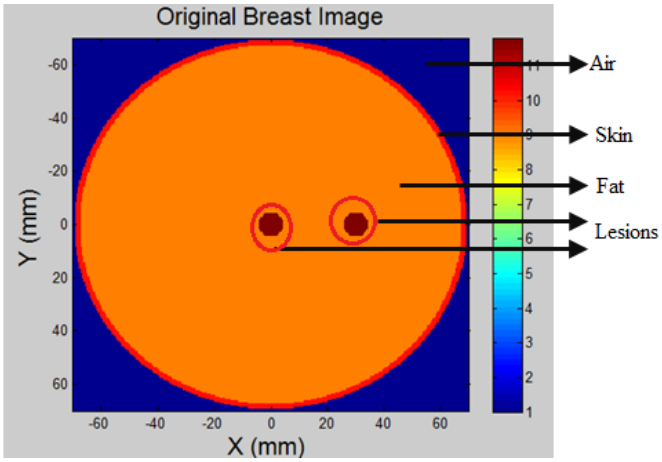

Figure 5.4 2D view of the 3D breast model containing skin, fat and lesions (circled in red)

Table 5-2 Spherical lesion location and size

Number	**Location (mm)**			**Size (mm)**		
	x	y	z	σ_x	σ_y	σ_z
1	0	0	20	5	5	5
2	30	0	20	5	5	5

Figure 5.5 shows the regularly spaced, spiral and random antenna array configurations and the reconstructed 2D breast images using the regularly spaced antenna, spiral and random array configurations respectively. The breast model was placed at $z = 0$ mm and all antenna array configurations were placed at $z = -450$ mm. Colour bars plot signal intensity on a linear scale that is normalised to the maximum in the 2D image space. Table 5-3 compares the simulation results (lesion detection quantity) using various antenna array configurations.

Table 5-3 Simulation results using various antenna array configurations

Array	**Dielectric Contract**	**Antenna Number**	**Image**	**Lesion**			
				Size	**Number**	**Locations**	**Detection**
Regularly spaced	1.056	16	2D HMIA	5 mm	2	$x_1 = 0,$ $y_1 = 0,$ $z_1 = 20,$ $x_2 = 30,$ $y_2 = 0,$ $z_2 = 20$	0
Spiral							2
Random							2

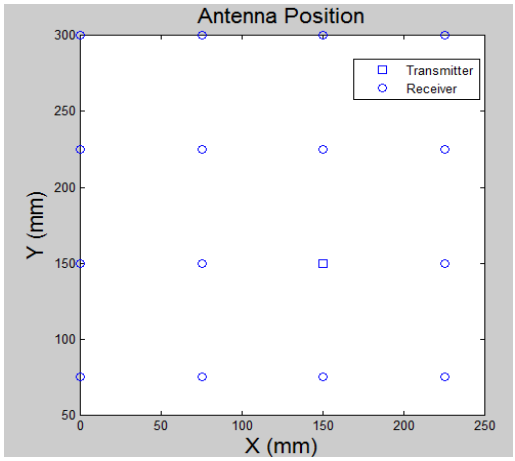

(a)

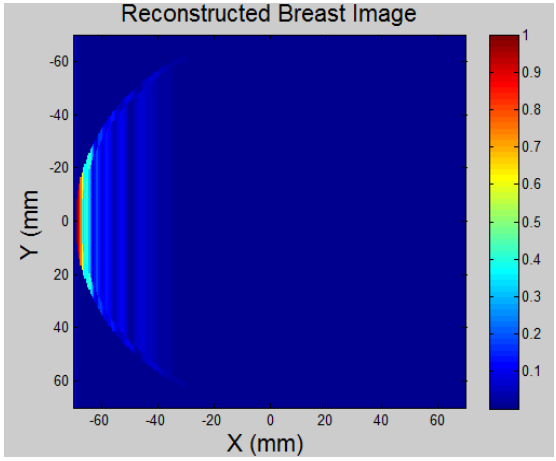

(b)

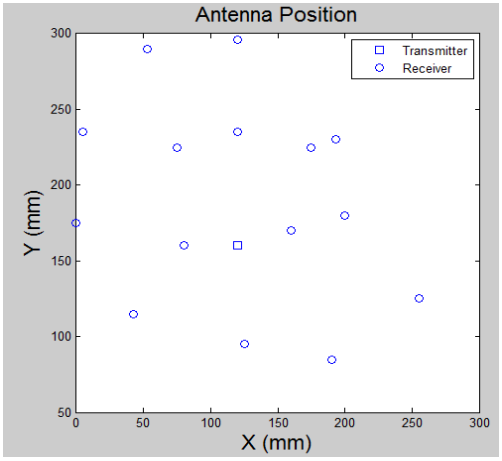

(c)

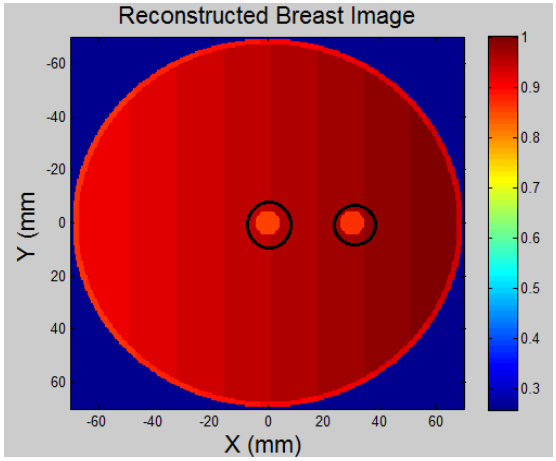

(d)

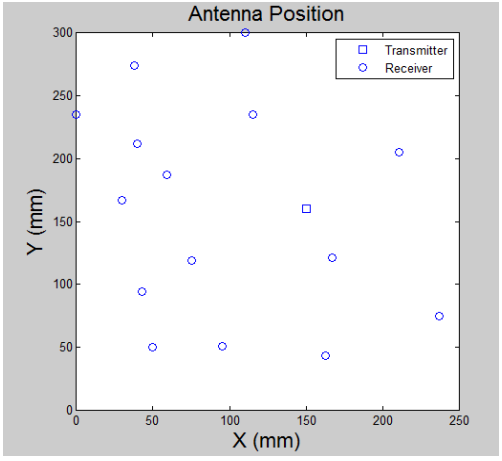

(e)

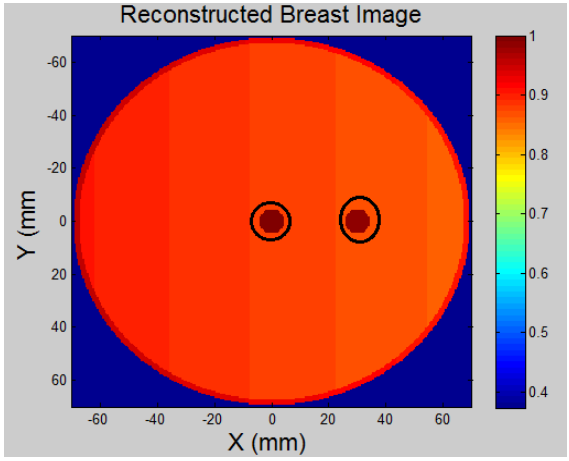

(f)

Figure 5.5 (a) Regularly spaced antenna array (b) Reconstructed breast phantom image using regularly spaced array (c) Spiral antenna array (d) Reconstructed breast phantom image using spiral antenna array (e) Radnom antenna array (f) Reconstructed breast phantom image using random antenna array

The reconstructed breast images in Figure 5.5 and Table 5-3 show that lesions were successfully detected using the spiral and random array configurations but cannot be

easily identified by visualization using the regularly spaced array configuration. This is because the regularly spaced array provides poor aperture uv coverage leading to a limited range of baseline values. The results confirmed that a high quality breast image can be obtained when the antenna array configuration offers dense sampling of the aperture uv plane over a wide range of baseline lengths.

Figure 5.6 compares the reconstructed breast images using a 16-element random antenna array. The antenna array plane was varied between $z = -50$ mm and $z = -600$ mm in 12 equal steps and the breast model was placed at $z = 0$ mm. Colour bars indicate the backscattered field from the breast model on a linear scale, normalised to the maximum in the 2D images space.

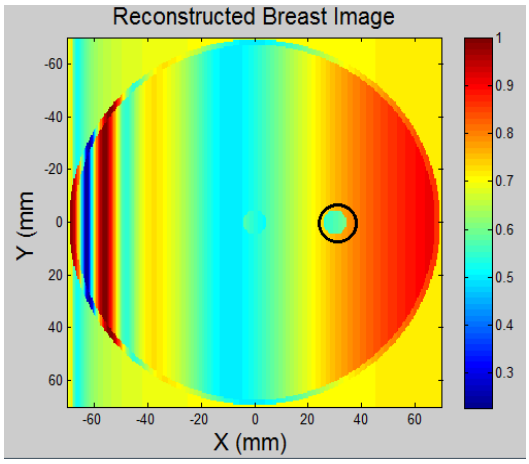

(a)

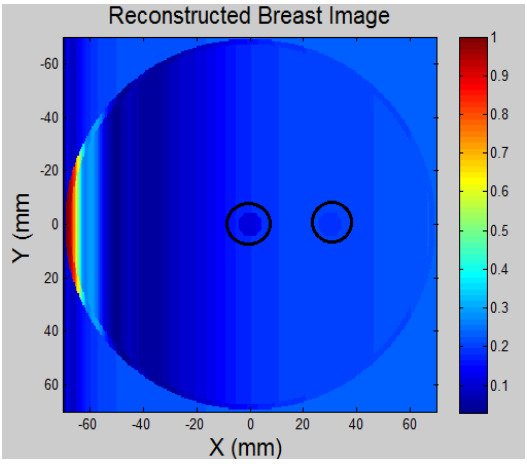

(b)

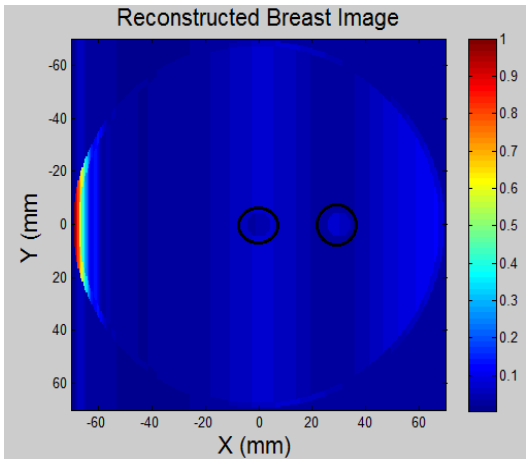

(c)

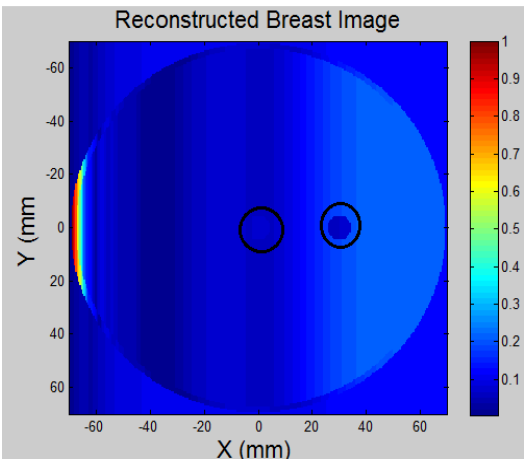

(d)

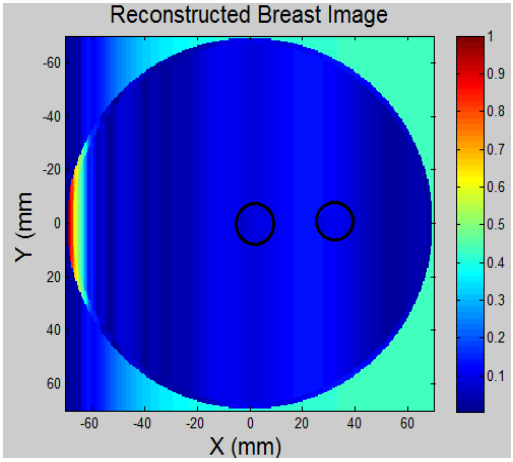
Reconstructed Breast Image
Y (mm
X (mm)

(e)

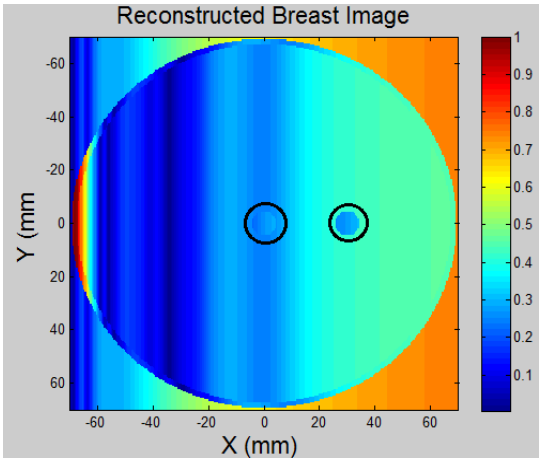
Reconstructed Breast Image
Y (mm
X (mm)

(f)

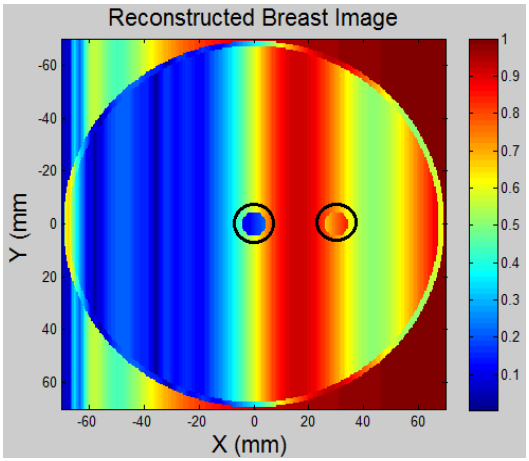
Reconstructed Breast Image
Y (mm
X (mm)

(g)

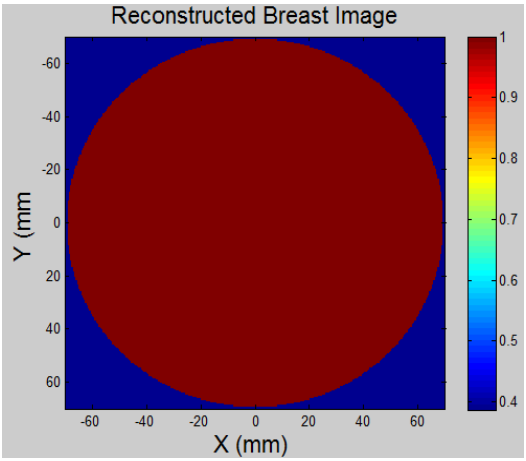
Reconstructed Breast Image
Y (mm
X (mm)

(h)

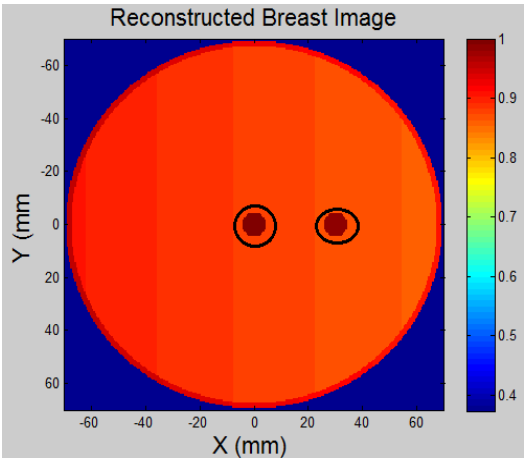
Reconstructed Breast Image
Y (mm
X (mm)

(i)

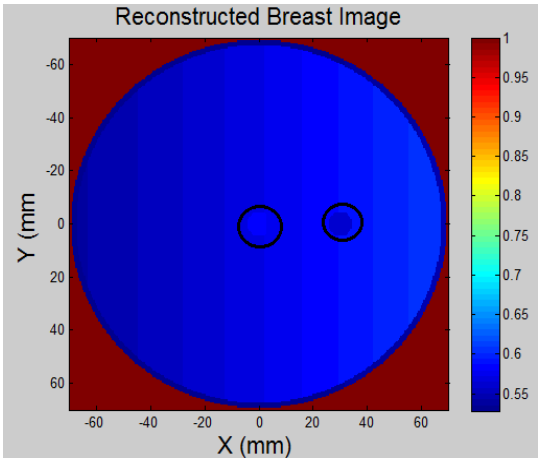
Reconstructed Breast Image
Y (mm
X (mm)

(j)

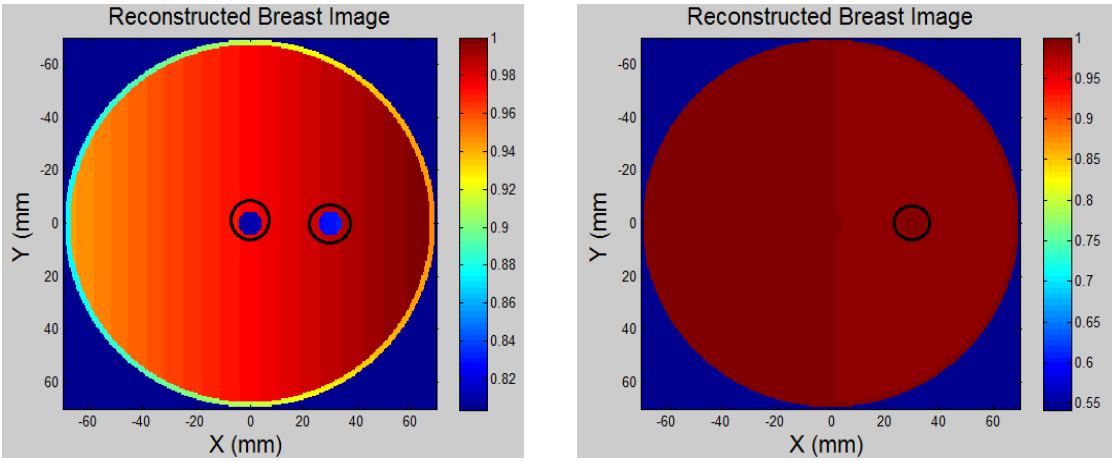

(k) (l)

Figure 5.6 2D reconstucted breast images with random antenna array was placed at (a) $z = -50$ mm (b) $z = -100$ mm (c) $z = -150$ mm (d) $z = -200$ mm (e) $z = -250$ mm (f) $z = -300$ mm (g) $z = -350$ mm (h) $z = -400$ mm (i) $z = -450$ mm (j) $z = -500$ mm (k) $z = -550$ mm (l) $z = -600$ mm

Table 5-4 summaries the simulation results of the same breast model that contains two lesions using a 16-element random antenna array configuration when the breast model was placed at different height.

Table 5-4 Simulation results using random array configuration with different measurement heights

Height (mm)	**Dielectric Contract**	**Antenna Number**	**Image**	**Lesion**			
				Size	**Locations**	**Detection**	**Artifacts**
50	1.056	16	2D HMIA	5 mm	$x_1 = 0,$ $y_1 = 0,$ $z_1 = 20,$ $x_2 = 30,$ $y_2 = 0,$ $z_2 = 20$	1	Yes
100						2	Yes
150						2	Yes
200						1	Yes
250						2	Yes
300						2	Yes
350						2	Yes
400						0	Yes
450						2	No
500						2	No
550						2	No
600						1	No

Figure 5.6 shows that two lesions were detected clearer within the reconstructed breast image when the antenna array plane was placed at the distance range between $z = -450$ mm and $z = -550$ mm. The simulation results demonstrated that the spiral and random antenna array configurations deliver clearer and more accurate images than the

regularly spaced configuration (see Figure 5.6 and Table 5-4). This is because the proposed antenna array configurations provide more dense sampling of the aperture plane over a wide range of the baseline lengths and offer the best possibility of detecting lesions anywhere within the breast. The best measurement distance range between antenna array and the breast model is 450 mm~550 mm. Measurement height out of this range can cause artifacts making the images harder to identify lesions.

5.7 Closure

In this chapter, a small flanged open-ended rectangular waveguide antenna was designed for practical implementation in breast lesion detection using the HMIA technique. The spiral, random and regularly spaced antenna array configurations and the application of HMIA technique for breast lesion detection were presented. A computer model was developed to evaluate the HMIA technique using various antenna array configurations.

Investigation of antenna array configurations to significantly improve the quality of medical imaging at low cost is another subject. The concept of using spiral and random antenna arrays for lesion detection using HMIA techniques is preliminary introduced in this work, they could also suit many other medical imaging applications, such as microwave imaging for brain stroke detection. Future research will find a unique solution to optimize the spatial resolution of the image by selecting the optimum antenna configurations.

The next chapter details an experimental implementation of the 2D and 3D HMIA techniques using a breast phantom.

Chapter 6 Experimental Set-up

6.1 Introduction

In this chapter, the experimental validation of the HMIA simulation models using a simplified breast phantom is presented. The significant parts of this work have been described in conference papers [CP3]-[CP5]. The equipment and devices used in the experiments are described in section 6.1. Experiments include 2D and 3D system set-ups, the choice of antenna, antenna positions and breast phantoms, as well as data collection are detailed in section 6.2. The experiment results and summary of this chapter are given in sections 6.3 and 6.4.

6.2 Equipment

Equipment and devices used in experiments are listed below:

- Agilent N5230A (10 MHz - 20 GHz) vector network analyser (PNA)
- 16 antennas
- 16 cables
- Microwave absorbing material
- Breast phantoms
- Macor glass ceramic plate (100 mm x 100 mm x 3 mm)
- Height gauge
- Spirit level
- USB hard drive
- Computer

6.3 Experiments

The design of the experimental system is based on the simulation system. This section will detail how to set-up simple 2D and 3D HMIA experimental systems to validate the proposed 2D and 3D HMIA imaging algorithms for breast lesion detection.

6.3.1 System Set-ups

Figure 6.1 shows the schematic diagram of the HMIA system experimental set-up

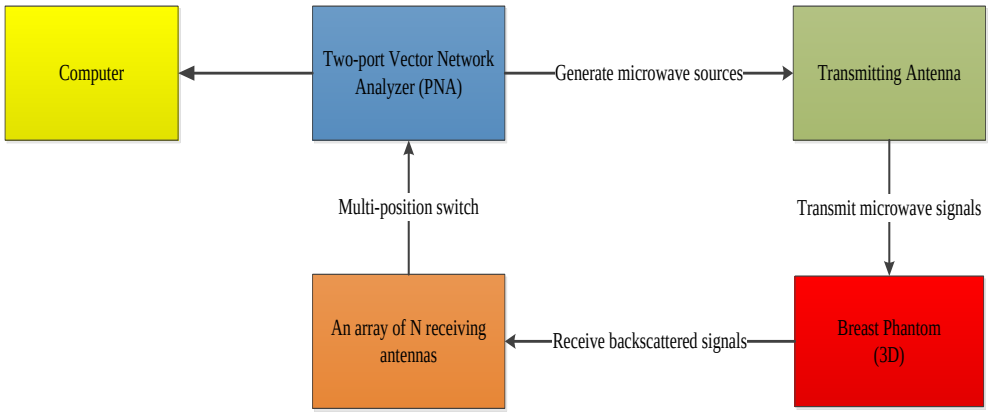

Figure 6.1 Schematic diagram of the HMIA system experimental set-up

6.3.1.1 2D HMIA System Set-up

Figure 6.2 shows the overall experimental set-up for the 2D HMIA system, this arrangement is similar to the simulation system. An array of 16 antennas was located inside a microwave absorbing material and was connected with an Agilent N5230A (10 MHz~20 GHz) vector network analyser (PNA). The breast phantom was placed on the top of a polystyrene box bridge and air was used as the host medium between the breast phantom and antenna array plane. A USB hard drive was connected to the PNA to store all the measured data and allow data transfer to the computer to display a breast image.

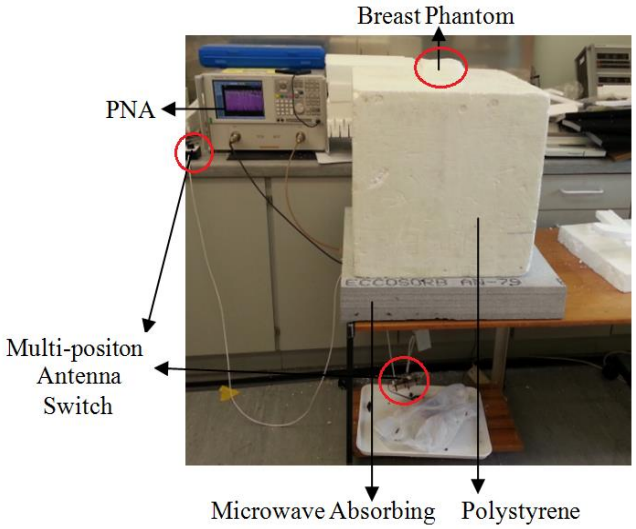

Figure 6.2 Photograph of the 2D HMIA experimental set-up

6.3.1.2 3D HMIA System Set-up

The 3D HMIA experimental set-up is shown in Figure 6.3. Unlike the 2D system, the 3D experiment system is designed to be movable in order to collect data at different heights. In the 3D HMIA system, two lab jacks were used to vertically displace the breast phantom from $z = 540$ mm to $z = 580$ mm in 40 equal steps. A height gauge was used to measure the vertical displacement of the phantom and a spirit level was used to balance the polystyrene box bridge during movement.

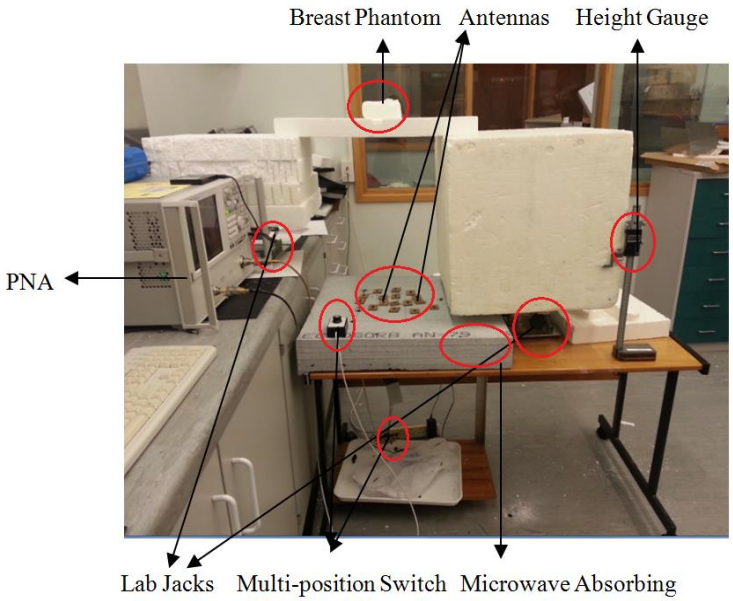

Figure 6.3 Photograph of the 3D HMIA experimental set-up

6.3.2 Flanged Open-ended Rectangular Waveguide Antenna (ORWA)

A WR 62 waveguide that has a cut-off frequency 9.5 GHz was used to make the designed ORWA as shown in Figure 6.4. A small SMA-Male connector was inserted through a side wall of the waveguide placed at 9 mm from the bottom of the antenna (termination) as the excitation port, which allows the waveguide connect to RG coaxial cable for measurement.

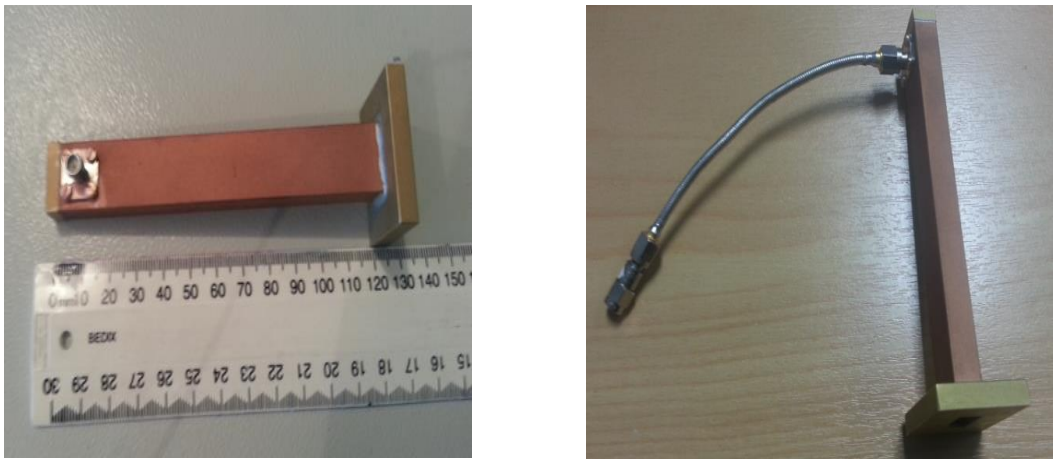

(a) (b)

Figure 6.4 Photograph of (a) the flanged ORWA (b) Flanged ORWA with connection cable

The designed antenna was tested using a two-port PNA. Figure 6.5 displays the measured magnitude of the reflection coefficient S_{11} of the waveguide antenna at the wide frequency spectrum from 10 GHz to 20 GHz. All measured return losses are below -10 dB. The best performance of the wave-guide antenna is achieved at the operating frequency which is at approximately 12.12 GHz with the return loss below -60 dB.

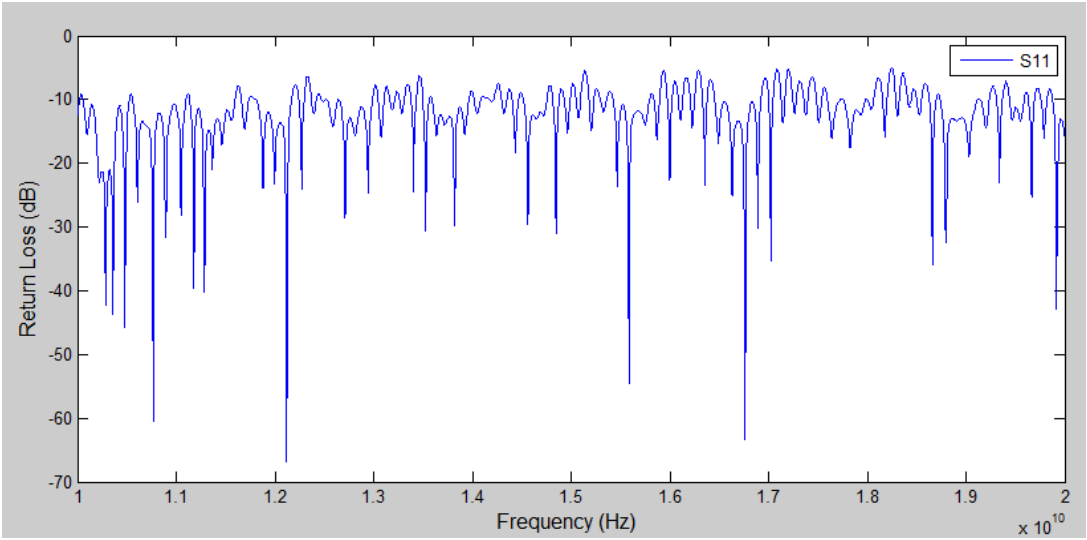

(a)

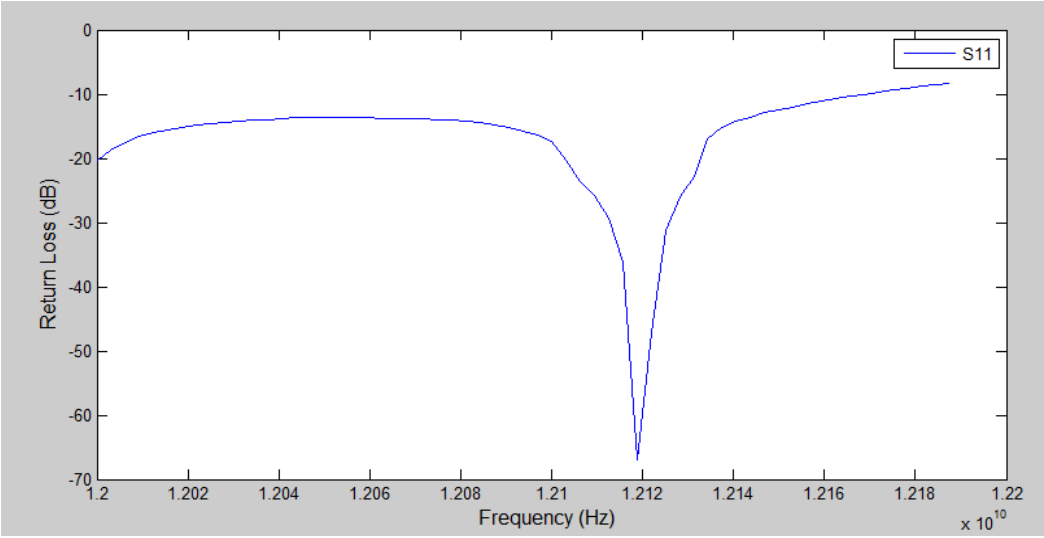

(b)

Figure 6.5 Measured return loss of antenna with frequency range between (a) 10 GHz to 20 GHz (b) 12 GHz to 12.2 GHz

6.3.3 Antenna Positions

Regularly spaced, spiral and random array configurations were selected for the experiments shown in Figure 6.6. An array of 16 antennas was surrounded with ECCOSORB AN-79 (600 mm x 600 mm) electromagnetic absorbing material to reduce ambient reflections (See Figure 6.7). The locations of antennas can be found in Appendix C.

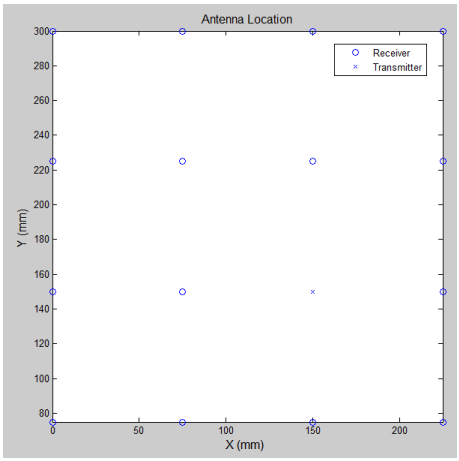

(a)

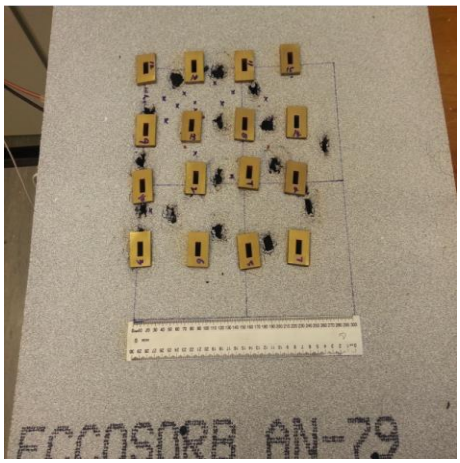

(b)

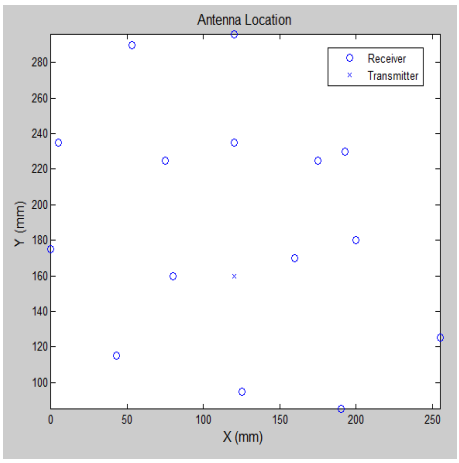

(c)

(d)

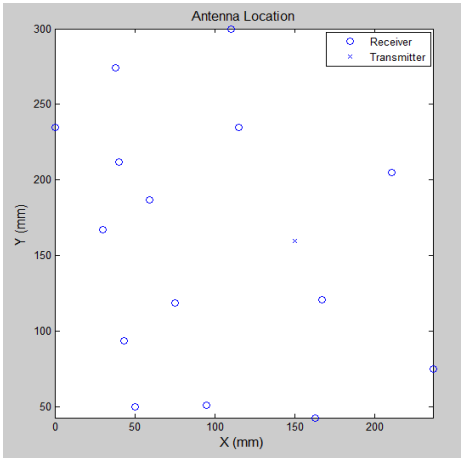

(e)

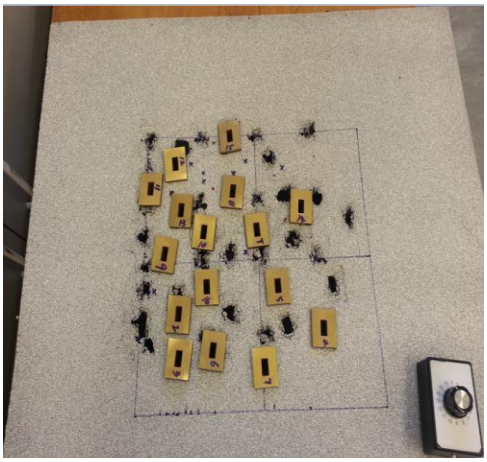

(f)

Figure 6.6 (a) Schematic of regularly spaced array (b) Photograph of regularly spaced array (c) Schematic of spiral array (d) Photograph of spiral array (e) Schematic of random array (f) Photograph of random array

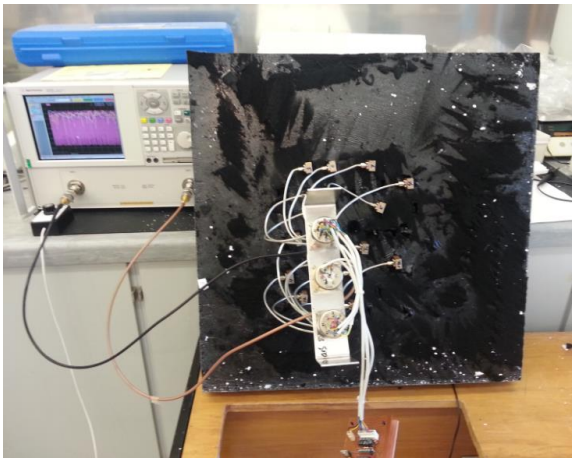

Figure 6.7 Bottom view of antenna array

6.3.4 Breast Phantoms

All breast phantoms consist of a region of breast tissue and lesions and each of the six breast phantoms consist of breast tissue, lesions and a thin layer of skin. All breast phantoms were shaped in a rectangle plastic box and were covered by thin plastic film. The latter has a negligible effect on the scattered electromagnetic field in the considered frequency range. Air was used as the host medium to fill the space between the breast phantom and antenna array.

Two types of breast fat tissues were used in the experiments. The first type of breast tissue (fat tissue 1) was made of 100% emulsifying ointment BP that contained 30% emulsifying wax, 50% white soft paraffin and 20% liquid paraffin. The second type of breast tissue (fat tissue 2) was made of 90% emulsifying ointment BP and 10% water.

The skin layer in the phantom was created using a 3-mm-thick MACOR machinable glass ceramic (MGC) plate (100 mm x 100 mm x 3 mm). According to the manufacturer, the dielectric constant of MGC is 5.67 at 8.5 GHz with a loss tangent of 0.0071.

Small metal balls (10 mm in diameter), grapes (4 mm to 15 mm in diameter), blueberries (4 mm to 7 mm in diameter) and cucumbers (2.5 mm to 5 mm in diameter) were inserted into the breast phantoms models to represent malignant tissue.

6.3.5 Dielectric Properties Measurement

The actual dielectric properties of the breast phantoms were measured before data collection. Measurements with frequencies ranging from 10 GHz to 20 GHz were conducted using Agilent N5230A PNA and an Agilent 85070 single port dielectric probe. Reflection coefficients were converted to dielectric permittivity and loss tangent by Agilent 85070 dielectric measurement software.

Calibration was performed using the guidance of the calibration software available in the PNA. The probe is measured in air, then when it is shorted through the use of a special shorting block, and finally when it is immersed in deionised water at a temperature of 21°C. Once the calibration was completed, the probe was placed on the surface of a phantom and a measurement was triggered manually. This measurement was repeated three times in order to obtain an average reading. After measuring each phantom, the probe was cleaned with tissue paper to prevent any oil that may accumulate on it during measurements. The electrical properties of the breast phantoms are summarized in Table 6-1, and measurement results for dielectric permittivity of various lesions (cucumber, grape, and blueberry) and fat tissues at frequency range of 10 GHz to 20 GHz are shown in Figure 6.8.

Table 6-1 Electrical properties of materials at 12.6 GHz

Material	**Real part of permittivity**	**Imaginary part of permittivity**	**Data source**
Fat tissue 1 (100% wax)	2.4307	0.2432	Measured
Fat tissue 2 (90% wax + 10% water)	3.1617	0.5334	Measured
Skin (ceramic plate) at 8.5 GHz	5.67	0.040257	Manufacturer
Lesion 1 (Grape)	23.8021	20.8695	Measured
Lesion 2 (Cucumber)	42.0014	2.4368	Measured
Lesion 3 (Blueberry)	27.7296	7.9791	Measured
Air	1	0	Published [142]

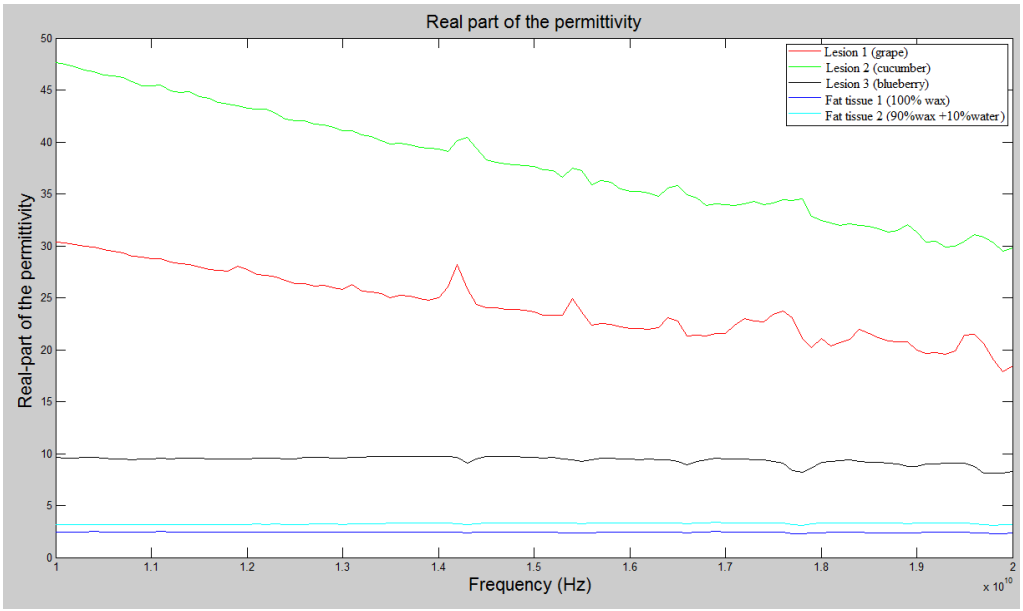

(a)

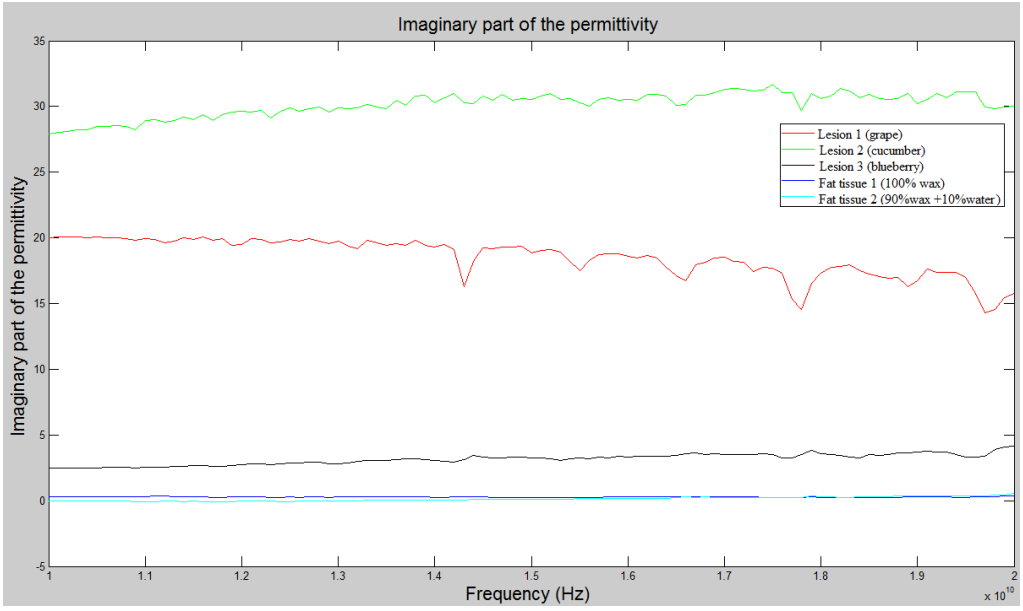

(b)

Figure 6.8 (a) Real part and (b) Imaginary part of the permittivity of the breast and lesion simulant materials

6.3.6 Data Collection

Although only a single frequency was applied for reconstructing the image, the wide frequency spectrum from 10 GHz to 20 GHz was collected for choosing the optimum frequency. Data was recorded at 3201 frequency points for choosing the optimum frequency between 10 GHz to 20 GHz and 101 measurements were averaged at each frequency. All 16 antennas were tested before data collection with one antenna acting as the transmitter, the others acting as the receivers.

6.3.6.1 Data Collection for the 2D HMIA System

In 2D HMIA measurement, the breast phantom was placed on the top of the polystyrene box bridge and air was used as the host medium between the breast phantom and the antenna array plane. During data collection, a two-port Agilent N5230A PNA was connected to antenna array plane to transmit microwave signals and receive the backscattered reflections from the breast phantom.

In all cases, transmission parameter S_{21} was first measured with no scattering object present between the antennas. This constitutes the incident field. Once the incident field was established, S_{21} transmission was measured again with various breast phantoms placed on the top of antenna array. The transmitter illuminated the breast phantom and the reflection coefficient S_{21} magnitude and phase of each receiver was recorded at a frequency of 12.6 GHz. The complex correlation of the scattered field data between all possible pairs of antennas was then computed to generate a complex visibility function required as input to the 2D imaging algorithm. The MATLAB code used to generate 2D and 3D breast phantom images from the measured data is detailed in Appendix D

6.3.6.2 Data Collection for the 3D HMIA System

In 3D HMIA measurement, the breast phantom was placed on the top of the polystyrene box bridge and air was used as the host medium between the breast phantom and antenna array plane. Two lab jacks were used to vertically displace the breast phantom from $z = 540$ mm to $z = 580$ mm in 40 equal steps. A height gauge was used to measure the vertical displacement of the phantom and a spirit level was used to balance the polystyrene box bridge during movement.

The breast phantom was illuminated by the transmitter and the magnitude and phase of the scattered field at each receiver was recorded at a frequency of 12.6 GHz. These data collection steps were repeated for each height of the phantom above the antenna array plane. The complex correlation of the scattered field data between all possible pairs of antennas was then computed to generate a complex visibility function which is required as an input to the 2D imaging algorithm. The MATLAB code used to generate 3D images from the measured reflection signals of the breast phantoms is detailed in Appendix E.

6.4 Experimental Results

The proposed experiments are divided into five major groups as detailed in Table 6-2.

Table 6-2 Experimental groups

Experiments	**Purpose**	**Array Configuration**	**Height between the breast phantom and the antenna array (mm)**	**Antenna Number**
Group I	Generate a 2D breast image to validate 2D HMIA imaging algorithm	• Spiral • Random	390~540	16
Group II	Generate a 3D breast image to validate 3D HMIA imaging algorithm	• Spiral	540~580	16
Group III	Validate the proposed spiral and random array configurations have the ability to produce high resolution breast images	• Regularly spaced • Spiral • Random	540~545	16
Group IV	Validate the HMIA system has the ability to detect small object	• Random	490	16
Group V	Validate the system on a more realistic phantom	• Random	540	15

6.4.1 Group I Results

Experiment I was set-up to validate that the 2D HMIA image reconstruction algorithm can generates a 2D breast image. The measured data of the first experiment is listed in Appendix F.

Various breast phantoms used in Group I experiment are presented in Figure 6.9 to Figure 6.12, where the spiral antenna array was placed at $Z = 0$ mm and the breast phantoms (180 mm x 160 mm x 40 mm) were located on the top of antenna array at $Z = 390$ mm. The reconstructed 2D images of the breast phantoms are shown in Figure 6.9 to Figure 6.12. Colour bars plot signal energy on a linear scale, normalised to the maximum in the 2D images space and values below 0.1 are rendered as blue.

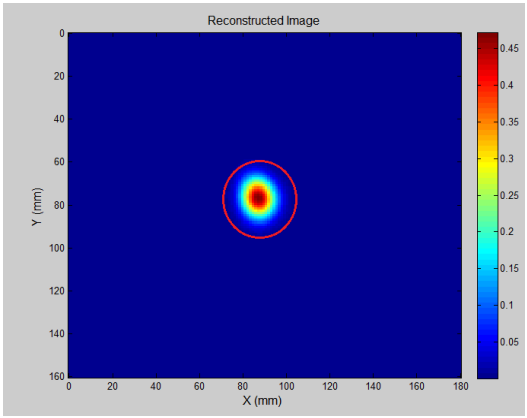

(a) (b)

Figure 6.9 (a) Photograph of the breast phantom (180 mm x160 mm x 40 mm) including fat and one lesion (15 mm in diameter grape) (b) Image of breast phantom containing fat and one lesion (circled in red)

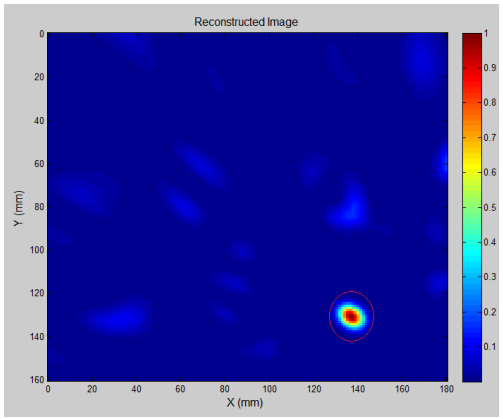

(a) (b)

Figure 6.10 (a) Photograph of the breast phantom (180 mm x160 mm x 40 mm) containing fat and one lesion (10 mm in diameter grape) (b) Image of breast phantom containing fat and one lesion (circled in red)

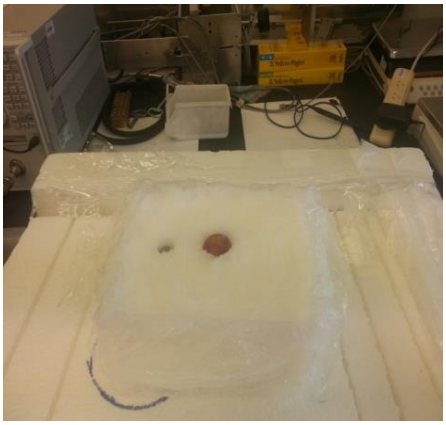

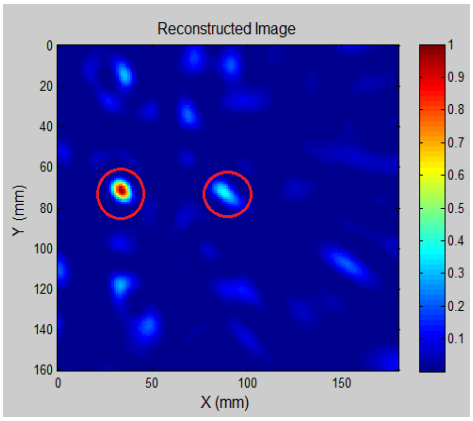

(a) (b)

Figure 6.11 (a) Photograph of the breast phantom (180 mm x160 mm x 40 mm) containing fat and two lesions (10 mm in diameter metal ball and 15 mm in diameter grape) (b) Image of breast phantom containing two lesions (circled in red)

(a)

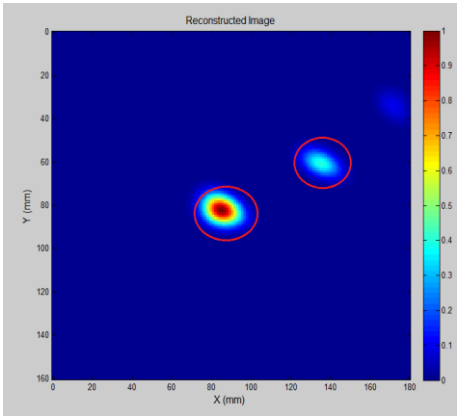

(b)

Figure 6.12 (a) Photograph of the complete breast phantom (180 mm x160 mm x 40 mm) including skin, fat and two lesions (10 mm and 15 mm in diameters grapes) (b) Image of breast phantom containing two lesions (circled in red)

Figure 6.13 shows the breast phantom (100 mm x 100 mm x 30 mm) containing skin, fat and one lesion (10 mm in diameter grape), where the spiral antenna array was placed at $Z = 0$ mm and the breast phantom was located on the top of array plane at $Z = 540$ mm.

(a)

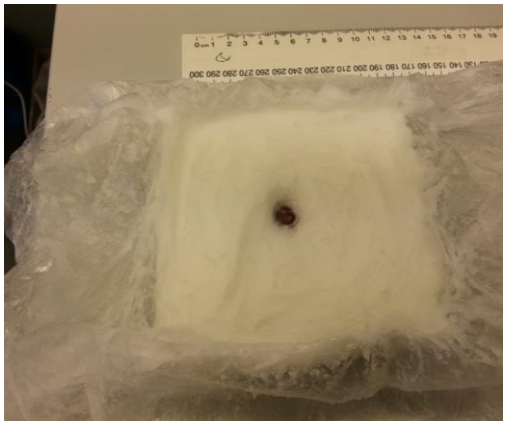

(b)

Figure 6.13 Photograph of the complete breast phantom (100 mm x 100 mm x 30 mm) containing skin, fat and one lesion (10 in diameter grape) (a) top view (b) inside view

Figure 6.14 clearly shows the simulated lesion in the reconstructed 2D phantom image. Colour bar plots signal energy on a linear scale, normalised to the maximum in the 2D image space and values below 0.1 are rendered as blue. Data used to produce the image shown in Figure 6.14 utilise a "zooming function" of power two to enhance the contrast with the background.

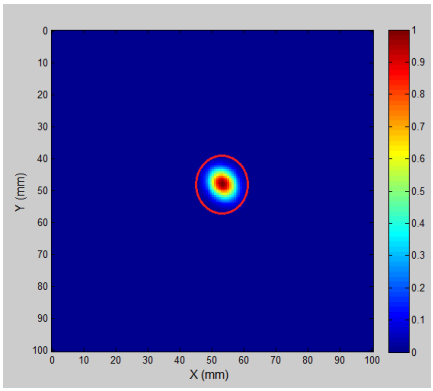

Figure 6.14 Image of breast phantom with one lesion

6.4.2 Group II Results

Group II was set-up to validate that the proposed 3D HMIA image reconstruction algorithm can generates a 3D breast image and the measured data of this group is listed in Appendix G. Figure 6.15 illustrates the phantom (180 mm x 160 mm x 40 mm) containing skin, fat and one lesion (10 mm in diameter grape) that was used in Group II. The lesion was located at ($X = 140$ mm, $Y = 50$ mm, $Z = 10$ mm) and the breast phantom was placed at a height above the antenna array plane that was varied between $Z = 540$ mm and $Z = 549$ mm in 10 equal steps.


Figure 6.15 Photograph of the breast phantom containing skin, fat and one lesion (10 mm in diameter grape)

Figure 6.16 clearly shows the simulated lesion in the reconstructed 3D breast phantom image.

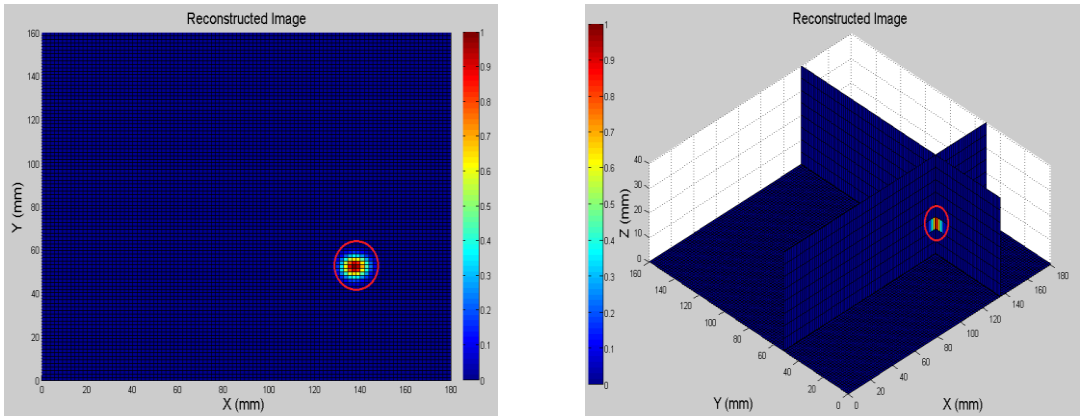

(a) (b)

(c) (d)

Figure 6.16 3D image of breast phantom with one lesion (a) top view (b)-(d) side views

Figure 6.17 displays the phantom (180 mm x 160 mm x 40 mm) containing fat and two lesions (10 mm and 15 mm in diameters grape), where the lesions were located at ($X = 90$ mm, $Y = 60$ mm, $Z = 25$ mm) and ($X = 30$ mm, $Y = 105$ mm, $Z = 25$ mm). It was placed at a height above the antenna array plane that was varied between $Z = 540$ mm and $Z = 549$ mm in 10 equal steps.

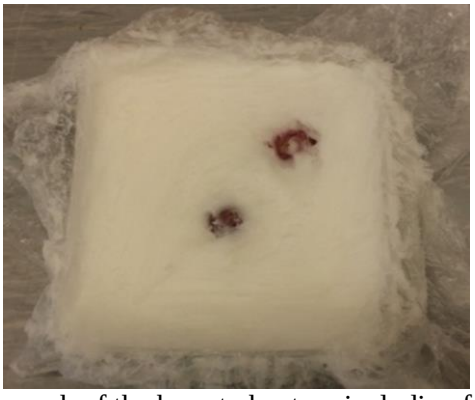

Figure 6.17 Photograph of the breast phantom including fat and two lesions

Figure 6.18 clearly shows the simulated lesion in the reconstructed 3D phantom image.

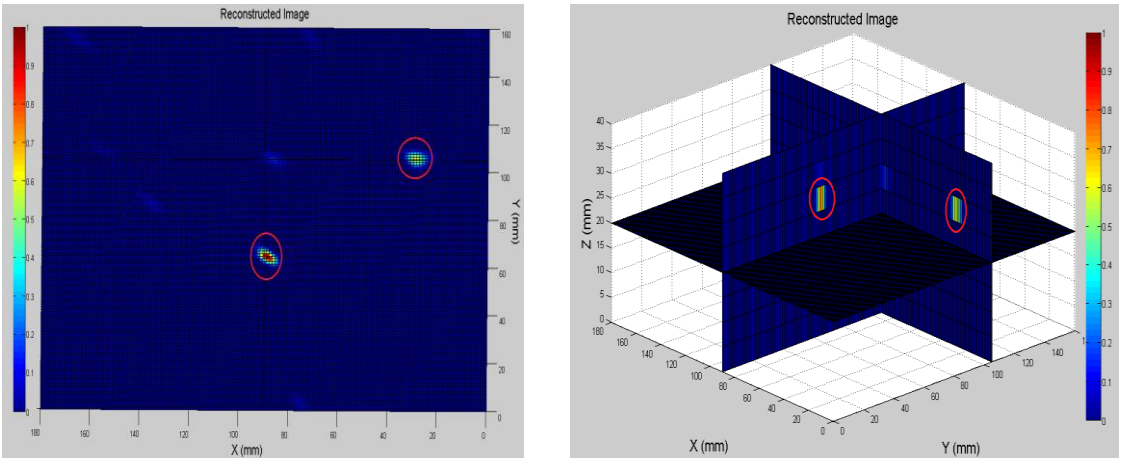

(a) (b)

Figure 6.18 (a) Top view of 3D breast image (b) Side view of 3D breast image

Figure 6.19 shows the complete phantom (100 mm x 100 mm x 30 mm) containing skin, fat and one lesion (10 mm in diameter grape), where the lesion was located at ($X = 50$ mm, $Y = 50$ mm, $Z = 15$ mm). It was placed at a height above the spiral antenna array plane that was varied between $Z = 540$ mm and $Z = 580$ mm in 40 equal steps.

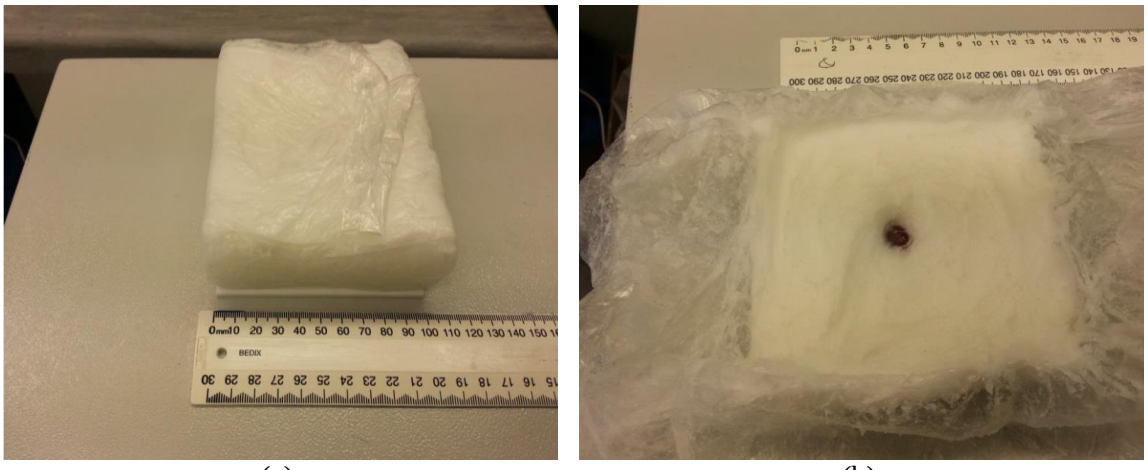

(a) (b)

Figure 6.19 Photograph of the complete breast phantom including skin, fat and one lesion (10 mm in diameter grape) (a) top view (b) inside view

Figure 6.20 displays the simulated lesion and skin in the reconstructed 3D phantom image.

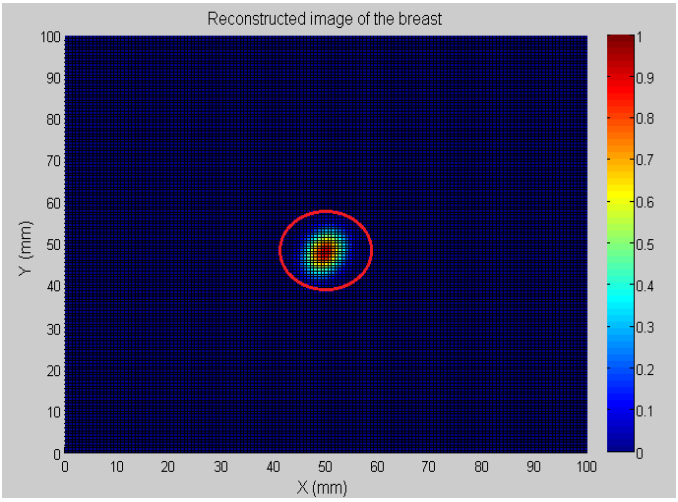

(a)

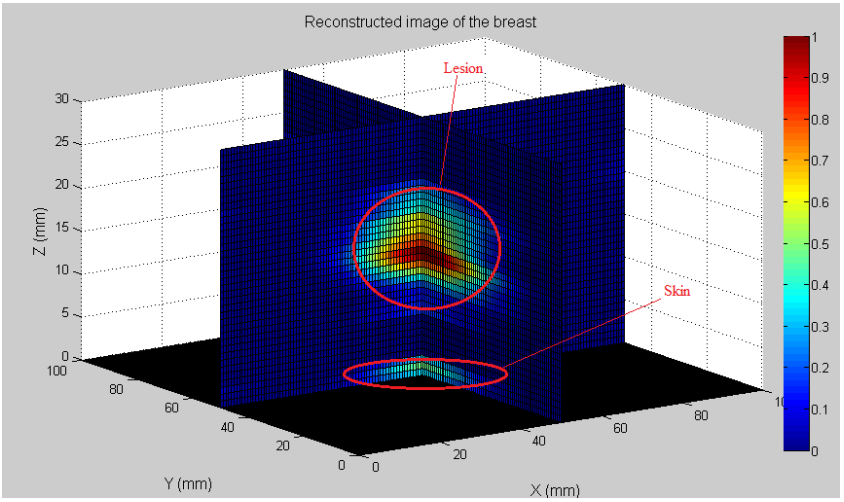

(b)

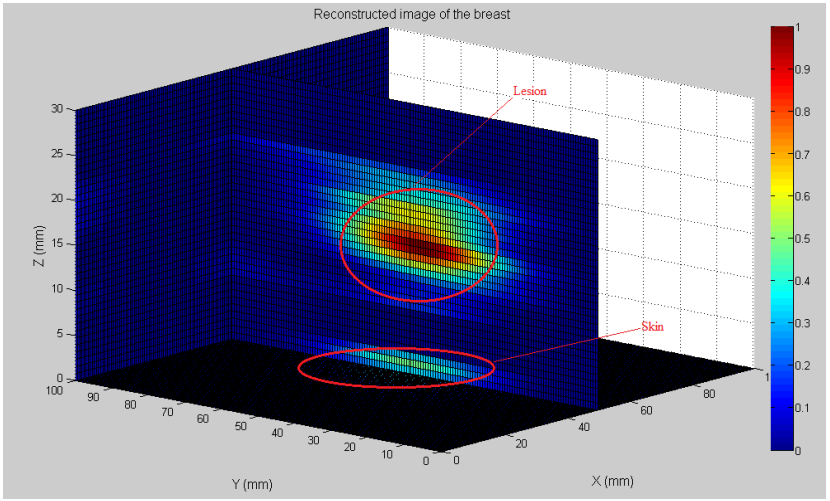

(c)

Figure 6.20 (a) Top view (b)-(c) Side views of 3D reconstructed breast phantom images

In Figure 6.16, Figure 6.18 and Figure 6.20, colour bars illustrate the backscattered electric field from the breast phantom on a linear scale, normalised to the maximum in the 3D volume. Values below 0.1 are rendered as blue. Data used to produce the image shown in Figure 6.16, Figure 6.18 and Figure 6.20 utilise a "zooming function" of power two to enhance the contrast with the background.

6.4.3 Group III Results

Group III validates the proposed spiral and random array configurations have the ability to produce better quality breast images compare to the widely used regularly spaced array. The measured data of Group III is listed in Appendix H.

Figure 6.21 illustrates the complete breast phantom (100 mm x 100 mm x 30 mm) including skin, fat and two lesions (10 mm and 15 mm diameters grapes) used in Group III, where two lesions are located at ($X = 50$ mm, $Y = 50$ mm, $Z = 20$ mm) and ($X = 70$ mm, $Y = 80$ mm, $Z = 20$ mm).

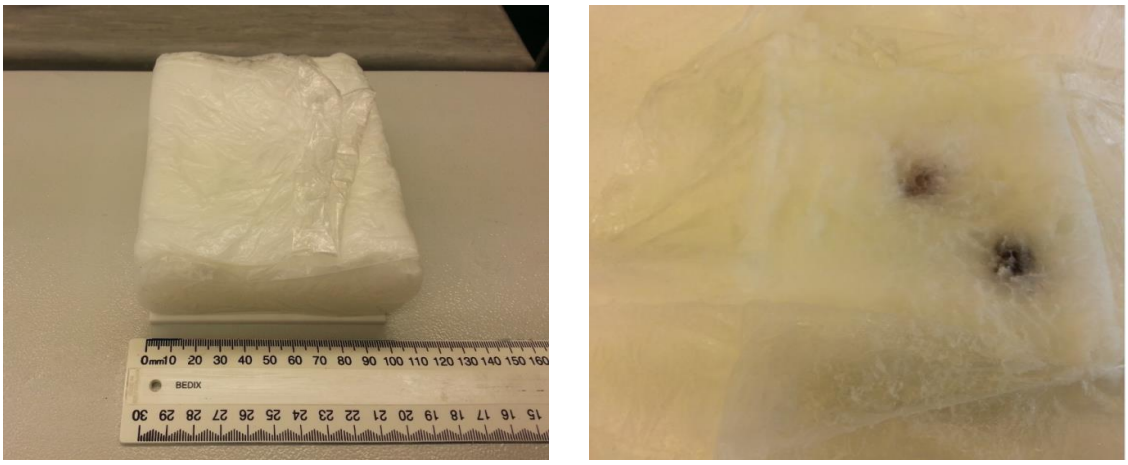

(a) (b)

Figure 6.21 Photograph of the complete breast phantom including skin, fat and two lesions (10 mm and 15 mm diameters grapes) (a) top view (b) inside view

The obtained 2D images of the breast phantom using regularly spaced, spiral and random array configurations are illustrated in Figure 6.22.

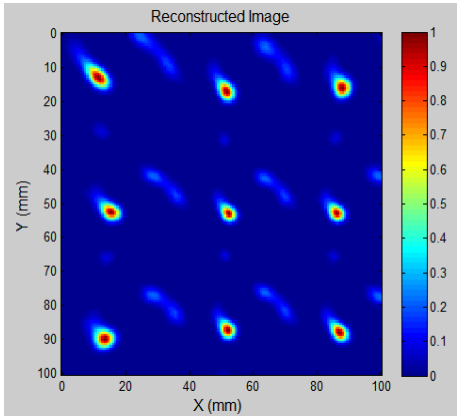

(a)

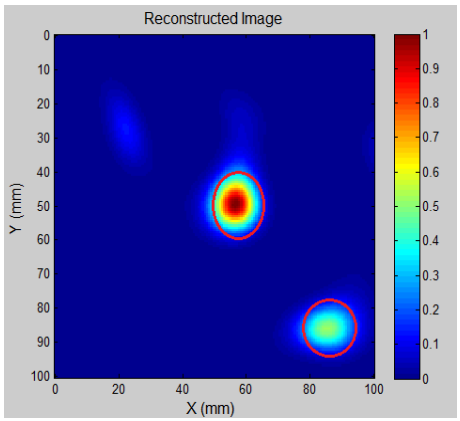

(b)

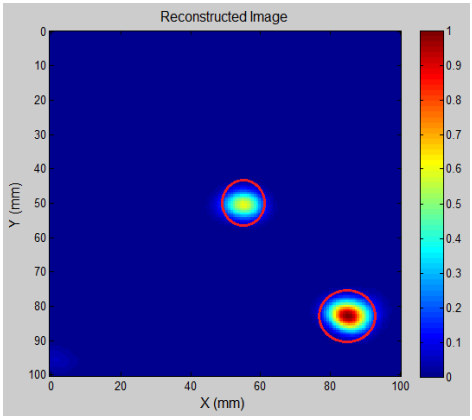

(c)

Figure 6.22 Reconstructed breast phantom images using (a) regular spaced antenna array (b) spiral antenna array (c) random antenna array

The received signals included direct coupling between the antennas as well as reflections from the breast phantom. The antenna coupling signal was obtained without the breast phantom present in the measurement. The 2D reconstructed images of the breast phantom shown in Figure 6.22 were obtained with this signal subtracted. Colour bars plot signal intensity on a linear scale that is normalised to the maximum in the 2D

image space. Data used to produce the image shown in in Figure 6.22 utilise a “zooming function” of power two to enhance the contrast with the background.. Values below 0.1 are rendered as blue.

The reconstructed breast images in Figure 6.22 show that lesions were successfully detected using the spiral and random array configurations but cannot be easily identified by visualization using the regularly spaced array configuration. This is because the regularly spaced array provides poor aperture uv coverage leading to a limited range of baseline values. The results confirmed that the high-resolution breast image could be obtained when the antenna array configuration offers dense sampling of the aperture uv plane over a wide range of baseline lengths.

6.4.4 Group IV Results

The experiment IV aims to prove the HMIA system has the ability to detect a small object. The measured data obtained can be found in Appendix I.

Figure 6.23 shows the complete breast phantom (100 mm x 100 mm x 30 mm) including skin, fat and three lesions (4 mm, 5 mm and 7 mm in diameters blueberries) at ($X = 20$ mm, $Y = 50$ mm, $Z = 25$ mm), ($X = 40$ mm, $Y = 50$ mm, $Z = 25$ mm) and ($X = 90$ mm, $Y = 50$ mm, $Z = 25$ mm). The phantom was placed on the top of the random antenna array at $Z = 490$ mm.

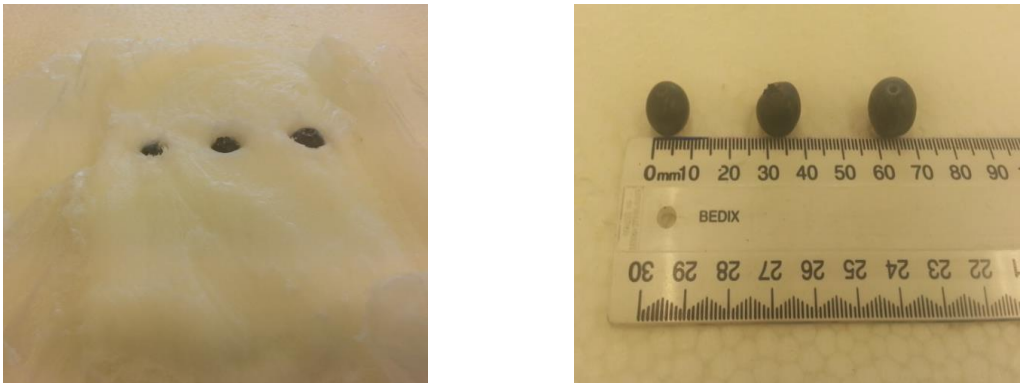

(a) (b)

Figure 6.23 (a) Photograph of the complete breast phantom including skin, fat and three lesions (b) Size of lesions

Figure 6.24 shows the 2D reconstructed image of the breast phantom with three lesions.

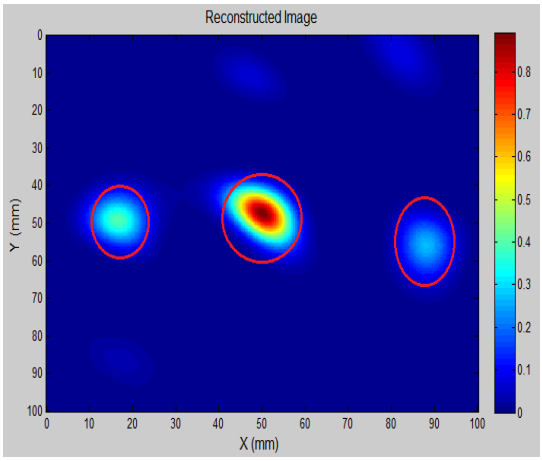

Figure 6.24 Image of breast phantom of three lesions

Figure 6.25 displays the breast phantom (100 mm x 100 mm x 30 mm) including fat and three lesions (4 mm, 5 mm, 7 mm in diameter) located at ($X = 20$ mm, $Y = 50$ mm, $Z = 25$ mm), ($X = 40$ mm, $Y = 50$ mm, $Z = 25$ mm) and ($X = 85$ mm, $Y = 50$ mm, $Z = 25$ mm).

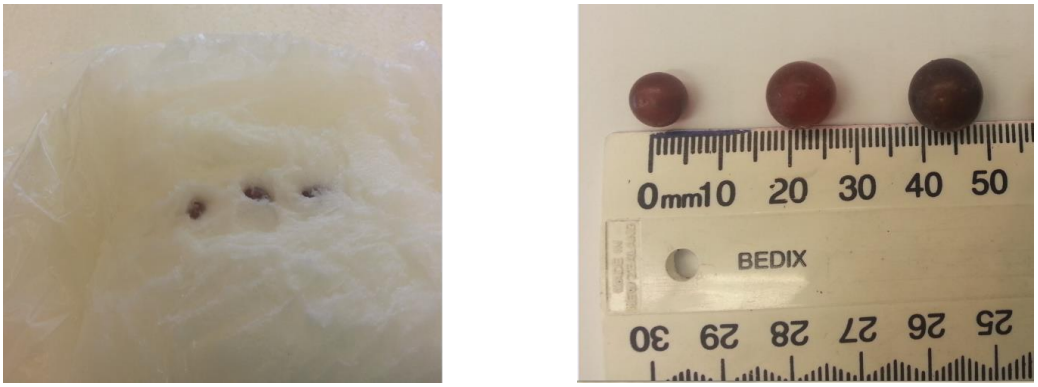

(a) (b)

Figure 6.25 (a) Photograph of the breast phantom containing skin, fat and three lesions (grapes) (b) Size of lesions (4 mm, 5 mm, 7 mm in diameters)

Figure 6.26 clearly shows the three simulated lesions in the reconstructed 2D phantom image.

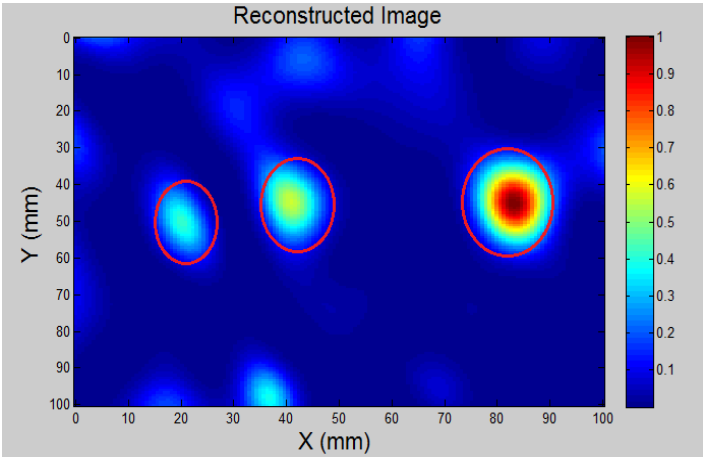

Figure 6.26 Image result of breast phantom

Figure 6.27 displays the phantom (100 mm x 100 mm x 30 mm) including skin, fat and two lesions (2.5 mm, 5 mm in diameters) located at ($X = 35$ mm, $Y = 50$ mm, $Z = 25$ mm) and ($X = 55$ mm, $Y = 60$ mm, $Z = 25$ mm). The breast phantom was placed on the top of the random array at $Z = 490$ mm.

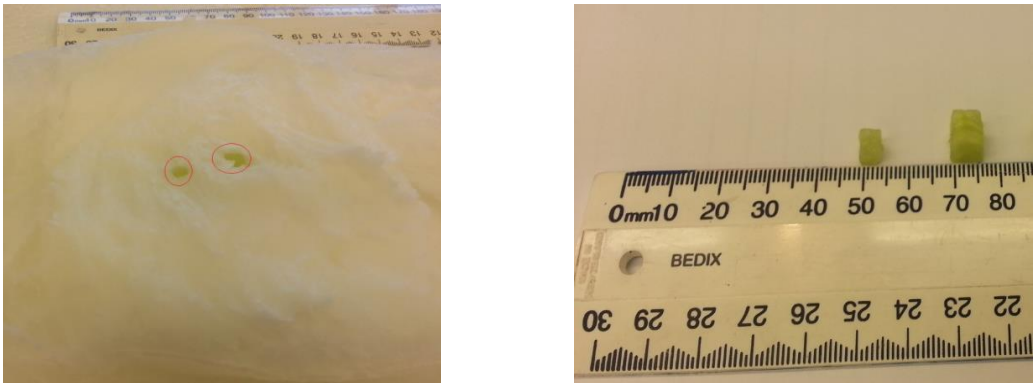

(a) (b)

Figure 6.27 (a) Photograph of the breast phantom containing skin, fat and two lesions (b) Size of lesions (2.5 mm, 5 mm in diameters)

Figure 6.28 demonstrates the 2D reconstructed image of the breast phantom of two lesions.

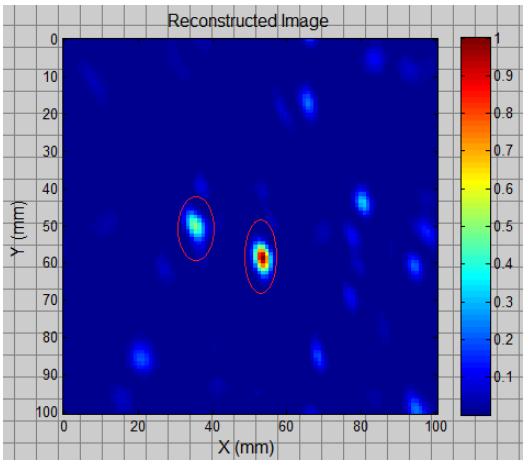

Figure 6.28 Image of breast phantom containing two lesions

Colour bars in Figure 6.24 , Figure 6.26 and Figure 6.28 plot signal energy on a linear scale, normalised to the maximum in the 3D volume. Values below 0.1 are rendered as blue. Data used to produce the images shown in Figure 6.24, Figure 6.26 and Figure 6.28 utilise a “zooming function” of power three to enhance the contrast with the background.

6.4.5 Group V Results

Group V validates the proposed HMIA image algorithm on a more realistic breast phantom, the measured data can be found in Appendix J. The breast phantom is made of skin, fat tissue and lesion. This is different from phantoms used in the first four groups as phantoms used in group V were made of fat tissue 2.

Figure 6.29 illustrates the breast phantom (100 mm x 100 mm x 40 mm) including skin, fat and one lesion (9 mm in diameter blueberry) located at ($X = 50$ mm, $Y = 50$ mm, $Z = 35$ mm), where the breast was place on the top of the random antenna array of 15 antennas at $Z = 540$ mm.

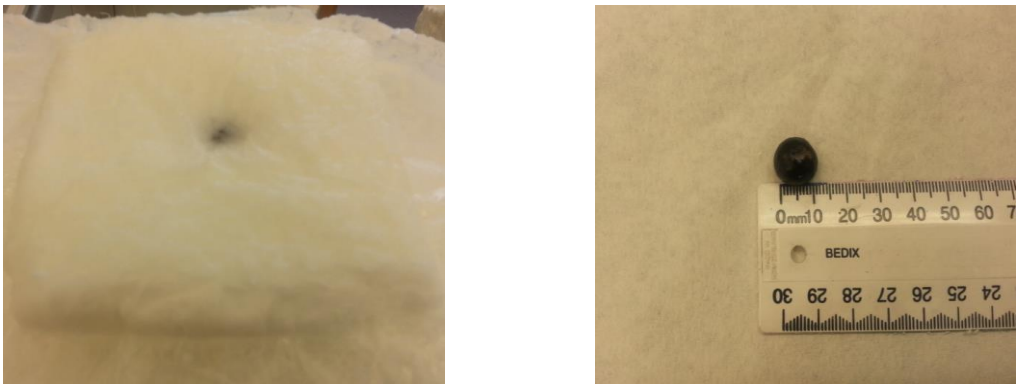

(a) (b)

Figure 6.29 (a) Photograph of the breast phantom containing skin, fat and one lesion (blueberry) (b) Size of lesion (9 mm in diameter)

Figure 6.30 clearly shows the simulated lesion in the reconstructed 2D breast image.

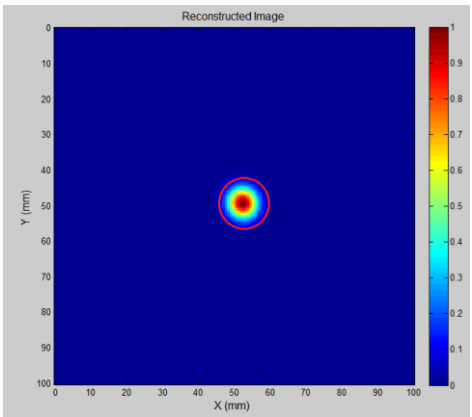

Figure 6.30 2D reconstructed breast image of one lesion

Figure 6.31 illustrates the breast phantom (100 mm x 100 mm x 40 mm) containing skin, fat and one lesion (7 mm in diameter grape) at ($X = 50$ mm, $Y = 50$ mm, $Z = 35$ mm), where the breast was placed on top of the random antenna array of 15 antennas at $Z = 540$ mm.

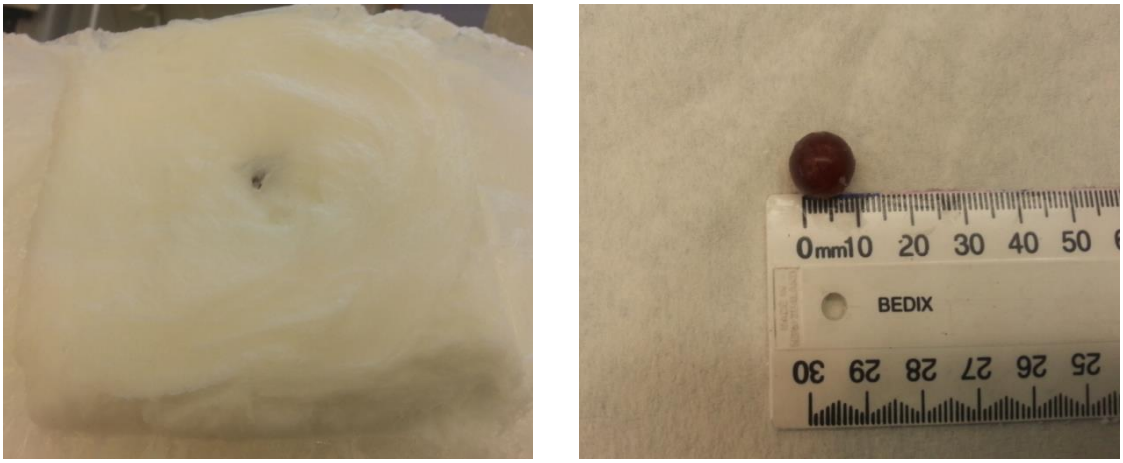

(a) (b)

Figure 6.31 (a) Photograph of the breast phantom containing skin, fat and one lesion (grape) (b) Size of lesion (7 mm in diameter)

The simulated lesion in the reconstructed 2D phantom image is shown in Figure 6.32.

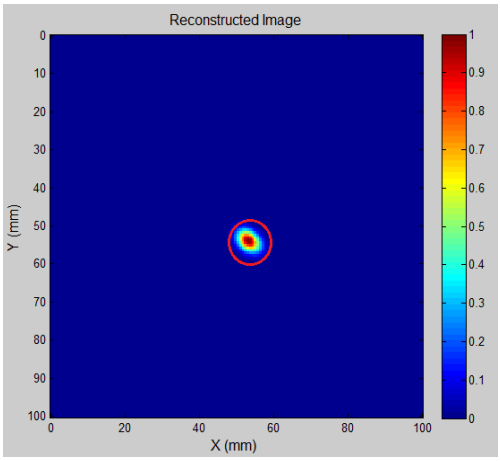

Figure 6.32 The 3:1 roomed 2D breast image of one lesion

Figure 6.33 illustrates the phantom (100 mm x 100 mm x 30 mm) including skin, fat and three lesions (13 mm, 10 mm, 10 mm in diameters) located at ($X = 40$ mm, $Y = 50$ mm, $Z = 25$ mm), ($X = 60$ mm, $Y = 50$ mm, $Z = 25$ mm) and ($X = 90$ mm, $Y = 55$

mm, $Z = 25$ mm), where the breast phantom was placed on top of the random array at $Z = 490$ mm.

Figure 6.33 Photograph of the breast phantom including skin, fat and three lesions

Figure 6.34 clearly shows the simulated three lesions within the reconstructed 2D phantom image.

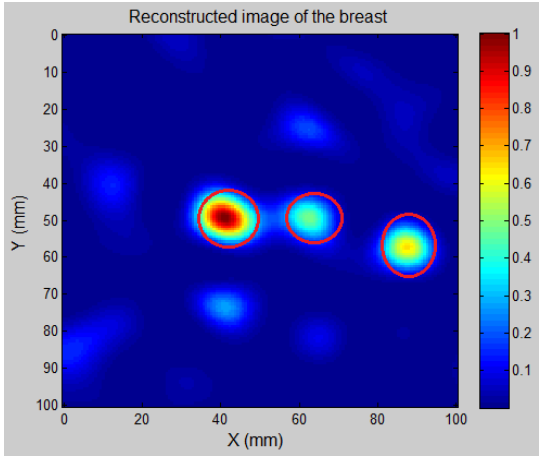

Figure 6.34 Image of breast phantom of three lesions

Colour bars in Figure 6.30, Figure 6.32 and Figure 6.34 plot signal energy on a linear scale, normalised to the maximum in the 3D volume and values below 0.1 are rendered as blue. Data used to produce the images shown in Figure 6.30 and Figure 6.32 utilise a "zooming function" of power three to enhance the contrast with the background and the data used to produce the image shown in Figure 6.34 utilise a "zooming function" of power two.

Table 6-3 shows the HMIA experimental results.

Table 6-3 HMIA experimental results

	Group I	**Group II**	**Group III**	**Group IV**	**Group V**
Breast Skin	Ceramic plate	Ceramic plate	Ceramic plate	Ceramic plate	Ceramic plate
Breast Fat	100% wax	100% wax	100% wax	100% wax	90% wax +10% water
Lesion	Grape	Grape	Grape	Grape, blueberry, cucumber	Grape, blueberry
Lesion Size (mm)	10, 15	10, 15	10	2.5 ~ 7	7 ~ 13
Dielectric Contract (of lesion and normal breast tissue)	9.79	9.79	9.79	7.53 ~ 9.79	7.53 ~ 9.79
Measurement Height (mm)	390~540	540~580	540~545	490	540
Antenna	Flanged Open-ended waveguide	Flanged Open-ended waveguide	Flanged Open-ended waveguide	Flanged Open-ended waveguide	Flanged Open-ended waveguide
Antenna Number	16	16	16	16	16
Array Configuration	Spiral, Random	Spiral,	Regularly spaced, Spiral, Random	Random	Random
Image Algorithm	2D HMIA	3D HMIA	2D HMIA	2D HMIA	2D HMIA
System set-up	Multiple breast phantoms in air	Multiple breast phantoms in air			
Image	2D	3D	2D	2D	2D
Detection	Multiple breast phantoms with small lesions (10 mm) can be detected, skin cannot be identified	Multiple breast phantoms with small lesions (10 mm) can be detected, skin can be identified	Lesions only can be identified using spiral and random array configurations	Multiple breast phantoms with small lesions (<3 mm) can be detected, skin cannot be identified	Multiple breast phantoms with small lesions (<7 mm) can be detected, even when two lesions are located very close (<10 mm)

6.5 Closure

In this chapter, five experimental groups were presented to validate the developed 2D and 3D HMIA image algorithms and the proposed random and spiral array configurations to validate whether they can produce better quality breast images compared to the widely used regularly spaced antenna array.

The obtained results in Figure 6.9 to Figure 6.14 indicated that the proposed 2D HMIA system has the ability to produce a 2D image and detect lesions with various sizes and locations. However, two lesions located at the same x, y coordinates but in different z-planes will not be imaged as separate lesions.

Experiment results of Group II (see Figure 6.16, Figure 6.18 and Figure 6.20) demonstrated the successful detection and localization of lesions in a 3D breast phantom, even when two lesions are located at the same x, y coordinates but in different z-planes. The results displayed in Figure 6.22 show that two lesions at different locations were successfully detected under random array and spiral array but not detected using the regular spaced array. It is can be seen that the reconstructed image of the breast phantom using random and spiral antenna array configurations offer better quality breast image compared to the obtained breast image using the regular spaced antenna array.

The achieved Group IV results showed that the designed system has the ability to detect lesions even smaller than 3 mm. The obtained Group V results demonstrated that the HMIA technique has the ability to detect small lesion within a more realistic breast phantom.

Chapter 7 Discussion

7.1 Introduction

The simulation and experimental solutions for the scattering problems of a 3D dielectric object was presented in the previous chapters. This chapter discusses the obtained simulation and experimental results, compares the experimental results with the published microwave imaging results and outlines an example of other applications using the developed HMIA image algorithms.

7.2 Discussion

New HMIA imaging algorithms to detect breast lesion were developed in this preliminary work. The computer simulation models were developed using MATLAB to demonstrate that the 2D and 3D HMIA techniques have the ability to detect small lesions within any location in the breast model. A suitable flanged open-end rectangular waveguide antenna was designed and a spiral and random antenna array configurations were proposed to significantly improve the breast image quality. Validation of the technique through both simulations and measurements on dielectric objects (breast phantoms) with inclusions (lesions) has been performed.

7.2.1 2D and 3D HMIA Imaging Algorithms

The 2D and 3D HMIA imaging algorithms were developed based on holographic and aperture synthesis imaging techniques, which are most important contributions of this work. The theory of 2D and 3D imaging algorithms were detailed in Chapter 3 and Chapter 4. The proposed 2D HMIA reconstruction algorithm calculates the complex

visibility data (measured from the phase and magnitude of each reflection signal from the breast) for each possible pair of antennas to form a 2D image by using an inversion Fourier transform, which is significantly different from the holographic method reported in [76], [77], [78], [79] (more typical at optical frequencies). The holographic method in [80], [81] is fixed along range and uses ultra-wideband information to attain depth resolution. In contrast, the proposed 3D HMIA image reconstruction uses physical displacement (scan of the distance) between the antenna array and the imaged breast along range in order to obtain breast depth information.

The main advantage of the 2D HMIA technique compared to the 3D HMIA technique is lower simulation cost of computing the scattering electromagnetic field and the imaging reconstruction processing. The most important limitation of the 2D HMIA technique is that only one lesion will be imaged if more than one lesion is located at the same x, y coordinates but in different z-planes.

7.2.2 Simulation Results

Figure 7.1, Figure 7.2 and Table 7-1 show sample simulation imaging results from the 2D and 3D HMIA systems. Both systems were designed to simulate in air with a 16-element antenna array.

The developed 3D HMIA image algorithm overcomes the limitations of the 2D HMIA system. Simulation results clearly demonstrate that detection and imaging of inclusions with dielectric contrast is possible using the HMIA techniques.

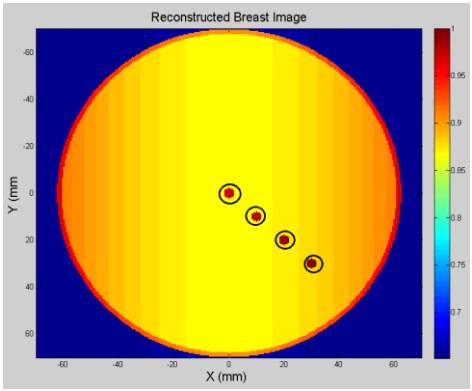

Figure 7.1 2D reconstructed breast image containing four lesions (circled in black, 2 mm in diameter) within 2D HMIA system, lesions were located at ($X_1 = 0$ mm, $Y_1 = 0$ mm, $Z_1 = 5$ mm), ($X_2 = 10$ mm, $Y_2 = 10$ mm, $Z_2 = 10$ mm), ($X_3 = 20$ mm, $Y_3 = 20$ mm, $Z_3 = 20$ mm), and ($X_4 = 30$ mm, $Y_4 = 30$ mm, $Z_4 = 20$ mm)

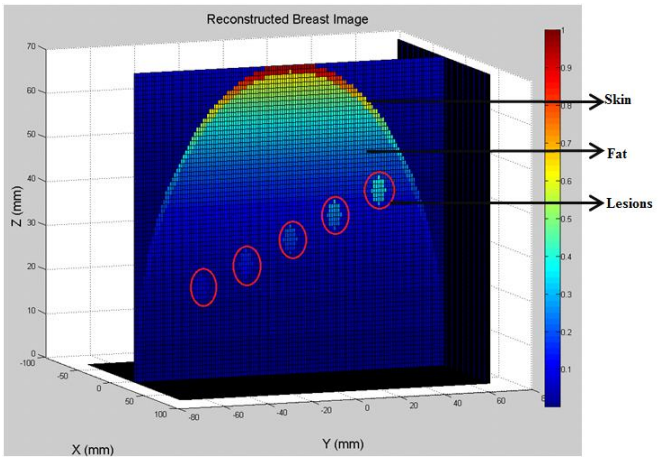

Figure 7.2 3D reconstructed image of skin, fat and five lesions (circled in red, 3 mm in diameter) with 3D HMIA system, lesions were located at ($X_1 = 0$ mm, $Y_1 = -40$ mm, $Z_1 = 20$ mm), ($X_2 = 0$ mm, $Y_2 = -20$ mm, $Z_2 = 25$ mm), ($X_3 = 0$ mm, $Y_3 = 0$ mm, $Z_3 = 30$ mm), ($X_4 = 0$ mm, $Y_4 = 20$ mm, $Z_4 = 35$ mm), and ($X_5 = 0$ mm, $Y_5 = 40$ mm, $Z_5 = 45$ mm)

Table 7-1 HMIA simulation results

Breast Model	3D hemispherical shaped breast model (radius :70 mm)	3D hemispherical shaped breast model (radius :70 mm)
Dielectric Contract (of lesion and normal breast tissue)	1.056	1.056
Measurement Height (the distance between breast and antenna array)	450 mm	450 mm ~ 460 mm
Antenna	Flanged Open-ended waveguide	Flanged Open-ended waveguide
Antenna Number	16	16
Array Configuration	Spiral	Random
Simulation Model	Born approximation	Born approximation
Imaging Algorithm	2D HMIA	3D HMIA
System set-up	Multiple breast models in air	Multiple breast models in air
Detection	small lesions (2 mm) can be detected	small lesions (3 mm) can be detected

7.2.3 Experimental Results

Multiple breast phantoms containing skin, fat tissue and malignant lesions were used in the experimental system to verify the HMIA approaches. The 2D and 3D experimental systems were designed based on the simulation systems. Both 2D and 3D HMIA systems contain 16 flanged ORWAs with an operation frequency of 12.6 GHz. No additional impedance matching medium was necessary between phantom and antenna array, only air, which greatly simplifies the practical implementation of such a system.

Figure 7.3 and Figure 7.4 illustrate a sample of the experimental imaging results from the 2D HMIA system, while Figure 7.5 displays the sample experimental imaging results from the 3D HMIA system. Table 7-2 summaries the quantitative analysis of the experimental results using 2D and 3D HMIA techniques.

The experimental results demonstrated that the developed 2D and 3D HMIA systems with 16 antennas arranged in the proposed 2D antenna array plane are capable of producing images of objects with various locations. The smallest object that can be detected is 2.5 mm (see Figure 7.3), Figure 7.4 showed that two lesions could be imaged as separate lesions even when they were located very close (less than 1 cm).

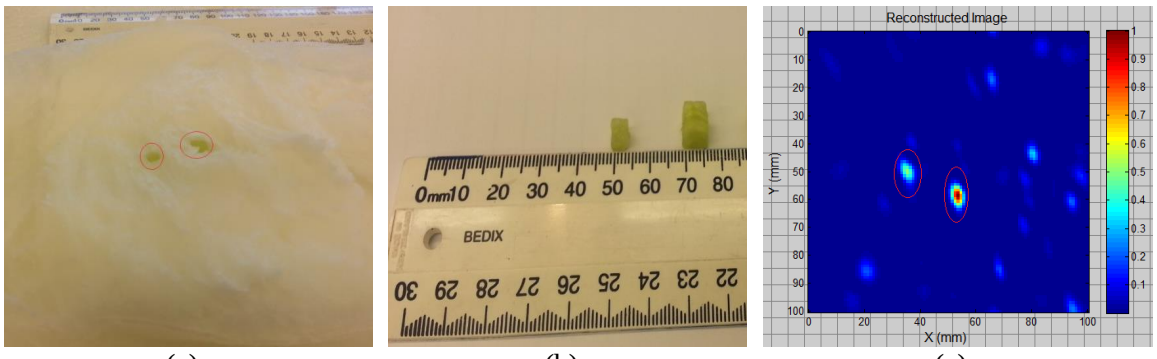

(a) (b) (c)

Figure 7.3 (a) Photograph of breast phantom (100 mm x 100 mm x 30 mm) containing skin, fat and two lesions (b) Size of lesions (2.5 mm, 5 mm) (c) 2D reconstructed image of 2 lesions (circled in red) with 2D HMIA system, lesions were located at($X = 35$ mm, $Y = 50$ mm, $Z = 25$ mm) and ($X = 55$ mm, $Y = 60$ mm, $Z = 25$ mm)

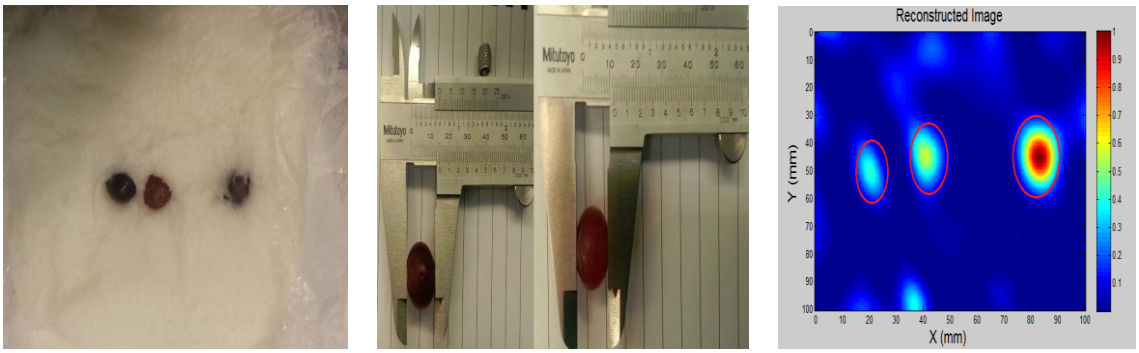

(a) (b) (c)

Figure 7.4 (a) Photograph of breast phantom (100 mm x 100 mm x 30 mm) containing skin, fat and three lesions (b) Size of lesions (13 mm, 10 mm, 10 mm in diameter) (c) 2D reconstructed image of three lesions (circled in red) with 2D HMIA system, lesions were located at at ($X = 40$ mm, $Y = 50$ mm, $Z = 25$ mm), ($X = 60$ mm, $Y = 50$ mm, $Z = 25$ mm) and ($X = 90$ mm, $Y = 55$ mm, $Z = 25$ mm)

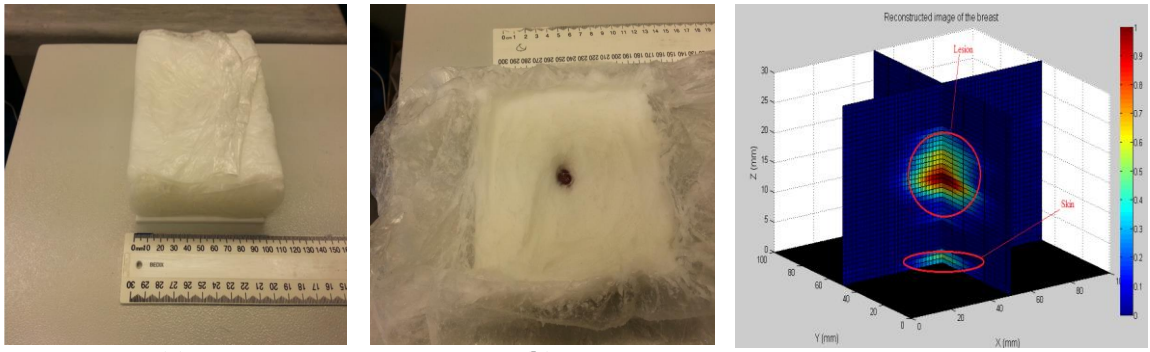

(a) (b) (c)

Figure 7.5 (a) Photograph of breast phantom (100 mm x 100 mm x 30 mm) containing skin, fat and one lesion (b) Size of lesions (10 mm in diameter) (c) 3D reconstructed image of one lesion (circled in red) with 3D HMIA system, lesion was located at at ($X = 50$ mm, $Y = 50$ mm, $Z = 15$ mm)

Table 7-2 HMIA experimental results

Dielectric Contract (of lesion and normal breast tissue)	7.53~9.79	9.79
Measurement Height (the distance between breast and antenna array)	390 mm~540 mm	540 mm~580 mm
Antenna	Flanged Open-ended waveguide	Flanged Open-ended waveguide
Antenna Number	16	16
Array Configuration	Spiral	Spiral
Image Algorithm	2D HMIA image reconstruction algorithm	3D HMIA image reconstruction algorithm
System set-up	Multiple breast phantoms in air	Multiple breast phantoms in air
Image	2D images	3D images
Detection	Multiple breast phantoms with small lesions (2.5 mm) can be detected, skin cannot be identified	Multiple breast phantoms with small lesions (10 mm) can be detected, skin can be identified

7.2.4 Comparison of Simulation and Experimental Results Using Various Antenna Array Configurations

Figure 7.6, Figure 7.7, Figure 7.8 and Table 7-3 display the simulated and experimental breast images of a 3D breast model including skin, fat and two lesions using regularly spaced, spiral and random antenna array configurations.

Results demonstrated that lesions cannot be identified using regularly spaced antenna array, but two lesions can be clearly identified using spiral and random array configurations. The proposed spiral and random antenna array configurations deliver clearer and more accurate images than the widely used regularly spaced configuration. This is because the proposed antenna array configurations provide dense sampling of the aperture plane over a wide range of projected baseline lengths and offer the best possibility of detecting lesions anywhere within the breast. These results further validate the possibility of microwave screening for breast lesion.

Table 7-3 Simulation and experimental results using various array configurations

	Simulation			**Experimental**		
Breast	breast model including skin, fat and two lesions			breast phantom including skin, fat and two lesions		
Dielectric Contract	1.056			9.79		
Measurement Height	450 mm			450 mm		
Antenna	Flanged Open-ended waveguide			Flanged Open-ended waveguide		
Antenna Number	16			16		
Array Configuration	Regularly spaced	Spiral	Random	Regularly spaced	Spiral	Random
Image Algorithm	2D HMIA			2D HMIA		
Image	2D image			2D image		
Detection (lesion number can be found)	0	2	2	0	2	2

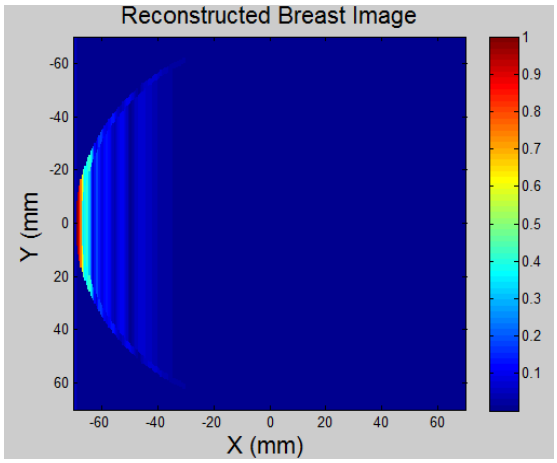

(a)

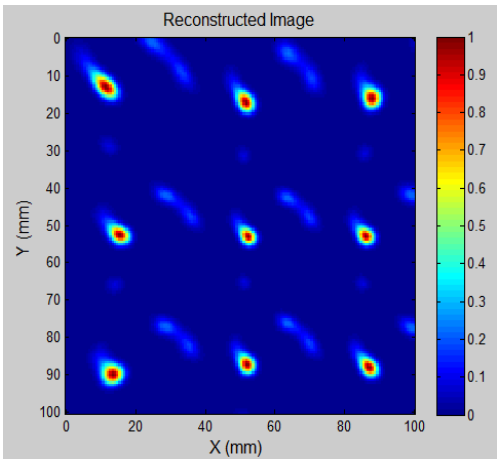

(b)

Figure 7.6 (a) Simultion breast image using a regularly spaced antenna array (b) Experimental breast phantom image using a regularly spaced array

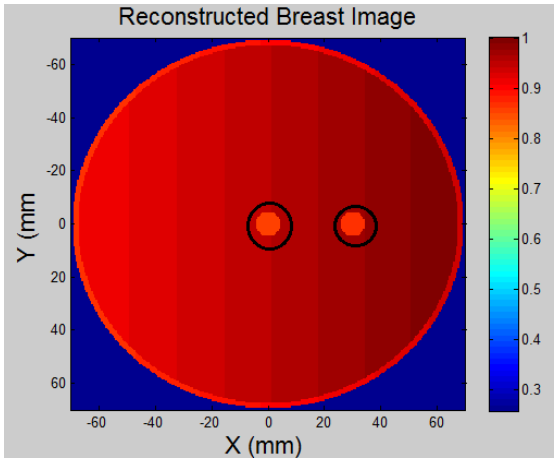

(a)

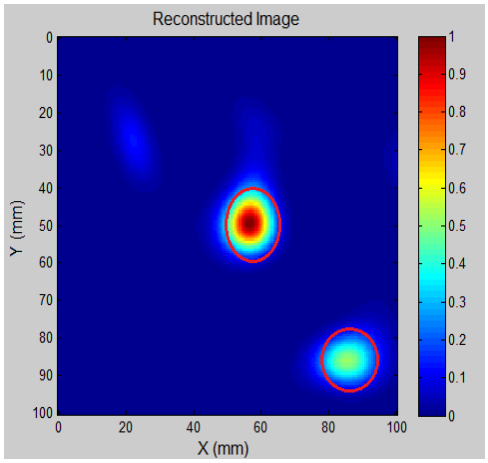

(b)

Figure 7.7 (a) Simultion breast image using a spiral antenna array (b) Experimental breast phantom image using a spiral antenna array

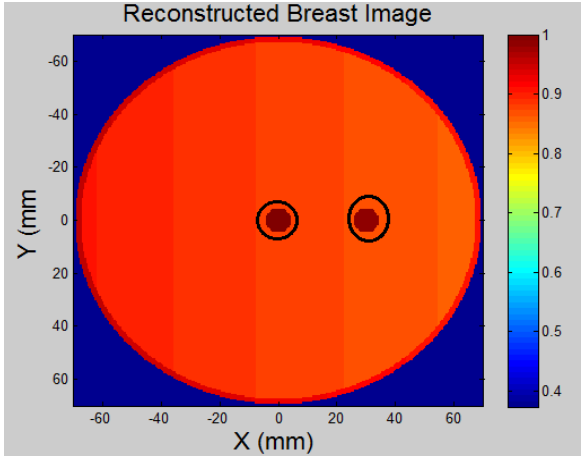

(a)

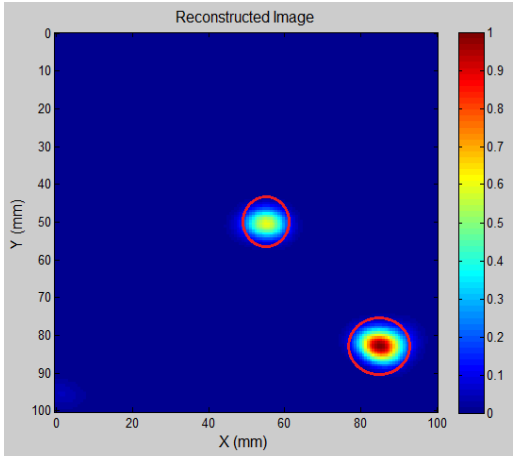

(b)

Figure 7.8 (a) Simultion breast image using a random antenna array (b) Experimental breast phantom image using a random antenna array

7.2.5 Comparison of Published Microwave Imaging Results with HMIA

Table 7-4 summarizes and compares the published results from the leading microwave imaging systems with the developed HMIA technique. These include the 2D slice tomographic system developed by Meaney *et al*., the MIST system developed by Hagness *et al*., the TSAR system developed by Fear *et al*, the 3D inverse scattering system developed at Duke by Liu *et al* and the UWB conform system developed at Bristol by Kemm *et al*. Finally, the experimental results from the proposed HMIA technique are compared.

Table 7-4 Comparison of published microwave imaging results [98] with HMIA results

PI	Location	Antenna	Elements	Imaging Method	Images	Detection
Meaney	Dartmouth	Monopole (Multi-frequency CW)	16 (15 min scan)	2D inversion methods	In vivo imaging 7 slices (2D) at 7 frequencies	130 subjects >1 cm detection
Hagness	Wisconsin	UWB Pyramidal Horn (Pulsed)	Single element scanned 49 positions	MIST combined with statistical methods	Multiple phantoms in layered media (skin, oil, lesion)	Multiple phantoms, 4 mm in diameter, 2 cm separation
Fear	Calgary	UWB Wu-King Monopole (Pulsed)	Single element scanned 49 positions	Quasi-3D TSAR and MIST	Phantoms embedded in layered media (skin, oil, lesion)	Single phantom, 1 cm in diameter (layered media) 4 mm in diameter (homogenous)
Liu	Duke	Patch (CW)	32-125 (<2 min scan)	3D inversion methods BIM-DTA*, DBIM-BCGS*	Multiple phantom in layered media (skin, fluid, lesion)	Multiple phantoms, <5 mm diameter (Homogenous) / <1 cm (layered), <2 cm separation
Kemm	Bristol	UWB Stacked Conformal patch (pulsed)	16 elements in 4 x 4 array	Delay and sum beam forming	Phantoms in homogenous liquid	Single phantom, <6 mm diameter
Pastorino	Genoa	No published results found	No published results found	Genetic Algorithm	Only simulated imaging results	Sub-wavelength detection (simulated)
Wang	AUT	Flanged Open-ended waveguide	16 elements	2D and 3D HMIA image algorithms	Multiple phantoms in air	Multiple phantoms (homogenous & inhomogeneous), 3 mm in diameter. 1 cm separation

*BIM-DTA: the Born iterative method with the diagonal tensor approximation; *DBIM-BCGS: the distorted Born iterative method with the stabilized biconjugate gradient fast Fourier transform

All measurements on breast phantoms have been completed in far-field range, where all breast phantoms were placed at least 390 mm away from the antenna array plane and small power (10 milliwatts) was selected. No heat affection to phantoms was caused and no any ablation was observed in all experiments. Experimental results show that the proposed techniques have the ability to detect lesions less than 3 mm that is more sensitive to other microwave approaches (see Table 7-4). Matching solution medium is not required in experiments, only air, which greatly simplifies the practical implementation of such a system and reduces the cost.

7.2.6 Limitations of HMIA

The major drawback of this initial work is that the breast phantoms are far from the reality. Although lesions were detected in simulation and experiments in this preliminary study of HMIA techniques, there is no evidence that a real breast lesion can be detected at this stage. The current experimental system is a very simplified system and the data collection time highly depends on the operator (manually adjust the measurement height), which requires long time for data collection. The data collection time for 15 receivers at one selected height to create a quality 2D image is approximately 10 min. To generate a 3D image, approximately 100 minutes is required to measure all 15 receivers at 10 measurement heights. Approximately 12 hours is required to measure all 15 receivers at 49 measurement heights to generate a high quality 3D image.

7.2.7 Other Applications of HMIA

Furthermore, the 2D HMIA technique has been applied for brain stroke detection (see conference paper 6 [CP6] and journal papers 3 and 4 [JP1]-[JP2]). Simulation results in

Figure 7.9 and Figure 7.10 observe that both ischemic stroke and hemorrhagic stroke could be successfully detected, which confirmed the proposed HMIA approach is highly sensitive as most microwave imaging approaches failed to detect a brain stroke.

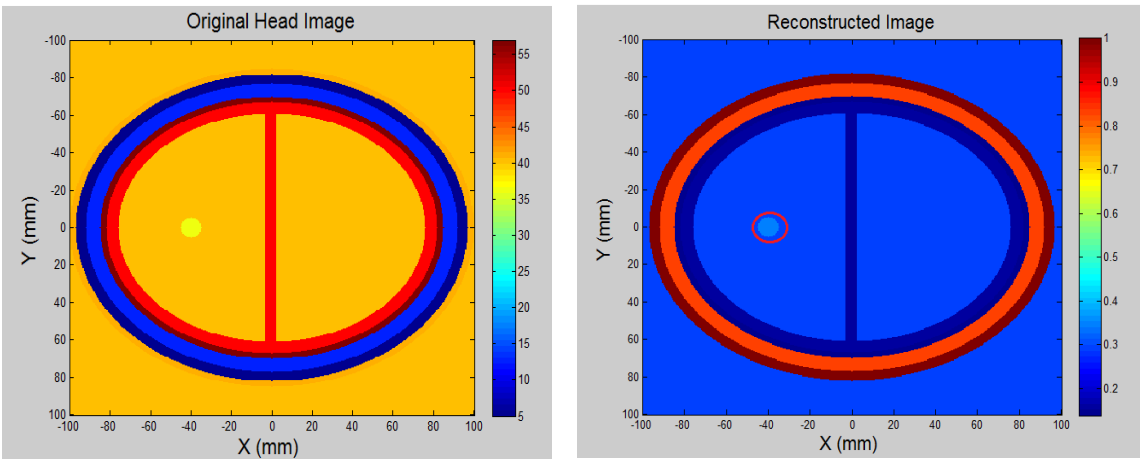

(a) (b)

Figure 7.9 (a) Original head model containing one ischemic stroke (5 mm in diameter) (b) Reconstructed image of simulated head model

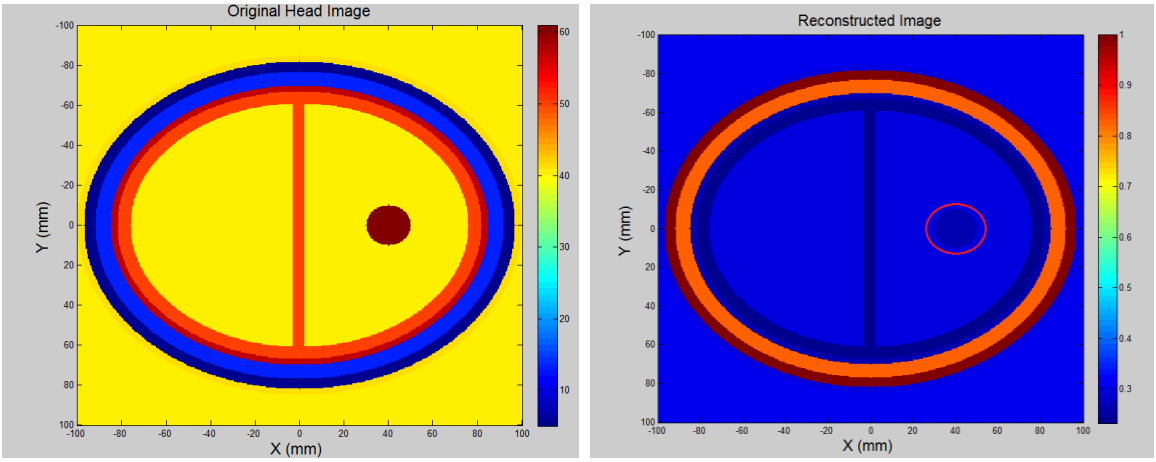

(a) (b)

Figure 7.10 (a) Original head model containging one hemorrhagic stroke (10 mm in diameter) (b) Reconstructed image of simulated head model

In summary, the developed HMIA techniques have the potential to become a screening and diagnostic tool for breast lesion detection that could largely supplant clinical breast examination through its high sensitivity, quantitative record storage, ease-of-use.

Chapter 8 Conclusions and Future Work

8.1 Introduction

The main aim of this study was to investigate a new microwave imaging approach for detecting lesion in dielectric object, which may has a potential for breast lesion detection in the future. At the end of this research, the proposed technique was expected to have the capability to detect and localize small inclusions within a dielectric object. This method was not expected to be fully sufficient on its own, but rather complimentary to other screening techniques such as X-rays, computed tomography and ultrasound.

Five objectives were identified to address this aim. This thesis describes the results of the investigation for these objectives. In Chapter 1 the background and objectives of this study was described. In Chapter 2 the literature review of the existing clinical methods and microwave imaging approaches for breast lesion detection were presented. A new 2D HMIA image reconstruction algorithm and simulation results were presented in Chapter 3. Chapter 4 described a novel 3D HMIA image reconstruction algorithm for breast lesion detection based on the 2D HMIA technique and simulation set-up and results were presented. Chapter 5 illustrated a new ORWA suitable for HMIA techniques and a spiral and random antenna array configurations which offered better quality breast images compared to regularly spaced antenna array were detailed. Chapter 6 demonstrated the experimental validation of the HMIA simulation models using various breast phantoms. Chapter 7 discussed the simulation and experimental results and other applications of the HMIA techniques.

8.2 Conclusions

In this section the conclusion of the investigation into each of the five objectives detailed in Chapter 1 are presented. The 2D and 3D HMIA techniques investigated in this thesis meet all of the design goals. Six conference papers [CP1]-[CP6] and two journal papers [JP1]-[JP2] are published, conference papers are attached at the end of the thesis. Six main contributions of this thesis are:

- 2D HMIA technique

A new 2D HMIA image reconstruction algorithm that allows for the detection and 2D localization of lesion responses has been developed and demonstrated on a simplified breast model using MATLAB simulation environment. Simulation results demonstrated that lesions as small as 2 mm in diameter anywhere within the breast model could be successfully detected. Details of the development of 2D HMIA system and simulations were presented in Chapter 3.

- 3D HMIA technique

A novel 3D HMIA image reconstruction algorithm that allows for the detection and 3D localization of lesion responses has been developed and demonstrated on a simplified breast model by applying the Born Approximation. The development of 3D HMIA system and simulations were presented in Chapter 4.

- Improvement of the image

The development of spiral and random antenna array configurations to create a high-resolution breast image using the minimum number of antennas were presented in Chapter 5. The obtained simulation breast images using different array configurations were compared and the performance of each imaging approach was evaluated by visual

inspection. The results showed that the proposed antenna array configurations have the ability to produce high-resolution breast images compared to the currently widely used regularly spaced array in microwave imaging for breast lesion detection.

- Small flanged open-ended rectangular waveguide antenna (ORWA)

A flanged ORWA was designed for breast lesion detection that operated at 12.12 GHz for a return loss below -60 dB. The best performance of an array of 16 antennas was achieved at 12.7 GHz. The antenna was designed to radiate directly into air without a matching solution medium that has similar dielectric properties to breast tissue. The development of flanged ORWA, simulation and experimental results were conducted in Chapter 5 and Chapter 6.

- Experimental systems development

A 2D and 3D simplified experimental systems were completed to demonstrate the 2D and 3D HMIA techniques have lesion detection capabilities even for small objects (2.5 mm in diameter). Additionally, the proposed spiral and random antenna array configurations have demonstrated the ability to produce better quality breast images compared to the widely used regularly spaced antenna array, which can significantly reduce the implementation costs.

- Additional HMIA applications

Furthermore, computer simulation models of 2D and 3D head models were developed to demonstrate the 2D HMIA technique has the potential to detect brain strokes. These works are detailed in conference paper 6 [CP6] and journal paper 3 [JP1]. Unlike the breast simulation model, the Method of Moments approach was applied to solve the total electric field for the head model. Simulation result showed that a small ischemic

stroke area (5 mm in diameter) inside of a high dielectric contrast shield, comprising the skull and cerebral spinal fluid could be detected using the 2D HMIA approach.

Although a simplified phantom and a simple waveguide antenna were considered in this first generation experimental system, the experimental results proved that the developed 2D and 3D HMIA techniques have the potential to become a screening and diagnostic tool for breast lesion detection. The benefits of HMIA techniques including significant improvement of imaging results, simplicity, safety and comfort compared to other screening modalities, such as X-ray mammography.

8.3 Future Work

Research of the HMIA techniques for breast lesion detection has progressed significantly since the commencement of the research described in this thesis. Experimental validation of the HMIA simulations using various breast phantoms have been undertaken and demonstrated a good agreement between experimental and simulated images. With the currently achieved results, the future studies could include:

- Developing a smart sensor that is more sensitive to lesions and specific to malignancies, and find a way that can perfectly reduce or remove the skin reflection
- Find a unique solution to optimize the spatial resolution of the image by selecting the optimum antenna array configurations
- Construct a more realistic and complex breast phantom that is more realistic to a human breast
- Further experiments on the use of the breast phantoms to investigate the performance of breast lesion detection algorithms

With further development, clinical trials of HMIA techniques for real breast lesion detection could be possible within 5 years. Ultimately, it is hoped that the research presented here will contribute to providing women with a safe, comfortable and low cost imaging technology for breast lesion detection.

Bibliography

[1] American Cancer Society (2012). Cancer facts & figures 2012. *American Cancer Society,* 2012.

[2] World Health Organization. Cancer mortality and morbidity. *Available:* http://www.who.int/gho/ncd/mortality_morbidity/cancer_text/en/index.html.

[3] Breastcancer.org, U.S. breast cancer statistics. *Available:* http://www.breastcancer.org/symptoms/understand_bc/statistics.

[4] Khatib, O. M. Guidelines for the early detection and screening of breast cancer. Available: *http://applications.emro.who.int/dsaf/dsa696.pdf.*

[5] Cancer. Available: *http://www.ncbi.nlm.nih.gov/pubmedhealth/PMH0002267/*, last visited on 12th January 2012.

[6] The New Zealand Breast Cancer Foundation. About breast vancer. *Available: http://www.nzbcf.org.nz/index.php/about-breast-cancer.*

[7] Cancer Society of New Zealand. Breast cancer. *Available:* http://www.cancernz.org.nz/assets/files/info/Breast_Cancer.pdf.

[8] Breastcancer.org. Breast cancer risk and risk factors. *Available: http://www.breastcancer.org/symptoms/understand_bc/risk*

[9] Cheng, Z., Xiuzhen, D., Feng, F., Zhenyu, J., & Canhua, X. (2007, August). Breast cancer detection based on multi-frequency EIS measurement. *29th Annual International Conference of the IEEE Engineering in Medicine and Biology Society*, pp.4158-4160.

[10] Liu, G. D., & Zhang, Y. R. (2010). An overview of active microwave imaging for early breast cancer detection. *Journal of Nanjing University of Posts and Telecommunications (Natural Science)*, 30 (1).

[11] Brown, M. L., Houn, F., Sickles, E. A., & Kessler, L. G. (1995). Screening mammography in community practice: positive predictive value of abnormal findings and yield of follow-up diagnostic procedures. *American journal of roentgenology*, 165 (6), pp.1373-1377.

[12] Nass, S. J., Henderson, I. C and Lashof, J. C. (2001). Mammography and beyond: developing technologies for the early detection of breast cancer. *National Academies Press.*

[13] American Recovery Reinvestment Act at NCI. Breast cancer: recovery act investment report. *Available:* http://www.cancer.gov/aboutnci/recovery/recoveryfunding/investmentreports/breast

[14] Guide D., Breast Cancer. *Available:* http://www.cancer.org/Cancer/BreastCancer/DetailedGuide/breast-cancer-detection

[15] Jackson, V. P., Hendrick, R. E., Feig, S. A., & Kopans, D. B. (1993). Imaging of the radiographically dense breast. *Radiology*, 188 (2), pp.297-301.

[16] Smith, R. A., Saslow, D., Sawyer, K. A., Burke, W., Costanza, M. E., Evans, W. P. I. I. I. & Sener, S. (2003). American Cancer Society guidelines for breast cancer screening: update 2003. *CA: a cancer journal for clinicians*, 53 (3), pp.141-169.

[17] Chaudhary, S. S., Mishra, R. K., Swarup, A. & Thomas, J. M. (1984). Dielectric properties of normal and malignant human breast tissues at radiowave and microwave frequencies. *Indian J. Biochem., Biophys.*, 21, pp. 76–79.

[18] Surowiec, A. J., Stuchly, S. S., Barr, J. R., & Swarup, A. (1988). Dielectric properties of breast carcinoma and the surrounding tissues. *IEEE Transactions on Biomedical Engineering*, 35 (4), pp.257-263.

[19] Joines, W. T., Zhang, Y., Li, C., & Jirtle, R. L. (1994). The measured electrical properties of normal and malignant human tissues from 50 to 900 MHz. *Medical physics*, 21 (4), pp.547.

[20] Gabriel, C. (1996). Compilation of the dielectric properties of body tissues at RF and microwave frequencies. King's Coll London (UK) dept of physics.

[21] Gabriel, C., Gabriel, S., & Corthout, E. (1999). The dielectric properties of biological tissues: I. literature survey. *Physics in medicine and biology*, 41 (11), pp.2231.

[22] Gabriel, S., Lau, R. W., & Gabriel, C. (1999). The dielectric properties of biological tissues: II. measurements in the frequency range 10 Hz to 20 GHz. *Physics in medicine and biology*, 41 (11), pp.2251.

[23] Gabriel, S., Lau, R. W., & Gabriel, C. (1999). The dielectric properties of biological tissues: III. Parametric models for the dielectric spectrum of tissues. *Physics in medicine and biology*, 41 (11), pp.2271.

[24] Lazebnik, M., Popovic, D., McCartney, L., Watkins, C. B., Lindstrom, M. J., Harter, J., & Hagness, S. C. (2007). A large-scale study of the ultrawideband microwave dielectric properties of normal, benign and malignant breast tissues obtained from cancer surgeries. *Physics in Medicine and Biology*, 52 (20), pp.2637.

[25] Lazebnik, M., Popovic, D., McCartney, L., Watkins, C. B., Lindstrom, M. J., Harter, J., & Hagness, S. C. (2007). A large-scale study of the ultrawideband microwave dielectric properties of normal, benign and malignant breast tissues obtained from cancer surgeries. *Physics in Medicine and Biology*, 52 (20), pp.6093.

[26] Meaney, P. M., Paulsen, K. D., Hartov, A., & Crane, R. K. (1995). An active microwave imaging system for reconstruction of 2-D electrical property distributions. *IEEE Transactions on Biomedical Engineering*, 42 (10), pp.1017-1026.

[27] Paulsen, K. D., & Meaney, P. M. (1999). Nonactive antenna compensation for fixed-array microwave imaging. I. model development. *IEEE Transactions on Medical Imaging*, 18 (6), pp.496-507.

[28] Meaney, P. M., Paulsen, K. D., Chang, J. T., Fanning, M. W., & Hartov, A. (1999). Nonactive antenna compensation for fixed-array microwave imaging. II. Imaging results. *IEEE Transactions on Medical Imaging*, 18 (6), pp.508-518.

[29] Meaney, P. M., Fanning, M. W., Li, D., Poplack, S. P., & Paulsen, K. D. (2000). A clinical prototype for active microwave imaging of the breast. *IEEE Transactions on Microwave Theory and Techniques*, 48 (11), pp.1841-1853

[30] Meaney, P. M., Paulsen, K. D., Pogue, B. W., & Miga, M. I. (2001). Microwave image reconstruction utilizing log-magnitude and unwrapped phase to improve high-contrast object recovery. *IEEE Transactions on Medical Imaging*, 20 (2), pp.104-116.

[31] Fang, Q., Meaney, P. M., & Paulsen, K. D. (2004). Microwave image reconstruction of tissue property dispersion characteristics utilizing multiple-frequency information. *IEEE Transactions on Microwave Theory and Techniques*, 52 (8), pp.1866-1875.

[32] Rubæk, T., Meaney, P. M., Meincke, P., & Paulsen, K. D. (2007). Nonlinear microwave imaging for breast-cancer screening using Gauss–Newton's method and the CGLS inversion algorithm. *IEEE Transactions on Antennas and Propagation, 55* (8), pp.2320-2331.

[33] Meaney, P. M., Fanning, M. W., Raynolds, T., Fox, C. J., Fang, Q., Kogel, C. A., & Paulsen, K. D. (2007). Initial clinical experience with microwave breast imaging in women with normal mammography. *Academic radiology*, 14 (2), pp.207-218.

[34] Fang, Q., Meaney, P. M., & Paulsen, K. D. (2010). Viable three-dimensional medical microwave tomography: Theory and numerical experiments. *IEEE Transactions on Antennas and Propagation*, 58 (2), pp.449-458.

[35] Hagness, S. C., Taflove, A., & Bridges, J. E. (1999). Three-dimensional FDTD analysis of a pulsed microwave confocal system for breast cancer detection: Design of an antenna-array element. *IEEE Transactions on Antennas and Propagation*, 47 (5), pp.783-791.

[36] Hagness, S. C., Taflove, A., & Bridges, J. E. (1998). Two-dimensional FDTD analysis of a pulsed microwave confocal system for breast cancer detection: Fixed-focus and antenna-array sensors. *IEEE Transactions on Biomedical Engineering*, 45 (12), pp.1470-1479.

[37] Li, X., & Hagness, S. C. (2001). A confocal microwave imaging algorithm for breast cancer detection. *IEEE Transactions on Microwave and Wireless Components Letters*, 11 (3), pp.130-132.

[38] Bond, E. J., Li, X., Hagness, S. C., & Van Veen, B. D. (2003). Microwave imaging via space-time beamforming for early detection of breast cancer. *IEEE Transactions on Antennas and Propagation*, 51 (8), pp.1690-1705.

[39] Li, X., Hagness, S. C., Van Veen, B. D., & van der Weide, D. (2003, June). Experimental investigation of microwave imaging via space-time beamforming for breast cancer detection. *IEEE MTT-S International Microwave Symposium Digest, 2003*, 1, pp.379-382.

[40] Davis, S. K., Bond, E. J., Hagness, S. C., & Van Veen, B. D. (2003). Microwave imaging via space-time beamforming for early detection of breast cancer: beamformer design in the frequency domain. *Journal of Electromagnetic Waves and Applications*, 17 (2), pp.357-381.

[41] Li, X., Davis, S. K., Hagness, S. C., Van Der Weide, D. W., & Van Veen, B. D. (2004). Microwave imaging via space-time beamforming: experimental investigation of tumor detection in multilayer breast phantoms. *IEEE Transactions on Microwave Theory and Techniques*, 52 (8), pp.1856-1865.

[42] Semenov, S. Y., Bulyshev, A. E., Abubakar, A., Posukh, V. G., Sizov, Y. E., Souvorov, A. E., & Williams, T. C. (2005). Microwave-tomographic imaging of the high dielectric-contrast objects using different image-reconstruction approaches. *IEEE Transactions on Microwave Theory and Techniques,*53 (7), pp.2284-2294.

[43] Semenov, S., Kellam, J., Sizov, Y., Nazarov, A., Williams, T., Nair, B., & Quinn, M. (2011). Microwave tomography of extremities: 1. Dedicated 2D

system and physiological signatures. *Physics in medicine and biology*, 56 (7), pp.2005.

[44] Semenov, S., Kellam, J., Nair, B., Williams, T., Quinn, M., Sizov, Y., & Pavlovsky, A. (2011). Microwave tomography of extremities: 2. functional fused imaging of flow reduction and simulated compartment syndrome. *Physics in medicine and biology*, 56 (7), pp.2019.

[45] Klemm, M., Leendertz, J., Gibbins, D., Craddock, I. J., Preece, A., & Benjamin, R. (2010). Microwave radar-based differential breast cancer imaging: imaging in homogeneous breast phantoms and low contrast scenarios. *IEEE Transactions on Antennas and Propagation*, 58 (7), pp.2337-2344.

[46] Chen, Y., Craddock, I. J., Kosmas, P., Ghavami, M., & Rapajic, P. (2010). Multiple-input multiple-output radar for lesion classification in ultrawideband breast imaging. *IEEE Journal of Selected Topics in Signal Processing*, 4 (1), pp.187-201.

[47] Henriksson, T., Klemm, M., Gibbins, D., Leendertz, J., Horseman, T., Preece, A. W., & Craddock, I. J. (2011, November). Clinical trials of a multistatic UWB radar for breast imaging. *IEEE Antennas and Propagation Conference (LAPC), 2011 Loughborough*, pp.1-4.

[48] Gilmore, C., Mojabi, P., Zakaria, A., Ostadrahimi, M., Kaye, C., Noghanian, S., & LoVetri, J. (2010). A wideband microwave tomography system with a novel frequency selection procedure. *IEEE Transactions on Biomedical Engineering*, 57 (4), pp.894-904.

[49] Gilmore, C., Mojabi, P., Zakaria, A., Pistorius, S., & LoVetri, J. (2010). On super-resolution with an experimental microwave tomography system. *IEEE Antennas and Wireless Propagation Letters*, 9, pp.393-396.

[50] Ostadrahimi, M., Mojabi, P., Noghanian, S., Shafai, L., Pistorius, S., & LoVetri, J. (2012). A novel microwave tomography system based on the scattering probe technique. *IEEE Transactions on Instrumentation and Measurement*, 61 (2), pp.379-390.

[51] Fhager, A., Gustafsson, M., & Nordebo, S. (2012). Image reconstruction in microwave tomography using a dielectric Debye model. *IEEE Transactions on Biomedical Engineering*, 59 (1), pp.156-166.

[52] Simonov, N. A., Jeon, S. I., Son, S. H., Lee, J. M., & Kim, H. J. (2012). 3D microwave breast imaging based on multistatic radar concept system. *Journal of the Korean Institute of Electromagnetic Engineering and Science*, 12 (1), pp.107-114.

[53] Jin, Y., Jiang, Y., & Moura, J. M. (2007, September). Time reversal beamforming for microwave breast cancer detection. *2007 IEEE International Conference on Image Processing, ICIP 2007*, 5, pp.V-13.

[54] Li, X., Bond, E. J., Van Veen, B. D., & Hagness, S. C. (2005). An overview of ultra-wideband microwave imaging via space-time beamforming for early-stage breast-cancer detection. *IEEE Antennas and Propagation Magazine*, 47 (1), pp.19-34.

[55] Fang, Q., Meaney, P. M., Geimer, S. D., Streltsov, A. V., & Paulsen, K. D. (2004). Microwave image reconstruction from 3-D fields coupled to 2-D parameter estimation. *IEEE Transactions on Medical Imaging*, 23 (4), pp.475-484.

[56] Fear, E. C., & Stuchly, M. A. (1999). Microwave system for breast tumor detection. *IEEE Microwave and Guided Wave Letters,* 9 (11), pp.470-472.

[57] Fear, E. C., & Stuchly, M. A. (2000). Microwave detection of breast cancer: a study of tumor response variations. *Proceedings of the 22nd Annual International Conference of the IEEE Engineering in Medicine and Biology Society, 2000,* 1, pp.74-77.

[58] Fear, E. C., Hagness, S. C., Meaney, P. M., Okoniewski, M., & Stuchly, M. A. (2002). Enhancing breast tumor detection with near-field imaging. *IEEE Microwave Magazine,* 3 (1), pp.48-56.

[59] Fear, E. C., Li, X., Hagness, S. C., & Stuchly, M. A. (2002). Confocal microwave imaging for breast cancer detection: Localization of tumors in three dimensions. *IEEE Transactions on Biomedical Engineering,* 49 (8), pp.812-822.

[60] Fear, E. C., Meaney, P. M., & Stuchly, M. A. (2003). Microwaves for breast cancer detection?. *IEEE Potentials,* 22 (1), pp.12-18.

[61] Fear, E. C. (2001). Microwave detection of breast cancer: a cylindrical configuration for confocal microwave imaging. *PhD thesis.*

[62] Fear, E., Low, A., Sill, J., & Stuchly, M. A. (2002). Microwave system for breast tumor detection: Experimental concept evaluation. *IEEE Antennas and Propagation Society International Symposium, 2002,* 1, pp. 819-822.

[63] Fear, E. C., Sill, J., & Stuchly, M. A. (2003). Experimental feasibility study of confocal microwave imaging for breast tumor detection. *IEEE Transactions on Microwave Theory and Techniques,* 51 (3), pp.887-892.

[64] Fear, E. G., & Sill, J. M. (2003, September). Preliminary investigations of tissue sensing adaptive radar for breast tumor detection. *Engineering in Medicine and Biology Society, 2003. Proceedings of the 25th Annual International Conference of the IEEE,* 4, pp.3787-3790.

[65] Sill, J. M., & Fear, E. C. (2005). Tissue sensing adaptive radar for breast cancer detection-experimental investigation of simple tumor models. *IEEE Transactions on Microwave Theory and Techniques,* 53 (11), pp.3312-3319.

[66] Fear, E. C. (2005). Microwave imaging of the breast. *Technology in cancer research & treatment,* 4 (1), pp.69.

[67] Kurrant, D. J., Fear, E. C., & Westwick, D. T. (2007, April). Tumor estimation in tissue sensing adaptive radar (TSAR) signals. *Canadian Conference on Electrical and Computer Engineering, 2007. CCECE 2007,* pp.860-863.

[68] Bourqui, J., Campbell, M. A., Sill, J., Shenouda, M., & Fear, E. C. (2009, January). Antenna performance for ultra-wideband microwave imaging. *IEEE Radio and Wireless Symposium, 2009. RWS'09,* pp.522-525.

[69] Rubæk, T., Kim, O. S., & Meincke, P. (2009). Computational validation of a 3-D microwave imaging system for breast-cancer screening. *IEEE Transactions on Antennas and Propagation,* 57 (7), pp.2105-2115.

[70] Craddock, I. J., Nilavalan, R., Leendertz, J., Preece, A., & Benjamin, R. (2005, July). Experimental investigation of real aperture synthetically organised radar for breast cancer detection. *2005 IEEE Antennas and Propagation Society International Symposium,* 1, pp.179-182.

[71] Hernández-López, M. A., Quintillán-González, M., González García, S., Rubio Bretones, A., & Gómez Martín, R. (2003). A rotating array of antennas for

confocal microwave breast imaging. *Microwave and optical technology letters*, 39 (4), pp.307-311.

[72] De Rodriguez, M. E., Vera-Isasa, M., & Del Río, V. S. (2008). 3-D microwave breast tumor detection: Study of system performance. *IEEE Transactions on Biomedical Engineering*, 55 (12), pp.2772-2777.

[73] Xie, Y., Guo, B., Xu, L., Li, J., & Stoica, P. (2006). Multistatic adaptive microwave imaging for early breast cancer detection. *IEEE Transactions on Biomedical Engineering*, 53 (8), pp.1647-1657.

[74] Carr, K. L., Cevasco, P., Dunlea, P., & Shaeffer, J. (2000). Radiometric sensing: An adjuvant to mammography to determine breast biopsy. *2000 IEEE MTT-S International Microwave Symposium Digest*, 2, pp. 929-932.

[75] Davis, S. K., Tandradinata, H., Hagness, S. C., & Van Veen, B. D. (2005). Ultrawideband microwave breast cancer detection: a detection-theoretic approach using the generalized likelihood ratio test. *IEEE Transactions on Biomedical Engineering*, 52 (7), pp.1237-1250.

[76] Smith, D., Leach, M., & Sambell, A. (2002). An indirect holographic method for determining antenna radiation patterns and imaging antenna fields. *2002 IEEE Antennas and Propagation Society International Symposium*, 3, pp.706-709.

[77] Smith, D., Leach, M., & Sambell, A. J. (2003). Microwave indirect holographic imaging using an adaptation of optical techniques. *IEEE Microwave and Wireless Components Letters*, 13 (9), pp.379-381.

[78] Elsdon, M., Smith, D., Leach, M., & Foti, S. J. (2006). Experimental investigation of breast tumor imaging using indirect microwave holography. *Microwave and optical technology letters*, 48 (3), pp.480-482.

[79] Elsdon, M., Leach, M., Fdo, M. J., Foti, S. J., & Smith, D. (2006, September). Early stage breast cancer detection using indirect microwave holography. *36th European Microwave Conference*, pp.1256-1259.

[80] Smith, D., Elsdon, M., Leach, M., FDO, M., & Foti, S. J. (2006). A Method for 3D Breast Cancer Imaging using Microwave Holography. *International Symposium on Antennas and Propagation*.

[81] Elsdon, M., Leach, M., Skobelev, S., & Smith, D. (2007, August). Microwave holographic imaging of breast cancer. *2007 IEEE International Symposium on Microwave, Antenna, Propagation and EMC Technologies for Wireless Communications*, pp.966-969.

[82] Smith, D., Leach, M., Elsdon, M., & Foti, S. J. (2007). Indirect holographic techniques for determining antenna radiation characteristics and imaging aperture fields. *IEEE Antennas and Propagation Magazine*, 49 (1), pp.54-67.

[83] Jayanthy, M., Selvanathan, N., Abu-Bakar, M., Smith, D., Elgabroun, H. M., Yeong, P. M., & Kumar, S. S. (2007). Microwave Holographic Imaging Technique for Tumour Detection. *3rd Kuala Lumpur International Conference on Biomedical Engineering*, pp.275-277.

[84] Ravan, M., Amineh, R. K., & Nikolova, N. K. (2010). Two-dimensional near-field microwave holography. *Inverse Problems*, 26 (5), pp.055011.

[85] Amineh, R. K., Ravan, M., Khalatpour, A., & Nikolova, N. K. (2011). Three-dimensional near-field microwave holography using reflected and transmitted signals. *IEEE Transactions on Antennas and Propagation*, 59 (12), pp.4777-4789.Hong, H. D., Sheffer, D. B., & Loughry, C. W. (1996). Holographic interferometry for early detection of breast cancer. Engineering in Medicine and

Biology Society, 1996. Bridging Disciplines for Biomedicine. *Proceedings of the 18th Annual International Conference of the IEEE*, 1, pp.189-190.

[87] Abbosh, A. (2009, June). Early breast cancer detection using hybrid imaging modality. *Antennas and Propagation Society International Symposium, 2009. APSURSI'09*, pp. 1-4.

[88] Lee, A., Types of medical imaging: X-ray, ultrasound, magnetic, and nuclear modalities, *Available: http://suite101.com/article/types-of-medical-imaging-a85622, last visited on 20th Dec, 2008.*

[89] Medical imaging. *Available:* http://www.fda.gov/Radiation-EmittingProducts/RadiationEmittingProductsandProcedures/MedicalImaging/default.htm, last visited on 12th January 2013.

[90] Sabiston Textbook of Surgery, 19th ed, 2012, Chapter 36 ISBN 9781437715606

[91] Understanding breast changes, NIH Publication: No. 02-3536, August 2004.

[92] Huynh, P. T., Jarolimek, A. M., & Daye, S. (1998). The false-negative mammogram. *Radiographics*, 18 (5), pp.1137-1154.

[93] Elmore, J. G., Barton, M. B., Moceri, V. M., Polk, S., Arena, P. J., & Fletcher, S. W. (1998). Ten-year risk of false positive screening mammograms and clinical breast examinations. *New England Journal of Medicine*, 338 (16), pp.1089-1096.

[94] Jackson, V. P., Hendrick, R. E., Feig, S. A., & Kopans, D. B. (1993). Imaging of the radiographically dense breast. *Radiology*, 188 (2), pp.297-301.

[95] Bird, R. E., Wallace, T. W., & Yankaskas, B. C. (1992). Analysis of cancers missed at screening mammography. *Radiology*, 184 (3), pp.613-617.

[96] Kalager, M., Zelen, M., Langmark, F., & Adami, H. O. (2010). Effect of screening mammography on breast-cancer mortality in Norway. *New England Journal of Medicine*, 363 (13), pp.1203-1210.

[97] Understanding breast changes, NIH Publication: No. 12-3536, August 2012.

[98] Stang, J. (2008). A 3D active microwave imaging system for breast cancer screening. *PhD thesis*.

[99] Karellas, A., & Vedantham, S. (2008). Breast cancer imaging: a perspective for the next decade. *Medical physics*, 35 (11), pp.4878.

[100] General Ultrasound Imaging,. Available: http://www.radiologyinfo.org/en/info.cfm?pg=genus, last visited on 12th January, 2013.

[101] Fatemi, M., & Greenleaf, J. F. (1998). Ultrasound-stimulated vibro-acoustic spectrography. *Science*, 280 (5360), pp.82-85.

[102] Fatemi, M., & Greenleaf, J. F. (1999). Vibro-acoustography: an imaging modality based on ultrasound-stimulated acoustic emission. *Proceedings of the National Academy of Sciences*, 96 (12), pp.6603-6608.

[103] Alizad, A., Fatemi, M., Whaley, D. H., & Greenleaf, J. F. (2004). Application of vibro-acoustography for detection of calcified arteries in breast tissue. *Journal of ultrasound in medicine*, 23 (2), pp.267-273.

[104] Alizad, A., Whaley, D. H., Greenleaf, J. F., & Fatemi, M. (2006). Critical issues in breast imaging by vibro-acoustography. *Ultrasonics*, 44, e217-e220.

[105] Nover, A. B., Jagtap, S., Anjum, W., Yegingil, H., Shih, W. Y., Shih, W. H., & Brooks, A. D. (2009). Modern breast cancer detection: a technological review. *Journal of Biomedical Imaging*, *2009*, 26.

[106] Orel, S. G., & Schnall, M. D. (2001). MR imaging of the breast for the detection, diagnosis, and staging of breast cancer. *Radiology*, 220 (1), 13-30.

[107] Warner, E., Plewes, D. B., Shumak, R. S., Catzavelos, G. C., Di Prospero, L. S., Yaffe, M. J., & Narod, S. A. (2001). Comparison of breast magnetic resonance imaging, mammography, and ultrasound for surveillance of women at high risk for hereditary breast cancer. *Journal of Clinical Oncology*, 19 (15), 3524-3531.

[108] Lehman, C. D., & Schnall, M. D. (2005). Imaging in breast cancer: magnetic resonance imaging. *Breast Cancer Res*, 7 (5), pp.215-219.

[109] Orel, S. (2008). Who should have breast magnetic resonance imaging evaluation?. *Journal of Clinical Oncology*, 26 (5), pp.703-711.

[110] Breast MRI (magnetic resonance imaging). *Available :* http://www.breastcancer.org/symptoms/testing/types/mri, last visited on 12th January, 2013.

[111] Rubæk, T (2008). Microwave imaging for breast-cancer screening, *PhD Thesis*.

[112] Porter, E. (2010). Microwave breast tumor detection: simulation and design of experiments with tissue phantoms. *Masters Abstracts International*, 49 (05).

[113] Infrared Medical Solutions. Understanding breast physiology, *Available: http://www.infraredmedicalsolutions.com/patients/about_breast_physiology*, last visited on 13th January 2013.

[114] MedicineNet.com, Breast Cancer, Available: *http://www.medicinenet.com/breast_cancer/article.htm*, last visited on 13th January, 2013.

[115] Xu, Y., Feng, D., & Wang, L. V. (2002). Exact frequency-domain reconstruction for thermoacoustic tomography I. planar geometry. *IEEE Transactions on Medical Imaging*, 21 (7), pp.823-828.

[116] Rubino, R. (2012). Numerical MRI-based breast model for microwave imaging. *Master Thesis Dissection*.

[117] Said, T., & Varadan, V. V. (2009, June). Variation of Cole-Cole model parameters with the complex permittivity of biological tissues. *Microwave Symposium Digest, 2009. MTT'09. IEEE MTT-S International*, pp.1445-1448.

[118] Ibrahim, W. M. A., & Algabroun, H. M. (2008). The family tree of breast microwave Imaging Techniques. *4th Kuala Lumpur International Conference on Biomedical Engineering 2008*, pp. 258-261.

[119] Kruger, R. A., Kopecky, K. K., Aisen, A. M., Reinecke, D. R., Kruger, G. A., & Kiser, W. L. (1999). Thermoacoustic CT with radio waves: a medical imaging paradigm. *Radiology*, 211 (1), pp.275-278.

[120] Kruger, R. A., Kiser, W. L., Reinecke, D. R., Kruger, G. A., & Eisenhart, R. L. (1999). Thermoacoustic computed tomography of the breast at 434 MHz. *IEEE MTT-S International Microwave Symposium Digest*, 1999, pp. 591-594.

[121] Wang, L. V., Zhao, X., Sun, H., & Ku, G. (1999). Microwave-induced acoustic imaging of biological tissues. *Review of Scientific Instruments*, 70 (9), pp.3744-3748.

[122] Xu, Y., Xu, M., & Wang, L. V. (2002). Exact frequency-domain reconstruction for thermoacoustic tomography. II. Cylindrical geometry. *Medical Imaging, IEEE Transactions on*, 21 (7), pp.829-833.

[123] Mouty, S., Bocquet, B., Ringot, R., Rocourt, N., & Devos, P. (2000). Microwave radiometric imaging (MWI) for the characterisation of breast tumours. *The European Physical Journal Applied Physics*, 10 (01), pp.73-78.

[124] Semenov, S. Y., Svenson, R. H., Boulyshev, A. E., Souvorov, A. E., Borisov, V. Y., Sizov, Y., & Baranov, V. Y. (1996). Microwave tomography: two-dimensional system for biological imaging. *IEEE Transactions on Biomedical Engineering*, 43 (9), pp.869-877.

[125] Souvorov, A. E., Bulyshev, A. E., Semenov, S. Y., Svenson, R. H., & Tatsis, G. P. (2000). Two-dimensional computer analysis of a microwave flat antenna array for breast cancer tomography. *IEEE Transactions on Microwave Theory and Techniques*,48 (8), pp.1413-1415.

[126] Bulyshev, A. E., Semenov, S. Y., Souvorov, A. E., Svenson, R. H., Nazarov, A. G., Sizov, Y. E., & Tatsis, G. P. (2001). Computational modeling of three-dimensional microwave tomography of breast cancer. *IEEE Transactions on Biomedical Engineering* , 48 (9), pp.1053-1056.

[127] Liu, Q. H., Zhang, Z. Q., Wang, T. T., Bryan, J. A., Ybarra, G. A., Nolte, L. W., & Joines, W. T. (2002). Active microwave imaging. I. 2-D forward and inverse scattering methods. *IEEE Transactions on Microwave Theory and Techniques*, 50 (1), pp.123-133.

[128] Zhang, Z. Q., Liu, Q. H., Xiao, C., Ward, E., Ybarra, G., & Joines, W. T. (2003). Microwave breast imaging: 3-D forward scattering simulation. *IEEE Transactions on Biomedical Engineering*, 50 (10), pp.1180-1189.

[129] Zhang, Z. Q., & Liu, Q. H. (2004). Three-dimensional nonlinear image reconstruction for microwave biomedical imaging. *IEEE Transactions on Biomedical Engineering*, 51 (3), pp.544-548.

[130] Gabor, D. (1948). A new microscopic principle. *Nature*, 161, pp.777-778.

[131] Holography, Available: light.ece.illinois.edu/ECE460/PDF/Holography.pdf

[132] Leith, E. N., & Upatnieks, J. (1962). Reconstructed wavefronts and communication theory. *JOSA*, 52 (10), pp.1123-1128.

[133] Mehta, P. C. & Rampal, V. V. (1993). Lasers and holography. *World Scientific Publishing Co. Pte. Ltd*, pp.258-261.

[134] Hong, H. D., Sheffer, D. B., & Loughry, C. W. (1996). Holographic interferometry for early detection of breast cancer. Engineering in medicine and biology society, 1996. Bridging sisciplines for biomedicine. *Proceedings of the 18th Annual International Conference of the IEEE* 1, pp.189-190.

[135] Woisetschlaeger, J., Sheffer, D. B., Mikati, H., Somasundaram, K., Loughry, C. W., Chawla, S. K., & Wesolowski, P. J. (1993). Breast cancer detection by holographic interferometry. *San Diego'92 International Society for Optics and Photonics*, pp.176-183.

[136] O'Halloran, M., Conceicao, R. C., Byrne, D., Glavin, M., & Jones, E. (2009). FDTD modeling of the breast: A review. *Progress In Electromagnetics Research B*, 18, pp.1-24.

[137] Foster, K. R. and Schwan, H. P. (1989). Dielectric properties of tissues and biological materials: A critial review. *Crit. Rev. Biomed. Eng*., 17, pp.25-104.

[138] Xu Li and Hagness, S. C. 2001. A confocal microwave imaging algorithm for breast cancer detection. *IEEE Microwave and Wireless Components Letters*, 11 (3), pp.130-132.

[139] Thompson, A. R., Moran, J. M., & Swenson Jr, G. W. (2001). Interferometry and synthesis in radio astronomy. *Wiley-Vch*, Chapter 3, pp.68-76.

[140] Silver, S. (1949). Microwave antenna theory and design. *MIT Radiation Laboratory Series, McGraw-Hill, New York*, Chapter 3.11.

[141] Born, M. and Wolf, E. (1980). Principles of optics, *Pergamon Press, Sixth Edition*, Chapter 10.4.2, pp.510.

[142] Hector, L. G., & Schultz, H. L. (1936). The dielectric constant of air at radiofrequencies. *Physics*, 7 (4), pp.133-136.

[143] Li, D., Meaney, P. M., & Paulsen, K. D. (2003). Conformal microwave imaging for breast cancer detection. *IEEE Transactions on Microwave Theory and Techniques*, 51 (4), pp.1179-1186.

[144] Klemm, M., Craddock, I., Leendertz, J., Preece, A., & Benjamin, R. (2008, July). Experimental and clinical results of breast cancer detection using UWB microwave radar. *IEEE Antennas and Propagation Society International Symposium, 2008,* pp. 1-4.

[145] Rubæk, T., & Meincke, P. (2006, November). Including antenna models in microwave imaging for breast cancer screening. *EuCAP 2006 First European Conference on Antennas and Propagation*, pp. 1-6.

[146] Klemm, M., Leendertz, J. A., Gibbins, D., Craddock, I. J., Preece, A., & Benjamin, R. (2009). Microwave radar-based breast cancer detection: Imaging in inhomogeneous breast phantoms. *IEEE Antennas and Wireless Propagation Letters*, 8, 1349-1352.

[147] O'Halloran, M., Glavin, M., & Jones, E. (2010). Rotating antenna microwave imaging system for breast cancer detection. *Progress In Electromagnetics Research*, 107, pp.203-217.

[148] Zhao, Y., Shao, W., & Wang, G. (2004, October). UWB microwave imaging for early breast cancer detection: effect of two synthetic antenna array configurations. *2004 IEEE International Conference on Systems, Man and Cybernetics*, 5, pp.4468-4473.

[149] Jones, D. L. (2004). Geometric Configuration Constraints for Large Deep Space Network Arrays. *The Interplanetary Network Progress Report*, 42, pp.157.

[150] Jones, D. L. (2005, March). Geometric configurations for large spacecraft-tracking arrays. *2003 IEEE Aerospace Conference Proceedings*, 2, pp.2_997-2_1002).

Appendix A MATLAB 2D Modelling Code

A. 1 Main Code for 2D HMIA Simulation Model

This code describes the implementation of the 2D HMIA system to form a 2D projection image of a 3D breast model. After the initial declaration of variables, initialization of the constants and setting the breast model size and location, the main calculation loop is entered. The main code includes a 3D numerical breast model (see A. 2 and A. 3), transmitting antenna model (see A. 4), receiving antenna model (see A. 5) and breast intensity model (A. 6). First, the variations of the frequency, complex relative permittivity of the breast and the host medium, amplitude of TE10 mode and aperture dimension of antenna are defined.

```
clc;
clear all;
close all;
freq=1.26e10;%frequency Hz
c=3e11;%speed in free space (vacuum) mm/s
J=sqrt(-1);
permit0=8.854e-9;%Permittivity of free space (F/mm)- Farads per
millimeter
permitfat=9-0.4*J;%complex relative permittivity of breast tissue
permitskin=9.3-4*J;%complex relative permittivity of skin
permitlesion =9.5-7*J;%complex relative  permittivity of lesion
permitb=1;%Permittivity of background
lamdafat=c/(freq.*sqrt(permitfat));%wavelength in skin(in mm)
lamdaskin=c/(freq.*sqrt(permitskin));%wavelength in fat (in mm)
lamdalesion=c/(freq.*sqrt(permitlesion));%wavelength in lesion (in mm)
lamdab=c/(freq.*sqrt(permitlesion));%wavelength in background
lamda0=c/freq; %wavelength in in free space;
k0=2*pi/lamda0; % wavenumber in free space;
kfat=2*pi/lamdafat; % wavenumber in breast tissue;
kskin=2*pi/lamdaskin; % wavenumber in skin ;
klesion=2*pi/lamdalesion; % wavenumber in lesion ;
kb=2*pi/lamdab;%wavenumber in background
Eo=1; % Amplitude of TE10 mode
A=15.788; %Broad aperture dimension of antenna
B=7.5; %Narrow aperture dimension of antenna
Height=-450;%Antenna position at the z-direction
dx=0.5;
dy=dx;
dz=0.25;
dV=dx*dy*dz;% breast volume element
x1=-70:dx:70;
y1=-70:dy:70;
z1=0:dz:70;
```

```
[x,y]=meshgrid(x1,y1); z=meshgrid(z1);
X0=0; Y0=0; Z0=0;%location of skin
X1=0; Y1=0; Z1=0;%location of fat
X2=0; Y2=-40; Z2=0;%location of lesion
X3=0; Y3=-20; Z3=0;%location of lesion
X4=0; Y4=0; Z4=0;%location of lesion
X5=0; Y5=20; Z5=0;%location of lesion
X6=0; Y6=40; Z6=0;%location of lesion
R=70;%radius of the breast
R1=R-2;%size of skin
a2=2; b2=2; c2=2;%size of lesion in x, y, z directions
a3=3; b3=3; c3=3;%size of lesion in x, y, z directions
a4=3; b4=3; c4=3;%size of lesion in x, y, z directions
a5=4; b5=4; c5=4;%size of lesion in x, y, z directions
a6=5; b6=5; c6=5;%size of lesion in x, y, z directions
Skin= Breast3DModel(x,y,z,X0,Y0,Z0,R);%skin model
Fat= Breast3DModel(x,y,z,X1,Y1,Z1,R1);%fat model
Lesion1=Lesion3DModel(x,y,z,X2,Y2,Z2,a2,b2,c2);%lesion model
Lesion2=Lesion3DModel(x,y,z,X3,Y3,Z3,a3,b3,c3);%lesion model
Lesion3=Lesion3DModel(x,y,z,X4,Y4,Z4,a4,b4,c4);%lesion model
Lesion4=Lesion3DModel(x,y,z,X5,Y5,Z5,a5,b5,c5);%lesion model
Lesion5=Lesion3DModel(x,y,z,X6,Y6,Z6,a6,b6,c6);%lesion model

% A 3D numerical breast model
zz2=Skin+Fat+Lesion1+Lesion2+Lesion3+Lesion4+Lesion5;
ind1=zz2==0; ind2=zz2==1; ind3=zz2==2; ind4=zz2==3;
zz2(ind1)=permitb; zz2(ind2)=permitskin; zz2(ind3)=permitfat;
zz2(ind4)=permitlesion; zz2(~(ind1|ind2|ind3|ind4))=permitb;
x=abs(zz2);
y=abs(zz2);
permitbreast=zz2;% complex relative permittivity of the breast

Tr=load('TransimittingAntenna.txt'); %load transmitting Antenna
Tr(:,3)=Height;

%Transmitter function, calculate incident field at x, y, z directions
[Number,Transmitter]=Transmitter(Tr,x,y,z,kb,Eo,A,B);
Eincx=0; Eincy=0; Eincz=0;
l=0; m=0;
for i=1:Number
    Eincx=Eincx+Transmitter(i).Eincx;
    Eincy=Eincy+Transmitter(i).Eincy;
    Eincz=Eincz+Transmitter(i).Eincz;
    l=l+Transmitter(i).l;
    m=m+Transmitter(i).m;
end
Eincx=Eincx./Number; Eincy=Eincy./Number; Eincz=Eincz./Number;
l=l./Number; m=m./Number;
Rx=load('SpiralAarraySimulation4.txt');%load receiving Antenna
Rx(:,3)=Height;
%receiving antenna function
[N,Antenna]=Antenna2DModel(dV,Rx,abs(zz2),abs(zz2),abs(z),k0,kb,permit
breast,permitb,Eincx,Eincy,Eincz);
pr=N*(N-1);
%breast indensity function
[BreastIndensity]=BreastIndensity(Rx,l,m,Antenna,lamdab);
% matrix to store baseline lengths
UV = zeros(pr, 3); % cycle through pairs,
Im=0;
k=0;
for i = 1:N
    for j =1:N
        k=k+1;
```

```
        %calculate UV coverage
        U(k)=BreastIndensity(i,j).u;
        V(k)=BreastIndensity(i,j).v;
        %calculate breast intensity distribution
        Im=Im+BreastIndensity(i,j).Im;
    end
end
Im=Im./max(max(Im)); %normalized to maximum in the 3D volume
% plot antenna position
figure(1)
clf()
set(axes,'XDir','reverse')
plot(Tr(:,1),Tr(:,2),'s') %plot transimitter
hold on;
plot(Rx(:,1),Rx(:,2),'O') %plot receivers
axis square
legend('Transmitter', 'Receiver')
xlabel('X (mm)','FontSize',16)
ylabel('Y (mm)','FontSize',16)
title('Antenna Position','FontSize',16)
%plot UV coverage
figure(2)
plot(U,V,'.')
xlabel('U ','FontSize',16)
ylabel('V ','FontSize',16)
title('UV Coverage','FontSize',16)
%plot orignial breast model
figure(3)
imagesc(x1,y1,abs(zz2))
colorbar()
xlabel('X (mm) ','FontSize',16)
ylabel('Y (mm) ','FontSize',16)
title('Original Breast Image','FontSize',16)
%plot 2D reconstructed image of breast model
figure(4)
imagesc(x1,y1,abs(Im))
colorbar()
xlabel('X (mm) ','FontSize',16)
ylabel('Y (mm ','FontSize',16)
title('Reconstructed Breast Image','FontSize',16)
```

Load transmitter file `'TransimittingAntenna.txt'`

```
%x(mm)  y(mm)  z(mm)
120    160    0
```

Load receiving antenna file `'SpiralAarraySimulation4.txt'`

```
%x(mm)  y(mm)  z(mm)
80     160    0
200    180    0
160    170    0
190    85     0
255    125    0
125    95     0
175    225    0
0      175    0
53     290    0
120    296    0
5      235    0
75     225    0
120    235    0
193    230    0
43     115    0
```

A. 2 Breast Model

This code simulates a hemispherical shaped breast model. Skin and fat can be simulated using this model.

```
function [el]=Breast3DModel(x,y,z,X0,Y0,Z0,R)
%X0, Y0, Z0: location of the breast
%R: radius of the breast
el=(x-X0).^2./(R^2)+(y-Y0).^2./(R^2)+(z-Z0).^2./(R^2)<1;
```

A. 3 Lesion Model

This code simulates a spherical or elliptical shaped 3D lesion model.

```
function [el]=Lesion3DModel(x,y,z,X0,Y0,Z0,a,b,c)
%X0, Y0, Z0: location of the breast
%a , b, c: size of the breast in x, y, z directions
el=(x-X0).^2./(a^2) +(y-Y0).^2./(b^2)+(z-Z0).^2./(c^2)<1;
```

A. 4 Transmitting Antenna Model

This code describes the implementation of the transmitting antenna model and the incident electric field of the antenna is calculated. The antenna model includes eight subfuctions: UnitVector, Distance, IncidentAngle, Green, xyz2lmn, RadiationPattern, Polar and Ein. These subfuctions are used to calculate the unit vector of a vector, the distance between a point within the breast and the transmitter, the incident angle of the the transmitting antenna, direction cosines in spherical polar coordinates system, radiation pattern, polarization vector electric field and incident electric field respectively.

```
function [M,Transmitter]=Transmitter(Tr, x, y, z, kb, Eo, A,B)
[M,N]=size(Tr);%calculate transmitting antenna number
Transmitter=struct('x','y','z','Tx','Ty','Tz','R','theta','phi','Phi',
'l','m','n','Fx','Fy','Fz','Eincx','Eincy','Eincz','');
Txr=zeros(M,3);
      for j=1:M
      %calculate unit vector parallel to the vector
      Txr(j,:)=UnitVector(Tr(j,:));
      end
      for i=1:M
      %calculate transmitting antenna position in x, y, z directions
```

```
        Transmitter(i).x=Tr(i,1);
        Transmitter(i).y=Tr(i,2);
        Transmitter(i).z=Tr(i,3);
        %calculate unit vector of transmitting antenna in x, y, z
        directions
        Transmitter(i).Tx=Txr(i,1);
        Transmitter(i).Ty=Txr(i,2);
        Transmitter(i).Tz=Txr(i,3);
        %calculate unit vector parallel to the distance between a point
        within the breast and the antenna
        Transmitter(i).R=Distance(Transmitter(i).Tx,Transmitter(i).Ty,Tr
        ansmitter.Tz,x,y,z);
        %calculate incident angle
        [Transmitter(i).theta,Transmitter(i).phi]=IncidentAngle(Transmit
        ter(i).x,Transmitter(i).y,Transmitter.z,x,y,z,Transmitter(i).R);
        %Green function
        Transmitter(i).Phi=Green(kb,Transmitter(i).R);
        %calculate polarisation vector
        [Transmitter(i).l,Transmitter(i).m,Transmitter(i).n]=xyz2lmn(Tra
        nsmitter(i).theta,Transmitter(i).phi);
        Transmitter(i).h=RadiationPattern(A,B,kb,Transmitter(i).theta,Tr
        ansmitter(i).phi);
        %calculate polarisation vector
        [Transmitter(i).Fx,Transmitter(i).Fy,Transmitter(i).Fz]=Polar(Tr
        ansmitter(i).theta,Transmitter(i).phi);
        %calculate incident electric field at x,y,z positions
        [Transmitter(i).Eincx,Transmitter(i).Eincy,Transmitter(i).Eincz]
        =Ein(kb,Eo,Transmitter(i).Phi,A,B,Transmitter(i).h,Transmitter(i
        ).Fx,Transmitter(i).Fy,Transmitter(i).Fz);
        end
end
```

Subfunction UnitVector: calculates the unit vector of a vector.

```
function [vector]=UnitVector(vector)
%Normalize a [1xn] or [nx1] vector
%Description: This function will simplify the process of creating a
unit
%vector in one direction by dividing a vector by its length.
%Use: [vectorOut] = fcn_createUnitVector(vectorIn[1xn])
% or [vectorOut] = fcn_createUnitVector(vectorIn[mx1])
[r c] = size(vector);
%Convert the vector to columns
if (r > c && c == 1);
    vector = vector';
elseif (r < c && r==1);
    %do Nothing
else
    error('Input vector must be [mx1] or [1xn]');
end
%Process the unit transform
vector = vector./norm(vector);
end
```

Subfunction Distance: calculates the distance between a point within the breast and the transmitter.

```
function R=Distance(x1,y1,z1,x2,y2,z2)
% calculate distance of two points A(x1,y1,z1) and B(x2,y2,z2)
R=sqrt((x2-x1).^2+(y2-y1).^2+(z2-z1).^2);
end
```

Subfunction IncidentAngle: calculates the incident angle of a transmitting antenna

```
function [theta,phi]=IncidentAngle(x1,y1,z1,x2,y2,z2,R)
%x1,y1,z1: a point A(x1,y1,z1)
%x2,y2,z2: a point B(x2,y2,z2)
%R:the distance between two points A and B
theta=acos((z2-z1)./R);
phi=atan2(y2-y1,x2-x1);
end
```

Subfunction Green: simulates Green's function $G = \frac{e^{-jk_b R}}{R}$

```
%Green's function
function Phi=Green(kb,R)
%R: the distance between a point within the breast and a transmitter
%kb: propagation constant in the host medium
J=sqrt(-1);
Phi=exp(-J*kb*R)./R;
end
```

Subfunction xyz2lmn: calculates direction cosines by use spherical polar coordinates

```
function [l,m,n]=xyz2lmn(theta,phi)
%calculate direction cosines by using spherical polar coordinates
l=sin(theta).*cos(phi);
m=sin(theta).*sin(phi);
n=sqrt(1-l.^2-m.^2);
end
```

Subfunction RadiationPattern: calculates radiation pattern

```
function h=RadiationPattern(A,B,kb,theta,phi)
% calculate radiation pattern
%A: Broad aperture dimension of antenna
%B: Narrow aperture dimension of antenna
a=sinc(kb.*B.*sin(theta).*sin(phi)./2);
b=cos(kb.*A.*sin(theta).*cos(phi)./2);
c=1-(kb.*A.*sin(theta).*cos(phi)./pi).^2;
h=a.*(b./c);
end
```

Subfunction Polar: calculates polarization vector electric field

```
function [Fx,Fy,Fz]=Polar(theta,phi)
Fx=sin(theta).^2.*cos(phi).*sin(phi);
Fy=sin(theta).^2.*sin(phi).^2-(1+cos(theta));
Fz=sin(theta).*sin(phi).*(1+cos(theta));
end
```

Subfunction Ein: calculates incident electric field at x, y, z positions

```
function [Eincx,Eincy,Eincz]=Ein(kb,Eo,Phio,A,B,h,Fx,Fy,Fz)
J=sqrt(-1);
%incident electric field at x, y, z positions
Eincx=(-J*kb./(2*pi^2)).*Eo.*Phio.*A.*B.*h.*Fx;
Eincy=(-J*kb./(2*pi^2)).*Eo.*Phio.*A.*B.*h.*Fy;
Eincz=(-J*kb./(2*pi^2)).*Eo.*Phio.*A.*B.*h.*Fz;
end
```

A. 5 Antenna Model

This code describes the implementation of the receiving antenna model and the backscattered electric field from the breast is calculated. The antenna model includes five subfuctions: UnitVector, Distance, ReceiverAngle, Green, and xyz2lmn. These subfuctions are used to calculate the unit vector of a vector, the distance between a point within the breast and a receiver, the receiving angle of a receiver, radiation and direction cosines in spherical polar coordinates system.

```
Function [N, Antenna]=Antenna2DModel(dV, Rx, x, y, z, k0, kb,
permitbreast, permitb, Eincx, Eincy, Eincz)
%dV: volume element
%Rx: load antenna file
%x, y, z: a point within the breast
%kb: propagation constant in host medium
%permitbreast: complex relative permittivity of the breast
%permitb: complex relative permittivity of background
%Eincx: incident electric field in x direction
%Eincy: incident electric field in y direction
%Eincy: incident electric field in z direction
N=length(Rx);%calculate antenna number
Antenna=struct('x','y','z','Rx','Ry','Rz','R','Phi','sp','Do','Es','')
;
RR=zeros(N,3);
for j=1:N
      %calculate unit vector parallel to the vector
      RR(j,:)=UnitVector(Rx(j,:));
end
for i = 1:N
      Antenna(i).x=Rx(i,1); %calculate antenna position in x direction
      Antenna(i).y=Rx(i,2);%calculate antenna position in y direction
      Antenna(i).z=Rx(i,3); %calculate antenna position in z direction
      %calculate unit vector of antenna position in x, y, z directions
      Antenna(i).Rx=RR(i,1);
      Antenna(i).Ry=RR(i,2);
      Antenna(i).Rz=RR(i,3);
      %calculate unit vector parallel to the distance between a point
      within the breast and the antenna
      Antenna(i).R0=Distance(Antenna(i).Rx,Antenna(i).Ry,Antenna(i).Rz
      ,x,y,z);
      Antenna(i).Phi=Green(kb,Antenna(i).R0); %Green's function
      %calculate polarisation vector
      Antenna(i).sp=(Eincx.*Antenna(i).Rx)+(Eincy.*Antenna(i).Ry)+(Ein
      cz.*Antenna(i).Rz);
      Antenna(i).Do=Eincy-Antenna(i).sp.*Antenna(i).Ry;
      %calculate the backscattered filed from the breast using born
      approximation
      Antenna(i).Es=(k0^2/4/pi).*sum(sum(sum((permitbreast-
      permitb).*Antenna(i).Do.*Antenna(i).Phi.*dV)));
      end
end
```

Subfunction UnitVector: calculates the unit vector of a vector

```
function [vector]=UnitVector(vector)
%Normalize a [1xn] or [nx1] vector
%Description: This function will simplify the process of creating a
unit
%vector in one direction by dividing a vector by its length.
%Use: [vectorOut] = fcn_createUnitVector(vectorIn[1xn])
% or [vectorOut] = fcn_createUnitVector(vectorIn[mx1])
[r c] = size(vector);
%Convert the vector to columns
if (r > c && c == 1);
      vector = vector';
elseif (r < c && r==1);
      %do Nothing
else
      error('Input vector must be [mx1] or [1xn]');
end
%Process the unit transform
vector = vector./norm(vector);
end
```

Subfunction Distance: calculates the distance between a point within the breast and a receiving antenna

```
function R=Distance(x1,y1,z1,x2,y2,z2)
% calculate distance of two points A(x1,y1,z1) and B(x2,y2,z2)
R=sqrt((x2-x1).^2+(y2-y1).^2+(z2-z1).^2);
end
```

Subfunction ReceiverAngle: calculates the receiving angle of a receiver

```
function [theta,phi]=ReceiverAngle(x1,y1,z1,x2,y2,z2,R)
%x1,y1,z1: a point A(x1,y1,z1)
%x2,y2,z2: a point B(x2,y2,z2)
%R:the distance between two points A and B
theta=acos((z2-z1)./R);
phi=atan2(y2-y1,x2-x1);
end
```

Subfunction Green: simulates Green's function $G = \frac{e^{-jk_b R}}{R}$

```
function Phi=Green(kb, R)
%R: the distance between a point within the breast and a antenna
%kb: propagation constant in host medium
J=sqrt(-1);
Phi=exp(-J*kb*R)./R;
end
```

Subfunction xyz2lmn: calculates direction cosines using spherical polar coordinates

```
function [l,m,n]=xyz2lmn(theta,phi)
%calculate direction cosines by using spherical polar coordinates
l=sin(theta).*cos(phi);
m=sin(theta).*sin(phi);
n=sqrt(1-l.^2-m.^2);
end
```

A. 6 Breast Intensity Distribution Model in 2D HMIA

In this model, the complex visibility data and the breast intensity distribution in 2D HMIA system are calculated.

```
function [BreastIntensity]=BreastIntensity(Rx,l,m,Antenna,lambdab)
%this function will calculate the complex visibility data and the
breast intensity distribution
%Rx: load receiving antenna file
%l, m: load direction cosines in spherical polar coordinate system
%Antenna: load antenna function
%lambdab: load wavelength in background
N=length(Rx);%calculate antenna number
BreastIntensity=struct('u','v','w','F','G','I');
J=sqrt(-1);
for i=1:N
      for j=1:N
      %caculate u, v, w
      BreastIntensity(i,j).u=(Antenna(j).x-Antenna(i).x)./lambdab;
      BreastIntensity(i,j).v=(Antenna(j).y-Antenna(i).y)./lambdab;
      BreastIntensity(i,j).w=(Antenna(j).z-Antenna(i).z)./lambdab;
      %fast Fourier transform function
      BreastIntensity(i,j).F=exp(-
      J*2*pi*(BreastIntensity(i,j).u.*l+BreastIntensity(i,j).v.*m));
      %inverse fast Fourier transform function
      BreastIntensity(i,j).F1=exp(J*2*pi*(BreastIntensity(i,j).u.*l+Br
      eastIntensity(i,j).v.*m));
      %calculate complex visibility data
      BreastIntensity(i,j).G=Antenna(i).Es.*conj(Antenna(j).Es).*Breas
      tIntensity(i,j).F;
      %calculate breast intensity distribution
      BreastIntensity(i,j).I=BreastIntensity(i,j).G.*BreastIntensity(i
      ,j).F1;
      end
end

end
```

Appendix B MATLAB 3D Modelling Code

B. 1 Main Code for 3D HMIA Simulation Model

This code describes the implementation the 3D HMIA system to form a 3D image of a 3D breast model. After the initial declaration the variables, initialization of the constants and setting the breast model size and location, the main calculation loop is entered. The main code includes the 3D breast model (see A. 2 and A. 3), 3D transmitting antenna model (see B. 2), 3D receiving antenna model (see B. 3) and 3D breast intensity model (see B. 4). First, the variations of the frequency, complex relative permittivity of the breast and the host medium, amplitude of TE10 mode and aperture dimension of antenna are defined. The 3D model of breast is obtained by load the breast, skin and lesion file, and 3D Gaussian function is used to present the breast model.

```
clc;
clear all;
close all;
freq=1.26e10;%frequency Hz
c=3e11;%speed in free space (vacuum) mm/s
J=sqrt(-1);
permit0=8.854e-9;%Permittivity of free space (F/mm)- Farads per
millimeter
permitfat=9-0.4*J;%complex relative permittivity of breast tissue
permitskin=9.3-4*J;%complex relative permittivity of skin
permitlesion=9.5-7*J;%complex relative  permittivity of lesion
permitb=1;%Permittivity of background
lamdafat=c/(freq.*sqrt(permitfat));%wavelength in skin(in mm)
lamdaskin=c/(freq.*sqrt(permitskin));%wavelength in fat (in mm)
lamdalesion=c/(freq.*sqrt(permitlesion));%wavelength in lesion (in mm)
lamdab=c/(freq.*sqrt(permitlesion));%wavelength in background
lamda0=c/freq; %wavelength in in free space;
k0=2*pi/lamda0; % wavenumber in free space;
kfat=2*pi/lamdafat; % wavenumber in breast tissue;
kskin=2*pi/lamdaskin; % wavenumber in skin ;
klesion=2*pi/lamdalesion; % wavenumber in lesion ;
kb=2*pi/lamdab;%wavenumber in background
Eo=1; % Amplitude of TE10 mode
A=15.788; %Broad aperture dimension of antenna
B=7.5; %Narrow aperture dimension of antenna
dx=1;
dy=dx;
dz=1;
x1=-70:dx:70;
y1=-70:dy:70;
z1=0:dz:70;
```

```
[x,y,z]=meshgrid(x1,y1,z1);
dH=1;
Height=-450;%Antenna position at the z-direction
H=Height-10:dH:Height;
X0=0; Y0=0; Z0=0;%location of skin
X1=0; Y1=0; Z1=0;%location of fat
X2=0; Y2=-40; Z2=0;%location of lesion
X3=0; Y3=-20; Z3=0;%location of lesion
X4=0; Y4=0; Z4=0;%location of lesion
X5=0; Y5=20; Z5=0;%location of lesion
X6=0; Y6=40; Z6=0;%location of lesion
R=70;%Radius of the breast
R1=R-2; %size of skin
a2=2; b2=2; c2=2;%size of lesion in x, y, z directions
a3=3; b3=3; c3=3;%size of lesion in x, y, z directions
a4=3; b4=3; c4=3;%size of lesion in x, y, z directions
a5=4; b5=4; c5=4;%size of lesion in x, y, z directions
a6=5; b6=5; c6=5;%size of lesion in x, y, z directions
Skin=Breast3DModel(x,y,z,X0,Y0,Z0,R);%skin model
Fat=Breast3DModel(x,y,z,X1,Y1,Z1,R1);%fat model
Lesion1=Lesion3DModel(x,y,z,X2,Y2,Z2,a2,b2,c2);%lesion model
Lesion2=Lesion3DModel(x,y,z,X3,Y3,Z3,a3,b3,c3);%lesion model
Lesion3=Lesion3DModel(x,y,z,X4,Y4,Z4,a4,b4,c4);%lesion model
Lesion4=Lesion3DModel(x,y,z,X5,Y5,Z5,a5,b5,c5);%lesion model
Lesion5=Lesion3DModel(x,y,z,X6,Y6,Z6,a6,b6,c6);%lesion model

%A 3D numerical breast model
zz2=Skin+Fat+Lesion1+Lesion2+Lesion3+Lesion4+Lesion5;
ind1=zz2==0;
ind2=zz2==1;
ind3=zz2==2;
ind4=zz2==3;
zz2(ind1)=permitb;
zz2(ind2)=permitskin;
zz2(ind3)=permitfat;
zz2(ind4)=permitlesion;
zz2(~(ind1|ind2|ind3|ind4))=permitb;
x=abs(zz2);
y=abs(zz2);
permitbreast=zz2;% complex relative permittivity of the breast
dV=dx*dy*dz;% breast volume element

Tr=load('RandomTr.txt'); %load transimitting Antenna
%Transmitter function, calculate incident field at x,y,z directions
[Number,Transmitter]=JTransmitter3D(siz,H,Tr,x,y,z,kb,Eo,A,B);
Eincx=0;
Eincy=0;
Eincz=0;
l=0;
m=0;
for i=1:Number
    for j=1:siz
    Eincx=Eincx+Transmitter(i,j).Eincx;
    Eincy=Eincy+Transmitter(i,j).Eincy;
    Eincz=Eincz+Transmitter(i,j).Eincz;
    l=l+Transmitter(i,j).l;
    m=m+Transmitter(i,j).m;
    end
end
Eincx=Eincx./Number;
Eincy=Eincy./Number;
Eincz=Eincz./Number;
l=l./Number;
```

```
m=m./Number;
Rx=load('RandomArray.txt');%load receiving Antenna
%receiving antenna function
[N,Antenna3D]=Antenna3D(dV,siz,Rx,H,abs(zz2),abs(zz2),abs(z),k0,kb,per
mitbreast,permitb,Eincx,Eincy,Eincz);
pr=N*(N-1);

%breast indensity function
[BreastIndensity]=BreastIndensity3D(siz,l,m,Antenna3D,lamdab,N);

% matrix to store baseline lengths
UV = zeros(pr, 3);% cycle through pairs,
k=0;
Im=0;
for i = 1:N
   for j =i+1:N
      for p=1:siz
      k=k+1;
      %calculate UV coverage
       U(k)=BreastIndensity(i,j,p).u;
       V(k)=BreastIndensity(i,j,p).v;
         for q=p+1:siz
            Im=Im+(BreastIndensity(i,j,p).I-
            BreastIndensity(i,j,q).I)./dH;
         end %calculate breast intensity distribution
      end
   end
end

%normalized to maximum in the 3D volume
Im=Im./max(max(max(Im)));

% plot antenna position
figure(1)
clf()
set(axes,'XDir','reverse')
plot(Tr(:,1),Tr(:,2),'s') %plot transmitter
hold on;
plot(Rx(:,1),Rx(:,2),'O') %plot receivers
axis square
legend('Transmitter', 'Receiver')
xlabel('X (mm)','FontSize',16)
ylabel('Y (mm)','FontSize',16)
title('Antenna Position','FontSize',16)

%plot UV coverage
figure(2)
plot(U,V,'.')
xlabel('U ','FontSize',16)
ylabel('V ','FontSize',16)
title('UV Coverage','FontSize',16)

[x,y,z]=meshgrid(x1,y1,z1);
%plot original breast model
figure(3)
slice(x,y,z,abs(zz2),0,70,1)
colorbar()
xlabel('X (mm) ','FontSize',16)
ylabel('Y (mm) ','FontSize',16)
zlabel('Z (mm) ','FontSize',16)
title('Original Breast Image','FontSize',16)
```

```
%plot 3D reconstructed image of breast model
figure(4)
slice(x,y,z,abs(Im),0,70,1)
colorbar()
xlabel('X (mm) ','FontSize',16)
ylabel('Y (mm) ','FontSize',16)
zlabel('Z (mm) ','FontSize',16)
title('Reconstructed Breast Image','FontSize',16)
```

Load transmitter file `'RandomTr.txt'`

```
%x(mm)  y(mm)  z(mm)
150    160    0
```

Load receiving antenna file `'RandomArray.txt'`

```
%x(mm)  y(mm)  z(mm)
43     94     0
50     50     0
237    75     0
167    121    0
95     51     0
163    43     0
115    235    0
30     167    0
59     187    0
0      235    0
38     274    0
40     212    0
211    205    0
110    300    0
75     119    0
```

B. 2 3D Transmitting Antenna Model

This code describes the implementation of the transmitting antenna model in 3D HMIA system; the incident electric field of the antenna is calculated. The antenna model includes eight subfuctions: UnitVector, Distance, IncidentAngle, Green, xyz2lmn, RadiationPattern, Polar and Ein. The code of subfunctions can be found in A. 4.

```
function [M,Transmitter3D]=Transmitter3D(siz,Tr,x,y,z,kb,A,B,Eo,H)
%input: siz, Tr, x, y, z, kb, A, B, Eo, H
%output: M, Transmitter3D
%siz: steps
%Tr: load transmitter file
%x,y,z: a point within the breast
%kb: wave number in host medium
%Eo: Amplitude of TE10 mode
%A: Broad aperture dimension of antenna
%B: Narrow aperture dimension of antenna
[M,N]=size(Tr);%calculate transmitting antenna number
Transmitter3D=struct('x','y','z','Tx','Ty','Tz','R','theta','phi','Phi
','Fx','Fy','Fz','Eincx','Eincy','Eincz');
for i=1:M
      for j=1:siz
      %calculate antenna position in x direction
      Transmitter3D(i,j).q(i,1)=Tr(i,1);
      %calculate antenna position in x direction
      Transmitter3D(i,j).q(i,2)=Tr(i,2);
      %calculate antenna position in z direction at height q
      Transmitter3D(i,j).q(i,3)=Tr(i,3)+H(j);
      %calculate unit vector parallel to the vector
      Transmitter3D(i,j).Trx(i,:)=createUnitVector(Transmitter3D(i,j).
      q(i,:));
      end
end

for i = 1:M
      for j=1:siz
      %calculate antenna position in x,y,z directions at height q
      Transmitter3D(i,j).x = Transmitter3D(i,j).q(i,1);
      Transmitter3D(i,j).y = Transmitter3D(i,j).q(i,2);
      Transmitter3D(i,j).z = Transmitter3D(i,j).q(i,3);
      %calculate unit vector of antenna position in x,y,z directions
      at height q
      Transmitter3D(i,j).Tx =Transmitter3D(i,j).Trx(i,1);
      Transmitter3D(i,j).Ty =Transmitter3D(i,j).Trx(i,2);
      Transmitter3D(i,j).Tz =Transmitter3D(i,j).Trx(i,3);
      %calculate the distance between a point within the breast and a
      receiving antenna
      Transmitter3D(i,j).R=Distance(x,y,z,Transmitter3D(i,j).Tx,Transm
      itter3D(i,j).Ty,Transmitter3D(i,j).Tz);
      %calculate the incident angle
      [Transmitter3D(i,j).theta,Transmitter3D(i,j).phi]=IncidentAngle(
      Transmitter3D(i,j).Tx,Transmitter3D(i,j).Ty,Transmitter3D(i,j).T
      z,x,y,z,Transmitter3D(i,j).R);
      Transmitter3D(i,j).Phi=Green(kb,Transmitter3D(i,j).R);
```

```
        Transmitter3D(i,j).h=RadiationPattern(A,B,kb,Transmitter3D(i,j).
        theta,Transmitter3D(i,j).phi);
        [Transmitter3D(i,j).Fx,Transmitter3D(i,j).Fy,Transmitter3D(i,j).
        Fz]=Polar(Transmitter3D(i,j).theta,Transmitter3D(i,j).phi);
        [Transmitter3D(i,j).Eincx,Transmitter3D(i,j).Eincy,Transmitter3D
        (i,j).Eincz]=Ein(kb,Eo,Transmitter3D(i,j).Phi,A,B,Transmitter3D(
        i,j).h,Transmitter3D(i,j).Fx,Transmitter3D(i,j).Fy,Transmitter3D
        (i,j).Fz);
        end
end
end
```

B. 3 3D Receiving Antenna Model

This code describes the implementation of the receiving antenna model in 3D HMIA system, the backscattered electric field from the breast is calculated. The antenna model includes five subfuctions: UnitVector, Distance, ReceiverAngle, Green, and xyz2lmn. The code for subfuctions can be found in A. 5.

```
function[N,Antenna3D]=Antenna3D(dV,siz,Rx,H,x,y,z,k0,kb,permitbreast,p
ermitb,Eincx,Eincy,Eincz)
%dV: volume element
%siz: steps in height (in mm)
%Rx: load antenna file
%H: distance between the breast model and antenna array plane
%x, y, z: a point within the breast
%kb: propagation constant in background
%permitbreast: complex relative permittivity of the breast
%permitb: complex relative permittivity of host medium
%Eincx: incident electric field in x direction
%Eincy: incident electric field in y direction
%Eincy: incident electric field in z direction
N=length(Rx);%calculate antenna number
Antenna3D=struct('q','x','y','z','Rx','Ry','Rz','R1','Phi1','theta','p
hi','sp','Do','Es','theta2','phi2','l','m','n','s');
for i=1:N
      for j=1:siz
      Antenna3D(i,j).q=zeros(N,3);
      Antenna3D(i,j).RR=zeros(N,3);
      end
end

for i=1:N
      for j=1:siz
      %calculate antenna position in x direction
      Antenna3D(i,j).q(i,1)=Rx(i,1);
      %calculate antenna position in x direction
      Antenna3D(i,j).q(i,2)=Rx(i,2);
      %calculate antenna position in z direction at height q
      Antenna3D(i,j).q(i,3)=Rx(i,3)+H(j);
      %calculate unit vector parallel to the vector
      Antenna3D(i,j).RR(i,:)=createUnitVector(Antenna3D(i,j).q(i,:));
      end
end

for i = 1:N
      for j=1:siz
      %calculate antenna position in x, y, z directions at height q
      Antenna3D(i,j).x = Antenna3D(i,j).q(i,1);
      Antenna3D(i,j).y = Antenna3D(i,j).q(i,2);
      Antenna3D(i,j).z = Antenna3D(i,j).q(i,3);
      %calculate unit vector of antenna position in x, y, z directions
      at height q
      Antenna3D(i,j).Rx =Antenna3D(i,j).RR(i,1) ;
      Antenna3D(i,j).Ry =Antenna3D(i,j).RR(i,2) ;
      Antenna3D(i,j).Rz = Antenna3D(i,j).RR(i,3) ;
```

```
        %calculate the distance between a point within the breast and a
        receiving antenna
        Antenna3D(i,j).R=Distance(x,y,z,Antenna3D(i,j).Rx,Antenna3D(i,j)
        .Ry,Antenna3D(i,j).Rz);
        %calculate the receiving angle of a receiver
        [Antenna3D(i,j).theta,Antenna3D(i,j).phi]=ReceiverAngle(Antenna3
        D(i,j).Rx,Antenna3D(i,j).Ry,Antenna3D(i,j).Rz,x,y,z,Antenna3D(i,
        j).R);
        %Green function
        Antenna3D(i,j).Phi=Green(kb,Antenna3D(i,j).R);
        %calculate direction cosines by use spherical polar coordinates
        [Antenna3D(i,j).l,Antenna3D(i,j).m,Antenna3D(i,j).n]=xyz2lmn(Ant
        enna3D(i,j).theta,Antenna3D(i,j).phi);
        Antenna3D(i,j).sp=(Eincx.*Antenna3D(i,j).Rx)+(Eincy.*Antenna3D(i
        ,j).Ry)+(Eincz.*Antenna3D(i,j).Rz);
        Antenna3D(i,j).Do= Eincy-Antenna3D(i,j).sp.*Antenna3D(i,j).Ry;
        %calculate the back-scattered electric field from the breast
        Antenna3D(i,j).Es=sum(sum(sum((k0^2/4/pi).*(permitbreast-
        permitb).*Antenna3D(i,j).Do.*Antenna3D(i,j).Phi.*dV)));
        end
end
end
```

B. 4 Breast Intensity Distribution Model in 3D HMIA

In this model, the complex visibility data and the breast intensity distribution in 3D HMIA system are calculated.

```
Function[BreastIntensity3D]=BreastIntensity3D(siz,l,m,n,Antenna3D,lamb
dab,N)
%siz: height shift steps;
%l,m,n: load direction cosines in spherical polar coordinate system
%Antenna:load antenna function
%lambdab:load wavelength in host medium
%N: receiver number
BreastIntensity3D=struct('u','v','D','I','F','F1');
BreastIntensity3D=repmat(BreastIntensity3D,N-1,N);
J=sqrt(-1);
for i=1:N
      for j = 1:N
            for q=1:siz
            %caculate u,v,w when the height between the breast and
            antenna array plane is q
            BreastIntensity3D(i,j,q).u=(Antenna3D(j,q).x-
            Antenna3D(i,q).x)./lambdab;
            BreastIntensity3D(i,j,q).v=(Antenna3D(j,q).y-
            Antenna3D(i,q).y)./lambdab;
            BreastIntensity3D(i,j,q).w=(Antenna3D(j,q).z-
            Antenna3D(i,q).z)./lambdab;
            %fast Fourier transform function
            BreastIndensity3D(i,j,q).F=exp(-
            J*2*pi*(BreastIntensity3D(i,j,q).u.*l+BreastIntensity3D(i,
            j,q).v.*m+BreastIntensity3D(i,j,q).w.*n));
            %inverse fast Fourier transform function
            BreastIntensity3D(i,j,q).F1=exp(J*2*pi*(BreastIntensity3D(
            i,j,q).u.*l+BreastIntensity3D(i,j,q).v.*m+BreastIntensity3
            D(i,j,q).w.*n));
            %calculate complex visibility data
            BreastIntensity3D(i,j,q).G=Antenna3D(i,q).Es.*conj(Antenna
            3D(j,q).Es).*BreastIntensity3D(i,j,q).F;
            %calculate breast intensity distribution
            BreastIntensity3D(i,j,q).I=Antenna3D(i,q).Es.*conj(Antenna
            3D(j,q).Es).*BreastIntensity3D(i,j,q).F1;
            end
      end
end

end
```

Appendix C Antenna Locations

C. 1. Transmitter location on spaced array plane

Transmitter Number	X (mm)	Y (mm)	Z (mm)
Tr	150	150	0

C. 2. Receiver location on spaced array plane

Receiver Number	X (mm)	Y (mm)	Z (mm)
R1	75	150	0
R2	0	75	0
R3	225	150	0
R4	150	75	0
R5	75	75	0
R6	225	75	0
R7	150	225	0
R8	0	225	0
R9	75	300	0
R10	150	300	0
R11	0	300	0
R12	75	225	0
R13	225	225	0
R14	225	300	0
R15	0	150	0

C. 3. Transmitter location on spiral array plane

Transmitter Number	X (mm)	Y (mm)	Z (mm)
Tr	120	160	0

C. 4. Receiver location on spiral array plane

Receiver Number	X (mm)	Y (mm)	Z (mm)
R1	80	160	0
R2	200	180	0
R3	160	170	0
R4	190	85	0
R5	255	125	0
R6	125	95	0
R7	175	225	0
R8	0	175	0
R9	53	290	0
R10	120	296	0
R11	5	235	0
R12	75	225	0
R13	120	235	0
R14	193	230	0
R15	43	115	0

C. 5. Transmitter location on random array plane

Transmitter Number	X (mm)	Y (mm)	Z (mm)
Tr	150	160	0

C. 6. Receiver location on random array plane

Receiver Number	X (mm)	Y (mm)	Z (mm)
R1	43	94	0
R2	50	50	0
R3	237	75	0
R4	167	121	0
R5	95	51	0
R6	163	43	0
R7	115	235	0
R8	30	167	0
R9	59	187	0
R10	0	235	0
R11	38	274	0
R12	40	212	0
R13	211	205	0
R14	110	300	0
R15	75	119	0

Appendix D MATLAB 2D Experiment Analysis Code

All of the 2D experiments were analysed using MATLAB code applied directly to the raw data from the 2D HMIA experimental system. For each 2D experiment series individual analysis MATLAB m-files were created. For each type of 2D experiment the common elements are shown here. Three subfunctions: Distance(), magnitude() and Cphase() are also listed in this section.

```
%This code analyse the raw data from the 2-D HMIA experimental system
%input: measured magnitude of the breast phantom
%input: measured phase of the breast phantom
%input: measured magnitude of the background (without object)
%input: measured phase of the background (without object)
%output: antenna location
%output: UV coverage
%output: 2D projection breast image of a 3D breast phantom
%output: 2D image of measured background (without object)
close all
clear all
clc;
J=sqrt(-1);      %imaginary unit
freq=12.6e9;     %frequency Hz
c=3e11;           %speed in free space mm/s
lamda=c/(freq); %wavelength in free space (background)
k1=2*pi/(lamda);    %wave number in host medium;
%load measured magnitude of the breast phantom
MP=load('MagofTwoGrapewithSkinatRandom.txt');
%load measured phase of the breast phanton
MR1=load('PhaseofTwoGrapewithSkinatRandom.txt');
%load magnitude of the background (without object)
MPO1=load('MagofNoObjectUnderRandomArray.txt');
%load phase of the background (without object)
RO1=load('PhaseofNoObjectUnderRandomArray.txt');
%caculate the magnitude of the breast phantom with background
subtraction
MB1=magnitude(MP-MPO1);
%caculate complex phase of the breast phantom with background
subtraction
RMx1=(Cphase(MB1,MR1-RO1));
%caculate the magnitude of the background (without object)
MB2=magnitude(MPO1);
%caculate the complex phase of the background (without object)
RMx2=(Cphase(MB2,RO1));
P=load('RandomAntenna.txt');%load receiver file
Tr=load('RandomTransimitter.txt');%load transmitter file
step=150;%steps
%measurement plane size at x, y directions (in mm)
x=50:100/(step-1):150;
y=100:100/(step-1):200;
D=meshgrid(0:30/(step-1):30);%breast depth/height
[x1,y1]=meshgrid(x,y);
H=490;%height between the breast phantom and the antenna array
```

```
z1=ones(step).*(H)+D; %distance between the breast phantom and the
antenna array
N=15;
l0=0;
m0=0;
for i=1:N
      % Antenna location in x, y, z directions
      X(i)=P(i,1);
      Y(i)=P(i,2);
      Z(i)=P(i,3);
      %calculates the distance between a point within the breast and a
      receiver
      R0=Distance(x1,y1,z1,X(i),Y(i),Z(i));
      %read the measured backscatter field from the breast at 12.6 GHz
      Es0(i)=RMx1(833,i);
      %read the measured data of background at 12.6 Ghz
      Es1(i)=RMx2(833,i);
      l0=l0+sin(acos((z1-Z(i))./R0)).*cos(atan2(y1-Y(i),x1-X(i)));
      m0=m0+sin(acos((z1-Z(i))./R0)).*sin(atan2(y1-Y(i),x1-X(i)));
end
l0=l0./N;
m0=m0./N;
I0=0;
I1=0;
for i=1:N
      for j=1:N
      % UV coverage
      U(i,j)=(P(j,1)-P(i,1))/lamda;
      V(i,j)=(P(j,2)-P(i,2))/lamda;
      %2D project image of the breast phantom
      I0=I0+Es0(j).*conj(Es0(i)).*exp(
      J*2*pi*(U(i,j).*l0+V(i,j).*m0));
      %background image
      I1=I1+Es1(j).*conj(Es1(i)).*exp(
      J*2*pi*(U(i,j).*l0+V(i,j).*m0));
      end
end

%normalized to maximum in the 3D volume
Im=I0./max(max(I0));     %reconstructed breast image
Im1=I1./max(max(I1));    %reconstructed background
x2=0:100/(step-1):100;   %breast length
y2=0:100/(step-1):100;   %breast width

%plot antenna location
figure(1)
plot(X,Y,'O');
hold on
plot(Tr(1),Tr(2),'X');
title('Antenna Location','FontSize',12)
xlabel('X (mm) ','FontSize',12)
ylabel('Y (mm) ','FontSize',12)
legend('Receiver','Transmitter',2);
axis image;

%plot reconstructed breast image
figure(2)
imagesc(x2,y2,abs(Im));
title('Reconstructed image of the breast','FontSize',12)
xlabel('X (mm) ','FontSize',12)
ylabel('Y (mm) ','FontSize',12)
colorbar();
axis image;
```

```
%plot 2:1 zoomed reconstructed image
figure(3)
imagesc(x2,y2,abs((Im).^2));
title('Reconstructed image of the breast','FontSize',12)
xlabel('X (mm) ','FontSize',12)
ylabel('Y (mm) ','FontSize',12)
colorbar();
axis image;

%plot reconstructed image of background
figure(4)
imagesc(x2,y2,abs(Im1));
title('Reconstructed image of background','FontSize',12)
xlabel('X (mm) ','FontSize',12)
ylabel('Y (mm) ','FontSize',12)
colorbar();
axis image;
```

Subfuction Distance: calculates the distance between two points

```
function R=Distance(x1,y1,z1,x2,y2,z2)
% calculate distance of two points A(x1, y1, z1) and B(x2, y2, z2)
%input: two points A(x1, y1, z1) and B(x2, y2, z2)
%output: distance between two points A(x1, y1, z1) and B(x2, y2, z2)
R=sqrt((x2-x1).^2+(y2-y1).^2+(z2-z1).^2);
end
```

Subfuction magnitude: calculates the measured magnitude from the object

```
function [m]=magnitude(p)
%This code calculate the magnitude of the measured data
m=(10.^(p./20));
end
```

Subfuction Cphase: calculates the measured complex phase of the object

```
function [z]=Cphase(m,theta)
%This code calculates the complex phase from the measured data
%input: m, theta
%output: complex phase
%m: magnitude
%theta: phase
J=sqrt(-1);
x=(m).*cos(theta*pi/180);
y=(m).*sin(theta*pi/180);
z=(x+y.*J);
end
```

Appendix E MATLAB 3D Experiment Analysis Code

All of the 3D experiments were analysed using MATLAB code applied directly to the measured raw data from the 3D HMIA experimental system. For each 3D experiment series, individual analysis MATLAB m-files were created. For each type of 3D experiment, the common elements are shown in this section. This code contains three subfunctions that are detailed in Appendix D.

```
%This code analyse the raw data from the 3D HMIA experimental system
%input: measured magnitude of the breast phantom
%input: measured phase of the breast phantom
%input: measured magnitude of the background (without object)
%input: measured phase of the background (without object)
%output: antenna location
%output: UV coverage
%output: 3D projection breast image of a 3D breast phantom
clear all;
clc;
J=sqrt(-1);      %imaginary unit
freq=12.6e9;     %frequency Hz
c=3e11;           %speed in free space mm/s
lamda=c/(freq); %wavelength in free space (background)
k1=2*pi/(lamda); %wave number in host medium;

%Defines which files should be read
NMO1=load('MagOfNoObjectL0.txt');
NRO1=load('PhaseofNoObjectL0.txt');
L0MP1=load('MagofGrapewithSkinL0.txt');
L0R1=load('PhaseofGrapewithSkinL0.txt');
L1MP1=load('MagofGrapewithSkinL1.txt');
L1R1=load('PhaseofGrapewithSkinL1.txt');
L2MP1=load('MagofGrapewithSkinL2.txt');
L2R1=load('PhaseofGrapewithSkinL2.txt');
L3MP1=load('MagofGrapewithSkinL3.txt');
L3R1=load('PhaseofGrapewithSkinL3.txt');
L4MP1=load('MagofGrapewithSkinL4.txt');
L4R1=load('PhaseofGrapewithSkinL4.txt');
L5MP1=load('MagofGrapewithSkinL5.txt');
L5R1=load('PhaseofGrapewithSkinL5.txt');
L6MP1=load('MagofGrapewithSkinL6.txt');
L6R1=load('PhaseofGrapewithSkinL6.txt');
L7MP1=load('MagofGrapewithSkinL7.txt');
L7R1=load('PhaseofGrapewithSkinL7.txt');
L8MP1=load('MagofGrapewithSkinL8.txt');
L8R1=load('PhaseofGrapewithSkinL8.txt');
L9MP1=load('MagofGrapewithSkinL9.txt');
L9R1=load('PhaseofGrapewithSkinL9.txt');
L10MP1=load('MagofGrapewithSkinL10.txt');
L10R1=load('PhaseofGrapewithSkinL10.txt');
L11MP1=load('MagofGrapewithSkinL11.txt');
L11R1=load('PhaseofGrapewithSkinL11.txt');
L12MP1=load('MagofGrapewithSkinL12.txt');
```

```
L12R1=load('PhaseofGrapewithSkinL12.txt');
L13MP1=load('MagofGrapewithSkinL13.txt');
L13R1=load('PhaseofGrapewithSkinL13.txt');
L14MP1=load('MagofGrapewithSkinL14.txt');
L14R1=load('PhaseofGrapewithSkinL14.txt');
L15MP1=load('MagofGrapewithSkinL15.txt');
L15R1=load('PhaseofGrapewithSkinL15.txt');
L16MP1=load('MagofGrapewithSkinL16.txt');
L16R1=load('PhaseofGrapewithSkinL16.txt');
L17MP1=load('MagofGrapewithSkinL17.txt');
L17R1=load('PhaseofGrapewithSkinL17.txt');
L18MP1=load('MagofGrapewithSkinL18.txt');
L18R1=load('PhaseofGrapewithSkinL18.txt');
L19MP1=load('MagofGrapewithSkinL19.txt');
L19R1=load('PhaseofGrapewithSkinL19.txt');
L20MP1=load('MagofGrapewithSkinL20.txt');
L20R1=load('PhaseofGrapewithSkinL20.txt');
L21MP1=load('MagofGrapewithSkinL21.txt');
L21R1=load('PhaseofGrapewithSkinL21.txt');
L22MP1=load('MagofGrapewithSkinL22.txt');
L22R1=load('PhaseofGrapewithSkinL22.txt');
L23MP1=load('MagofGrapewithSkinL23.txt');
L23R1=load('PhaseofGrapewithSkinL23.txt');
L24MP1=load('MagofGrapewithSkinL24.txt');
L24R1=load('PhaseofGrapewithSkinL24.txt');
L25MP1=load('MagofGrapewithSkinL25.txt');
L25R1=load('PhaseofGrapewithSkinL25.txt');
L26MP1=load('MagofGrapewithSkinL26.txt');
L26R1=load('PhaseofGrapewithSkinL26.txt');
L27MP1=load('MagofGrapewithSkinL27.txt');
L27R1=load('PhaseofGrapewithSkinL27.txt');
L28MP1=load('MagofGrapewithSkinL28.txt');
L28R1=load('PhaseofGrapewithSkinL28.txt');
L29MP1=load('MagofGrapewithSkinL29.txt');
L29R1=load('PhaseofGrapewithSkinL29.txt');
L30MP1=load('MagofGrapewithSkinL30.txt');
L30R1=load('PhaseofGrapewithSkinL30.txt');
L31MP1=load('MagofGrapewithSkinL31.txt');
L31R1=load('PhaseofGrapewithSkinL31.txt');
L32MP1=load('MagofGrapewithSkinL32.txt');
L32R1=load('PhaseofGrapewithSkinL32.txt');
L33MP1=load('MagofGrapewithSkinL33.txt');
L33R1=load('PhaseofGrapewithSkinL33.txt');
L34MP1=load('MagofGrapewithSkinL34.txt');
L34R1=load('PhaseofGrapewithSkinL34.txt');
L35MP1=load('MagofGrapewithSkinL35.txt');
L35R1=load('PhaseofGrapewithSkinL35.txt');
L36MP1=load('MagofGrapewithSkinL36.txt');
L36R1=load('PhaseofGrapewithSkinL36.txt');
L37MP1=load('MagofGrapewithSkinL37.txt');
L37R1=load('PhaseofGrapewithSkinL37.txt');
L38MP1=load('MagofGrapewithSkinL38.txt');
L38R1=load('PhaseofGrapewithSkinL38.txt');
L39MP1=load('MagofGrapewithSkinL39.txt');
L39R1=load('PhaseofGrapewithSkinL39.txt');
P=load('AntennaLocation2.txt');%load receiver file
Tr=load('TransimittingAntenna2.txt');%load transmitter file
NB1=magnitude(NMO1);%magnitude of no object
NRMx1=(Cphase(NB1,NRO1));%complex phase of no object
%caculate the magnitude and the complex phase of the background with
the distance between background and the array plane is z=540 mm
Layer0MB=magnitude(L0MP1); Layer0RMx=(Cphase(Layer0MB,L0R1));
```

```
%caculate the magnitude and the complex phase of the breast phantom
with the breast phantom moved from z=540 mm to z=579 mm in 40 steps
Layer1MB=magnitude(L1MP1); Layer1RMx=(Cphase(Layer1MB,L1R1));
Layer2MB=magnitude(L2MP1); Layer2RMx=(Cphase(Layer2MB,L2R1));
Layer3MB=magnitude(L3MP1); Layer3RMx=(Cphase(Layer3MB,L3R1));
Layer4MB=magnitude(L4MP1); Layer4RMx=(Cphase(Layer4MB,L4R1));
Layer5MB=magnitude(L5MP1); Layer5RMx=(Cphase(Layer5MB,L5R1));
Layer6MB=magnitude(L6MP1); Layer6RMx=(Cphase(Layer6MB,L6R1));
Layer7MB=magnitude(L7MP1); Layer7RMx=(Cphase(Layer7MB,L7R1));
Layer8MB=magnitude(L8MP1); Layer8RMx=(Cphase(Layer8MB,L8R1));
Layer9MB=magnitude(L9MP1); Layer9RMx=(Cphase(Layer9MB,L9R1));
Layer10MB=magnitude(L10MP1); Layer10RMx=(Cphase(Layer10MB,L10R1));
Layer11MB=magnitude(L11MP1); Layer11RMx=(Cphase(Layer11MB,L11R1));
Layer12MB=magnitude(L12MP1); Layer12RMx=(Cphase(Layer12MB,L12R1));
Layer13MB=magnitude(L13MP1); Layer13RMx=(Cphase(Layer13MB,L13R1));
Layer14MB=magnitude(L14MP1); Layer14RMx=(Cphase(Layer14MB,L14R1));
Layer15MB=magnitude(L15MP1); Layer15RMx=(Cphase(Layer15MB,L15R1));
Layer16MB=magnitude(L16MP1); Layer16RMx=(Cphase(Layer16MB,L16R1));
Layer17MB=magnitude(L17MP1); Layer17RMx=(Cphase(Layer17MB,L17R1));
Layer18MB=magnitude(L18MP1); Layer18RMx=(Cphase(Layer18MB,L18R1));
Layer19MB=magnitude(L19MP1); Layer19RMx=(Cphase(Layer19MB,L19R1));
Layer20MB=magnitude(L20MP1); Layer20RMx=(Cphase(Layer20MB,L20R1));
Layer21MB=magnitude(L21MP1); Layer21RMx=(Cphase(Layer21MB,L21R1));
Layer22MB=magnitude(L22MP1); Layer22RMx=(Cphase(Layer22MB,L22R1));
Layer23MB=magnitude(L23MP1); Layer23RMx=(Cphase(Layer23MB,L23R1));
Layer24MB=magnitude(L24MP1); Layer24RMx=(Cphase(Layer24MB,L24R1));
Layer25MB=magnitude(L25MP1); Layer25RMx=(Cphase(Layer25MB,L25R1));
Layer26MB=magnitude(L26MP1); Layer26RMx=(Cphase(Layer26MB,L26R1));
Layer27MB=magnitude(L27MP1); Layer27RMx=(Cphase(Layer27MB,L27R1));
Layer28MB=magnitude(L28MP1); Layer28RMx=(Cphase(Layer28MB,L28R1));
Layer29MB=magnitude(L29MP1); Layer29RMx=(Cphase(Layer29MB,L29R1));
Layer30MB=magnitude(L30MP1); Layer30RMx=(Cphase(Layer30MB,L30R1));
Layer31MB=magnitude(L31MP1); Layer31RMx=(Cphase(Layer31MB,L31R1));
Layer32MB=magnitude(L32MP1); Layer32RMx=(Cphase(Layer32MB,L32R1));
Layer33MB=magnitude(L33MP1); Layer33RMx=(Cphase(Layer33MB,L33R1));
Layer34MB=magnitude(L34MP1); Layer34RMx=(Cphase(Layer34MB,L34R1));
Layer35MB=magnitude(L35MP1); Layer35RMx=(Cphase(Layer35MB,L35R1));
Layer36MB=magnitude(L36MP1); Layer36RMx=(Cphase(Layer36MB,L36R1));
Layer37MB=magnitude(L37MP1); Layer37RMx=(Cphase(Layer37MB,L37R1));
Layer38MB=magnitude(L38MP1); Layer38RMx=(Cphase(Layer38MB,L38R1));
Layer39MB=magnitude(L39MP1); Layer39RMx=(Cphase(Layer39MB,L39R1));
step=100;%steps
%measurement plane size at x, y directions (in mm)
x1=15:150/(step-1):165;
y1=15:150/(step-1):165;
D=meshgrid(0:30/(step-1):30);
[x,y]=meshgrid(x1,y1);
%caculates the distance between the breast phantom and the antenna
array when the breast phantom moved from z=540 mm to z=579 mm
z0=ones(step).*(540)+D;z1=ones(step).*(541)+D;z2=ones(step).*(542)+D;
z3=ones(step).*(543)+D;z4=ones(step).*(544)+D;z5=ones(step).*(545)+D;
z6=ones(step).*(546)+D;z7=ones(step).*(547)+D;z8=ones(step).*(548)+D;
z9=ones(step).*(549)+D;z10=ones(step).*(550)+D;
z11=ones(step).*(551)+D; z12=ones(step).*(552)+D;
z13=ones(step).*(553)+D; z14=ones(step).*(554)+D;
z15=ones(step).*(555)+D; z16=ones(step).*(556)+D;
z17=ones(step).*(557)+D; z18=ones(step).*(558)+D;
z19=ones(step).*(559)+D; z20=ones(step).*(560)+D;
z21=ones(step).*(561)+D; z22=ones(step).*(562)+D;
z23=ones(step).*(563)+D; z24=ones(step).*(564)+D;
z25=ones(step).*(565)+D; z26=ones(step).*(566)+D;
z27=ones(step).*(567)+D; z28=ones(step).*(568)+D;
z29=ones(step).*(569)+D; z30=ones(step).*(570)+D;
```

```
z31=ones(step).*(571)+D; z32=ones(step).*(572)+D;
z33=ones(step).*(573)+D; z34=ones(step).*(574)+D;
z35=ones(step).*(575)+D; z36=ones(step).*(576)+D;
z37=ones(step).*(577)+D; z38=ones(step).*(578)+D;
z39=ones(step).*(579)+D;
N=15;   %receiver number
l0=0; m0=0; l1=0; m1=0; l2=0; m2=0; l3=0; m3=0; l4=0; m4=0; l5=0;
m5=0; l6=0; m6=0; l7=0; m7=0; l8=0; m8=0; l9=0; m9=0; l10=0; m10=0;
l11=0; m11=0; l12=0; m12=0; l13=0; m13=0; l14=0; m14=0; l15=0; m15=0;
l16=0; m16=0; l17=0; m17=0; l18=0; m18=0; l19=0; m19=0; l20=0; m20=0;
l21=0; m21=0; l22=0; m22=0; l23=0; m23=0; l24=0; m24=0; l25=0; m25=0;
l26=0; m26=0; l27=0; m27=0; l28=0; m28=0; l29=0; m29=0; l30=0; m30=0;
l31=0; m31=0; l32=0; m32=0; l33=0; m33=0; l34=0; m34=0; l35=0; m35=0;
l36=0; m36=0; l37=0; m37=0; l38=0; m38=0; l39=0; m39=0;
for i=1:N
       %Antenna location in x,y,z directions
       X(i)=P(i,1); % Antenna location
       Y(i)=P(i,2);
       Z(i)=P(i,3);
      %calculates the distance between a point within the breast and a
      receiver when the breast phantom moved from z=540 mm to z=579 mm
       R0=Distance(x,y,z0,X(i),Y(i),Z(i));
       R1=Distance(x,y,z1,X(i),Y(i),Z(i));
       R2=Distance(x,y,z2,X(i),Y(i),Z(i));
       R3=Distance(x,y,z3,X(i),Y(i),Z(i));
       R4=Distance(x,y,z4,X(i),Y(i),Z(i));
       R5=Distance(x,y,z5,X(i),Y(i),Z(i));
       R6=Distance(x,y,z6,X(i),Y(i),Z(i));
       R7=Distance(x,y,z7,X(i),Y(i),Z(i));
       R8=Distance(x,y,z8,X(i),Y(i),Z(i));
       R9=Distance(x,y,z9,X(i),Y(i),Z(i));
       R10=Distance(x,y,z10,X(i),Y(i),Z(i));
       R11=Distance(x,y,z11,X(i),Y(i),Z(i));
       R12=Distance(x,y,z12,X(i),Y(i),Z(i));
       R13=Distance(x,y,z13,X(i),Y(i),Z(i));
       R14=Distance(x,y,z14,X(i),Y(i),Z(i));
       R15=Distance(x,y,z15,X(i),Y(i),Z(i));
       R16=Distance(x,y,z16,X(i),Y(i),Z(i));
       R17=Distance(x,y,z17,X(i),Y(i),Z(i));
       R18=Distance(x,y,z18,X(i),Y(i),Z(i));
       R19=Distance(x,y,z19,X(i),Y(i),Z(i));
       R20=Distance(x,y,z20,X(i),Y(i),Z(i));
       R21=Distance(x,y,z21,X(i),Y(i),Z(i));
       R22=Distance(x,y,z22,X(i),Y(i),Z(i));
       R23=Distance(x,y,z23,X(i),Y(i),Z(i));
       R24=Distance(x,y,z24,X(i),Y(i),Z(i));
       R25=Distance(x,y,z25,X(i),Y(i),Z(i));
       R26=Distance(x,y,z26,X(i),Y(i),Z(i));
       R27=Distance(x,y,z27,X(i),Y(i),Z(i));
       R28=Distance(x,y,z28,X(i),Y(i),Z(i));
       R29=Distance(x,y,z29,X(i),Y(i),Z(i));
       R30=Distance(x,y,z30,X(i),Y(i),Z(i));
       R31=Distance(x,y,z31,X(i),Y(i),Z(i));
       R32=Distance(x,y,z32,X(i),Y(i),Z(i));
       R33=Distance(x,y,z33,X(i),Y(i),Z(i));
       R34=Distance(x,y,z34,X(i),Y(i),Z(i));
       R35=Distance(x,y,z35,X(i),Y(i),Z(i));
       R36=Distance(x,y,z36,X(i),Y(i),Z(i));
       R37=Distance(x,y,z37,X(i),Y(i),Z(i));
       R38=Distance(x,y,z38,X(i),Y(i),Z(i));
       R39=Distance(x,y,z39,X(i),Y(i),Z(i));
```

```
%read the all measured backscatter field from the breast with
backrgound subtruction at 12.6 Ghz when the breast phantom moved
from z=540 mm to z=579 mm
 Es0(i)=Layer0RMx(833,i)-NRMx1(833,i);
 Es1(i)=Layer1RMx(833,i)-NRMx1(833,i);
 Es2(i)=Layer2RMx(833,i)-NRMx1(833,i);
 Es3(i)=Layer3RMx(833,i)-NRMx1(833,i);
 Es4(i)=Layer4RMx(833,i)-NRMx1(833,i);
 Es5(i)=Layer5RMx(833,i)-NRMx1(833,i);
 Es6(i)=Layer6RMx(833,i)-NRMx1(833,i);
 Es7(i)=Layer7RMx(833,i)-NRMx1(833,i);
 Es8(i)=Layer8RMx(833,i)-NRMx1(833,i);
 Es9(i)=Layer9RMx(833,i)-NRMx1(833,i);
 Es10(i)=Layer10RMx(833,i)-NRMx1(833,i);
 Es11(i)=Layer11RMx(833,i)-NRMx1(833,i);
 Es12(i)=Layer12RMx(833,i)-NRMx1(833,i);
 Es13(i)=Layer13RMx(833,i)-NRMx1(833,i);
 Es14(i)=Layer14RMx(833,i)-NRMx1(833,i);
 Es15(i)=Layer15RMx(833,i)-NRMx1(833,i);
 Es16(i)=Layer16RMx(833,i)-NRMx1(833,i);
 Es17(i)=Layer17RMx(833,i)-NRMx1(833,i);
 Es18(i)=Layer18RMx(833,i)-NRMx1(833,i);
 Es19(i)=Layer19RMx(833,i)-NRMx1(833,i);
 Es20(i)=Layer20RMx(833,i)-NRMx1(833,i);
 Es21(i)=Layer21RMx(833,i)-NRMx1(833,i);
 Es22(i)=Layer22RMx(833,i)-NRMx1(833,i);
 Es23(i)=Layer23RMx(833,i)-NRMx1(833,i);
 Es24(i)=Layer24RMx(833,i)-NRMx1(833,i);
 Es25(i)=Layer25RMx(833,i)-NRMx1(833,i);
 Es26(i)=Layer26RMx(833,i)-NRMx1(833,i);
 Es27(i)=Layer27RMx(833,i)-NRMx1(833,i);
 Es28(i)=Layer28RMx(833,i)-NRMx1(833,i);
 Es29(i)=Layer29RMx(833,i)-NRMx1(833,i);
 Es30(i)=Layer30RMx(833,i)-NRMx1(833,i);
 Es31(i)=Layer31RMx(833,i)-NRMx1(833,i);
 Es32(i)=Layer32RMx(833,i)-NRMx1(833,i);
 Es33(i)=Layer33RMx(833,i)-NRMx1(833,i);
 Es34(i)=Layer34RMx(833,i)-NRMx1(833,i);
 Es35(i)=Layer35RMx(833,i)-NRMx1(833,i);
 Es36(i)=Layer36RMx(833,i)-NRMx1(833,i);
 Es37(i)=Layer37RMx(833,i)-NRMx1(833,i);
 Es38(i)=Layer38RMx(833,i)-NRMx1(833,i);
 Es39(i)=Layer39RMx(833,i)-NRMx1(833,i);
 l0=l0+sin(acos((z0-Z(i))./R0)).*cos(atan2(y-Y(i),x-X(i)));
 m0=m0+sin(acos((z0-Z(i))./R0)).*sin(atan2(y-Y(i),x-X(i)));
 l1=l1+sin(acos((z1-Z(i))./R1)).*cos(atan2(y-Y(i),x-X(i)));
 m1=m1+sin(acos((z1-Z(i))./R1)).*sin(atan2(y-Y(i),x-X(i)));
 l2=l2+sin(acos((z2-Z(i))./R2)).*cos(atan2(y-Y(i),x-X(i)));
 m2=m2+sin(acos((z2-Z(i))./R2)).*sin(atan2(y-Y(i),x-X(i)));
 l3=l3+sin(acos((z3-Z(i))./R3)).*cos(atan2(y-Y(i),x-X(i)));
 m3=m3+sin(acos((z3-Z(i))./R3)).*sin(atan2(y-Y(i),x-X(i)));
 l4=l4+sin(acos((z4-Z(i))./R4)).*cos(atan2(y-Y(i),x-X(i)));
 m4=m4+sin(acos((z4-Z(i))./R4)).*sin(atan2(y-Y(i),x-X(i)));
 l5=l5+sin(acos((z5-Z(i))./R5)).*cos(atan2(y-Y(i),x-X(i)));
 m5=m5+sin(acos((z5-Z(i))./R5)).*sin(atan2(y-Y(i),x-X(i)));
 l6=l6+sin(acos((z6-Z(i))./R6)).*cos(atan2(y-Y(i),x-X(i)));
 m6=m6+sin(acos((z6-Z(i))./R6)).*sin(atan2(y-Y(i),x-X(i)));
 l7=l7+sin(acos((z7-Z(i))./R7)).*cos(atan2(y-Y(i),x-X(i)));
 m7=m7+sin(acos((z7-Z(i))./R7)).*sin(atan2(y-Y(i),x-X(i)));
 l8=l8+sin(acos((z8-Z(i))./R8)).*cos(atan2(y-Y(i),x-X(i)));
 m8=m8+sin(acos((z8-Z(i))./R8)).*sin(atan2(y-Y(i),x-X(i)));
 l9=l9+sin(acos((z9-Z(i))./R9)).*cos(atan2(y-Y(i),x-X(i)));
 m9=m9+sin(acos((z9-Z(i))./R9)).*sin(atan2(y-Y(i),x-X(i)));
```

```
        l10=l10+sin(acos((z10-Z(i))./R10)).*cos(atan2(y-Y(i),x-X(i)));
        m10=m10+sin(acos((z10-Z(i))./R10)).*sin(atan2(y-Y(i),x-X(i)));
        l11=l11+sin(acos((z11-Z(i))./R11)).*cos(atan2(y-Y(i),x-X(i)));
        m11=m11+sin(acos((z11-Z(i))./R11)).*sin(atan2(y-Y(i),x-X(i)));
        l12=l12+sin(acos((z12-Z(i))./R12)).*cos(atan2(y-Y(i),x-X(i)));
        m12=m12+sin(acos((z12-Z(i))./R12)).*sin(atan2(y-Y(i),x-X(i)));
        l13=l13+sin(acos((z13-Z(i))./R13)).*cos(atan2(y-Y(i),x-X(i)));
        m13=m13+sin(acos((z13-Z(i))./R13)).*sin(atan2(y-Y(i),x-X(i)));
        l14=l14+sin(acos((z14-Z(i))./R14)).*cos(atan2(y-Y(i),x-X(i)));
        m14=m14+sin(acos((z14-Z(i))./R14)).*sin(atan2(y-Y(i),x-X(i)));
        l15=l15+sin(acos((z15-Z(i))./R15)).*cos(atan2(y-Y(i),x-X(i)));
        m15=m15+sin(acos((z15-Z(i))./R15)).*sin(atan2(y-Y(i),x-X(i)));
        l16=l16+sin(acos((z16-Z(i))./R16)).*cos(atan2(y-Y(i),x-X(i)));
        m16=m16+sin(acos((z16-Z(i))./R16)).*sin(atan2(y-Y(i),x-X(i)));
        l17=l17+sin(acos((z17-Z(i))./R17)).*cos(atan2(y-Y(i),x-X(i)));
        m17=m17+sin(acos((z17-Z(i))./R17)).*sin(atan2(y-Y(i),x-X(i)));
        l18=l18+sin(acos((z18-Z(i))./R18)).*cos(atan2(y-Y(i),x-X(i)));
        m18=m18+sin(acos((z18-Z(i))./R18)).*sin(atan2(y-Y(i),x-X(i)));
        l19=l19+sin(acos((z19-Z(i))./R19)).*cos(atan2(y-Y(i),x-X(i)));
        m19=m19+sin(acos((z19-Z(i))./R19)).*sin(atan2(y-Y(i),x-X(i)));
        l20=l20+sin(acos((z20-Z(i))./R20)).*cos(atan2(y-Y(i),x-X(i)));
        m20=m20+sin(acos((z20-Z(i))./R20)).*sin(atan2(y-Y(i),x-X(i)));
        l21=l21+sin(acos((z21-Z(i))./R21)).*cos(atan2(y-Y(i),x-X(i)));
        m21=m21+sin(acos((z21-Z(i))./R21)).*sin(atan2(y-Y(i),x-X(i)));
        l22=l22+sin(acos((z22-Z(i))./R22)).*cos(atan2(y-Y(i),x-X(i)));
        m22=m22+sin(acos((z22-Z(i))./R22)).*sin(atan2(y-Y(i),x-X(i)));
        l23=l23+sin(acos((z23-Z(i))./R23)).*cos(atan2(y-Y(i),x-X(i)));
        m23=m23+sin(acos((z23-Z(i))./R23)).*sin(atan2(y-Y(i),x-X(i)));
        l24=l24+sin(acos((z24-Z(i))./R24)).*cos(atan2(y-Y(i),x-X(i)));
        m24=m24+sin(acos((z24-Z(i))./R24)).*sin(atan2(y-Y(i),x-X(i)));
        l25=l25+sin(acos((z25-Z(i))./R25)).*cos(atan2(y-Y(i),x-X(i)));
        m25=m25+sin(acos((z25-Z(i))./R25)).*sin(atan2(y-Y(i),x-X(i)));
        l26=l26+sin(acos((z26-Z(i))./R26)).*cos(atan2(y-Y(i),x-X(i)));
        m26=m26+sin(acos((z26-Z(i))./R26)).*sin(atan2(y-Y(i),x-X(i)));
        l27=l27+sin(acos((z27-Z(i))./R27)).*cos(atan2(y-Y(i),x-X(i)));
        m27=m27+sin(acos((z27-Z(i))./R27)).*sin(atan2(y-Y(i),x-X(i)));
        l28=l28+sin(acos((z28-Z(i))./R28)).*cos(atan2(y-Y(i),x-X(i)));
        m28=m28+sin(acos((z28-Z(i))./R28)).*sin(atan2(y-Y(i),x-X(i)));
        l29=l29+sin(acos((z29-Z(i))./R29)).*cos(atan2(y-Y(i),x-X(i)));
        m29=m29+sin(acos((z29-Z(i))./R29)).*sin(atan2(y-Y(i),x-X(i)));
        l30=l30+sin(acos((z30-Z(i))./R30)).*cos(atan2(y-Y(i),x-X(i)));
        m30=m30+sin(acos((z30-Z(i))./R30)).*sin(atan2(y-Y(i),x-X(i)));
        l31=l31+sin(acos((z31-Z(i))./R31)).*cos(atan2(y-Y(i),x-X(i)));
        m31=m31+sin(acos((z31-Z(i))./R31)).*sin(atan2(y-Y(i),x-X(i)));
        l32=l32+sin(acos((z32-Z(i))./R32)).*cos(atan2(y-Y(i),x-X(i)));
        m32=m32+sin(acos((z32-Z(i))./R32)).*sin(atan2(y-Y(i),x-X(i)));
        l33=l33+sin(acos((z33-Z(i))./R33)).*cos(atan2(y-Y(i),x-X(i)));
        m33=m33+sin(acos((z33-Z(i))./R33)).*sin(atan2(y-Y(i),x-X(i)));
        l34=l34+sin(acos((z34-Z(i))./R34)).*cos(atan2(y-Y(i),x-X(i)));
        m34=m34+sin(acos((z34-Z(i))./R34)).*sin(atan2(y-Y(i),x-X(i)));
        l35=l35+sin(acos((z35-Z(i))./R35)).*cos(atan2(y-Y(i),x-X(i)));
        m35=m35+sin(acos((z35-Z(i))./R35)).*sin(atan2(y-Y(i),x-X(i)));
        l36=l36+sin(acos((z36-Z(i))./R36)).*cos(atan2(y-Y(i),x-X(i)));
        m36=m36+sin(acos((z36-Z(i))./R36)).*sin(atan2(y-Y(i),x-X(i)));
        l37=l37+sin(acos((z37-Z(i))./R37)).*cos(atan2(y-Y(i),x-X(i)));
        m37=m37+sin(acos((z37-Z(i))./R37)).*sin(atan2(y-Y(i),x-X(i)));
        l38=l38+sin(acos((z38-Z(i))./R38)).*cos(atan2(y-Y(i),x-X(i)));
        m38=m38+sin(acos((z38-Z(i))./R38)).*sin(atan2(y-Y(i),x-X(i)));
        l39=l39+sin(acos((z39-Z(i))./R39)).*cos(atan2(y-Y(i),x-X(i)));
        m39=m39+sin(acos((z39-Z(i))./R39)).*sin(atan2(y-Y(i),x-X(i)));
end
l0=l0./N; l1=l1./N; l2=l2./N; l3=l3./N; l4=l4./N; l5=l5./N; l6=l6./N;
```

```
l7=l7./N; l8=l8./N; l9=l9./N; l10=l10./N; l11=l11./N; l12=l12./N;
l13=l13./N; l14=l14./N; l15=l15./N; l16=l16./N; l17=l17./N;
l18=l18./N; l19=l19./N; l20=l20./N; l21=l21./N; l22=l22./N;
l23=l23./N; l24=l24./N; l25=l25./N; l26=l26./N; l27=l27./N;
l28=l28./N; l29=l29./N; l30=l30./N; l31=l31./N; l32=l32./N;
l33=l33./N; l34=l34./N; l35=l35./N; l36=l36./N; l37=l37./N;
l38=l38./N; l39=l39./N; m0=m0./N; m1=m1./N; m2=m2./N; m3=m3./N;
m4=m4./N; m5=m5./N; m6=m6./N; m7=m7./N; m8=m8./N; m9=m9./N;
m10=m10./N; m11=m11./N; m12=m12./N; m13=m13./N; m14=m14./N;
m15=m15./N; m16=m16./N; m17=m17./N; m18=m18./N; m19=m19./N;
m20=m20./N; m21=m21./N; m22=m22./N; m23=m23./N; m24=m24./N;
m25=m25./N; m26=m26./N; m27=m27./N; m28=m28./N; m29=m29./N;
m30=m30./N; m31=m31./N; m32=m32./N; m33=m33./N; m34=m34./N;
m35=m35./N; m36=m36./N; m37=m37./N; m38=m38./N; m39=m39./N;
I0=0; I1=0; I2=0; I3=0; I4=0; I5=0; I6=0; I7=0; I8=0; I9=0; I10=0;
I11=0; I12=0; I13=0; I14=0; I15=0; I16=0; I17=0; I18=0; I19=0; I20=0;
I21=0; I22=0; I23=0; I24=0; I25=0; I26=0; I27=0; I28=0; I29=0; I30=0;
I31=0; I32=0; I33=0; I34=0; I35=0; I36=0; I37=0; I38=0; I39=0;
for i=1:N
      for j=1:N
      % UV coverage
      U(i,j)=(P(j,1)-P(i,1))/lamda;
      V(i,j)=(P(j,2)-P(i,2))/lamda;
      %2D projection images of 3-D breast phantom when the phantom
      moved from z=540 mm to z=579 mm
      I0=I0+Es0(j).*conj(Es0(i)).*exp(J*2*pi*(U(i,j).*l0+V(i,j).*m0));
      I1=I1+Es1(j).*conj(Es1(i)).*exp(J*2*pi*(U(i,j).*l1+V(i,j).*m1));
      I2=I2+Es2(j).*conj(Es2(i)).*exp(J*2*pi*(U(i,j).*l2+V(i,j).*m2));
      I3=I3+Es3(j).*conj(Es3(i)).*exp(J*2*pi*(U(i,j).*l3+V(i,j).*m3));
      I4=I4+Es4(j).*conj(Es4(i)).*exp(J*2*pi*(U(i,j).*l4+V(i,j).*m4));
      I5=I5+Es5(j).*conj(Es5(i)).*exp(J*2*pi*(U(i,j).*l5+V(i,j).*m5));
      I6=I6+Es6(j).*conj(Es6(i)).*exp(J*2*pi*(U(i,j).*l6+V(i,j).*m6));
      I7=I7+Es7(j).*conj(Es7(i)).*exp(J*2*pi*(U(i,j).*l7+V(i,j).*m7));
      I8=I8+Es8(j).*conj(Es8(i)).*exp(J*2*pi*(U(i,j).*l8+V(i,j).*m8));
      I9=I9+Es9(j).*conj(Es9(i)).*exp(J*2*pi*(U(i,j).*l9+V(i,j).*m9));
I10=I10+Es10(j).*conj(Es10(i)).*exp(J*2*pi*(U(i,j).*l10+V(i,j).*m10));
I11=I11+Es11(j).*conj(Es11(i)).*exp(J*2*pi*(U(i,j).*l11+V(i,j).*m11));
I12=I12+Es12(j).*conj(Es12(i)).*exp(J*2*pi*(U(i,j).*l12+V(i,j).*m12));
I13=I13+Es13(j).*conj(Es13(i)).*exp(J*2*pi*(U(i,j).*l13+V(i,j).*m13));
I14=I14+Es14(j).*conj(Es14(i)).*exp(J*2*pi*(U(i,j).*l14+V(i,j).*m14));
I15=I15+Es15(j).*conj(Es15(i)).*exp(J*2*pi*(U(i,j).*l15+V(i,j).*m15));
I16=I16+Es16(j).*conj(Es16(i)).*exp(J*2*pi*(U(i,j).*l16+V(i,j).*m16));
I17=I17+Es17(j).*conj(Es17(i)).*exp(J*2*pi*(U(i,j).*l17+V(i,j).*m17));
I18=I18+Es18(j).*conj(Es18(i)).*exp(J*2*pi*(U(i,j).*l18+V(i,j).*m18));
I19=I19+Es19(j).*conj(Es19(i)).*exp(J*2*pi*(U(i,j).*l19+V(i,j).*m19));
I20=I20+Es20(j).*conj(Es20(i)).*exp(J*2*pi*(U(i,j).*l20+V(i,j).*m20));
I21=I21+Es21(j).*conj(Es21(i)).*exp(J*2*pi*(U(i,j).*l21+V(i,j).*m21));
I22=I22+Es22(j).*conj(Es22(i)).*exp(J*2*pi*(U(i,j).*l22+V(i,j).*m22));
I23=I23+Es23(j).*conj(Es23(i)).*exp(J*2*pi*(U(i,j).*l23+V(i,j).*m23));
I24=I24+Es24(j).*conj(Es24(i)).*exp(J*2*pi*(U(i,j).*l24+V(i,j).*m24));
I25=I25+Es25(j).*conj(Es25(i)).*exp(J*2*pi*(U(i,j).*l25+V(i,j).*m25));
I26=I26+Es26(j).*conj(Es26(i)).*exp(J*2*pi*(U(i,j).*l26+V(i,j).*m26));
I27=I27+Es27(j).*conj(Es27(i)).*exp(J*2*pi*(U(i,j).*l27+V(i,j).*m27));
I28=I28+Es28(j).*conj(Es28(i)).*exp(J*2*pi*(U(i,j).*l28+V(i,j).*m28));
I29=I29+Es29(j).*conj(Es29(i)).*exp(J*2*pi*(U(i,j).*l29+V(i,j).*m29));
I30=I30+Es30(j).*conj(Es30(i)).*exp(J*2*pi*(U(i,j).*l30+V(i,j).*m30));
I31=I31+Es31(j).*conj(Es31(i)).*exp(J*2*pi*(U(i,j).*l31+V(i,j).*m31));
I32=I32+Es32(j).*conj(Es32(i)).*exp(J*2*pi*(U(i,j).*l32+V(i,j).*m32));
I33=I33+Es33(j).*conj(Es33(i)).*exp(J*2*pi*(U(i,j).*l33+V(i,j).*m33));
I34=I34+Es34(j).*conj(Es34(i)).*exp(J*2*pi*(U(i,j).*l34+V(i,j).*m34));
I35=I35+Es35(j).*conj(Es35(i)).*exp(J*2*pi*(U(i,j).*l35+V(i,j).*m35));
I36=I36+Es36(j).*conj(Es36(i)).*exp(J*2*pi*(U(i,j).*l36+V(i,j).*m36));
I37=I37+Es37(j).*conj(Es37(i)).*exp(J*2*pi*(U(i,j).*l37+V(i,j).*m37));
```

```
I38=I38+Es38(j).*conj(Es38(i)).*exp(J*2*pi*(U(i,j).*l38+V(i,j).*m38));
I39=I39+Es39(j).*conj(Es39(i)).*exp(J*2*pi*(U(i,j).*l39+V(i,j).*m39));
      end
end
x3=0:100/(step-1):100;  % breast length
y3=0:100/(step-1):100;  %b reast width
% get 3D image
H(:,:,1)=I0-I1; H(:,:,2)=I1-I2; H(:,:,3)=I2-I3; H(:,:,4)=I3-I4;
H(:,:,5)=I4-I5; H(:,:,6)=I5-I6; H(:,:,7)=I6-I7; H(:,:,8)=I7-I8;
H(:,:,9)=I8-I9; H(:,:,10)=I9-I10; H(:,:,11)=I10-I11;H(:,:,12)=I11-I12;
H(:,:,13)=I12-I13; H(:,:,14)=I13-I14; H(:,:,15)=I14-I15;
H(:,:,16)=I15-I16; H(:,:,17)=I16-I17; H(:,:,18)=I17-I18;
H(:,:,19)=I18-I19; H(:,:,20)=I19-I20; H(:,:,21)=I20-I21;
H(:,:,22)=I21-I22; H(:,:,23)=I22-I23; H(:,:,24)=I23-I24;
H(:,:,25)=I24-I25; H(:,:,26)=I25-I26; H(:,:,27)=I26-I27;
H(:,:,28)=I27-I28; H(:,:,29)=I28-I29; H(:,:,30)=I29-I30;
H(:,:,31)=I30-I31; H(:,:,32)=I31-I32; H(:,:,33)=I32-I33;
H(:,:,34)=I33-I34; H(:,:,35)=I34-I35; H(:,:,36)=I35-I36;
H(:,:,37)=I36-I37; H(:,:,38)=I37-I38; H(:,:,39)=I38-I39;
[xx,yy,zz]=meshgrid(x3,y3,(0:30/38:30));
%normalized to maximum in the 3D volume
II=abs(H./max(max(max(H))));
%plot antenna location
figure(1)
plot(X,Y,'O');
hold on
plot(Tr(1),Tr(2),'s')
title('Antenna Location','FontSize',12)
xlabel('X (mm) ','FontSize',12)
ylabel('Y (mm) ','FontSize',12)
legend('Receiver','Transmitter',2);
axis image;
%plot reconstructed 3D image
figure(2)
slice(xx,yy,zz,abs(II),50,100,0)
title('Reconstructed image of the breast','FontSize',12)
xlabel('X (mm) ','FontSize',12)
ylabel('Y (mm) ','FontSize',12)
zlabel('Z (mm)','FontSize',12);
colorbar();
%plot 2: 1 zoomed reconstructed 3D image
figure(3)
slice(xx,yy,zz,abs(II.^2),50,100,0)
title('Reconstructed image of the breast','FontSize',12)
xlabel('X (mm) ','FontSize',12)
ylabel('Y (mm) ','FontSize',12)
zlabel('Z (mm)','FontSize',12);
colorbar();
```

Appendix F Experimental Results: Group I

F.1 Magnitude of breast phantom of one grape (15 mm in diameter) without skin at 15 receivers at 12.6 GHz

R1	R2	R3	R4	R5	R6	R7	R8	R9	R10	R11	R12	R13	R14	R15
2.72e-03	1.85e-03	1.13e-03	8.99e-04	1.63e-03	2.40e-04	3.30e-03	3.38e-03	1.02e-02	1.38e-03	2.54e-03	2.10e-03	1.09e-02	6.32e-04	5.67e-03

F.2 Phase of breast phantom of one grape (15 mm in diameter) without skin at 15 receivers at 12.6 GHz

R1	R2	R3	R4	R5	R6	R7	R8	R9	R10	R11	R12	R13	R14	R15
8.38e+01	-8.29e+01	-1.28e+02	8.27e+01	-1.29e+01	-9.96e+01	1.38e+02	1.43e+02	-1.67e+02	8.00e+01	-8.22e+01	5.01e+01	-4.88e+01	-4.62e+01	7.44e+00

F.3 Magnitude of breast phantom of one grape (10 mm in diameter) without skin at 15 receivers at 12.6 GHz

R1	R2	R3	R4	R5	R6	R7	R8	R9	R10	R11	R12	R13	R14	R15
-3.01E+01	-4.39E+01	-3.55E+01	-4.96E+01	-5.59E+01	-5.80E+01	-6.81E+01	-4.37E+01	-5.59E+01	-5.81E+01	-4.78E+01	-5.20E+01	-5.53E+01	-4.41E+01	-4.58E+01

F.4 Phase of breast phantom of one grape (10 mm in diameter) without skin at 15 receivers at 12.6 GHz

R1	R2	R3	R4	R5	R6	R7	R8	R9	R10	R11	R12	R13	R14	R15
-1.57E+02	-1.98E+01	-2.01E+01	-1.70E+02	-6.09E+01	1.77E+02	1.71E+02	-1.25E+02	-9.43E+01	-2.83E+01	2.40E+01	-1.10E+02	1.79E+02	1.79E+02	1.50E+02

F.5 Magnitude of breast phantom of one mental ball (10 mm) and one grape (15 mm) without skin at 15 receivers at 12.6 GHz

R1	R2	R3	R4	R5	R6	R7	R8	R9	R10	R11	R12	R13	R14	R15
2.96E-02	6.43E-03	1.68E-02	2.56E-03	1.36E-03	1.89E-03	1.43E-03	5.90E-03	6.75E-04	5.03E-04	2.07E-03	2.94E-03	2.02E-03	6.26E-03	5.45E-03

F.6 Phase of breast phantom of one mental ball (10 mm) and one grape (15 mm) without skin at 15 receivers at 12.6 GHz

R1	R2	R3	R4	R5	R6	R7	R8	R9	R10	R11	R12	R13	R14	R15
-1.63E+02	9.19E+01	-2.12E+01	1.61E+02	2.25E+01	-1.60E+02	-1.77E+02	-1.39E+02	-1.78E+02	1.33E+02	1.91E+01	-1.29E+02	1.28E+02	1.57E+02	1.77E+02

F.7 Magnitude of breast phantom of two grapes (10 mm and 15 mm in diameter) without skin at 15 receivers at 12.6 GHz

R1	R2	R3	R4	R5	R6	R7	R8	R9	R10	R11	R12	R13	R14	R15
-4.37E+01	-4.38E+01	-3.53E+01	-4.91E+01	-5.76E+01	-5.94E+01	-6.23E+01	-4.47E+01	-5.43E+01	-5.69E+01	-4.76E+01	-5.86E+01	-5.46E+01	-4.53E+01	-4.61E+01

F.8 Phase of breast phantom of two grapes (10 mm and 15 mm in diameter) without skin at 15 receivers at 12.6 GHz

R1	R2	R3	R4	R5	R6	R7	R8	R9	R10	R11	R12	R13	R14	R15
8.91E+01	9.07E+01	-2.21E+01	1.79E+02	-4.87E+01	-1.69E+02	1.29E+02	-1.30E+02	-5.14E+01	3.20E+01	2.77E+01	-1.77E+02	1.18E+02	-1.73E+02	1.62E+02

F.9 Magnitude of breast phantom of one grape (10 mm in diameter) with skin at 15 receivers at 12.6 GHz

R1	R2	R3	R4	R5	R6	R7	R8	R9	R10	R11	R12	R13	R14	R15
2.41E-03	1.81E-03	9.92E-04	9.04E-04	1.85E-03	2.47E-04	2.74E-03	3.73E-03	1.11E-02	1.89E-03	2.24E-03	1.55E-03	1.10E-02	5.20E-04	6.22E-03

F.10 Phase of breast phantom of one grape (10 mm in diameter) with skin at 15 receivers at 12.6 GHz

R1	R2	R3	R4	R5	R6	R7	R8	R9	R10	R11	R12	R13	R14	R15
7.99E+01	-9.25E+01	-1.28E+02	8.15E+01	-1.35E+01	-1.37E+02	1.51E+02	1.46E+02	-1.67E+02	7.33E+01	-8.98E+01	5.16E+01	-5.06E+01	-6.35E+01	-1.26E+00

Appendix G Experimental Results: Group II

G.1 Magnitude of breast phantom of one grape (10 mm in diameter) without skin at 15 receivers at 12.6 GHz with array plane placed at height 540 mm to 549 mm

Hight (mm)	R1	R2	R3	R4	R5	R6	R7	R8	R9	R10	R11	R12	R13	R14	R15
540	-3.01E+01	-4.39E+01	-3.55E+01	-4.96E+01	-5.59E+01	-5.80E+01	-6.81E+01	-4.37E+01	-5.59E+01	-5.81E+01	-4.78E+01	-5.20E+01	-5.53E+01	-4.41E+01	-4.58E+01
541	-3.01E+01	-4.49E+01	-3.56E+01	-5.92E+01	-6.07E+01	-5.86E+01	-6.56E+01	-4.40E+01	-5.56E+01	-5.72E+01	-4.77E+01	-6.58E+01	-5.29E+01	-4.53E+01	-4.63E+01
542	-3.02E+01	-4.43E+01	-3.56E+01	-6.01E+01	-5.89E+01	-5.91E+01	-7.25E+01	-5.41E+01	-5.54E+01	-5.74E+01	-4.73E+01	-6.20E+01	-5.32E+01	-4.51E+01	-4.58E+01
543	-3.02E+01	-4.49E+01	-3.55E+01	-4.96E+01	-5.58E+01	-5.98E+01	-6.93E+01	-4.40E+01	-5.57E+01	-5.76E+01	-4.77E+01	-5.28E+01	-4.40E+01	-4.42E+01	-4.55E+01
544	-3.03E+01	-4.42E+01	-3.54E+01	-5.06E+01	-5.47E+01	-5.76E+01	-6.19E+01	-4.35E+01	-5.98E+01	-5.94E+01	-4.82E+01	-4.98E+01	-5.99E+01	-4.34E+01	-4.56E+01
545	-3.03E+01	-4.47E+01	-3.52E+01	-5.19E+01	-5.39E+01	-5.73E+01	-5.95E+01	-4.34E+01	-5.89E+01	-6.09E+01	-4.78E+01	-4.78E+01	-6.65E+01	-4.33E+01	-4.61E+01
546	-3.05E+01	-4.47E+01	-3.48E+01	-5.23E+01	-5.40E+01	-5.72E+01	-5.73E+01	-4.37E+01	-6.27E+01	-6.19E+01	-5.12E+01	-4.66E+01	-6.37E+01	-4.36E+01	-4.71E+01
547	-3.04E+01	-4.51E+01	-3.49E+01	-5.26E+01	-5.50E+01	-5.81E+01	-5.81E+01	-4.38E+01	-6.26E+01	-5.11E+01	-5.15E+01	-4.66E+01	-6.00E+01	-4.41E+01	-4.76E+01
548	-3.04E+01	-4.44E+01	-3.49E+01	-5.25E+01	-5.52E+01	-5.38E+01	-4.43E+01	-4.40E+01	-5.54E+01	-6.39E+01	-5.12E+01	-4.76E+01	-5.94E+01	-4.57E+01	-4.83E+01
549	-3.02E+01	-4.40E+01	-3.53E+01	-5.22E+01	-5.59E+01	-5.36E+01	-5.97E+01	-4.43E+01	-5.23E+01	-5.03E+01	-5.12E+01	-4.96E+01	-5.92E+01	-4.68E+01	-4.81E+01

G.2 Phase of breast phantom of one grape (10 mm in diameter) without skin at 15 receivers at 12.6 GHz with array plane placed at height 540 mm to 549 mm

Hight (mm)	R1	R2	R3	R4	R5	R6	R7	R8	R9	R10	R11	R12	R13	R14	R15
540	-1.64E+02	9.11E+01	-2.21E+01	1.67E+02	-6.14E+01	-1.31E+02	-1.13E+02	-1.27E+02	-8.55E+01	-3.33E+01	5.67E+00	-8.29E+01	6.61E+01	-1.76E+02	1.53E+02
541	-1.60E+02	9.20E+01	-2.28E+01	-4.26E+01	-5.53E+01	-1.49E+02	1.26E+02	-1.29E+02	-7.07E+01	2.68E+01	2.87E+01	-1.39E+02	1.04E+02	-1.71E+02	1.63E+02
542	-1.59E+02	9.40E+01	-2.14E+01	-7.62E+01	-4.83E+01	-1.42E+02	1.22E+02	-7.43E+01	-7.23E+01	1.09E+01	2.22E+01	-9.03E+01	9.03E+01	-1.73E+02	1.63E+02
543	-1.59E+02	8.66E+01	-1.83E+01	1.75E+02	-5.69E+01	-1.28E+02	-1.12E+02	-1.23E+02	-8.10E+01	-2.24E+01	9.81E+00	-8.03E+01	-1.75E+02	-1.74E+02	1.58E+02
544	-1.59E+02	9.26E+01	-1.81E+01	1.73E+02	-6.31E+01	-1.26E+02	-1.36E+02	-1.22E+02	-6.91E+01	-4.93E+01	4.06E+00	-8.85E+01	6.93E+01	-1.77E+02	1.56E+02
545	-1.59E+02	9.17E+01	-1.73E+01	1.75E+02	-7.16E+01	-1.24E+02	-1.42E+02	-1.23E+02	-9.35E+01	-8.21E+01	-1.08E+02	-1.03E+02	1.02E+02	1.77E+02	1.52E+02
546	-1.60E+02	9.31E+01	-1.88E+01	1.80E+02	-7.83E+01	-1.32E+02	-1.43E+02	-1.27E+02	-8.10E+01	-1.15E+02	2.33E+00	-1.18E+02	1.47E+02	1.72E+02	1.50E+02
547	-1.58E+02	9.46E+01	-1.88E+01	-1.78E+02	-8.48E+01	-1.72E+02	-1.58E+02	-1.30E+02	-3.20E+01	1.84E+01	1.40E+01	-1.33E+02	1.41E+02	1.67E+02	1.53E+02
548	-1.57E+02	9.78E+01	-2.09E+01	-1.76E+02	-9.25E+01	-1.45E+02	-1.30E+02	-1.28E+02	-2.60E+01	1.48E+02	2.17E+01	-1.53E+02	1.18E+02	1.64E+02	1.57E+02
549	-1.57E+02	9.85E+01	-2.16E+01	-1.71E+02	-9.25E+01	-1.50E+02	-1.49E+02	-1.28E+02	-3.62E+01	2.11E+01	2.00E+01	-1.65E+02	9.21E+01	1.67E+02	1.59E+02

G.3 Magnitude of breast phantom of two grapes (10 mm and 15 mm in diameter) without skin at 15 receivers at 12.6 GHz with array plane placed at height 540 mm to 550 mm

Hight (mm)	R1	R2	R3	R4	R5	R6	R7	R8	R9	R10	R11	R12	R13	R14	R15
540	-4.37E+01	-4.38E+01	-3.53E+01	-4.91E+01	-5.76E+01	-5.94E+01	-6.23E+01	-4.47E+01	-5.43E+01	-5.69E+01	-4.76E+01	-5.86E+01	-5.46E+01	-4.53E+01	-4.61E+01
541	-3.00E+01	-4.37E+01	-3.54E+01	-4.98E+01	-5.66E+01	-5.90E+01	-6.47E+01	-4.49E+01	-5.68E+01	-5.64E+01	-4.74E+01	-6.48E+01	-5.52E+01	-4.46E+01	-4.57E+01
542	-2.99E+01	-4.36E+01	-3.53E+01	-5.05E+01	-5.45E+01	-6.02E+01	-8.37E+01	-4.47E+01	-5.31E+01	-5.67E+01	-4.78E+01	-5.57E+01	-5.65E+01	-4.39E+01	-4.50E+01
543	-3.00E+01	-4.40E+01	-3.52E+01	-5.13E+01	-5.42E+01	-6.03E+01	-7.38E+01	-4.43E+01	-5.37E+01	-5.71E+01	-4.85E+01	-5.18E+01	-5.76E+01	-4.34E+01	-4.46E+01
544	-3.02E+01	-4.47E+01	-3.49E+01	-5.24E+01	-5.37E+01	-6.00E+01	-6.93E+01	-4.36E+01	-5.67E+01	-5.82E+01	-5.02E+01	-4.89E+01	-5.98E+01	-4.32E+01	-4.53E+01
545	-3.04E+01	-4.51E+01	-3.47E+01	-5.37E+01	-5.42E+01	-5.82E+01	-6.37E+01	-4.34E+01	-6.18E+01	-6.14E+01	-5.06E+01	-4.82E+01	-6.39E+01	-4.36E+01	-4.68E+01
546	-3.05E+01	-4.48E+01	-3.47E+01	-5.38E+01	-5.45E+01	-5.86E+01	-6.33E+01	-4.40E+01	-6.03E+01	-6.38E+01	-5.08E+01	-4.77E+01	-6.51E+01	-4.42E+01	-4.74E+01
547	-3.05E+01	-4.41E+01	-5.42E+01	-5.40E+01	-5.54E+01	-5.60E+01	-6.21E+01	-4.44E+01	-5.72E+01	-6.79E+01	-5.05E+01	-4.82E+01	-6.36E+01	-4.49E+01	-4.76E+01
548	-3.03E+01	-4.35E+01	-3.51E+01	-5.41E+01	-5.55E+01	-5.51E+01	-5.96E+01	-4.54E+01	-5.30E+01	-7.15E+01	-4.99E+01	-4.88E+01	-6.30E+01	-4.59E+01	-4.72E+01
549	-3.00E+01	-4.28E+01	-3.54E+01	-5.46E+01	-5.53E+01	-5.43E+01	-5.73E+01	-4.59E+01	-5.07E+01	-7.82E+01	-5.07E+01	-5.16E+01	-6.50E+01	-4.67E+01	-4.62E+01
550	-2.99E+01	-4.30E+01	-3.55E+01	-5.54E+01	-5.54E+01	-5.34E+01	-5.42E+01	-4.51E+01	-4.93E+01	-8.12E+01	-5.22E+01	-5.45E+01	-6.56E+01	-4.66E+01	-4.58E+01

G.4 Phase of breast phantom of two grapes (10 mm and 15 mm in diameter) without skin at 15 receivers at 12.6 GHz with array plane placed at height 540 mm to 550 mm

Hight (mm)	R1	R2	R3	R4	R5	R6	R7	R8	R9	R10	R11	R12	R13	R14	R15
540	8.91E+01	9.07E+01	-2.21E+01	1.79E+02	-4.87E+01	-1.69E+02	1.29E+02	-1.30E+02	-5.14E+01	3.20E+01	2.77E+01	-1.77E+02	1.18E+02	-1.73E+02	1.62E+02
541	-1.56E+02	9.17E+01	-1.88E+01	1.77E+02	-4.70E+01	-1.63E+02	1.26E+02	-1.25E+02	2.69E+01	2.19E+01	2.35E+01	-1.38E+02	1.09E+02	-1.71E+02	1.64E+02
542	-1.57E+02	9.05E+01	-1.62E+01	1.70E+02	-4.67E+01	-1.60E+02	1.02E+02	-1.18E+02	-6.67E+01	-8.56E-01	1.35E+01	-7.50E+01	8.95E+01	-1.73E+02	1.53E+02
543	-1.59E+02	8.91E+01	-1.61E+01	1.65E+02	-5.47E+01	-1.65E+02	-9.82E+01	-1.18E+02	-7.53E+01	-1.71E+01	1.04E+01	-7.86E+01	7.98E+01	-1.76E+02	1.45E+02
544	-1.59E+02	8.60E+01	-1.54E+01	1.68E+02	-6.05E+01	-1.52E+02	-9.54E+01	-1.21E+02	-8.07E+01	-3.86E+01	8.13E+00	-9.95E+01	6.50E+01	1.78E+02	1.38E+02
545	-1.59E+02	8.99E+01	-1.62E+01	1.72E+02	-6.92E+01	-1.44E+02	-1.06E+02	-1.27E+02	-6.46E+01	-5.44E+01	1.43E+01	-1.14E+02	7.23E+01	1.71E+02	1.36E+02
546	-1.57E+02	9.33E+01	-1.73E+01	1.80E+02	-7.04E+01	-1.38E+02	-1.04E+02	-1.31E+02	-2.11E+01	-7.49E+01	1.89E+01	-1.31E+02	9.97E+01	1.70E+02	1.39E+02
547	-1.56E+02	9.70E+01	1.79E+02	1.75E+02	-7.07E+01	-1.40E+02	-1.03E+02	-1.32E+02	-9.53E+00	-6.62E+01	2.01E+01	-1.41E+02	9.20E+01	1.67E+02	1.45E+02
548	-1.53E+02	9.70E+01	-1.83E+01	-1.77E+02	-7.08E+01	-1.47E+02	-1.07E+02	-1.30E+02	-1.93E+01	-9.40E+01	1.58E+01	-1.57E+02	7.06E+01	1.70E+02	1.52E+02
549	-1.55E+02	9.57E+01	-1.98E+01	-1.76E+02	-7.37E+01	-1.55E+02	-1.17E+02	-1.22E+02	-3.52E+01	-8.20E+01	8.31E+00	-1.65E+02	3.35E+01	1.75E+02	1.54E+02
550	-1.56E+02	8.89E+01	-1.77E+01	-1.68E+02	-7.60E+01	-1.71E+02	-1.38E+02	-1.14E+02	-5.52E+01	1.74E+02	8.32E+00	-1.67E+02	-3.93E+01	-1.74E+02	1.54E+02

G.5 Magnitude of breast phantom of one grape (10 mm in diameter) with skin at 15 receivers at 12.6 GHz with array plane placed at height 540 mm to 580 mm

Height (mm)	R1	R2	R3	R4	R5	R6	R7	R8	R9	R10	R11	R12	R13	R14	R15
540	-2.96E+01	-4.34E+01	-3.57E+01	-5.50E+01	-5.49E+01	2.67E-03	1.35E-03	4.27E-03	2.12E-03	9.03E-04	4.36E-03	2.58E-03	1.75E-03	4.64E-03	6.19E-03
541	3.46E-02	6.53E-03	1.76E-02	2.96E-03	1.55E-03	1.78E-03	1.53E-03	5.73E-03	2.83E-03	1.14E-03	3.10E-03	5.92E-04	4.60E-04	5.37E-03	6.33E-03
542	3.42E-02	7.34E-03	1.73E-02	2.91E-03	1.93E-03	1.62E-03	1.31E-03	6.54E-03	2.86E-03	1.13E-03	2.54E-03	3.07E-04	1.09E-03	5.62E-03	6.15E-03
543	3.38E-02	6.65E-03	1.77E-02	2.85E-03	1.58E-03	1.21E-03	1.43E-03	7.19E-03	2.70E-03	8.36E-04	2.43E-03	1.22E-03	1.03E-03	5.88E-03	5.50E-03
544	3.19E-02	6.13E-03	1.85E-02	2.82E-03	1.29E-03	7.72E-04	1.53E-03	7.34E-03	2.36E-03	8.30E-04	2.51E-03	1.84E-03	1.32E-03	5.84E-03	4.76E-03
545	3.04E-02	5.66E-03	1.88E-02	2.89E-03	1.00E-03	1.02E-04	1.48E-03	7.58E-03	2.14E-03	8.59E-04	3.16E-03	2.24E-03	2.01E-03	6.12E-03	3.96E-03
546	2.85E-02	5.13E-03	1.89E-02	3.16E-03	9.75E-04	7.03E-04	1.33E-03	7.38E-03	1.66E-03	8.90E-04	3.84E-03	2.65E-03	2.68E-03	5.80E-03	3.20E-03
547	2.91E-02	6.50E-03	1.70E-02	3.22E-03	2.05E-03	2.22E-03	8.02E-04	5.42E-03	7.60E-04	2.16E-03	5.49E-03	2.10E-03	3.74E-03	6.24E-03	5.01E-03
548	2.78E-02	6.08E-03	1.72E-02	2.38E-03	2.11E-03	3.02E-03	2.38E-03	6.90E-03	8.95E-04	1.97E-03	6.44E-03	1.75E-03	4.74E-03	7.95E-03	6.17E-03
549	3.43E-02	8.00E-03	1.75E-02	1.61E-03	2.29E-03	2.62E-03	4.03E-04	5.64E-03	1.26E-03	1.98E-03	4.08E-03	2.49E-03	3.05E-03	6.94E-03	6.28E-03
550	3.40E-02	8.16E-03	1.73E-02	1.32E-03	1.93E-03	2.43E-03	5.91E-04	6.24E-03	1.13E-03	1.85E-03	3.27E-03	3.37E-03	2.60E-03	6.91E-03	5.66E-03
551	3.30E-02	7.90E-03	1.77E-02	1.27E-03	1.70E-03	2.19E-03	8.88E-04	6.90E-03	9.67E-04	1.49E-03	2.47E-03	3.96E-03	2.14E-03	6.63E-03	5.05E-03
552	3.17E-02	7.40E-03	1.82E-02	1.66E-03	1.12E-03	1.82E-03	9.71E-04	7.39E-03	1.02E-03	1.14E-03	1.81E-03	4.40E-03	1.50E-03	6.41E-03	4.01E-03
553	2.97E-02	6.67E-03	1.84E-02	2.59E-03	8.83E-04	1.45E-03	9.90E-04	7.45E-03	9.44E-04	7.54E-04	2.15E-03	4.60E-03	7.06E-04	5.98E-03	2.93E-03

554	**2.83E-02**	**6.42E-03**	**1.81E-02**	**3.14E-03**	**2.97E-04**	**9.43E-04**	**1.15E-03**	**7.08E-03**	**1.19E-03**	**5.30E-04**	**2.78E-03**	**4.71E-03**	**6.65E-04**	**5.36E-03**	**2.74E-03**
555	**2.83E-02**	**6.32E-03**	**1.77E-02**	**3.63E-03**	**5.77E-04**	**7.96E-04**	**1.33E-03**	**6.59E-03**	**1.61E-03**	**3.38E-04**	**3.29E-03**	**4.63E-03**	**8.44E-04**	**4.72E-03**	**3.61E-03**
556	**2.98E-02**	**6.60E-03**	**1.65E-02**	**3.92E-03**	**1.41E-03**	**8.49E-04**	**1.61E-03**	**5.93E-03**	**2.07E-03**	**3.90E-04**	**4.08E-03**	**3.80E-03**	**1.37E-03**	**4.09E-03**	**5.31E-03**
557	**3.11E-02**	**6.52E-03**	**1.65E-02**	**4.03E-03**	**1.75E-03**	**1.17E-03**	**1.52E-03**	**5.65E-03**	**2.33E-03**	**5.02E-04**	**4.53E-03**	**2.68E-03**	**1.49E-03**	**4.34E-03**	**6.19E-03**
558	**3.27E-02**	**6.93E-03**	**1.63E-02**	**3.99E-03**	**1.95E-03**	**1.19E-03**	**1.49E-03**	**5.47E-03**	**2.49E-03**	**6.77E-04**	**4.63E-03**	**1.44E-03**	**1.32E-03**	**4.66E-03**	**6.67E-03**
559	**3.37E-02**	**7.11E-03**	**1.69E-02**	**3.53E-03**	**2.01E-03**	**1.37E-03**	**1.50E-03**	**5.84E-03**	**2.66E-03**	**6.06E-04**	**4.45E-03**	**1.01E-03**	**1.16E-03**	**5.46E-03**	**6.83E-03**
560	**3.33E-02**	**6.91E-03**	**1.75E-02**	**2.93E-03**	**2.07E-03**	**1.34E-03**	**1.43E-03**	**6.25E-03**	**2.52E-03**	**4.04E-04**	**4.03E-03**	**1.97E-03**	**9.03E-04**	**5.99E-03**	**6.37E-03**
561	**3.29E-02**	**6.72E-03**	**1.75E-02**	**2.77E-03**	**1.91E-03**	**1.19E-03**	**1.37E-03**	**6.69E-03**	**2.37E-03**	**2.51E-04**	**3.66E-03**	**2.89E-03**	**4.38E-04**	**6.35E-03**	**5.86E-03**
562	**3.19E-02**	**6.53E-03**	**1.83E-02**	**2.27E-03**	**1.54E-03**	**1.08E-03**	**1.19E-03**	**6.92E-03**	**1.96E-03**	**1.50E-04**	**3.26E-03**	**4.09E-03**	**4.07E-04**	**6.78E-03**	**4.87E-03**
563	**3.25E-02**	**6.54E-03**	**1.83E-02**	**2.51E-03**	**1.65E-03**	**1.02E-03**	**1.47E-03**	**6.81E-03**	**2.43E-03**	**1.05E-04**	**3.66E-03**	**3.29E-03**	**2.18E-04**	**6.52E-03**	**5.40E-03**
564	**3.17E-02**	**6.37E-03**	**1.86E-02**	**2.44E-03**	**1.51E-03**	**8.78E-04**	**1.44E-03**	**6.93E-03**	**2.27E-03**	**1.76E-04**	**3.70E-03**	**3.87E-03**	**4.05E-04**	**6.66E-03**	**4.79E-03**
565	**3.07E-02**	**6.07E-03**	**1.88E-02**	**2.55E-03**	**1.18E-03**	**8.11E-04**	**1.31E-03**	**6.85E-03**	**1.85E-03**	**4.22E-04**	**3.68E-03**	**4.51E-03**	**7.13E-04**	**6.71E-03**	**3.93E-03**
566	**2.95E-02**	**5.89E-03**	**1.87E-02**	**2.61E-03**	**8.92E-04**	**8.34E-04**	**1.05E-03**	**6.75E-03**	**1.27E-03**	**6.00E-04**	**3.71E-03**	**4.91E-03**	**1.12E-03**	**6.71E-03**	**3.25E-03**
567	**2.88E-02**	**5.77E-03**	**1.84E-02**	**2.65E-03**	**8.48E-04**	**1.36E-03**	**9.49E-04**	**6.50E-03**	**7.23E-04**	**8.48E-04**	**3.71E-03**	**5.04E-03**	**1.68E-03**	**6.55E-03**	**2.98E-03**
568	**2.83E-02**	**5.78E-03**	**1.82E-02**	**2.73E-03**	**1.16E-03**	**1.75E-03**	**6.76E-04**	**6.12E-03**	**2.05E-04**	**1.03E-03**	**3.72E-03**	**5.11E-03**	**2.07E-03**	**6.31E-03**	**3.04E-03**
569	**2.87E-02**	**6.24E-03**	**1.76E-02**	**2.64E-03**	**1.36E-03**	**2.12E-03**	**3.66E-04**	**5.69E-03**	**2.48E-04**	**1.33E-03**	**3.78E-03**	**4.94E-03**	**2.28E-03**	**6.01E-03**	**3.65E-03**
570	**2.98E-02**	**6.82E-03**	**1.68E-02**	**2.57E-03**	**1.73E-03**	**2.35E-03**	**2.53E-04**	**5.24E-03**	**9.01E-04**	**1.48E-03**	**3.68E-03**	**4.60E-03**	**2.46E-03**	**5.52E-03**	**4.54E-03**
571	**3.00E-02**	**7.13E-03**	**1.63E-02**	**2.67E-03**	**1.84E-03**	**2.42E-03**	**3.21E-04**	**5.05E-03**	**1.29E-03**	**1.65E-03**	**3.72E-03**	**3.94E-03**	**2.58E-03**	**5.38E-03**	**5.17E-03**

572	**3.20E-02**	**7.31E-03**	**1.60E-02**	**2.56E-03**	**2.04E-03**	**2.60E-03**	**4.30E-04**	**4.90E-03**	**1.56E-03**	**1.73E-03**	**3.57E-03**	**3.49E-03**	**2.66E-03**	**5.49E-03**	**5.74E-03**
573	**3.31E-02**	**7.40E-03**	**1.60E-02**	**2.27E-03**	**2.07E-03**	**2.76E-03**	**5.36E-04**	**5.09E-03**	**1.87E-03**	**1.77E-03**	**3.27E-03**	**2.85E-03**	**2.68E-03**	**5.70E-03**	**5.93E-03**
574	**3.39E-02**	**7.49E-03**	**1.62E-02**	**2.01E-03**	**2.18E-03**	**2.75E-03**	**7.86E-04**	**5.46E-03**	**2.02E-03**	**1.59E-03**	**2.76E-03**	**2.32E-03**	**2.67E-03**	**5.88E-03**	**6.20E-03**
575	**3.43E-02**	**7.40E-03**	**1.68E-02**	**1.68E-03**	**2.02E-03**	**2.67E-03**	**9.62E-04**	**6.18E-03**	**2.23E-03**	**1.43E-03**	**2.15E-03**	**1.80E-03**	**2.48E-03**	**6.05E-03**	**6.21E-03**
576	**3.43E-02**	**7.36E-03**	**1.72E-02**	**1.76E-03**	**1.86E-03**	**2.47E-03**	**1.13E-03**	**6.66E-03**	**2.32E-03**	**1.29E-03**	**1.66E-03**	**1.77E-03**	**2.33E-03**	**6.04E-03**	**6.03E-03**
577	**3.40E-02**	**7.18E-03**	**1.78E-02**	**1.72E-03**	**1.52E-03**	**2.07E-03**	**1.33E-03**	**7.25E-03**	**2.47E-03**	**1.13E-03**	**1.62E-03**	**1.73E-03**	**2.08E-03**	**5.98E-03**	**5.53E-03**
578	**3.28E-02**	**6.94E-03**	**1.81E-02**	**2.26E-03**	**1.22E-03**	**1.61E-03**	**1.27E-03**	**7.89E-03**	**2.29E-03**	**7.00E-04**	**2.13E-03**	**1.93E-03**	**1.90E-03**	**5.77E-03**	**4.65E-03**
579	**3.19E-02**	**6.62E-03**	**1.82E-02**	**2.51E-03**	**8.29E-04**	**1.13E-03**	**1.24E-03**	**8.15E-03**	**2.11E-03**	**4.89E-04**	**2.84E-03**	**2.18E-03**	**1.95E-03**	**5.60E-03**	**4.14E-03**

G.6 Phase of breast phantom of one grape (10 mm in diameter) with skin at 15 receivers at 12.6 GHz with array plane placed at height 540 mm to 580 mm

Height (mm)	R1	R2	R3	R4	R5	R6	R7	R8	R9	R10	R11	R12	R13	R14	R15
540	-1.55E+02	9.11E+01	-2.11E+01	-3.24E+01	-3.20E+01	-1.74E+02	-1.36E+02	-1.20E+02	-5.12E+01	-2.83E+01	2.69E+00	1.56E+02	7.78E+01	-1.79E+02	1.62E+02
541	-1.59E+02	8.87E+01	-1.66E+01	1.59E+02	-4.03E+01	1.70E+02	-1.59E+02	-1.03E+02	-7.85E+01	-9.90E+01	-7.89E+00	6.65E+01	-2.69E-01	-1.68E+02	1.48E+02
542	-1.59E+02	8.54E+01	-1.40E+01	1.70E+02	-5.06E+01	1.74E+02	-1.59E+02	-1.13E+02	-6.94E+01	-9.52E+01	2.12E+01	-6.97E+01	-3.00E+01	-1.68E+02	1.43E+02
543	-1.60E+02	7.96E+01	-1.37E+01	1.70E+02	-5.52E+01	1.61E+02	-1.69E+02	-1.15E+02	-7.73E+01	-1.25E+02	3.34E+01	-8.27E+01	-7.48E+01	-1.70E+02	1.37E+02
544	-1.62E+02	8.21E+01	-1.45E+01	1.76E+02	-5.63E+01	1.47E+02	1.78E+02	-1.18E+02	-8.58E+01	-1.63E+02	4.55E+01	-9.97E+01	-1.22E+02	-1.74E+02	1.30E+02
545	-1.63E+02	8.26E+01	-1.73E+01	1.78E+02	-4.66E+01	-1.44E+02	1.61E+02	-1.23E+02	-9.48E+01	1.54E+02	5.00E+01	-1.14E+02	-1.54E+02	-1.75E+02	1.34E+02
546	-1.61E+02	9.33E+01	-1.97E+01	1.77E+02	-1.46E+01	-6.09E+01	1.46E+02	-1.28E+02	-9.99E+01	1.10E+02	4.98E+01	-1.29E+02	1.77E+02	-1.76E+02	1.49E+02
547	-1.51E+02	1.09E+02	-2.01E+01	1.66E+02	-1.47E+01	-1.19E+02	7.17E+01	-1.38E+02	-9.03E+01	2.12E+01	2.30E+01	-1.49E+02	1.05E+02	-1.78E+02	1.72E+02
548	-1.50E+02	1.07E+02	-1.75E+01	1.63E+02	-3.72E+01	-1.45E+02	2.88E+01	-1.26E+02	-7.44E+01	-1.19E+01	7.31E+00	-1.24E+02	6.85E+01	1.79E+02	1.60E+02
549	-1.56E+02	9.83E+01	-1.72E+01	1.61E+02	-5.67E+01	-1.71E+02	-4.24E+01	-1.14E+02	-8.64E+01	-4.07E+01	-4.18E+00	-8.62E+01	3.27E+01	1.78E+02	1.42E+02
550	-1.58E+02	9.37E+01	-1.81E+01	1.68E+02	-6.49E+01	1.79E+02	-5.62E+01	-1.12E+02	-8.38E+01	-5.75E+01	-8.76E+00	-9.41E+01	1.34E+01	1.76E+02	1.36E+02
551	-1.60E+02	9.13E+01	-1.72E+01	-1.72E+02	-7.16E+01	1.68E+02	-6.39E+01	-1.13E+02	-8.19E+01	-6.78E+01	-7.17E+00	-1.04E+02	-4.00E+00	1.73E+02	1.31E+02
552	-1.62E+02	8.73E+01	-1.85E+01	-1.55E+02	-8.26E+01	1.63E+02	-8.96E+01	-1.18E+02	-6.87E+01	-8.73E+01	1.56E+01	-1.17E+02	-3.66E+01	1.69E+02	1.30E+02
553	-1.61E+02	8.97E+01	-1.91E+01	-1.51E+02	-9.11E+01	1.59E+02	-8.89E+01	-1.25E+02	-5.53E+01	-8.83E+01	3.75E+01	-1.30E+02	-8.07E+01	1.66E+02	1.38E+02

554	-1.58E+02	9.17E+01	-2.15E+01	-1.55E+02	-5.50E+01	1.68E+02	-1.02E+02	-1.29E+02	-3.46E+01	-8.14E+01	4.34E+01	-1.47E+02	-1.52E+02	1.62E+02	1.62E+02
555	-1.55E+02	9.40E+01	-2.20E+01	-1.59E+02	-1.32E+00	-1.65E+02	-1.05E+02	-1.32E+02	-3.32E+01	-7.65E+01	4.24E+01	-1.64E+02	1.65E+02	1.65E+02	1.78E+02
556	-1.56E+02	9.19E+01	-2.63E+01	-1.74E+02	2.49E+00	-1.43E+02	-1.33E+02	-1.33E+02	-4.59E+01	-4.81E+01	3.54E+01	1.63E+02	1.40E+02	1.76E+02	1.76E+02
557	-1.53E+02	9.65E+01	-2.13E+01	-1.79E+02	-6.83E+00	-1.38E+02	-1.43E+02	-1.29E+02	-5.84E+01	-5.00E+01	3.09E+01	1.42E+02	1.23E+02	-1.75E+02	1.71E+02
558	-1.53E+02	9.85E+01	-1.76E+01	1.73E+02	-1.78E+01	-1.54E+02	-1.56E+02	-1.24E+02	-6.88E+01	-3.90E+01	2.33E+01	1.13E+02	1.06E+02	-1.67E+02	1.62E+02
559	-1.55E+02	9.68E+01	-1.63E+01	1.68E+02	-3.53E+01	-1.57E+02	-1.73E+02	-1.20E+02	-8.32E+01	-5.86E+01	1.35E+01	4.49E+00	7.34E+01	-1.67E+02	1.50E+02
560	-1.56E+02	9.65E+01	-1.51E+01	1.67E+02	-4.24E+01	-1.63E+02	-1.80E+02	-1.18E+02	-9.47E+01	-6.92E+01	9.19E+00	-4.55E+01	6.39E+01	-1.67E+02	1.42E+02
561	-1.57E+02	9.40E+01	-1.56E+01	1.66E+02	-5.03E+01	-1.66E+02	1.74E+02	-1.19E+02	-1.07E+02	-7.78E+01	8.96E+00	-6.16E+01	6.19E+01	-1.69E+02	1.36E+02
562	-1.60E+02	9.24E+01	-1.79E+01	1.67E+02	-5.36E+01	-1.62E+02	1.62E+02	-1.21E+02	-1.26E+02	3.56E+01	1.23E+01	-8.27E+01	9.85E+01	-1.73E+02	1.29E+02
563	-1.59E+02	9.18E+01	-1.57E+01	1.66E+02	-5.21E+01	-1.65E+02	1.70E+02	-1.20E+02	-1.11E+02	-1.25E+02	1.54E+01	-6.75E+01	8.69E+01	-1.71E+02	1.32E+02
564	-1.60E+02	9.29E+01	-1.72E+01	1.68E+02	-5.53E+01	-1.71E+02	1.61E+02	-1.23E+02	-1.18E+02	9.67E+01	1.86E+01	-7.58E+01	1.36E+02	-1.72E+02	1.30E+02
565	-1.62E+02	9.21E+01	-2.01E+01	1.68E+02	-5.72E+01	-1.55E+02	1.50E+02	-1.26E+02	-1.30E+02	7.80E+01	1.93E+01	-8.83E+01	1.50E+02	-1.76E+02	1.31E+02
566	-1.59E+02	9.59E+01	-2.00E+01	1.74E+02	-4.95E+01	-1.31E+02	1.35E+02	-1.29E+02	-1.42E+02	6.98E+01	1.97E+01	-1.03E+02	1.39E+02	-1.80E+02	1.36E+02
567	-1.58E+02	9.81E+01	-2.29E+01	1.76E+02	-2.79E+01	-1.09E+02	1.20E+02	-1.31E+02	-1.52E+02	5.83E+01	1.81E+01	-1.16E+02	1.33E+02	1.76E+02	1.50E+02
568	-1.55E+02	1.03E+02	-2.19E+01	1.77E+02	-1.42E+01	-1.10E+02	1.12E+02	-1.32E+02	-1.73E+02	4.35E+01	1.70E+01	-1.29E+02	1.22E+02	1.75E+02	1.65E+02
569	-1.51E+02	1.06E+02	-2.23E+01	1.75E+02	-1.02E+01	-1.17E+02	8.20E+01	-1.30E+02	4.53E+01	3.13E+01	1.68E+01	-1.39E+02	1.10E+02	1.77E+02	1.75E+02
570	-1.48E+02	1.07E+02	-2.10E+01	1.75E+02	-1.09E+01	-1.28E+02	-1.78E+01	-1.25E+02	1.34E+01	5.84E+00	1.32E+01	-1.54E+02	9.24E+01	1.79E+02	1.78E+02
571	-1.47E+02	1.07E+02	-1.85E+01	1.73E+02	-1.41E+01	-1.35E+02	-4.23E+01	-1.21E+02	-4.07E+00	-3.18E+00	9.37E+00	-1.59E+02	7.72E+01	-1.78E+02	1.76E+02

572	**-1.46E+02**	**1.07E+02**	**-1.62E+01**	**1.79E+02**	**-2.09E+01**	**-1.47E+02**	**-5.99E+01**	**-1.15E+02**	**-1.54E+01**	**-1.57E+01**	**7.03E+00**	**-1.65E+02**	**6.66E+01**	**-1.76E+02**	**1.72E+02**
573	**-1.48E+02**	**1.04E+02**	**-1.50E+01**	**1.75E+02**	**-2.85E+01**	**-1.53E+02**	**-9.34E+01**	**-1.11E+02**	**-2.61E+01**	**-2.42E+01**	**2.37E+00**	**-1.66E+02**	**5.11E+01**	**-1.74E+02**	**1.67E+02**
574	**-1.48E+02**	**1.02E+02**	**-1.25E+01**	**1.80E+02**	**-3.49E+01**	**-1.63E+02**	**-1.01E+02**	**-1.07E+02**	**-3.26E+01**	**-3.61E+01**	**1.16E+00**	**-1.63E+02**	**3.70E+01**	**-1.72E+02**	**1.60E+02**
575	**-1.50E+02**	**9.96E+01**	**-9.49E+00**	**-1.76E+02**	**-4.28E+01**	**-1.70E+02**	**-1.14E+02**	**-1.05E+02**	**-4.26E+01**	**-4.60E+01**	**1.64E+00**	**-1.53E+02**	**1.26E+01**	**-1.74E+02**	**1.53E+02**
576	**-1.53E+02**	**9.65E+01**	**-1.03E+01**	**-1.72E+02**	**-5.08E+01**	**1.77E+02**	**-1.17E+02**	**-1.05E+02**	**4.95E+01**	**-5.98E+01**	**1.46E+01**	**-1.43E+02**	**-5.30E+00**	**-1.74E+02**	**1.47E+02**
577	**-1.54E+02**	**9.52E+01**	**-1.07E+01**	**-1.65E+02**	**-6.02E+01**	**1.67E+02**	**-1.26E+02**	**-1.06E+02**	**-5.85E+01**	**-7.45E+01**	**4.58E+01**	**-1.31E+02**	**-3.25E+01**	**-1.76E+02**	**1.41E+02**
578	**-1.56E+02**	**9.30E+01**	**-1.06E+01**	**-1.57E+02**	**-6.78E+01**	**1.57E+02**	**-1.35E+02**	**-1.11E+02**	**-6.72E+01**	**-8.89E+01**	**6.67E+01**	**-1.21E+02**	**-6.52E+01**	**-1.79E+02**	**1.38E+02**
579	**-1.58E+02**	**9.19E+01**	**-1.23E+01**	**-1.57E+02**	**-6.87E+01**	**1.49E+02**	**-1.47E+02**	**-1.15E+02**	**-7.19E+01**	**-1.10E+02**	**7.02E+01**	**-1.19E+02**	**-9.13E+01**	**-1.80E+02**	**1.37E+02**

Appendix H Experimental Results: Group III

H.1 Magnitude of breast phantom of two grapes (10 mm and 15 mm in diameter) with skin under regular spaced array at 12.6 GHz

R1	R2	R3	R4	R5	R6	R7	R8	R9	R10	R11	R12	R13	R14	R15
1.25E-02	2.75E-03	1.19E-02	1.35E-03	8.56E-04	2.58E-03	3.03E-03	3.35E-03	2.57E-03	8.13E-04	1.67E-03	7.34E-03	9.46E-04	7.84E-04	4.83E-03

H.2 Phase of breast phantom of two grapes (10 mm and 15 mm in diameter) with skin under regular spaced array at 12.6 GHz

R1	R2	R3	R4	R5	R6	R7	R8	R9	R10	R11	R12	R13	R14	R15
-1.24E+02	7.19E+01	2.28E+01	1.63E+02	-8.09E+01	8.99E+01	1.10E+02	-1.11E+02	-3.66E+00	2.29E+01	-9.46E+01	8.45E+01	1.72E+02	-9.11E+00	5.52E+01

H.3 Magnitude of breast phantom of two grapes (10 mm and 15 mm in diameter) with skin under spiral array at 12.6 GHz

R1	R2	R3	R4	R5	R6	R7	R8	R9	R10	R11	R12	R13	R14	R15
2.72E-02	5.79E-03	1.75E-02	2.85E-03	2.01E-03	7.08E-04	2.12E-03	4.51E-03	1.19E-03	2.44E-03	3.84E-03	3.23E-03	3.54E-03	3.90E-03	7.13E-03

H.4 Phase of breast phantom of two grapes (10 mm and 15 mm in diameter) with skin under spiral array at 12.6 GHz

R1	R2	R3	R4	R5	R6	R7	R8	R9	R10	R11	R12	R13	R14	R15
-1.65E+02	1.04E+02	-2.76E+01	1.68E+02	4.24E+01	-1.51E+02	7.60E+01	-1.52E+02	1.14E+01	5.23E+01	1.43E+01	-1.51E+02	1.34E+02	1.42E+02	1.51E+02

H.5 Magnitude of breast phantom of two grapes (10 mm and 15 mm in diameter) with skin under random array at 12.6 GHz

R1	R2	R3	R4	R5	R6	R7	R8	R9	R10	R11	R12	R13	R14	R15
2.42E-03	2.39E-03	1.77E-03	7.04E-04	5.71E-04	1.10E-03	4.99E-03	5.08E-03	1.05E-02	1.81E-03	2.40E-03	1.43E-03	1.18E-02	6.31E-04	5.48E-03

H.6 Phase of breast phantom of two grapes (10 mm and 15 mm in diameter) with skin under random array at 12.6 GHz

R1	R2	R3	R4	R5	R6	R7	R8	R9	R10	R11	R12	R13	R14	R15
8.39E+01	-9.70E+01	-1.65E+02	1.16E+02	-2.89E+01	1.75E+02	1.34E+02	1.60E+02	-1.65E+02	8.80E+01	-7.99E+01	9.15E+01	-3.30E+01	-8.86E+01	1.46E+01

Appendix I Experimental Results: Group IV

I.1 Magnitude of breast phantom of three blueberries (4 mm, 5 mm, 7mm in diameter) with skin under random array at 12.6 GHz

R1	R2	R3	R4	R5	R6	R7	R8	R9	R10	R11	R12	R13	R14	R15
3.80E-03	2.54E-03	2.43E-03	1.66E-03	3.01E-03	2.04E-03	3.84E-03	3.21E-03	1.04E-02	1.51E-03	2.39E-03	4.29E-03	1.13E-02	2.66E-03	7.47E-03

I.2 Phase of breast phantom of three blueberries (4 mm, 5 mm, 7mm in diameter) with skin under random array at 12.6 GHz

R1	R2	R3	R4	R5	R6	R7	R8	R9	R10	R11	R12	R13	R14	R15
1.04E+02	9.65E+00	1.03E+02	1.05E+02	3.56E+01	6.09E+01	1.16E+02	1.29E+02	-1.37E+02	1.87E+01	-8.28E+01	8.50E+01	-4.71E+01	-1.02E+02	6.43E+01

I.3 Magnitude of breast phantom of two cucumbers with skin under random array at 12.6 GHz

R1	R2	R3	R4	R5	R6	R7	R8	R9	R10	R11	R12	R13	R14	R15
3.98E-03	2.39E-03	2.24E-03	1.60E-03	2.99E-03	2.17E-03	3.96E-03	2.99E-03	1.03E-02	1.73E-03	2.56E-03	4.25E-03	1.14E-02	2.57E-03	7.54E-03

I.4 Phase of breast phantom of two cucumbers with skin under random array at 12.6 GHz

R1	R2	R3	R4	R5	R6	R7	R8	R9	R10	R11	R12	R13	R14	R15
1.04E+02	1.81E+01	1.06E+02	1.01E+02	4.52E+01	6.39E+01	1.16E+02	1.30E+02	-1.37E+02	1.40E+01	-7.37E+01	8.48E+01	-4.77E+01	-9.71E+01	6.32E+01

Appendix J Experimental Results: Group V

J.1 Magnitude of breast phantom of one blueberry (9 mm in diameter) with skin under random array at 12.6 GHz

R1	R2	R3	R4	R5	R6	R7	R8	R9	R10	R11	R12	R13	R14	R15
2.72E-03	1.30E-03	7.41E-04	8.64E-04	1.72E-03	3.53E-04	2.54E-03	4.20E-03	1.10E-02	2.37E-03	2.22E-03	5.53E-04	1.16E-02	3.02E-04	6.04E-03

J.2 Phase of breast phantom of one blueberry (9mm in diameter) with skin under random array at 12.6 GHz

R1	R2	R3	R4	R5	R6	R7	R8	R9	R10	R11	R12	R13	R14	R15
6.53E+01	-5.95E+01	-1.64E+02	1.13E+02	-3.23E+01	1.40E+02	1.41E+02	1.40E+02	-1.63E+02	6.25E+01	-9.40E+01	1.49E+02	-5.17E+01	-9.41E+01	7.00E+00

J.3 Magnitude of breast phantom of one grape (7 mm in diameter) with skin under random array at 12.6 GHz

R1	R2	R3	R4	R5	R6	R7	R8	R9	R10	R11	R12	R13	R14	R15
2.41E-03	1.81E-03	9.92E-04	9.04E-04	1.85E-03	2.47E-04	2.74E-03	3.73E-03	1.11E-02	1.89E-03	2.24E-03	1.55E-03	1.10E-02	5.20E-04	6.22E-03

J.4 Phase of breast phantom of one grape (7 mm in diameter) with skin under random array at 12.6 GHz

R1	R2	R3	R4	R5	R6	R7	R8	R9	R10	R11	R12	R13	R14	R15
7.99E+01	-9.25E+01	-1.28E+02	8.15E+01	-1.35E+01	-1.37E+02	1.51E+02	1.46E+02	-1.67E+02	7.33E+01	-8.98E+01	5.16E+01	-5.06E+01	-6.35E+01	-1.26E+00

J.5 Magnitude of breast phantom of three grapes (10 mm, 10 mm and 15 mm in diameter) with skin under random array at 12.6 GHz

R1	R2	R3	R4	R5	R6	R7	R8	R9	R10	R11	R12	R13	R14	R15
2.57E-03	2.41E-03	1.70E-03	8.64E-04	8.33E-04	4.22E-04	4.48E-03	4.25E-03	1.05E-02	5.25E-04	3.28E-03	1.34E-03	1.14E-02	9.16E-04	6.03E-03

J.6 Phase of breast phantom of three grapes (10 mm, 10 mm and 15 mm in diameter) with skin under random array at 12.6 GHz

R1	R2	R3	R4	R5	R6	R7	R8	R9	R10	R11	R12	R13	R14	R15
7.51E+01	-8.39E+01	-1.64E+02	7.66E+01	-1.80E+01	-1.71E+02	1.32E+02	1.65E+02	-1.61E+02	4.71E+01	-7.04E+01	5.44E+01	-3.83E+01	-6.78E+01	1.09E+01

Conference Paper 1

Holographic Microwave Imaging Array for Early Breast Cancer Detection

Lulu Wang Ray Simpkin Al-Jumaily, A. M.

Status: Published 2012

Conference: 2012 ASME International Mechanical Engineering Congress & Exposition

November 9-15, 2012 Houston, Texas, United States

Proceedings of IMECE2012
2012 ASME International Mechanical Engineering Congress & Exposition
November 9-15, 2012 Houston, Texas, United States

IMECE2012-8591

HOLOGRAPHIC MICROWAVE IMAGING ARRAY FOR EARLY BREAST CANCER DETECTION

Lulu Wang
luwang@aut.ac.nz
Institute of Biomedical Technologies
Auckland University of Technology
Auckland, New Zealand

Ray Simpkin
r.simpkin@irl.cri.nz
Medical Device Technology
Industrial Research Limited
Auckland, New Zealand

Al-Jumaily, A. M.
ahmed.al-jumaily@aut.ac.nz
Institute of Biomedical Technologies
Auckland University of Technology
Auckland, New Zealand

Abstract

This paper presents a new Holographic Microwave Imaging Array (HMIA) technique for early breast cancer detection, which is based on microwave holography and aperture synthesis imaging techniques. Using published data for the dielectric properties of normal breast tissues and malignant tumours, a two-dimensional (2D) mathematical model was developed under the MATLAB environment to demonstrate the proposed imaging technique. The computer simulations showed that tumours as small as 2 mm in diameter anywhere within the breast could be successfully detected. The significant imaging improvement was achieved by optimizing antenna array configurations to offer the best possibility of detecting tumours of various size, shape and position.

Keywords— Microwave Imaging, Holographic Microwave Imaging Array, Breast Cancer Detection, Interferometry

I INTRODUCTION

Breast cancer is the most frequently diagnosed cancer and the second leading cause of cancer death among females [1]. Early detection of breast cancer by regular breast screening detection with treatment has been shown to sharply reduce the breast cancer related mortality and increase the survival rate [2]. Medical imaging techniques [3] have become essential elements in the early detection and diagnosis of breast cancer. Although X-ray mammography is the current gold-standard medical imaging tool and offers several obvious advantages, however, it also has several short comings. These include missing approximately 10%-30% of all breast cancers [4-5].

Microwave imaging is one of the most promising complimentary techniques to X-ray mammography for early detection of breast cancer. Whereas X-rays detect structural changes in tissue cells, microwaves detect changes in dielectric properties that occur before the structural changes occur [6]. The idea has been to exploit the differences in dielectric permittivity of various human tissues that cause scattering of radio waves [7-9]. It has been shown that malignant and healthy tissues have different dielectric properties due to the higher water content in cancerous tissue [10]. Normal breast tissue, which is mostly fatty tissue, is relatively transparent to microwaves up to frequencies of 10 GHz. So far, the most developed approach exploits variations of Synthetic Aperture RADAR (SAR) techniques [7, 11-12]. However, difficulties include large reflections of the radio pulse from skin, and very high cost of ultra-high speed digital electronics required for imaging in real-time.

In this paper, a Holographic Microwave Imaging Array (HMIA) for early breast cancer detection is addressed based on a real-time aperture synthesis imaging technique. Compared to SAR, the holographic microwave technique [13-15] does not require expensive ultra-high speed electronics, as narrow-band signal is used enabling real-time imaging at significantly lower cost [16]. To demonstrate that HMIA can produce good quality images, a MATLAB computer model was

developed. Computer simulations carried out for the selected array configuration are presented. The rest of the paper is organized as follows. Section II describes the methodology of the proposed HMIA technique. Section III presents the theory and Section IV details the simulation, results with discussion and conclusions are drawn in Section V and Section VI.

II METHODOLOGY

A contrast in permittivity between cancerous and healthy tissues causes some of the incident microwave radiation to be back-scattered. This back-scattered radiation can be then received by an array of small microwave antennas and analyzed. An image of the breast can be obtained based on the interferometric aperture synthesis technique, which measures all cross-correlations between the back-scattered signals collected by pairs of small antennas and recovers the breast image by processing these correlation measurements (see Fig.1).

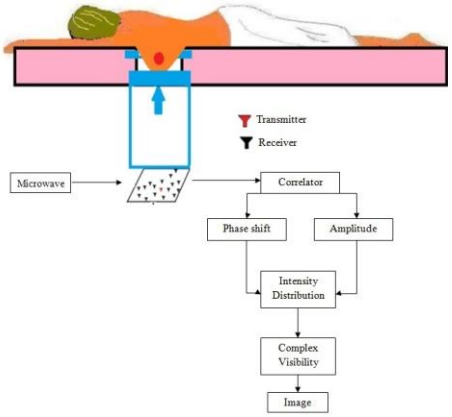

Fig. 1: HOLOGRAPHIC MICROWAVE IMAGING ARRAY SYSTEM

III THEORY

Fig.2 shows a schematic of HMIA system. A known incident field is transmitted by a transmitter and the response is measured on 12 receivers. In Fig.2 (A) the background medium (fat tissue), in which the microwave imaging system is embedded, is characterized by the permittivity, ε_{bg}, and conductivity, σ_{bg}, and the rectangle area in the centre of the antenna group represents the imaging domain. This domain is irradiated by one transmitting antenna (red) and the total field is measured by 12 receiving antennas (black) positioned 500 mm away from the domain. When an object (tumour) with contrast in the constitutive parameters, ε_{obj}, and conductivity, σ_{obj}, is positioned inside the imaging domain, a scattered field will arise (see Fig.2 (B)). The total field, E_{tot}, is the sum of the incident field, E_{inc}, and the back-scattered field, E_{scat}:

$$E_{tot} = E_{inc} + E_{scat} \tag{1}$$

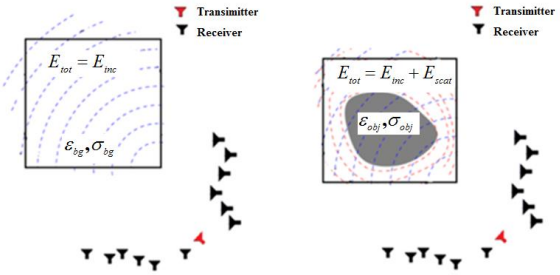

(A) (B)

Fig. 2: SCHEMATIC OF HMIA SYSTEM (A) TUMOUR FREE SYSTEM (B) TUMOUR CONTAINED SYSTEM

HMIA measures the scattered radiation of the breast, which is composed of a set of correlation interferometer pairs. The electromagnetic signals received by each pair are cross correlated to get the so called visibility function. The geometry of a three-dimensional (3D) HMIA imaging is shown in Fig.3 where x, y and z represent antenna locations in the array plane. If a point $P(x, y, z)$ is assumed in the breast, under far-field conditions, the visibility function of the electric field for two antennas located at r_1 and r_2 is defined as:

$$V(\underline{r_1}, \underline{r_2}) = < \underline{E_{scat}}\left(\underline{r_1}\right) \cdot \underline{E^*_{scat}}(\underline{r_2}) > \tag{2}$$

Where the asterisk denotes the complex conjugate and $\langle\rangle$ stands for the expected value (time average).

Equation (2) can be written as:

$$\begin{aligned} &V(\underline{r_1}, \underline{r_2}) \\ &= \left(\frac{k_0^2}{4\pi}\right)^2 \iiint_V \iiint_{V'} (\varepsilon(\underline{s}) \\ &- \varepsilon_1)(\varepsilon(\underline{s'}) \\ &- \varepsilon_1)^* \, E_{tot}(\underline{s}) \cdot E^*_{tot}(\underline{s'}) \frac{e^{-jk_1(R-R')}}{RR'} dV dV' \end{aligned} \tag{3}$$

Where $k_1 = \frac{2\pi}{\lambda_1} = 2\pi f_0 \sqrt{\varepsilon_1}/c$

See Table 1 for definitions of symbols used in eq. (3) and elsewhere in this paper.

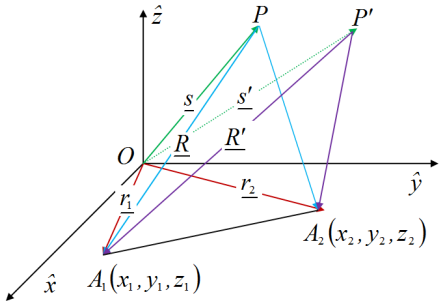

Fig. 3: GEOMETRY OF HMIA MEASUREMENT BY A PAIR OF ANTENNAS

Table 1 SYMBOL DEFINITIONS

Symbol	Definitions
j	$\sqrt{-1}$
k_1	Propagation constant in host medium
k_0	Propagation constant in free space
E_0	Wave amplitude of TE10 mode at within waveguide aperture
R_0	Position vector from a point in the breast to the transmitting antenna
A	Broad aperture dimension of antenna aperture
B	Narrow aperture dimension of antenna aperture
$h(\theta,\phi)$	Radiation pattern function
$\underline{P}(\theta,\phi)$	Polarisation vector
(θ,ϕ)	Incident angle
ε	Complex relative permittivity of tumour
ε_1	Complex relative permittivity of host medium
$R = \lvert\underline{R}\rvert$	Distance from a point in the breast to the receiving antenna
$\hat{R}$	Unit vector parallel to the vector R
$\underline{R}$	Position vector from a point in the tumour to the receiving antenna
E_{tot}	Total electric field
E_{inc}	Incident electric field
E_{scat}	Back-scattered electric field
f_0	The centre frequency
c	The light speed in free space

A. *Far-Field Geometry*

If the distance from a point P to the receiving antenna A_1 is very large compared with the size of antenna array plane, that is, $R \gg r_1$, then:

$$R = \lvert\underline{R}\rvert = \sqrt{(\underline{r_1} - \underline{s}) \cdot (\underline{r_1} - \underline{s})} = \sqrt{r_1^2 + s^2 - 2\underline{r_1} \cdot \underline{s}} \cong s - \frac{\underline{r_1} \cdot \underline{s}}{s} = s - \underline{r_1} \cdot \underline{\hat{s}}$$

Where the "dot" denotes scalar product and $\underline{\hat{s}}$ is a unit vector. Similarly, the distance from another point P' in the breast to the receiving antenna A_2 can be calculated as:

$$R' = \lvert\underline{R'}\rvert = s' - \underline{r_2} \cdot \underline{\hat{s'}}$$

Then $\frac{e^{-jk_1(R-R')}}{RR'} \approx \frac{1}{ss'} e^{-jk_1(s-s')} e^{jk_1(\underline{r_2}\cdot\underline{\hat{s}} - \underline{r_1}\cdot\underline{\hat{s}})}$

B. *Visibility Function*

The six-fold integral of eq. (3) can be simplified by noting that the phase factor $e^{-jk_1(s-s')}$ oscillates rapidly as we scan over all possible pairs of points (P, P') within the domain of integration. Consequently, the only significant contribution to the value of the integral in eq. (3) arises from points for which the phase varies slowly. This situation corresponds to the case for which the points (P, P') coincide. Therefore, we allow $\underline{s} - \underline{s'} \to 0$ so that $s = s'$, and obtain the following volume integral for the visibility function where the integration is over the volume of the scatterer:

$$V\left(\underline{r_1}, \underline{r_2}\right) = \left(\frac{k_0^2}{4\pi}\right)^2 \iiint_{Vol} \left(\left| \varepsilon(\underline{s}) - \varepsilon_1 \right|^2 \right) E_{tot}(\underline{s}) \cdot E_{tot}^*(\underline{s'}) \frac{e^{-jk_1\left(\underline{r_1} - \underline{r_2'}\right)\cdot\underline{\hat{s}}}}{s^2} dV \quad (4)$$

We now define $I(\underline{s}) = \left(\frac{k_0^2}{4\pi}\right)^2 |\varepsilon - \varepsilon_1|^2 \underline{E_{tot}}(\underline{s}) \cdot \underline{E_{tot}^*}(\underline{s})$ to be the breast intensity function at the position $\underline{s}$ (see Fig.4), and define the baseline vector, $\underline{D} = (\underline{r_1} - \underline{r_2})/\lambda_1$ so that (4) can be written as follows:

$$V(\underline{D}) = \iiint_{Vol} I(\underline{s}) \frac{e^{-j2\pi \underline{D}\cdot\underline{\hat{s}}}}{s^2} dV' \quad (5)$$

We now define the Cartesian components of the unit vector $\underline{\hat{s}}$ in terms of spherical polar angles (θ, ϕ) as $\hat{s} = \sin\theta\cos\phi\,\underline{\hat{x}} + \sin\theta\sin\phi\,\underline{\hat{y}} + \cos\theta\,\underline{\hat{z}}$ and do likewise for the volume element dV' so that $dV' = s^2 \sin\theta\, d\theta d\phi ds$ (see Fig.4).

Defining new variables (l, m, n) such that $l = \sin\theta\cos\phi$, $m = \sin\theta\sin\phi$ and $n = \cos\theta = \sqrt{1 - l^2 - m^2}$ gives $dV' = s^2 dl dm ds/n$ and allows eq. (5) to be cast into a more useful form as follows:

$$V(\underline{D}) = \iiint_{Vol} I(\underline{s}) \frac{e^{-j2\pi \underline{D}\cdot\underline{\hat{s}}}}{n} dldmds$$

Writing the Cartesian components of the baseline vector $\underline{D}$ as (u, v, w) such that $u = (x_2 - x_1)/\lambda_1$, $v = (y_2 - y_1)/\lambda_1$, $w = (z_2 - z_1)/\lambda_1$, and the visibility function becomes:

$$V(u, v, w) = \int_l \int_m \int_s \frac{I(s, l, m)}{\sqrt{1 - l^2 - m^2}} e^{-j2\pi\Phi} dldmds \qquad (6)$$

Where $\Phi = \underline{D} \cdot \underline{\hat{s}} = ul + vm + wn$

If all antennas are assumed to be located on a 2D plane then it follows that $w = 0$. We now define a line integral along the radial coordinate, s, so that:

$$\tilde{I}(l, m) = \int_s \frac{I(s, l, m)}{\sqrt{1 - l^2 - m^2}} ds \qquad (7)$$

Using (7) leads to the following 2D integral over the variables (l, m) for the visibility function:

$$V(u, v, 0) = \iint \tilde{I}(l, m) e^{-j2\pi(ul+vm)} dldm \qquad (8)$$

It is evident that the visibility function in eq. (8) is the 2D Fourier transform of the 2D intensity function $\tilde{I}(l, m)$ which is consistent with the Van Cittert-Zernike theorem [17]. Therefore, by Fourier inversion we obtain for the 2D intensity function:

$$\tilde{I}(l, m) = \iint V(u, v, 0) e^{-j2\pi(ul+vm)} dldm \qquad (9)$$

Equation (9) shows that if we make measurements of the visibility function $V(u, v, 0)$ that span (u, v) space, then a 2D image can be determined by Fourier inversion. The 2D image is the intensity function $\tilde{I}(l, m)$ which is defined by the line integral in eq. (7) and represents the scattering intensity in the breast integrated over each radial vector. As such, it represents a projection of the 3D intensity function onto a 2D plane in (l, m) space. The determination of a full 3D image is beyond the scope of this paper and is the subject of ongoing research. The remainder of this paper describes computer simulations relating to 2D images governed by eq. (9).

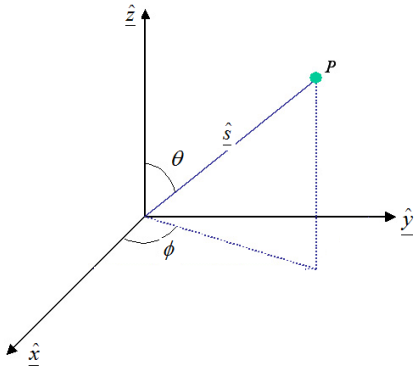

Fig. 4: GEOMETRY OF SPHERICAL POLAR COORDINATE SYSTEM

IV SIMULATION

A. System Configuration

A possible implementation of HMIA is presented in Fig.1. The patient lies face-down on the table in a prone position with her breast flattened against the table. The table has a window in contact with the patient's breast made of material with a dielectric constant ($\varepsilon_r = 9, \sigma = 0.7$ S/m), which is close to that of normal average breast tissue. A 13-element array (100 mm x 100 mm) is placed at a distance of 500 mm from the breast with one of the elements being a transmitter and others being receivers. More than 100 different antenna array configurations have been studied, which includes regularly spaced array configuration, random array configuration and spiral array configuration. One of the most suitable array configurations is shown in Fig.5. One transmitter is represented as 'X', receivers are represented as 'O' and they are randomly located in the array plane. In order to prevent unwanted interferences from the outside, the system is concealed in a microwave absorbent material cylinder.

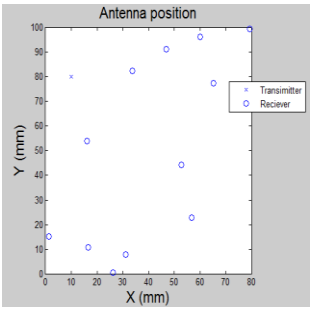

Fig. 5: ANTENNA ARRAY CONFIGURATION

B Breast Model

The breast model was assumed to be fully contained in a rectangle imaging domain with length 15 cm. For better breast cancer detection, the breast needs to be compressed firmly, thus the breast was assumed as a rectangle box (see Fig.1). For simplicity, the system was designed for operation at a single frequency of 10 GHz. In practice, the relative permittivity of the tumour

could be somewhat larger than that of the fat tissue. Values for the real part of the relative permittivity of tumour tissue can be as high as 50 [7]. The use of a small permittivity contrast greatly simplifies the forward model for the scattered field without sacrificing the underlying physics of the HMIA method. A tumour ($\varepsilon_r = 9.5, \sigma = 0.7$ S/m) was assumed located inside normal breast tissue ($\varepsilon_r = 9, \sigma = 0.7$ S/m). The skin surrounding the breast tissue box is assigned ($\varepsilon_r = 9.3, \sigma = 0.7$ S/m). The space between the table and antenna array was assumed filled with lossless dielectric ($\varepsilon_r = 9, \sigma = 0$ S/m) material.

C Antenna and Scattered Field Model

A small open-ended rectangular waveguide is assumed as a transmitting antenna. The radiated far-field E_{inc} from such antenna is well-represented by the following expression (see also Table 1):

$$E_{inc}(R_0, \theta, \phi) = \frac{-jk_1}{2\pi^2} E_0 \frac{e^{-jk_1 R_0}}{R_0} ABh(\theta, \phi)\underline{P}(\theta, \phi) \quad (10)$$

The back-scattered electric field from breast can be found by applying the Stratton & Chu formulation [18] which gives the following integral over the volume of the breast:

$$E_{scat} = \frac{k_0^2}{4\pi} \int_{Vol} (\varepsilon - \varepsilon_1)\,[aE_{tot} + b(E_{tot} \cdot \hat{R})\hat{R}] \frac{e^{-jk_1 R}}{R} dV \quad (11)$$

Where $a = 1 - \frac{j}{k_1 R} - \frac{1}{(k_1 R)^2}$,
$b = -1 + \frac{3j}{k_1 R} + \frac{3}{(k_1 R)^2}$.

When $k_1 R \gg 1$, the above factors can be approximated by $a \approx 1, b \approx -1$. For the purposes of demonstrating the HMIA technique, it is computationally advantageous to consider a small permittivity contrast between the tumour and host medium (fat tissue/skin), that is $(\varepsilon - \varepsilon_1)$ is assumed to be small. In this case, the backscattered far-field can be readily determined using the Born Approximation, which allows the total electric field E_{tot} to be approximated by the incident field, so that we obtain:

$$E_{scat} = \frac{k_0^2}{4\pi} \int_{Vol} (\varepsilon - \varepsilon_1)\,[E_{inc} + (E_{inc} \cdot \hat{R})\hat{R}] \frac{e^{-jk_1 R}}{R} dV \quad (12)$$

Also, in the far-field, we can put $E_{inc} \cdot \hat{R} \approx 0$, then we obtain:

$$E_{scat} = \frac{k_0^2}{4\pi} \int_{Vol} (\varepsilon - \varepsilon_1)\, E_{inc} \frac{e^{-jk_1 R}}{R} dV \quad (13)$$

Combining eq. (13) and eq. (2), a computer model was developed under the MATLAB environment to simulate the complex visibility function that is detailed in section III. The Fourier relationship of eq. (9) was then used to generate a 2D image.

V RESULTS AND DISCUSSION

Fig.6 shows the 2D view of the original breast model and the real part of the reconstructed images of the breast with 5 spherical tumours (2 mm, 3 mm, 4 mm, 5 mm and 6 mm in diameter) located at $(x = -60,\ y = 0)$, $(x = -30,\ y = 0)$, $(x = 60,\ y = 0)$, $(x = -10,\ y = 0)$, $(x = 20,\ y = 0)$ and $(x = 60,\ y = 0)$, respectively. Fig.7 illustrates the original and real part of the reconstructed breast images with 3 spherical tumours (2 mm in diameter) located at $(x = 0,\ y = 0)$, $(x = 20,\ y = 20)$ and $(x = 30,\ y = 30)$, respectively. Fig.8 displays the original and real part of reconstructed breast images with 3 tumours in random size and location.

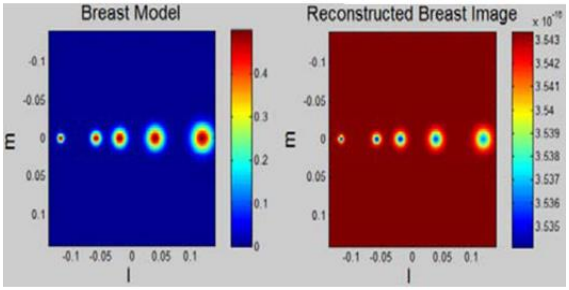

Fig. 6: ORIGINAL AND REAL PART OF RECONSTRCUTED BREAST IMAGES WITH 5 TUMOURS

The original and reconstructed images of the breast in Fig. 6 - Fig.8 are compared. It can be seen that all tumours of different sizes and locations are successfully detected and clearly identified in the reconstructed image. In this model, all tumours were placed within the same layer within the breast. In the future, a computer model for a full 3D

imaging system, including breast skin, is planned along with experimental work on breast phantoms.

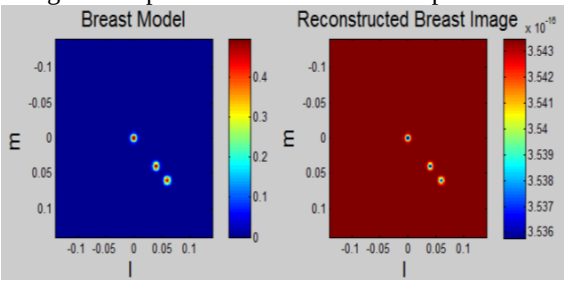

Fig. 7: ORIGINAL AND REAL PART OF RECONSTRCUTED BREAST IMAGES WITH 3 TUMOURS (2-MM-DIAMETER)

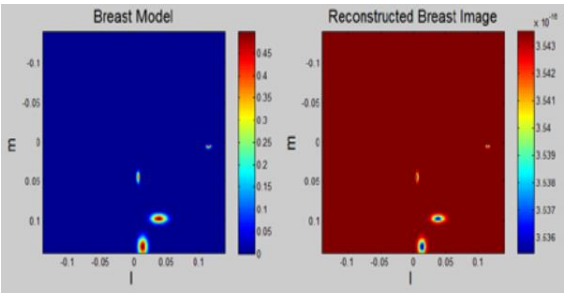

Fig. 8: ORIGINAL AND REAL PART OF RECONSTRCUTED BREAST IMAGES WITH 3 TUMOURS (RANDOM SIZE, LOCATION)

VI CONCLUSION

In this paper, a new holographic microwave imaging array (HMIA) for early breast cancer detection is introduced, which is based on real-time aperture synthesis and holographic imaging techniques. The simulated results show that the proposed HMIA system has the potential to detect tumours of various sizes at various locations.

REFERENCES

[1] Liu G.D. and Zhang Y.R., "An Overview of Active Microwave Imaging for Early Breast Cancer Detection," Journal of Nanjing University of Posts and Telecommunications (Natural Science), 30 (1), 2010.

[2] Smith R.A., Saslow D., Sawyer K.A., Burke W., Costanza M.E., Evans W.P., Foster R.S., Hendrick H.J.E.E. and Sener S., "American cancer society guidelines for breast cancer screening," Updated 2003. CA: A Cancer J for Clinician, 2003.

[3] Breast Cancer: Recovery Act Investment Report American Recovery Reinvestment Act at NCI. http://www.cancer.gov/aboutnci/recovery/recoveryfunding/investmentreports/breast, September 2010.

[4] Elsdon M., Leach M., FDO M.J., Foti S.J. and Smith D., "Early Stage Breast Cancer Detection using Indirect Microwave Holography," Microwave Conference, 2006. 36th European, pp.1256 - 1259, 10-15 Sept, 2006.

[5] Guide D., Breast Cancer. http://www.cancer.org/Cancer/BreastCancer/DetailedGuide/breast-cancer-detection

[6] Lee A., Types of Medical Imaging: X-ray, Ultrasound, Magnetic, and Nuclear Modalities. http://www.suite101.com/content/typesof-medicalimaginga85622#ixzz1GX1hQUQL, Dec 20, 2008.

[7] Fear E. C., Li X., Hagness S. C. and Stuchly M. A., "Confocal microwave imaging for breast cancer detection: Localization of tumors in three dimensions," IEEE Transactions on Biomedical Engineering, 49 (8) pp.812-822, 2002.

[8] Gabriel C. and Peyman A, "Dielectric measurement: Error analysis and assessment of uncertainty," Physics in Medicine and Biology, 51 (23) pp.6033-6046, 2006.

[9] Gabriel S., Lau R. W. and Gabriel C, "The dielectric properties of biological tissues: II. Measurements in the frequency range 10 Hz to 20 GHz," Physics in Medicine and Biology, 41 (11) pp.2251-2269, 1996(a).

[10] Yuanwei J., Yi J. and Moura J, "Time Reversal Beamforming for Microwave Breast Cancer Detection," IEEE International Conference on Image Processing, 2007, 5 : pp. 13-16, November 12, 2007.

[11] Bond E. J., Li, X., Hagness S. C. and Van Veen B. D., "Microwave imaging via space-time beamforming for early detection of breast cancer," IEEE Transactions on Antennas and Propagation, 51 (8) : pp.1690-1705, 2003.

[12] Sill J. M. and Fear E. C., "Tissue sensing adaptive radar for breast cancer detection - experimental investigation of simple tumor models," IEEE Transactions on Microwave Theory and Techniques, 53 (11) : pp.3312 - 3319, Nov, 2005.

[13] Davis S. K., Tandradinata H., Hagness S. C. and Van Veen B. D., "Ultra-wideband microwave breast cancer detection: a detection-theoretic approach using the generalized likelihood ratio test," IEEE Transactions on Biomedical Engineering, 52 (7) pp.1237-125053, 2005.

[14] Michael E., Sergei Skobelev M.L. and Smith D., "Microwave Holographic Imaging of Breast Cancer," Microwave, Antenna, Propagation and EMC Technologies for Wireless Communications, International Symposium on 2007, pp.966 - 969, 2007.

[15] Shakti K. Davis, B.D.V.V., Susan C. Hagness and Frederick K., "Breast Tumor Characterization Based on Ultrawideband Microwave Backscatter," IEEE Transactions on Biomedical Engineering, 55 (1), 2008.

[16] Smith D., M.L., Michael E. and Foti S.J., "Indirect Holographic Techniques for Determining Antenna Radiation Characteristics and Imaging Aperture Fields," IEEE Antennas and Propagation Magazine, Vol.49, No.1, Feb. 2007.

[17] Born & Wolf, Principles of Optics, chapter 10.4.2, page 510, Pergamon Press, Sixth Edition, 1980.

[18] Silver S. (editor), Microwave Antenna Theory and Design, chapter 3.11, MIT Radiation Laboratory Series, McGraw-Hill, New York, 1949.

Conference Paper 2

3D Breast Cancer Imaging Using Holographic Microwave

Lulu Wang Ray Simpkin Al-Jumaily, A. M.

Status: Published 2012

Conference: IVCNZ2012 Proceedings of the 27th Conference on Image and Vision Computing New Zealand

IVCNZ ’12 November 26 - 28 2012, Dunedin, New Zealand

3D BREAST CANCER IMAGING USING HOLOGRAPHIC MICROWAVE INTERFEROMETRY

Lulu Wang
luwang@aut.ac.nz
Institute of Biomedical Technologies
Auckland University of Technology
Auckland, New Zealand

Ray Simpkin
r.simpkin@irl.cri.nz
Medical Device Technology
Industrial Research Limited
Auckland, New Zealand

Al-Jumaily, A. M.
ahmed.al-jumaily@aut.ac.nz
Institute of Biomedical Technologies
Auckland University of Technology
Auckland, New Zealand

ABSTRACT

Due to the critical need for complementary or/and alternative modalities to current X-ray mammography for early-stage breast cancer detection, a 3D holography microwave imaging array (HMIA) system has been developed. This work describes how 3D images can be reconstructed from 3D breast intensity distribution using of holographic microwave and aperture synthesis imaging techniques. The obtained 3D simulation results have demonstrated the feasibility and superiority of detecting small malignant breast tumours using the proposed random antenna array. Simulation results demonstrate that the proposed technique has the potential to detect tumours of various sizes at various locations.

Categories and Subject Descriptors

I.4 [Image Processing and Computer Vision]: Three-Dimensional Graphics and Realism

General Terms

Visible line/surface algorithms

Keywords

Holographic Microwave, Holographic Microwave Imaging, Breast Cancer Detection, Interferometric

1. INTRODUCTION

Breast cancer is the most commonly diagnosed cancer in women, as well as the second leading cause of death during the last decade [1]. The use of microwave techniques as a complimentary tool for breast cancer detection has been proposed by many [2-5]. In the medical area the ability of microwaves to penetrate to considerable depths beneath the skin in a non-ionizing safe manner coupled with the large differences in material properties between healthy and malignant tissues has also stimulated much research interest [6].

The work described here has investigated an approach which focuses upon using holographic microwave imaging array (HMIA) for breast cancer detection, which is based on a real-time aperture synthesis imaging technique. Aperture synthesis interferometer is applied to obtain the complex visibility data from the collected phase information, and then reconstruct a 2D image using Inverse Fast Fourier Transform (IFFT). A 3D mathematic computer model is developed under MATLAB environment to demonstrate that the proposed HMIA can produce good quality breast images with the inclusion of a skin layer. Computer simulation results indicate that a single microwave frequency can provide the size and location of the embedded tumour.

This paper is organized as follows: Section 2 describes the holographic microwave imaging array theory. Section 3 details the simulation set up. Section 4 presents results. Section 5 concludes this work.

2. THEORY

The HMIA system contains one transmitter and an array of 15 receivers randomly located at a distance away from breast. During patient exams, the patient is to lie prone on an exam bed above the imaging system with her breast flattened against the breast window that is made of material close to the normal average breast tissue (see Figure.1). The transmitter is fixed at a distance away from breast, and an array of 15 small receivers is placed in a far-field away from breast that is moved from

Permission to make digital or hard copies of part or all of this work for personal or classroom use is granted without fee provided that copies are not made or distributed for profit or commercial advantage and that copies bear this notice and the full citation on the first page. Copyrights for components of this work owned by others than ACM must be honored. Abstracting with credit is permitted. To copy otherwise, to republish, to post on servers or to redistribute to lists, requires prior specific permission and/or a fee.
IVCNZ '12 November 26 - 28 2012, Dunedin, New Zealand
Copyright 2012 ACM 978-1-4503-1473-2/12/11 ...$15.00.

$z = H_1$ mm to $z = H_n$ mm in M steps. The system is designed for operation at a single frequency of 10 GHz.

The geometry of a three-dimensional (3D) HMIA imaging is shown in Figure.2. If a point $P(x, y, z)$ is assumed in the breast, under far-field conditions, the visibility function of the back-scattered electric field for two antennas located at $\underline{r_1}$ and $\underline{r_2}$ is defined as:

$$G(\underline{r_1}, \underline{r_2}) = < \underline{E_{scat}}\left(\underline{r_1}\right) \cdot \underline{E^*_{scat}}(\underline{r_2}) > \quad (1)$$

Where the asterisk denotes the complex conjugate and $\langle\rangle$ stands for the expected value (time average).

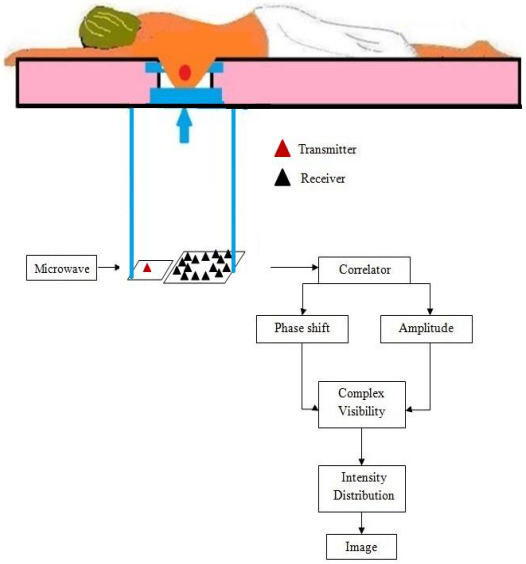

Figure 1: Holographic microwave imaging array system

Equation (1) can be written as:

$$G(\underline{r_1}, \underline{r_2}) = \left(\frac{k_0^2}{4\pi}\right)^2 \iiint_V \iiint_{V'} \left(\varepsilon(\underline{s}) - \varepsilon_1\right)\left(\varepsilon(\underline{s'}) - \varepsilon_1\right)^* \underline{E_{tot}}(\underline{s}) \cdot \underline{E^*_{tot}}(\underline{s'}) \frac{e^{-jk_1(R-R')}}{RR'} dV dV \quad (2)$$

Where $\underline{E_{tot}}(\underline{s})$=Total electric field (incident plus scattered) at a point inside the breast with position vector, $\underline{s}$, $j = \sqrt{-1}$, $k_0 = 2\pi/\lambda_0$, $k_1 = 2\pi/\lambda_1$, λ_0=Wavelength in free space, λ_1=Wavelength in host medium, ε=Complex relative permittivity of the breast, ε_1=Complex relative permittivity of host medium, f_0=The center frequency, c=The light speed in free space, $R = |\underline{R}|$=Distance from a point in the breast to the receiving antenna.

If the distance from a point P to the receiving antenna A_1 is very large compared to the size of antenna array plane, that is, $R \gg |\underline{r_1}|$, then:

$$R = |\underline{R}| \cong s - \frac{\underline{r_1} \cdot \underline{s}}{s} = s - \underline{r_1} \cdot \underline{\hat{s}}$$

Where the "dot" denotes scalar product and $\underline{\hat{s}}$ is a unit vector. Similarly, the distance from another point P' in the breast to the receiving antenna A_2 can be calculated as:

$$R' = |\underline{R'}| = s' - \underline{r_2} \cdot \underline{\hat{s'}}$$

Then $\frac{e^{-jk_1(R-R')}}{RR'} \approx \frac{1}{ss'} e^{-jk_1(s-s')} e^{jk_1(\underline{r_2}\cdot\underline{\hat{s'}} - \underline{r_1}\cdot\underline{\hat{s}})}$

The six-fold integral of (3) can be simplified by noting that the phase factor $e^{-jk_1(s-s')}$ oscillates rapidly as we scan over all possible pairs of points (P, P') within the domain of integration. Consequently, the only significant contribution to the value of the integral in (3) arises from points for which the phase varies slowly. This situation corresponds to the case for which the points (P, P') coincide. Therefore, we allow $\underline{s} - \underline{s'} \to 0$ so that $s = s'$, and obtain the following volume integral for the visibility function where the integration is over the volume of the scatterer, V:

$$G\left(\underline{r_1}, \underline{r_2}\right) = \left(\frac{k_0^2}{4\pi}\right)^2 \iiint_{Vol} \left(|\varepsilon(\underline{s}) - \varepsilon_1|^2\right) \underline{E_{tot}}(\underline{s}) \cdot \underline{E^*_{tot}}(\underline{s'}) \frac{e^{-jk_1\left(\underline{r_1}-\underline{r_2'}\right)\cdot\underline{\hat{s}}}}{s^2} dV' \quad (3)$$

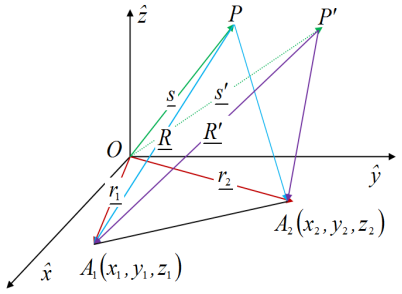

Figure 2: Geometry of HMIA measurement by a pair of antennas

Equation (3) can be written as follows:

$$G(\underline{D}) = \iiint_{Vol} I(\underline{s}) \frac{e^{-j2\pi \underline{D}\cdot\hat{\underline{s}}}}{s^2} dV' \quad (4)$$

Where $I(\underline{s}) = \left(\frac{k_0^2}{4\pi}\right)^2 |\varepsilon - \varepsilon_1|^2 \underline{E}_{tot}(\underline{s}) \cdot \underline{E}^*_{tot}(\underline{s})$ is defined as the breast intensity function at the position, $\underline{s}$. $\underline{D} = (\underline{r_1} - \underline{r_2})/\lambda_1$.

Equation (4) changes to a more useful form by use of spherical polar coordinate system (see Figure 3):

$$G(\underline{D}) = \iiint_{Vol} I(\underline{s}) \frac{e^{-j2\pi \underline{D}\cdot\hat{\underline{s}}}}{n} dldmds$$

Where $\hat{s} = \sin\theta\cos\phi\,\hat{\underline{x}} + \sin\theta\sin\phi\,\hat{\underline{y}} + \cos\theta\,\hat{\underline{z}}$,

$dV' = s^2 \sin\theta\, d\theta d\phi ds = s^2 dldmds/n$,

$l = \sin\theta\cos\phi$,

$m = \sin\theta\sin\phi$

$n = \cos\theta = \sqrt{1 - l^2 - m^2}$

The visibility function becomes:

$$G(u,v,w) = \int_l \int_m \int_s \frac{I(s,l,m)}{\sqrt{1-l^2-m^2}} e^{-j2\pi\Phi} dldmds \quad (5)$$

Where $\Phi = \underline{D}\cdot\hat{\underline{s}} = ul + vm + wn$

$u = (x_2 - x_1)/\lambda_1$,

$v = (y_2 - y_1)/\lambda_1$,

$w = (z_2 - z_1)/\lambda_1$.

If all antennas are assumed to be located on a 2D plane then it follows that $w = 0$. We now define a line integral along the radial coordinate, s, so that:

$$\check{I}(l,m) = \int_s \frac{I(s,l,m)}{\sqrt{1-l^2-m^2}} ds \quad (6)$$

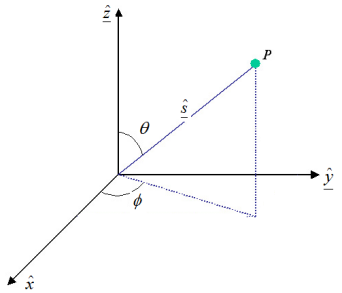

Figure 3: Spherical polar coordinate system

Using (6) leads to the following 2D integral over the variables (l,m) for the visibility function:

$$G(u,v,0) = \iint \check{I}(l,m) e^{-j2\pi(ul+vm)}\, dldm \quad (7)$$

It can be seen that (7) is the 2D Fourier transform of the 2D intensity function $\check{I}(l,m)$ which is consistent with the Van Cittert-Zernike theorem [8]. Therefore, by Fourier inversion we obtain the 2D intensity function:

$$\check{I}(l,m) = \iint G(u,v,0) e^{-j2\pi(ul+vm)}\, dldm \quad (8)$$

Equation (8) shows that if we make measurements of the visibility function $G(u,v,0)$ that span (u,v) space, then a 2D image can be determined by Fourier inversion. The 2D image is the intensity function $\check{I}(l,m)$ which is defined by the line integral in (6) and represents the scattering intensity in the breast integrated over each radial vector. As such, it represents a projection of the 3D intensity function onto a 2D plane in (l,m) space.

We assume a breast model contains multi-layers as shown in Figure 4, one fixed transmitter is located at a distance of H to breast model, the receiving antenna array plane is designed can be moved from H_1 (mm) to H_n (mm) in M steps, where H_1 is the distance between receiving antenna array plane and breast model (see Figure 5). Then the tumour at the breast depth location, z_n, within the same breast model is defined as:

$$z_n = s_n cos\theta_n \quad (9)$$

Where θ_n is the receiving angler of the same receiver on the receiving antenna array plane to the detected object at the position, s_n, with the receiving antenna array plane to breast model at the distance, H_n. Thus, ds, in (6) becomes:

$$ds = \frac{dz}{cos\theta_n} = \frac{dz}{\sqrt{1-l^2-m^2}}$$

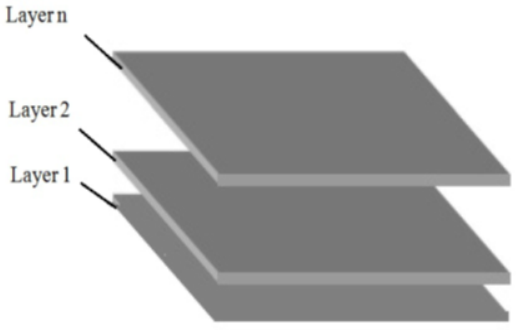

Figure 4: 3D imaging of breast layers

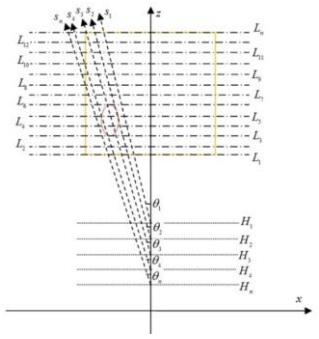

Figure 5: Block diagram showing the scattering characterization scheme from different receiving height H_n

The back-scattered electric field from breast at each height is collected, the 3D integral of breast intensity function through a selected height, $H = H_n$, can be obtained as:

$$I(H = z_n, l, m) = \frac{d\tilde{I}(l,m) \cdot (1 - l^2 - m^2)}{dz} \quad (10)$$

The breast intensity integral difference at two different heights is calculated as:

$$\frac{d\tilde{I}}{dz} = \frac{\tilde{I}_{z_n} - \tilde{I}_{z_{n-1}}}{z_n - z_{n-1}} \quad (11)$$

A reconstructed 3D image of the breast intensity function is then computed using (10) and (11) using measured data obtained by placing the receiver array plane at difference heights.

3. SIMULATION

3.1 Array Configuration

Figure 1 illustrates a possible implementation of HMIA. The patient lies face-down on the table in a prone position with her breast flattened against the table. The table has a window in contact with the patient's breast made of material with a dielectric constant ($\varepsilon_r = 9,\ \sigma = 0.7$ S/m), which is close to that of normal average breast tissue.

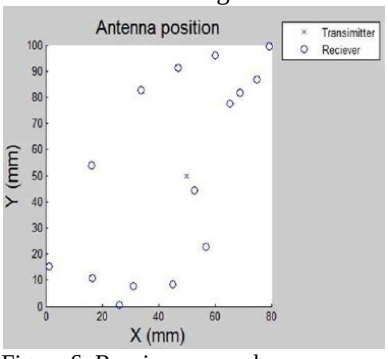

Figure 6: Receiver array plane

One transmitter is located at (x=50 mm, y=50 mm, z=-450 mm). A 2D 15-element receiver array plane (see Figure 6) is placed and moved from z=-450 mm to z=-460 mm in 40 steps. The breast model is located at (x=0 mm, y=0 mm, z=-70 mm) and is assumed to be fully contained in a rectangle imaging domain with length 140 mm.

3.2 Breast Model

For better breast cancer detection, the breast needs to be compressed firmly, thus the breast is assumed as a box (140 mm x 140 mm x 70 mm) (see Figure 7). For simplicity, the system was designed for operation at a single frequency of 10 GHz. In practice, the relative permittivity of the tumour could be somewhat larger than that of the fat tissue. Values for the real part of the relative permittivity of tumour tissue can be as high as 50 [9]. The use of a small permittivity contrast greatly simplifies the forward model for the scattered field without sacrificing the underlying physics of the HMIA method. A spherical tumour ($\varepsilon_r = 9.5, \sigma = 0.7$ S/m) was assumed located inside normal breast tissue($\varepsilon_r = 9,\ \sigma = 0.7$ S/m). Skin layer ($\varepsilon_r = 9.3,\ \sigma = 0.7$ S/m) was modelled as 2 mm thick. Gaussian function was selected to present breast model. The space between the table and antenna array was assumed filled with a lossless dielectric ($\varepsilon_r = 9,\ \sigma = 0$ S/m) material.

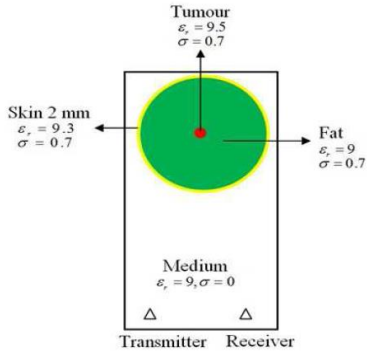

Figure 7: HMIA simulation showing antennas and breast model

3.3 Antenna and Scattered Field Model

A known incident field is transmitted by a transmitter and the response is measured on 15 receivers. HMIA measures the scattered radiation of the breast, which is composed of a set of correlation interferometer pairs. The electromagnetic signals received by each pair are cross correlated to get the visibility function. The space between the bed and antenna array is filled with the same material as the breast window to reduce the reflection from the skin layer.

A small open-ended rectangular wave-guide is assumed as a transmitting antenna. The radiated far-field from such antenna is well-represented by

the following expression:

$$\underline{E}_{inc}(R_0,\theta,\phi) = \frac{-jk_1}{2\pi^2}\underline{E}_0\frac{e^{-jk_1R_0}}{R_0}ABh(\theta,\phi)\underline{P}(\theta,\phi) \quad (13)$$

Where $\underline{E}_0$=Wave amplitude of TE_{10}mode within wave-guide aperture

R_0=Position vector from a point in the breast to the transmitting antenna

A=Broad aperture dimension of antenna aperture

B=Narrow aperture dimension of antenna aperture

$h(\theta,\phi)$=Antenna far-field radiation pattern

$\underline{P}(\theta,\phi)$=Polarisation vector

The back-scattered electric field from breast can be found by applying the Stratton & Chu formulation [7] which gives the following integral over the volume of the breast:

$$\underline{E}_{scat} = \frac{k_0^2}{4\pi}\int_{Vol}(\varepsilon-\varepsilon_1)\,[a\underline{E}_{tot} + b(\underline{E}_{tot}\cdot\underline{\hat{R}})\underline{\hat{R}}]\frac{e^{-jk_1R}}{R}dV \quad (14)$$

Where $a = 1 - \frac{j}{k_1R} - \frac{1}{(k_1R)^2}$,

$b = -1 + \frac{3j}{k_1R} + \frac{3}{(k_1R)^2}$.

$\underline{\hat{R}}$=Unit vector parallel to the vector $\underline{R}$

$\underline{R}$=Position vector from a point in the breast to the receiving antenna

When $k_1R \gg 1$, the above factors can be approximated by $a \approx 1, b \approx -1$.Therefore, under these far-field conditions (14) becomes:

$$\underline{E}_{scat} = \frac{k_0^2}{4\pi}\int_{Vol}(\varepsilon-\varepsilon_1)\,[\underline{E}_{inc} + (\underline{E}_{inc}\cdot\underline{\hat{R}})\underline{\hat{R}}]\frac{e^{-jk_1R}}{R}dV \quad (15)$$

For the purposes of demonstrating the HMIA technique, it is computationally advantageous to consider a small permittivity contrast between the tumour and host medium (fat tissue/skin), that is $(\varepsilon-\varepsilon_1)$ is assumed to be small. Thus, the backscattered far-field can be readily determined using the Born Approximation, which allows the total electric field, $\underline{E}_{tot}$, to be approximated by the incident field, $\underline{E}_{inc}$, so that we obtain:

$$\underline{E}_{scat} = \frac{k_0^2}{4\pi}\int_{Vol}(\varepsilon-\varepsilon_1)\,[\underline{E}_{inc} - (\underline{E}_{inc}\cdot\underline{\hat{R}})\cdot\underline{\hat{R}}]\frac{e^{-jk_1R}}{R}dV \quad (16)$$

A computer model was developed under the MATLAB environment by combining (16) and (1) to simulate the complex visibility function that is detailed in section 2. The Fourier relationship (8) was then used to generate a 2D image and (12) was used to generate a 3D image.

4. RECONSTRUCTED IMAGING

Figure 8 shows the original, 2D and 3D view of the reconstructed 3D breast model with 5 spherical tumours (2 mm in diameter) located in different z-plane (see Table 1), respectively.

Figure 9 shows the original, 2D and 3D view of the reconstructed 3D breast model with 2 tumours are randomly located within the breast in random shape (see Table 2), respectively.

The original and reconstructed 3D breast images (40 × 40 × 40 pixels) in Figure 8 and Figure 9 are compared. It can be seen that all tumours of different sizes and locations are successfully detected and clearly identified in the reconstructed image even when they are in random shape and location. Tumours placed at different layers within the breast are also fully detected with the imaging algorithm.

Table.1: Location and size of spherical shaped tumour

No	Position (mm)			Size (mm)		
	x	y	z	σ_x	σ_y	σ_z
1	-50	0	-10	2	2	2
2	-30	0	-20	2	2	2
3	0	0	-30	2	2	2
4	20	0	-40	2	2	2
5	50	0	-40	2	2	2

Table.2 Location and size of randomly shaped tumour

No	Position (mm)			Size (mm)		
	x	y	z	σ_x	σ_y	σ_z
1	6.7992	66.5155	10	2.3992	4.1727	4.9086
2	5.7642	2.4112	50	1.2332	3.4964	4.8925

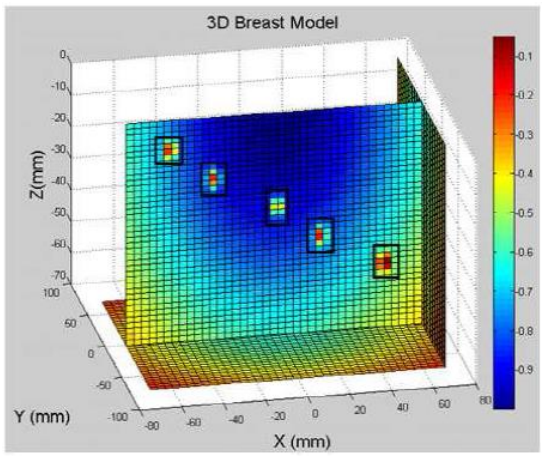

(a)

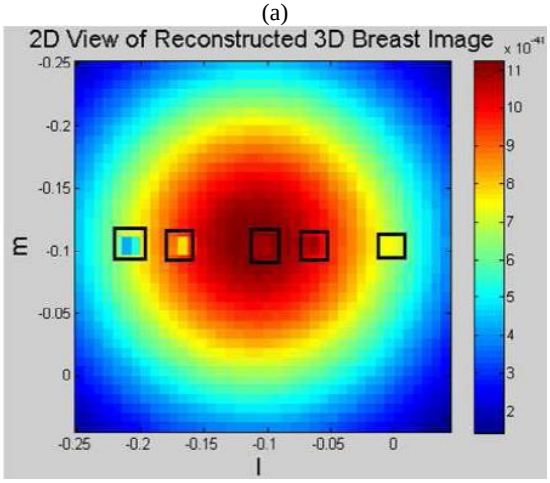

(b)

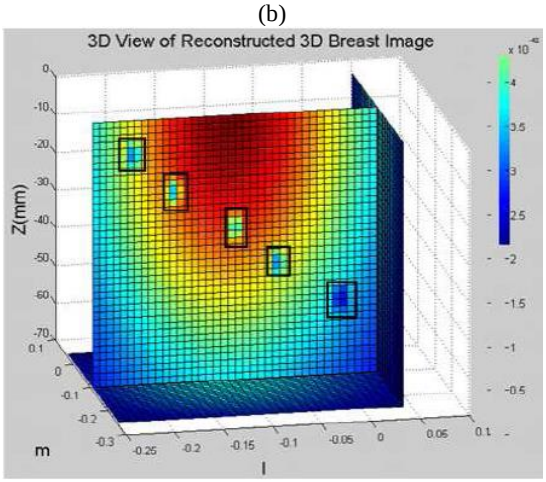

(c)

Figure 8: (a) Original 3D breast model with 5 tumours; (b) 2D view of reconstructed 3D breast image; (c) 3D view of reconstructed 3D breast image

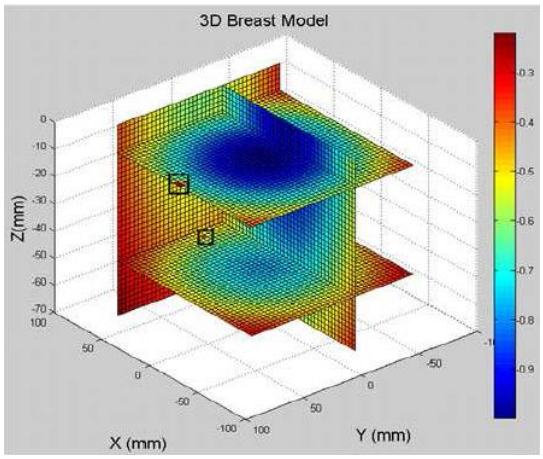

(a)

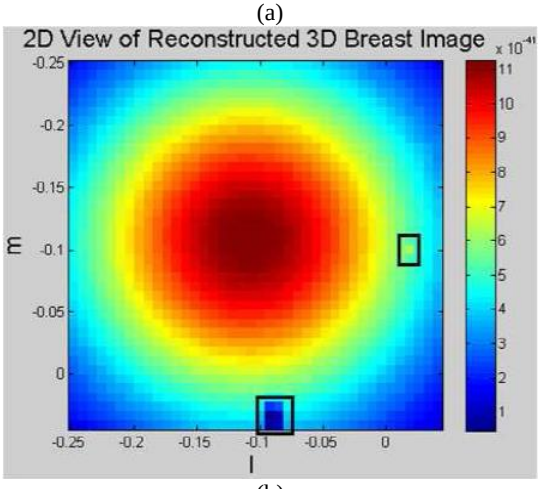

(b)

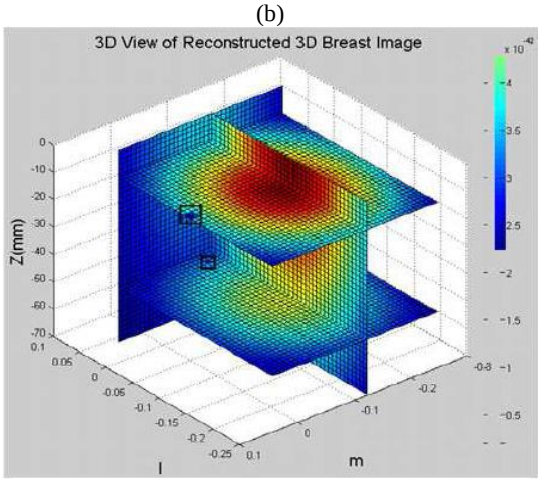

(c)

Figure 9: (a) Original 3D breast model with 2 tumours; (b) 2D view of reconstructed 3D breast image; (c) 3D view of reconstructed 3D breast image

5. CONCLUSIONS

The work described in this paper has demonstrated the possibility of applying holographic microwave imaging array to early stage breast cancer detection. The 3D computational model is developed to demonstrate the proposed imaging technique, the system exploits breast-tissue physical properties unique to

the microwave spectrum, namely, the translucent nature of normal breast tissues (without lesions) and the high dielectric contrast between malignant tumours and the surrounding normal breast tissues. Tumours with different size, shape and location could be detected against the background. This technique has potential benefits in terms of simplicity, safety and comfort compared to other screening modalities, such as X-ray.

6. ACKNOWLEDGMENTS

The authors gratefully acknowledge the support of the Institute of Biomedical Technologies (IBTec) at the Auckland University of Technology (AUT), and the support of Industrial Research Limited (IRL), Auckland, New Zealand.

7. REFERENCES

[1] American Cancer Society. 2012. Cancer Facts & Figures 2012, American Cancer Society.

[2] Du Li, Meaney, P.M. and Paulsen, K.D. 2003. Conformal microwave imaging for breast cancer detection, IEEE Transactions on Microwave Theory and Techniques, 51, 4, 1179-1186.

[3] Xu Li and Hagness, S. C. 2001. A confocal microwave imaging algorithm for breast cancer detection, IEEE Microwave and Wireless Components Letters, 11, 3, 130-132.

[4] Fear, E. C. and Stuchly, M. A. 2000. Microwave detection of breast cancer, IEEE Transactions on Microwave Theory and Techniques, 48, 11, 1854-1863.

[5] Craddock, I., Leendertz, J. , Preece, A. and Benjamin, R. 2008. Experimental and clinical results of breast cancer detection using UWB microwave radar. In Antennas and Propagation Society International Symposium, AP-S 2008, San Diego, CA, July 2008, IEEE Transactions on Antennas and Propagation, 1-4.

[6] Fear, E. C. and Stuchly, M. A. 1999. Microwave system for breast tumour detection, IEEE Microwave Guided Wave Letter, 9, 11, 470-472.

[7] Silver, S. 1984. Radiation from current distributions. In Microwave Antenna Theory and Design. Silver, S. Ed. Peter Peregrinus Ltd, London, UK, 87-90.

[8] Born, M. and Wolf, E. 1999. Interference and diffraction with partially coherent light. In Principles of Optics. Seventh Edition. Cambridge University Press, Cambridge, UK, 572-577.

[9] Fear, E. C., Li, X., Hagness, S. C. and Stuchly, M. A. 2002. Confocal microwave imaging for breast cancer detection: Localization of tumors in three dimensions, IEEE Transactions on Biomedical Engineering, 49, 8, 812-822.

Conference Paper 3

Holographic Microwave Imaging: Experimental Investigation of Breast Tumour Detection

Lulu Wang Ray Simpkin Al-Jumaily, A. M.

Status: Published 2013

Conference: Proceedings of 2013 IEEE International Workshop on Electromagnetics

1-3 August, 2013, Hong Kong, China

Holographic Microwave Imaging: Experimental Investigation of Breast Tumour Detection

Lulu Wang[1], Ray Simpkin[2] and A. M. Al-Jumaily[1]
[1] Institute of Biomedical Technologies, Auckland University of Technology, Auckland, New Zealand
Email: luwang@aut.ac.nz, ahmed.al-jumaily@aut.ac.nz
[2] Callaghan Innovation, Auckland, New Zealand
Email: ray.simpkin@callaghaninnovation.govt.nz

Abstract

This paper presents a two-dimensional (2-D) Holographic Microwave Imaging Array (HMIA) technique for early breast tumor detection and demonstrates its efficacy using experimental data obtained with a breast phantom. The system is designed for operation at a single frequency of 12.6 GHz, which includes one transmitter and an array of 15 receivers that is placed at a far-field under the breast phantom. The breast phantom consists of a homogeneous normal breast tissue, a small malignant tumour and skin. The matching solution medium is not necessary in this system. Air is used between the antennas and breast phantom. During operation, the single transmitter transmits microwave sources into the breast phantom and the back-scattered signals are recorded and analysed by an array of 15 receivers. This technique uses the phase differences introduced during the collection of target responses in order to determine the correct spatial location of the different structures that constitute the final image. The experimental results showed that small tumors (<5 mm) at different locations could be successfully detected by using the proposed 2-D HMIA technique.

1. INTRODUCTION

Microwave imaging is one of the most promising alternative methods for early-stage breast cancer detection and has been investigated by many groups [1]-[9]. Recent clinical trial results [10] demonstrated that microwave breast imaging has the potential to replace X-ray mammography and become a clinical implementation in the future. Microwave based imaging techniques for breast cancer detection are non-ionizing, do not require breast compression, is less invasive than X-rays and is potentially low cost.

We investigating a new Holographic Microwave Imaging Array (HMIA) system for early-stage breast cancer detection that is based on holographic and real-time aperture synthesis far-field imaging techniques. The physical basis of this technique is the same as other microwave imaging approaches, which investigates the dielectric properties of malignant and healthy breast tissues at microwave frequencies. Compared to radar based microwave imaging [2], the holographic microwave technique [4] does not require expensive ultra high speed electronics as a narrow-band signal is used enabling imaging at significantly lower cost. Our first generation of experimental investigation of the breast phantoms have been completed to demonstrate that HMIA can produce good quality breast images. The experimental results showed that small tumours (<5 mm in diameter) of various sizes and shapes in different locations of the breast have been successfully detected by the proposed HMIA approach.

2. 2D HOLOGRAPHIC MICROWAVE IMAGING ARRAY (HMIA)

The architecture of the HMIA system is illustrated in Fig. 1. During data collection, the single transmitter generates microwave sources into the breast phantom and the backscattered electric field from the breast phantom is measured by an array of 15 microwave receivers. The measurements are obtained using a vector network analyzer (PNA).

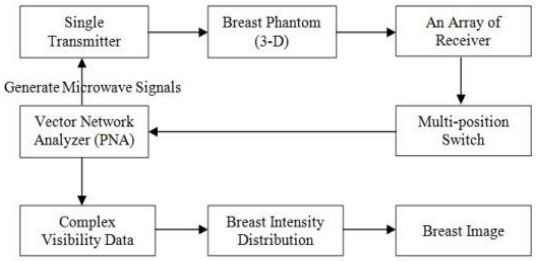

Fig. 1: Block diagram of holographic microwave imaging array system

The phase and magnitude of the received signal at each antenna is then used to calculate the complex visibility function for each possible pair of antennas from which a 2D image can be formed by an inverse Fourier Transform.

Fig. 2 shows the geometry relevant to 3D HMIA imaging, where x, y and z represent antenna locations in the array plane. If a point $P(x', y', z')$ is assumed in the breast, under far-field conditions, the visibility function of the back-scattered electric

field, $\underline{E}_{scat}$, for any two antennas located at $\underline{r}_1$ and $\underline{r}_2$ is defined as:

$$G(\underline{r}_1, \underline{r}_2) = < \underline{E}_{scat}\left(\underline{r}_1\right) \cdot \underline{E}^*_{scat}(\underline{r}_2) > \qquad (1)$$

The asterisk in Equation (1) denotes the complex conjugate, while <> stands for the expected value (time average).

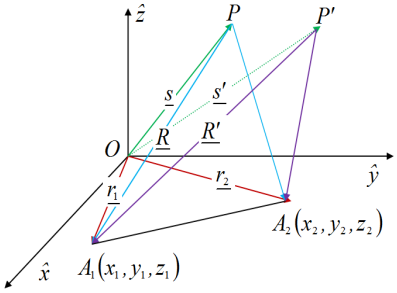

Fig. 2: Geometry of HMIA measurement by a pair of antennas

Defining the breast intensity function at the position $\underline{s}$ as:

$$I(\underline{s}) = \left(\frac{k_0^2}{4\pi}\right)^2 \left|\varepsilon(\underline{s}) - \varepsilon_1\right|^2 \underline{E}_{tot}(\underline{s}) \cdot \underline{E}^*_{tot}(\underline{s}) \qquad (2)$$

Where k_0 is the wave number in free space, $\varepsilon(\underline{s})$ is the complex relative permittivity distribution of the object, ε_1 is the complex relative permittivity of the host medium and $\underline{E}_{tot}(\underline{s})$ is the total electric field (incident plus scattered) at a point inside the breast with position vector $\underline{s}$.

If all antennas are assumed to be located on a 2D plane, writing the Cartesian components of the baseline vector $\underline{D}$ as (u, v, w) such that:

$$u = (x_2 - x_1)/\lambda_1$$
$$v = (y_2 - y_1)/\lambda_1$$
$$w = \frac{z_2 - z_1}{\lambda_1} = 0 \qquad (3)$$

Where λ_1 is the wavelength in host medium.

Fig. 3 shows the spherical polar coordinate system, defining new variables (l, m) as:

$$l = \sin\theta \cos\phi$$
$$m = \sin\theta \sin\phi \qquad (4)$$

The 2D breast intensity function $\tilde{I}(l, m)$ is obtained from our developed HMIA image algorithm [11].

$$\tilde{I}(l, m) = \iint G(u, v, 0) e^{j2\pi(ul+vm)}\, du dv \qquad (5)$$

The 2D image is the intensity function $\tilde{I}(l, m)$ represents the scattering intensity in the breast integrated along each radial vector.

To quantitatively assess imaging results, a zooming function can be applied to enhance the image contrast:

$$\tilde{I}_m(l, m) = [\tilde{I}(l, m)]^Q \qquad (6)$$

Equation (6) performs a Q: 1 zoom on an image of the breast. A computer model was developed using MATLAB the recently achieved simulation results can be found in [11]-[12].

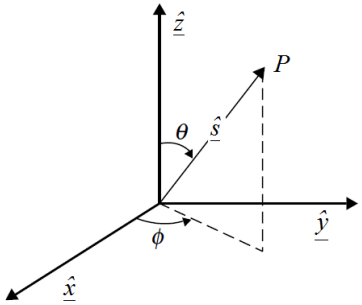

Fig. 3: Spherical polar coordinate system

3. Experiment

The 2D HMIA system experimental set-up is illustrated in Fig. 4. An array of 16 antennas were embedded in a sheet of microwave absorbing material ECCOSORB AN-79 (600 mm x 600 mm) to reduce ambient reflections. The antennas were connected to an Agilent N5230A (10 MHz - 20 GHz) vector network analyzer (PNA).

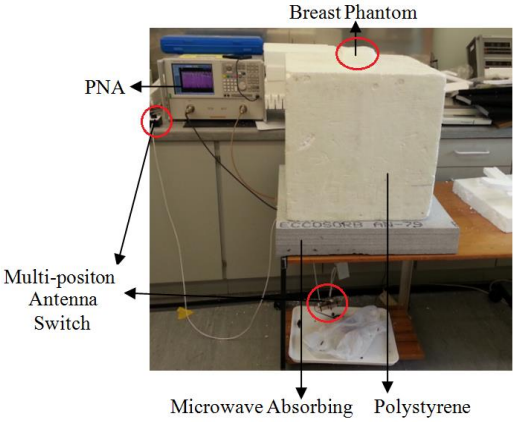

Fig. 4: Photo of 2D HMIA system experimental set-up

Fig. 5 shows the location for all antennas. A small open-ended rectangular wave-guide antenna (with 120 mm in length, 15.8 mm and 7.5 mm in the broad and narrow wall dimensions) was selected for experiments because of its low-cost

and ease of manufacture. The small size also allowed for the positioning of many antennas close to the imaging domain.

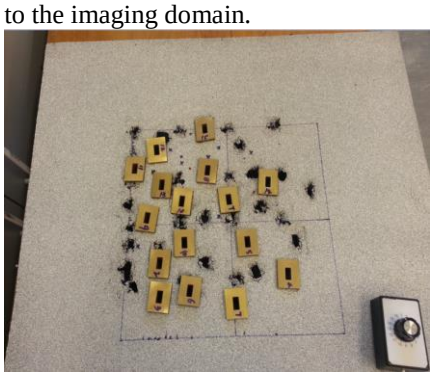

Fig. 5: Schematic of array configuration

A simplified breast phantom (100 mm x 100 mm x 30 mm) containing skin, fat tissue and malignant tumours was used in the experiments. Breast fat tissue was made of 90% Emulsifying Ointment BP (that contained 30% emulsifying wax, 50% white soft paraffin and 20% liquid paraffin) and 10% water. Small grapes (4 mm, 5 mm and 7 mm in diameter) were inserted into the breast phantoms modelled to represent malignant tissues. The skin layer in the phantom was created using a 3-mm-thick MACOR machinable glass ceramic (MGC) plate (100 mm x 100 mm). The breast phantom was shaped in a rectangular plastic box and was covered by a thin plastic film. The latter has a negligible effect on the scattered electromagnetic field in the desired frequency range. The electrical properties of the breast phantoms are summarized in TABLE 1.

TABLE 1: Permittivity Of Object At 12.6 GHz

Material	Real-part of permittivity	Imaginary-part of permittivity	Data source
Breast tissue	2.4307	0.2432	Measured
Tumour	23.8021	20.8695	Measured
Skin (at 8.5 GHz)	5.67	0.040257	Manufacturer
Air	1	0	Published

During data collection, the breast phantom was placed on the top of a polystyrene box at z=0 mm and the antenna array plane was placed at z=-450 mm. Air was used as the host medium between the breast phantom and the antenna array plane. The breast phantom was illuminated by the transmitter and the magnitude and phase of the scattered field at each antenna was recorded at a frequency of 12.6 GHz. The complex correlation of the scattered field data between all possible pairs of antennas was then computed to generate a complex visibility function and then the equation (5) was applied to generate a 2D image.

4. Experimental Results

The first breast phantom used in this research is shown in Fig. 6. It contains three tumours (4 mm, 5 mm, 7 mm in diameter) located at (x=20 mm, y=50 mm, z=25 mm), (x=40 mm, y=50 mm, z=25 mm) and (x=85 mm, y=50 mm, z=25 mm).

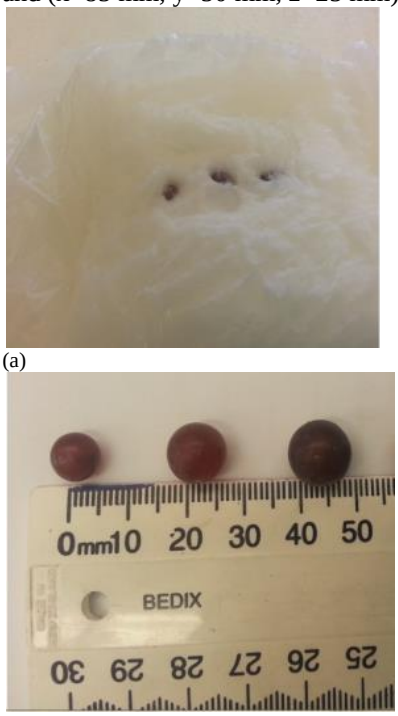

(a)

(b)

Fig. 6: (a) Phantom of three tumours (b) Size of tumours

The three simulated tumours in the reconstructed 2D phantom image as shown in Fig. 7.

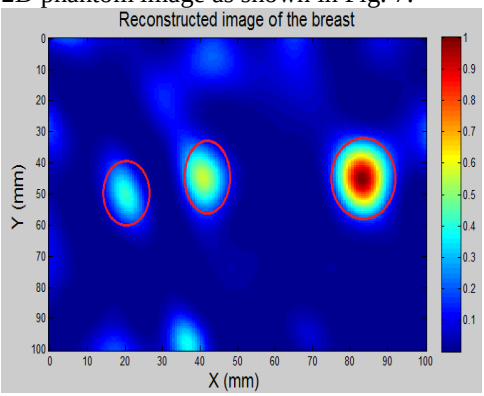

Fig. 7: Image result of breast phantom

Fig. 8 illustrates the breast phantom containing skin and three tumours (13 mm, 10 mm, 10 mm in diameter) located at (x=40 mm, y=50 mm, z=25 mm), (x=60 mm, y=50 mm, z=25 mm) and (x=90 mm, y=55 mm, z=25 mm).

(a)

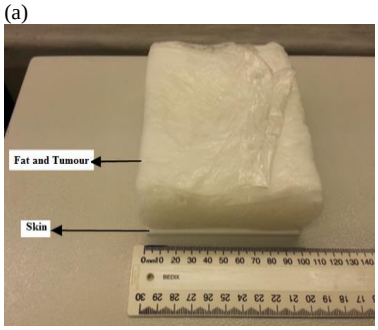

(b)

Fig. 8: Phantom containing skin and three tumours (a) inside view (b) side view

Fig. 9 clearly shows the three simulated tumours in the reconstructed 2D phantom image.

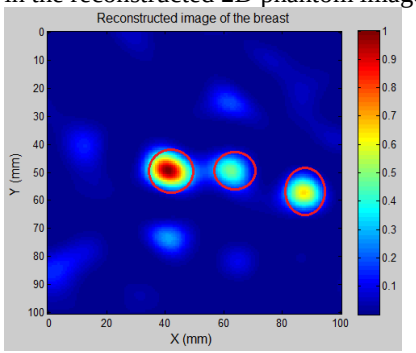

Fig. 9**:** Image result of breast phantom

Colour bars in reconstructed images plot signal energy on a linear scale, normalised to the maximum in the 3D volume. Values below 0.1 are rendered as blue. Data used to produce the images shown in Fig. 7 and Fig. 9 utilise a "zooming function" of power two to enhance the contrast with the background.

5. Conclusion

The work described in this paper has demonstrated the feasibility of the 2D HMIA image algorithm as a method for early breast cancer detection. No additional impedance matching medium was necessary between phantom and antenna array, only air, which greatly simplifies the practical implementation of such a system. The experimental results showed that tumours of different size, shape and location could be detected against the background. This technique has the potential to become a low-cost and easy-to-use screening and diagnostic tool for breast cancer detection that could supplement existing clinical methods.

Acknowledgement

The authors gratefully acknowledge the support of the Institute of Biomedical Technologies (IBTec) at the Auckland University of Technology (AUT), and the support of Callaghan Innovation, Auckland, New Zealand.

The authors also would like to acknowledge Mr. Terry Palmer and Mr. Tim Wyatt at Callaghan Innovation, for manufacturing the cables, switch assembly and waveguides for the experimental set-up.

References

[1] Meaney, P. M., Paulsen, K. D., Hartov, A., & Crane, R. K., "An active microwave imaging system for reconstruction of 2-D electrical property distributions", IEEE Transactions on Biomedical Engineering, Vol. 42, No. 10, pp. 1017-1026, 1995.

[2] Hagness, S. C., Taflove, A., & Bridges, J. E., "Two-dimensional FDTD analysis of a pulsed microwave confocal system for breast cancer detection: Fixed-focus and antenna-array sensors", IEEE Transactions on Biomedical Engineering, Vol. 45, No. 12, pp. 1470-1479, 1998.

[3] Fear, E. C., Li, X., Hagness, S. C., & Stuchly, M. A., "Confocal microwave imaging for breast cancer detection: Localization of tumors in three dimensions", IEEE Transactions on Biomedical Engineering, Vol. 49, No. 8, pp. 812-822, 2002.

[4] Smith, D., Leach, M., & Sambell, A., "An indirect holographic method for determining antenna radiation patterns and imaging antenna fields", IEEE Antennas and Propagation Society International Symposium, Vol. 3, pp. 706-709, 2002.

[5] Bond, E. J., Li, X., Hagness, S. C., & Van Veen, B. D., "Microwave imaging via space-time beamforming for early detection of breast cancer", IEEE Transactions on Antennas and Propagation, Vol. 51, No. 8, pp. 1690-1705, 2003.

[6] Li, X., Bond, E. J., Van Veen, B. D., & Hagness, S. C., "An overview of ultra-wideband microwave imaging via space-time beamforming for early-stage breast-cancer detection", IEEE Transactions on Antennas and Propagation Magazine, Vol. 47, No. 1, pp. 19-34, 2005.

[7] Davis, S. K., Tandradinata, H., Hagness, S. C., & Van Veen, B. D., "Ultrawideband microwave breast cancer detection: a detection-theoretic approach using the generalized likelihood ratio test", IEEE Transactions on Biomedical Engineering, Vol. 52, No. 7, pp. 1237-1250, 2005.

[8] Ibrahim, W. M. A., & Algabroun, H. M., "The Family Tree of Breast Microwave Imaging Techniques", 4th Kuala Lumpur International Conference on Biomedical Engineering pp. 258-261, Springer Berlin Heidelberg, 2008.

[9] Rubæk, T., Kim, O. S., & Meincke, P., "Computational validation of a 3-D microwave imaging system for breast-cancer screening", IEEE Transactions on Antennas and Propagation, Vol. 57, No. 7, pp. 2105-2115, 2009.

[10] Meaney, P. M., Fanning, M. W., Raynolds, T., Fox, C. J., Fang, Q., Kogel, C. A., & Paulsen, K. D., "Initial clinical experience with microwave breast imaging in women with normal mammography",. Academic radiology, Vol. 14, No. 2, pp. 207-218, 2007.

[11] Wang, L., Simpkin, R. and Al-Jumaily, A.M., "Holography Microwave Imaging Array for Early Breast Cancer Detection", Proceedings of 2012 ASME International Mechanical Engineering Congress & Exposition, Paper No. 85910, Houston, Texas, United States, 9th to 15th Nov, 2012.

[12] Wang, L., Simpkin, R., & Al-Jumaily, A. M., "3D breast cancer imaging using holographic microwave interferometry", Proceedings of the 27th Conference on Image and Vision Computing New Zealand, pp. 180-185, Nov, 2012.

Conference Paper 4

Three-Dimensional Holographic Microwave Imaging Array: Experimental Investigation of Tumour Detection in Breast Phantom

Lulu Wang Ray Simpkin Al-Jumaily, A. M.

Status: Accepted 2013

Conference: 2013 ASME International Mechanical Engineering Congress & Exposition

November 15-21, 2013 San Diego, CA, United States

Proceedings of IMECE2013
2013 ASME International Mechanical Engineering Congress & Exposition
November 15-21, 2013 San Diego, CA, United States

IMECE2013-63132

THREE-DIMENSIONAL HOLOGRAPHIC MICROWAVE IMAGING ARRAY: EXPERIMENTAL INVESTIGATION OF TUMOUR DETECTION IN BREAST PHANTOM

Wang, Lulu
luwang@aut.ac.nz
Institute of Biomedical Technologies
Auckland University of Technology
Auckland, New Zealand

Simpkin, Ray
ray.simpkin@callaghaninnovation.govt.nz
Callaghan Innovation
Auckland, New Zealand

Al-Jumaily, A. M.
ahmed.al-jumaily@aut.ac.nz
Institute of Biomedical Technologies
Auckland University of Technology
Auckland, New Zealand

ABSTRACT

This paper extends our previously presented two-dimensional (2-D) Holographic Microwave Imaging Array (HMIA) system for early breast tumour detection to three-dimensional (3-D) imaging, and demonstrates its efficacy using experimental data obtained with a breast phantom. This work describes an experimental set-up to collect data to form a 3-D breast image. The obtained experimental result proves that the 3-D HMIA system has potential to become a screening and diagnostic tool that could supplement clinical breast examination through its sensitivity, quantitative record storage, ease-of-use, and inherent low cost.

Keywords— Microwave Imaging, Holographic Microwave Imaging Array, Breast Cancer Detection, Interferometry

I INTRODUCTION

The potential use of microwave for breast cancer detection has received significant attention in recent years [1]. The physical basis for the microwave technique is tissue dependent microwave scattering and absorption in the breast due to the contrast in the dielectric properties between the malignant and normal breast tissues [2].

The 3-D HMIA for early breast cancer detection has been recently presented [3]. Simulation results showed that tumours as small as 2 mm in diameter within the breast model could be detected. This paper details the first-generation 3-D HMIA experimental set-up. The simplified breast phantom mimicks skin, malignant tissue and healthy fat tissue. In our initial experimental feasibility study of the HMIA approach, small malignant tumours at different locations were successfully imaged in a homogeneous 3-D background.

II EXPERIMENTAL SET-UP

Figure 1 displays the 3-D HMIA experimental set-up. An array of 16 antennas was surrounded with an ECCOSORB AN-79 (24 inch x 24 inch) electromagnetic absorbing material to reduce ambient reflections and antennas were positioned as shown in Figure 2.

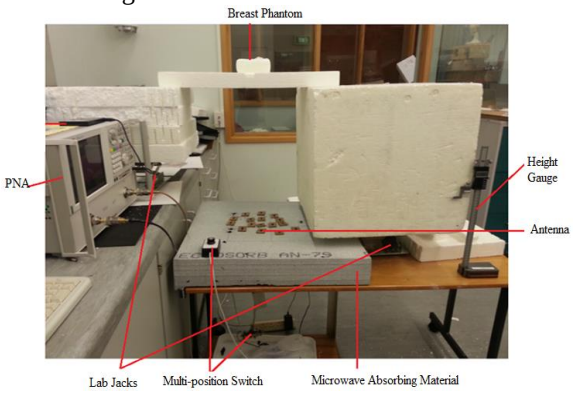

Figure 1: Photo of 3D HMIA system experimental set-up

The antenna array was connected with an Agilent N5230A (10 MHz - 20 GHz) vector network analyser (PNA). The breast phantom was placed on the top of the polystyrene box bridge and air was used as the host medium between the breast phantom and antenna array plane. Two lab jacks were used to vertically displace the breast phantom from $z = 540$ mm to $z = 570$ mm in 15 equal steps. A height gauge was used to measure the

vertical displacement of the phantom and a spirit level was used to balance the polystyrene box bridge during movement.

A small open-ended rectangular wave-guide antenna was selected for experiments because of its low-cost and ease of manufacture. The small size also allowed for the positioning of many antennas close to the imaging domain. The antenna is 120 mm in length, the broad and narrow wall dimensions of the antenna are 15.8 mm and 7.5 mm, respectively.

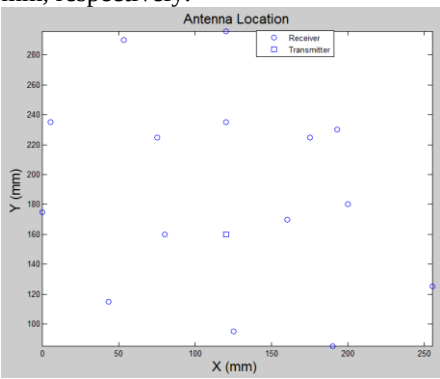

Figure 2: Schematic of array configuration

A simplified breast phantom was considered to include skin, fat tissue and malignant tumours. Breast fat tissue was simulated with Emulsifying Ointment BP that contains 30% emulsifying wax, 50% white soft paraffin and 20% liquid paraffin.

A small grape (10 mm in diameter) was inserted into the breast phantoms modeled to represent malignant tissue. The skin layer in the phantom was created using a 3-mm-thick MACOR machinable glass ceramic (MGC) plate (100 mm x 100 mm). According to the manufacturer, the dielectric constant of MGC is 5.67 at 8.5 GHz with a loss tangent of 0.0071.

Table 1 PERMITTIVITY OF PHANTOM MATERIAL

Material	Real-part of permittivity	Imaginary-part of permittivity	Data source
Breast tissue (wax)	2.4307	0.2432	Measured
Skin (ceramic plate)	5.67	0.040257	Manufacturer
Tumour (Grape)	21.2329	19.265	Measured
Air	1	0	Published

The electrical properties of the breast phantoms are summarized in Table 1, the ratio of breast tumour and normal fat tissue is approximately 8.7:1. The breast phantom was shaped in a rectangle plastic box and was covered by thin plastic film. The latter has a negligible effect on the scattered electromagnetic field in the considered frequency range. Air was selected as the host medium to fill the space between the breast phantom and antenna array.

The breast phantom was illuminated by the transmitter and the magnitude and phase of the scattered field at each receiver was recorded at a frequency of 12.6 GHz. These data collection steps were repeated for each height of the phantom above the antenna array plane. The complex correlation of the scattered field data between all possible pairs of antennas was then computed to generate a complex visibility function required as input to the 3-D imaging algorithm [3]

III RESULTS

The breast phantom (100 mm x 100 mm x 30 mm) contains skin and one tumour (10 mm in diameter) located at the center of the breast phantom. It was placed at a height above the antenna array plane that was varied between 540 mm and 570 mm in 15 equal steps. Figure 3 clearly shows the simulated tumour and skin layer in the reconstructed 3-D phantom image. Colour bar plots signal energy on a linear scale, normalised to the maximum in the 3-D volume. Values below 0.1 are rendered as blue. Data used to produce the image shown in Figure 3 utilise a "zooming function" of power two to enhance the contrast with the background.

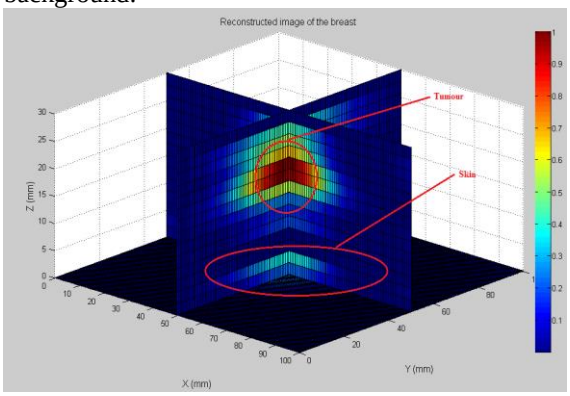

Figure 3: Side views of 3-D images of breast phantom

IV CONCLUSION

In this paper, a new 3-D holographic microwave imaging array (HMIA) for early breast cancer detection is described based on holographic imaging technique. The experimental result presented shows that the proposed 3-D HMIA system has the potential to become a screening and diagnostic tool that could supplement existing methods through its high sensitivity, quantitative record storage, ease-of-use, and inherent low cost.

ACKNOWLEDGMENT

The authors gratefully acknowledge the support of the Institute of Biomedical Technologies (IBTec) at the Auckland University of Technology (AUT), and the support of Callaghan Innovation, Auckland,

New Zealand. The authors also would like to acknowledge Mr. Terry Palmer and Mr. Tim Wyatt at Callaghan Innovation for manufacturing the cables, switches and waveguides used for the experimental set-up.

REFERENCES

[1] Abbosh, A. (2009, June). Early breast cancer detection using hybrid imaging modality. In *Antennas and Propagation Society International Symposium, 2009. APSURSI'09. IEEE* (pp. 1-4). IEEE.

[2] Meaney, P. M., Paulsen, K. D., Hartov, A., & Crane, R. K. (1995). An active microwave imaging system for reconstruction of 2-D electrical property distributions. *Biomedical Engineering, IEEE Transactions on*, *42* (10), 1017-1026.

[3] Wang, L., Simpkin, R., & Al-Jumaily, A. M. (2012, November). 3D breast cancer imaging using holographic microwave interferometry. In *Proceedings of the 27th Conference on Image and Vision Computing New Zealand* (pp. 180-185). ACM.

Conference Paper 5

Open-ended Waveguide Antenna for Microwave Breast Cancer Detection

Lulu Wang Ray Simpkin Al-Jumaily, A. M.

Status: Published 2013

Conference: Proceedings of 2013 IEEE International Workshop on Electromagnetics

1-3 August, 2013, Hong Kong, China

OPEN-ENDED WAVEGUIDE ANTENNA FOR MICROWAVE BREAST CANCER DETECTION

Lulu Wang[1], Ray Simpkin[2] and A. M. Al-Jumaily[1]
[1] Institute of Biomedical Technologies, Auckland University of Technology, Auckland, New Zealand
Email: luwang@aut.ac.nz, ahmed.al-jumaily@aut.ac.nz
[2] Callaghan Innovation, Auckland, New Zealand
Email: ray.simpkin@callaghaninnovation.govt.nz

Microwave imaging techniques for breast cancer detection have attacked many research groups recently. The key element for the microwave imaging system is the antenna. In this paper, a small flanged open-ended rectangular waveguide antenna (ORWA) is proposed for breast cancer detection. WR 62 waveguide that has cut-off frequency of 9.5 GHz is used in the design process. A 16-element antenna array plane is proposed for operation at a frequency of 12.6 GHz. The scattered field detection capability is also tested under our developed holographic microwave imaging array (HMIA) system for breast phantom detection. The experimental results show that the proposed ORWA has the ability to detect tumour as small as 2.5 mm within the breast phantom.

***Index Terms*— Antenna Array, Antenna Array Configuration, Flanged Antenna, Holographic Microwave Imaging Array, Open-ended Wave-guide Antenna**

I. INTRODUCTION

BREAST cancer is the most common cancer in women worldwide [1]. Research shows that only early detection (when the tumour less than 5 mm) and timely treatment can significantly increase the survival rate [2]. Currently available clinical breast cancer diagnosis tools include ultrasound, X-ray mammography and magnetic resonance imaging (MRI). However, these technologies have many limitations, such as unable to detect breast tumours at early stage, high rate of missed detections, ionizing radiation, or are too expensive to be widely available.

Microwave imaging investigates the high contrast of the dielectric property between the normal breast tissue and the malignant tissue [3]. Microwave imaging has been investigated by numerous research groups [2]-[9] because it has the potential to be both sensitive and specific to detect tumours at their early stage and more comfortable than common detection technologies. In addition, it is safe and cost effective compare to other diagnosis methods, such as X-ray mammography and MRI.

Designing a suitable antenna is one of the biggest challenges of constructing a microwave breast cancer imaging system. In a microwave imaging system, a transmitting antenna is used to illuminate the object with microwaves that travels through the object and is then detected with either a receiving antenna or with the same transmitting antenna. The measured data is then processed using a reconstruction algorithm to detect objects by studying the complex dielectric permittivity of the scattering object. Most antennas designs proposed recently have been applied to the time-domain based detection method which is capable of detecting the location of a tumour, but is not targeted for the reconstruction of the whole breast dielectric distribution [10].

This paper presents a simple small flanged open-ended rectangular waveguide antenna (ORWA) that operates at single frequency of 12.6 GHz. The performance of the proposed antenna has undergone significant testing to validate its performance. An array of 16 small ORWAs has been measured under our developed HMIA system [11] with a multi-layer breast phantom to study the backscattered field of the breast. The detection capability of the antenna array has been investigated and compared with simulation and experimental results.

II. ANTENNA DESIGN

To design an antenna suitable for an HMIA system, the following factors need to be considered:

- The antenna should be able to radiated the wave into the sample and to receive the backscattered field from the target
- The antenna should be compact enough to be located on to a scanning arrangement
- The antenna should be easy to move and relocated on the array plane to study the performance of antenna array
- The antenna should be cost effective and widely available

It is important to know how the aperture impedance varies with frequency when matching an ORWA to free space. Boyd [12] details how the aperture impedance presented to an open-ended waveguide antenna element can be adequately approximated by the impedance presented to the waveguide element by a larger air-filled simulator waveguide.

A. Open-ended Rectangular Waveguide Antenna (ORWA)

Fig. 1 shows the schematic of a small flanged ORWA. The excitation port P was placed at 9 mm from the end of waveguide and the dimensions are listed in Table I. This design was selected for HMIA experiments because of its low-cost and ease of manufacture. The small size also allowed for the positioning of many antennas close to the imaging domain.

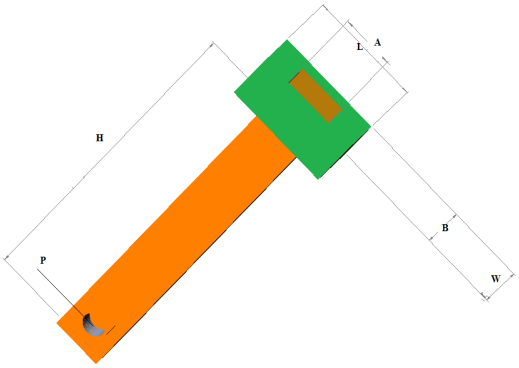

Fig. 1 Configuration of flanged open-ended rectangular waveguide antenna

Table I DIMENSIONS OF FLANGED ORWA

Parameter	Dimension (mm)
Width of waveguide (A)	15.8
Length of waveguide (B)	7.9
Height of waveguide (H)	120
Thickness of the waveguide walls	1
Length of flange (L)	38
Width of flange (W)	2
Thickness of the flange (T)	6
Length of excitation port from the end of waveguide (P)	9

The WR 62 waveguide which has a cut-off frequency of 9.5 GHz was used to design the ORWA shown in Fig. 2. A small Male SMA connector was inserted through the side wall of the waveguide and was placed at 9 mm from the bottom of the antenna (termination) as the excitation port. This enabled the waveguide to be connected with an RG coaxial cable for measurement and analysis.

Fig. 2. Photography of the flanged ORWA with connection cable

B. Antenna Array

A 16-element array was developed to investigate the feasibility of detecting breast tumours using HMIA. The flanged ORWA was used as both the transmitter and receiver. One of the most suitable antenna arrays for microwave breast cancer detection is shown in Fig. 3 where one ORWA acts as transmitting antenna and the remaining devices act as receiving antennas.

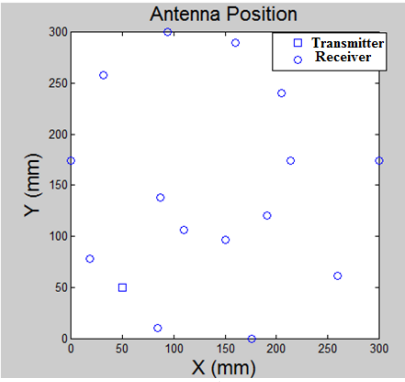

Fig. 3 Antenna array configuration

III Results

A. Antenna Characteristics

The proposed antenna design was tested using a two-port Agilent N5230A (10 MHz - 20 GHz) vector network analyzer (PNA). Although only a single frequency was applied for reconstructing the image, the wide frequency spectrum from 10 GHz to 20 GHz was collected to determine the optimum operating frequency. Data was recorded at 3201 frequency points for choosing the optimum frequency, and 101 measurements were averaged at each frequency.

Fig. 4 illustrates the measured magnitude of the reflection coefficient (S_{11}) of the waveguide antenna at the frequency spectrum from 10 GHz to 20 GHz. This showed that all the measured return losses are below -10 dB. The best performance of the wave-guide antenna is obtained at the operating frequency of approximately 12.12 GHz with return loss below -60 dB.

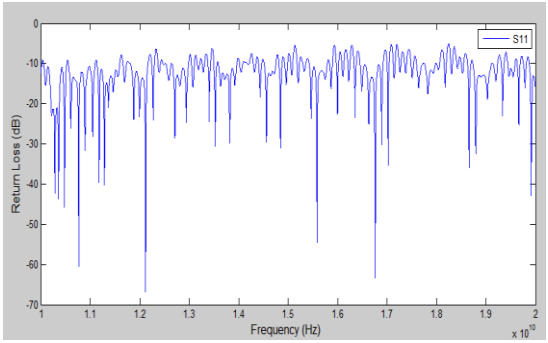

(a)

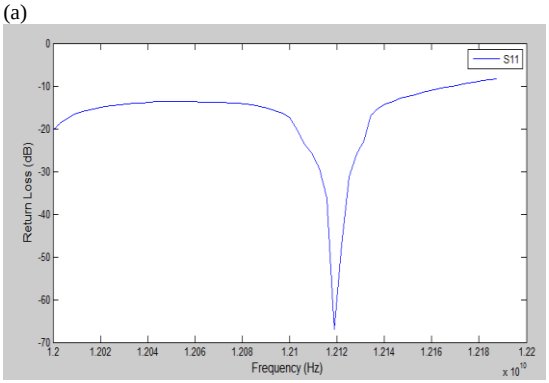

(b)

Fig. 4. Measured return loss of antenna with frequency range between (a) 10 GHz to 20 GHz (b) 12 GHz to 12.2 GHz

B. Tumor Detection

1) Experiment Set-up

The experimental system as shown in Fig 5 consisted of a breast phantom and an array of 16 antennas connected to an Agilent N5230A PNA. The reflection coefficient (S_{21}) was measured for each receiving antenna over the frequency range of 10 GHz to 20 GHz. The breast phantom was placed on the top of the polystyrene box bridge and air ($\varepsilon = 1$) was used as the host medium between the breast phantom and the antenna array plane. To get a 3D breast image, two lab jacks were used to move the breast phantom from $z = 540$ mm to $z = 580$ mm. A height gauge was used to measure the phantom movements of 1 mm in step and a spirit level was used to balance the polystyrene box bridge during movement.

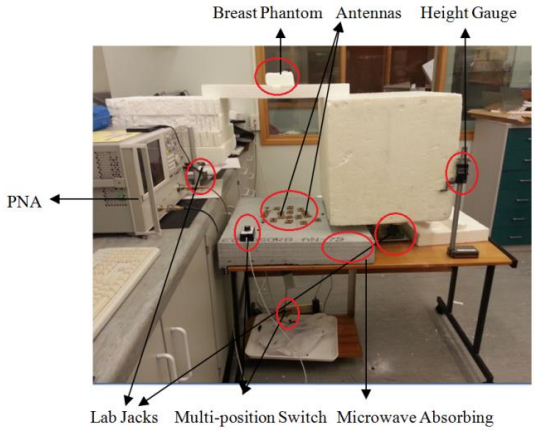

Fig. 5. Photography of antenna measurement set-up

The antenna array plane is shown in Fig. 6. The antennas were located in a spiral configuration and surrounded with a sheet of ECCOSORB AN-79 (600 mm x 600 mm) electromagnetic absorbing material to reduce ambient reflections.

Fig. 6. Photo of antenna array

The breast phantom stimulant material was constructed using emulsifying ointment BP. To simulate tumours, small grapes and cucumbers were inserted into the breast phantom. In this way, the permittivity ratio of the normal and the malignant tissue stimulant materials was between 7.84 and 12.95 as shown in Fig 7. A 3-mm-thick machinable glass ceramic plate was used to represent the skin layer. According to the manufacturer, the dielectric constant of the glass ceramic is 5.67 at 8.5 GHz with a loss tangent of 0.0071. The breast phantom was shaped in a rectangular plastic box (100 mm x 100 mm x 30 mm) and was covered by a thin plastic film. The latter has a negligible effect on the scattered electromagnetic field in the desired frequency range.

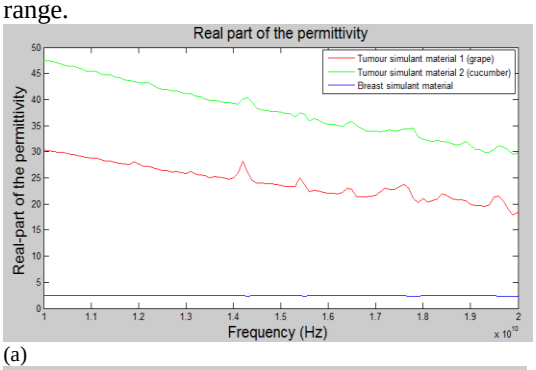

(a)

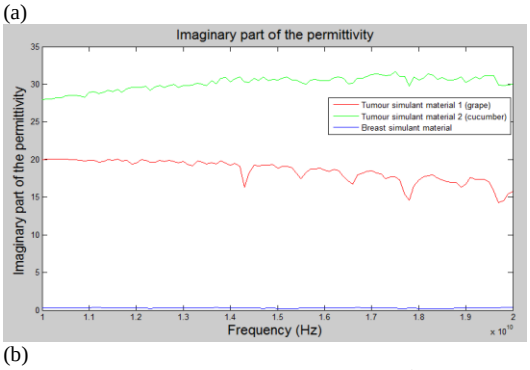

(b)

Fig. 7. (a) Real part and (b) Imaginary part of the permittivity of the breast and tumour simulant materials

The breast phantom was illuminated by the transmitting antenna and the magnitude and phase of the scattered field at each receiving antenna was recorded at a frequency of 12.6 GHz. These data collection steps were repeated for each height increment of the phantom above the antenna array plane. The complex correlation of the scattered field data between all possible pairs of antennas was then computed to generate a complex visibility function which is used as the input to the HMIA imaging algorithm [11].

2) Tumor Detection Results

Fig 8 shows the breast phantom containing one tumour (10 mm in diameter) with skin, where the tumour was located at (x=50 mm, y=50 mm, z=15 mm). It was placed at a height above the antenna array plane that was varied between $z = 541$ mm and $z = 580$ mm in 39 equal steps.

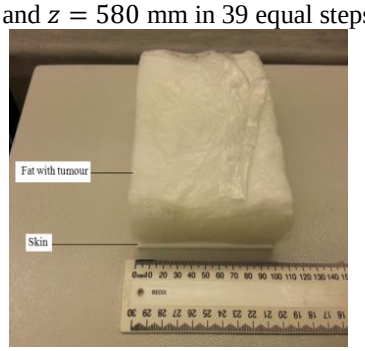

(a)

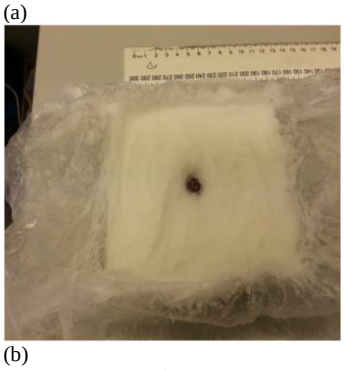

(b)

Fig. 8 Phantom of one tumour with skin (a) side view (b) top view

The simulated tumour and skin layer in the reconstructed 3D phantom image is demonstrated in Fig 9.

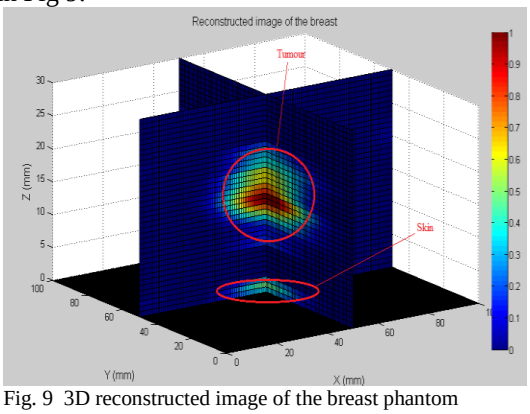

Fig. 9 3D reconstructed image of the breast phantom

Fig 10 shows the phantom containing skin and two tumours (2.5 mm and 5 mm), where tumours were located at (x=35 mm, y=50 mm, z=25 mm) and (x=55 mm, y=60 mm, z=25 mm). It was placed above the antenna array plane at z=490 mm.

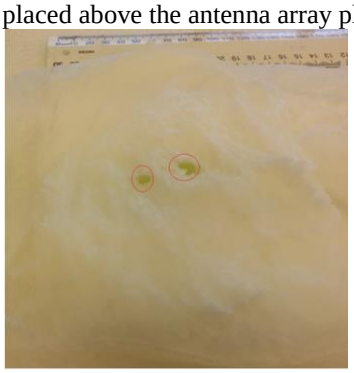

(a)

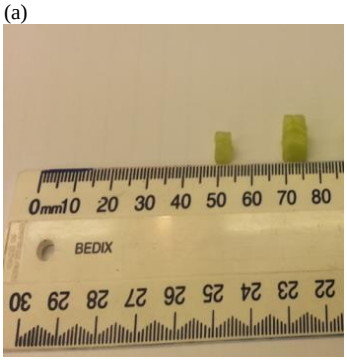

(b)

Fig. 10 Phantom of two tumours with skin (a) inside view (b) size of tumours

Fig 11 clearly shows the simulated two tumours in the 2D reconstructed image of the breast phantom.

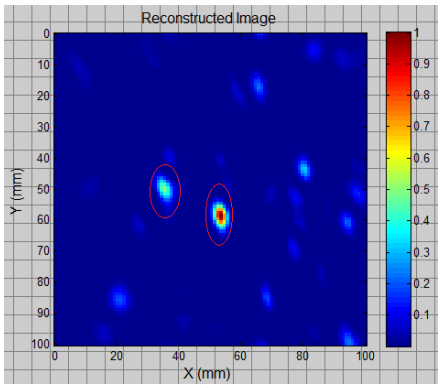

Fig. 11 2D Image of the breast phantom containing two tumours

In Fig 9 and Fig 11, colour bars plot signal intensity on a linear scale that is normalised to the maximum in the 3D volume, and the data used to produce the images utilises a -"zooming function"- of power two to enhance the contrast with the background. Values below 0.1 are rendered as blue.

IV. CONCLUSION

A flanged ORWA design for breast tumour detection has been presented in this paper. The antenna was designed to radiate directly into an air without a matching solution medium that has similar dielectric properties to breast tissue. ORWA has many advantages such as low-cost, ease of manufacture and ease of repositioning on the array plane. This enables the performance of an antenna array to be investigated. The small size also allowed for the positioning of many antennas close to the imaging domain. The best performance for a 16-element antenna array was achieved at 12.6 GHz. The experimental results demonstrated that the 16-element antenna array is capable of producing good-quality images of objects at various locations, even when tumour less than 3 mm.

ACKNOWLEDGMENT

The authors gratefully acknowledge the support of the Institute of Biomedical Technologies (IBTec) at the Auckland University of Technology (AUT), and the support of Callaghan Innovation, Auckland, New Zealand.

The authors also would like to acknowledge Mr. Terry Palmer and Mr. Tim Wyatt at Callaghan Innovation, for manufacturing the cables, switch assembly and waveguides for the experimental set-up.

REFERENCES

[1] American Cancer Society, "Cancer Facts & Figures 2012", *American Cancer Society*, 2012.

[2] Liu, G. D., & Zhang, Y. R., "An overview of active microwave imaging for early breast cancer detection", *Journal of Nanjing University of Posts and Telecommunications (Natural Science)*, Vol. 30, No. 1, 2010.

[3] Hagness, S. C., Taflove, A., & Bridges, J. E., "Two-dimensional FDTD analysis of a pulsed microwave confocal system for breast cancer detection: Fixed-focus and antenna-array sensors", *IEEE Transactions on Biomedical Engineering*, Vol. 45, No. 12, pp. 1470-1479, 1998.

[4] Fear, E. C., & Stuchly, M. A., "Microwave detection of breast cancer: a study of tumor response variations", *Proceedings of the 22nd Annual International Conference of the IEEE Engineering in Medicine and Biology Society*, Vol. 1, pp. 74-77, 2000.

[5] Fang, Q., Meaney, P. M., Geimer, S. D., Streltsov, A. V., & Paulsen, K. D., "Microwave image reconstruction from 3-D fields coupled to 2-D parameter estimation", *IEEE Transactions on Medical Imaging*, Vol. *23, No.* 4, pp. 475-484, 2004.

[6] Kosmas, P., & Rappaport, C. M., "Time reversal with the FDTD method for microwave breast cancer detection", *IEEE Transactions on Microwave Theory and Techniques*, Vol. 53, No. 7, pp. 2317-2323, 2005.

[7] Smith, D., Elsdon, M., Leach, M., FDO, M., & Foti, S. J., "A Method for 3D Breast Cancer Imaging using Microwave Holography", *International Symposium on Antennas and Propagation*, 2006.

[8] Tipa, R., & Baltag, O., "Microwave thermography for cancer detection", *Romanian Journal of Physics*, Vol. 51, No. 3/4, pp. 371, 2006.

[9] Rubæk, T., Kim, O. S., & Meincke, P., "Computational validation of a 3-D microwave imaging system for breast-cancer screening", *IEEE Transactions on Antennas and Propagation*, Vol. 57, No. 7, pp. 2105-2115, 2009.

[10] Yu, J., Yuan, M., & Liu, Q. H., "A wideband half oval patch antenna for breast imaging", *Progress In Electromagnetics Research*, Vol. 98, pp. 1-13, 2009.

[11] Wang, L., Simpkin, R., & Al-Jumaily, A. M., "3D breast cancer imaging using holographic microwave interferometry", *Proceedings of the 27th Conference on Image and Vision Computing New Zealand*, pp. 180-185, Nov, 2012.

[12] Boyd, C. R., "Impedance Matching of Open-Ended Waveguide Radiating Elements", *SBMO International Microwave Symposium*, 1987.

Conference Paper 6

Holographic Microwave Imaging for Brain Stroke Detection

Lulu Wang Ray Simpkin Al-Jumaily, A. M.

Status: Accepted 2013, Paper ID: SICASE 2013 – Paper 44.

Conference: 2013 Shanghai International Conference on Applied Science and Engineering, July 12-14, 2013, Shanghai, China

Microwave Imaging for Brain Stroke Detection

Lulu Wang[a], Ray Simpkin[b] and A. M. Al-Jumaily[a]

[a] Institute of Biomedical Technologies, Auckland University of Technology, Auckland, New Zealand
Email: luwang@aut.ac.nz, ahmed.al-jumaily@aut.ac.nz

[b]Callaghan Innovation, Auckland, New Zealand
E-mail: ray.simpkin@callaghaninnovation.govt.nz

Abstract

This paper proposes a new two-dimensional (2-D) holographic microwave imaging array (HMIA) technique for brain imaging with particular focus on stroke detection. The system is designed for operation at a single frequency of 2 GHz. A realistic 2-D head model that contains skin, fat, skull, cerebrospinal fluid (CSF), grey matter, white matter and stroke area is developed using MATLAB to demonstrate the proposed HMIA imaging algorithm. The matching solution medium is not necessary in this system. Air is used between the antennas and the head model. The method of moments (MoM) is employed for forward problem solving and the simulation results showed that small stroke area (5 mm in diameter) could be successfully detected with the HMIA approach.

Keyword: Microwave Imaging, Holographic Microwave Imaging Array, Aperture Synthesis Imaging, Brain Imaging, Brain Stroke

1. Introduction

A brain stroke is the third leading cause of death after the heart disease and cancer [1]. An incorrect determination of the stroke can lead to the death of the patient [2]. Microwave based imaging techniques create a map of electromagnetic wave scattering arising from the contrast in the dielectric properties of different tissues and have been investigated as one of the most promising medical imaging tools for many years [3-4]. The advantages of microwave imaging include a whole view of body tissue, lower cost, more comfortable and no radiations. Recent investigations [5-7] indicated that microwave imaging has the potential to determine perfusion related changes in the human brain and microwave based imaging approaches could be developed as a useful new imaging modality for stroke management.

Unlike these groups [5-7], we propose a new holographic microwave imaging array (HMIA) system for hemorrhagic stroke detection using the MoM forward problem solver and 2-D HMIA imaging algorithm. This paper details the 2-D HMIA imaging algorithm, the simulation model and simulation results.

2. Theory

Fig 1 shows the measurement of the HMIA system. The system contains an array of 16 small antennas, one is the transmitter and others are receivers, which are located around the head model in far-filed distance. The space between the operating bed and antenna array is filled with air ($\varepsilon_r = 1$). The system is designed for operating at a single frequency of 2 GHz [7]. When the transmitter transmits the electromagnetic field, the other 15 antennas receive the scattered electromagnetic field. The HMIA measures the scattered radiation of the head, which is composed of a set of correlation interferometer pairs. The electromagnetic signals received by each pair are cross-correlated to get the visibility function.

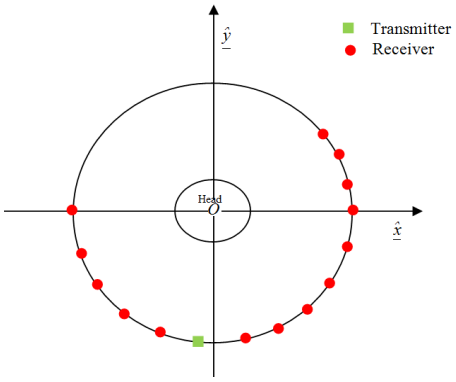

Fig 1 Structure of HMIA system

Fig 2 shows the geometry relevant to 2-D HMIA system. If two points $P(x,y)$ and $P'(x',y')$ are assumed within the head, the visibility function G_{ij} of the backscattered electric field $\underline{E}_{scat}$, of the head for any two antennas A_i and A_j located at $\underline{r_i}$ and $\underline{r_j}$ is defined as:

$$G(\underline{r_i},\underline{r_j}) = < \underline{E}_{scat}\left(\underline{r_i}\right) \cdot \underline{E}^*_{scat}(\underline{r_j}) > \qquad (1)$$

Where * denotes the complex conjugate and <> stands for the expected value (time average).

The backscattered electric field $\underline{E}_{scat}$ from the head at any receiver A_i, can be found by applying the Method of Moments (MoM) [8].

$$\underline{E}_{scat}\left(\underline{r}_i\right) = \left(-\frac{jk_b^2}{4}\right)\int_A \left|\varepsilon(\underline{s}) - \varepsilon_b\right| \underline{E}_T(\underline{s}) H_0^2(k_b \underline{R}) dA \qquad (2)$$

Where $j = \sqrt{-1}$, $k_b = 2\pi/\lambda_b$, λ_b is the wavelength in host medium, $\varepsilon(\underline{s})$ and ε_b are the complex relative permittivity distribution of the object and the host medium, $\underline{E}_T(\underline{s})$ is the total electric field (incident plus scattered) at a point inside the head with position vector $\underline{s}$, $H_0^2(k_b\underline{R}) \approx \sqrt{\frac{2}{\pi k_b R}} e^{-jk_b\underline{R}} e^{j\pi/4}$, $\underline{R}$ is the position vector from a point in the head to the receiving antenna, A is head area and dA is differential area element.

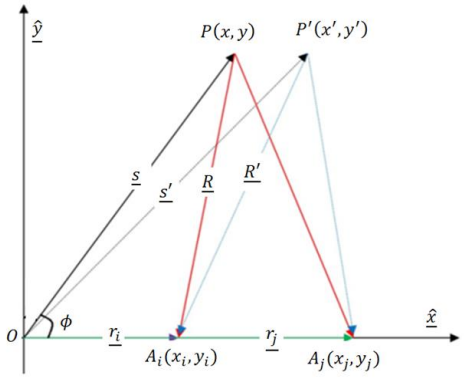

Fig 2 Geometry of HMIA measurement by a pair of antennas

Substituting for the scattered fields in (1) using (2) gives the following integral for the complex visibility function:

$$G(\underline{r}_i, \underline{r}_j) = (\frac{jk_b}{2})^3 \int_A \int_{A'} \left|\varepsilon(\underline{s}) - \varepsilon_b\right|^2 \underline{E}_T(\underline{s}) \cdot \underline{E}_T^*(\underline{s}') \frac{e^{-jk_b(R-R')}}{\sqrt{RR'}} dA dA' \qquad (3)$$

Where $R = \left|\underline{r}_i - \underline{s}\right|$ and $R' = \left|\underline{r}_j - \underline{s}'\right|$

If the distance from a point P to the receiving antenna A_i is sufficiently large to the size of antenna array plane, so that, $R \gg \left|\underline{r}_i\right|$, then:

$$R = \left|\underline{R}\right| = \sqrt{\left(\underline{r}_i - \underline{s}\right) \cdot \left(\underline{r}_i - \underline{s}\right)} = \sqrt{r_i^2 + s^2 - 2\underline{r}_i \cdot \underline{s}} \cong s - \frac{\underline{r}_i \cdot \underline{s}}{s} = s - \underline{r}_i \cdot \hat{\underline{s}} \qquad (4)$$

Where the "dot" denotes scalar product and $\hat{\underline{s}}$ is a unit vector. Similarly, the distance from another point P' in the head model to the receiving antenna A_j can be calculated as:

$$R' = \left|\underline{R'}\right| = s' - \underline{r_j} \cdot \widehat{\underline{s'}} \tag{5}$$

Submitting (4) and (5) in (3), then

$$G(\underline{r_i}, \underline{r_j}) = (\frac{jk_b}{2})^3 \int_A \left|\varepsilon(\underline{s}) - \varepsilon_b\right|^2 \underline{E_T}(\underline{s}) \cdot \underline{E_T^*}(\underline{s'}) \frac{e^{-jk_b(\underline{r_i} - \underline{r_j})\cdot\hat{\underline{s}}}}{s} dA \tag{6}$$

Defining the head intensity function at the position $\underline{s}$ as:

$$I(\underline{s}) = (\frac{jk_b}{2})^3 \left|\varepsilon(\underline{s}) - \varepsilon_b\right|^2 \underline{E_T}(\underline{s}) \cdot \underline{E_T^*}(\underline{s}) \tag{7}$$

and defining the baseline vector $\underline{D}$ of any two antennas A_i and A_j as:

$$\underline{D} = (\underline{r_i} - \underline{r_j})/\lambda_b \tag{8}$$

Substituting (7) and (8) in (6), equation (6) changes to:

$$G(\underline{D}) = \int_A I(\underline{s}) \frac{e^{-j\underline{D}\cdot\hat{\underline{s}}}}{s} dA \tag{9}$$

Let the Cartesian components of the unit vector $\hat{\underline{s}}$ be expressed in polar coordinates (ϕ, s) as follows:

$$\begin{gathered} \hat{\underline{s}} = cos\,\phi\, \hat{\underline{x}} + sin\phi \hat{\underline{y}} \\ dA = sdsd\phi \end{gathered} \tag{10}$$

Defining new variables (l, m) as:

$$\begin{gathered} l = cos\,\phi \\ m = sin\phi \end{gathered} \tag{11}$$

Submitting (10) and (11) in (9), the visibility function can be rewritten as:

$$G(\underline{D}) = \int_A I(\underline{s})\, e^{-j2\pi \underline{D}\cdot\hat{\underline{s}}} d\phi ds \tag{12}$$

Writing the Cartesian components of the baseline vector as (u, v):

$$u = (x_j - x_i)/\lambda_b$$
$$v = (y_j - y_i)/\lambda_b \tag{13}$$

The visibility function then becomes:

$$G(u,v) = \int_l \int_m I(l,m)\, e^{-j2\pi(ul+vm)} dldm \tag{14}$$

It is evident that the visibility function (14) is the 2-D Fourier transform of the 2-D intensity function which is consistent with the Van Cittert-Zernike theorem [12]. Therefore, we can obtain the head intensity distribution function by use of an inverse Fourier transform:

$$I(l,m) = \int_u \int_v G(u,v)\, e^{j2\pi(ul+vm)} dudv \tag{15}$$

3. Simulation

3.1 Head Model

Fig 3 displays the simulated 2-D head model that contains skin, fat, skull, cerebral spin fluid (CSF), grey matter, white matter and a hemorrhagic stroke area, and colour bar plots the dielectric properties of the head. The head model was surrounded with air as well as the space between the head model and antenna array. The dielectric properties of the head model are summarized in Table 1.

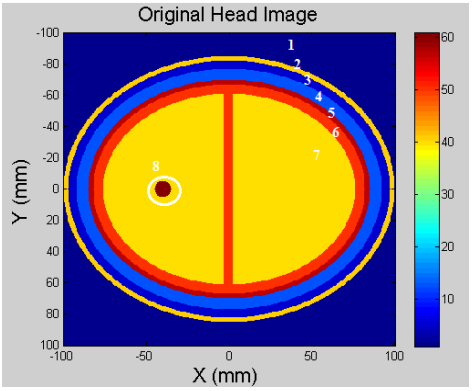

Fig 3 Simulated 2-D head model inside of the HMIA with a radius of 100 mm (1:matching solution medium, 2: Skin, 3: Fat, 4: Skull, 5: CSF, 6: Grey matter, 7: White matter, 8: Hemorrhagic stroke)

Table 1 Dielectric properties for the head model at 2 GHz [5-6]

No.	1	2	3	4	5	6	7	8
Region	Air	Skin	Fat	Skull	CSF	Grey matter	White matter	Hemorrhagic Stroke
Thickness (mm)		3	5	7	3	6		6
Dielectric properties	1	41-11 j	5-4 j	13-2 j	57-26 j	50-18 j	40-15 j	61-13 j

3.2 Antenna and Forward Scattering Problem

A wire antenna was simulated as the transmitter and receiver. The incident field of such antenna is given by:

$$\underline{E}_{inc}(\underline{s}) = \underline{E}_T(\underline{s}) + \frac{jk_b^2}{4}\int_A \left(\varepsilon(\underline{s}) - \varepsilon_b\right)\underline{E}_T(\underline{s})H_0^2(k_bR)dA \qquad (16)$$

The left-hand side of equation (16) is the incident field within the head model, which is always known. It remains to solve for the total field $\underline{E}_T$ which is computed using MoM [8] to convert an integral equation into a set of linear simulation equations. The total electric field $\underline{E}_T$ of the head at a point inside the head with position vector $\underline{s}$ is the sum of the scattered filed $\underline{E}_{scat}$ and the incident field $\underline{E}_{inc}$. Using the approach adopted by Richmond [10], we divide the area of head into small area elements ΔS and assume that the field and the permittivity is constant with each ΔS. The integral in equation (16) then becomes a sum over all the elemental areas. Equation (16) then becomes a matrix equation as follows:

$$\left[\underline{E}_{inc}(\underline{s})\right] = \left[[I] + [M]\right]\left[\underline{E}_T(\underline{s})\right] = [Q]\left[\underline{E}_T(\underline{s})\right] \qquad (17)$$

Where $[Q] = [I] + [M]$, $[I]$=Identity matrix $(N \times N)$, $[M]$==Square matrix $(N \times N)$ with elements M_{mn} defined as follows (m=row index, n=column index).

For the diagonal elements of [M], that is $m = n$

$$M_{mn} = \left(\varepsilon_n(\underline{s}) - \varepsilon_b\right)(1 + j\frac{\pi}{2}k_bH_1^2(k_ba)) \qquad (18)$$

Where $a = \sqrt{\frac{\Delta S}{\pi}}$, and $H_1^2(k_ba)$ is the first-order Hankel function of the second type with argument k_ba

For the off-diagonal elements of $[M]$, that is $m \neq n$.

$$M_{mn} = \frac{jk_b^2}{4} \Delta S \left(\varepsilon_n(\underline{s}) - \varepsilon_b\right) H_0^2(k_b R_{mn}) \tag{19}$$

Where $\Delta S = \pi a$, $R_{mn} = |r_m - r_n|$

The total field can be found by matrix inversion of equation (17):

$$\left[\underline{E_T}(\underline{s})\right] = [Q]^{-1}\left[\underline{E_{inc}}(\underline{s})\right] \tag{20}$$

3.3 Antenna Array

An array of 16 wire antennas including one transmitter and 15 receivers (Fig 4.) was placed around the head model in far-field (400 mm) distance.

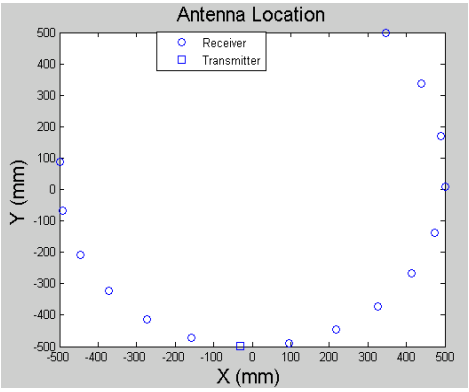

Fig 4 Schematic of array configuration

A computer model was developed using MATLAB by combining (2), (20) and (1) to simulate the complex visibility function that is detailed in section 2. The head intensity distribution function I was used to generate a 2-D head image.

4. Simulation Results

The 100 mm x 100 mm square region containing the object (head) and the background medium (air) is uniformly subdivided into 401 x 401 elementary square cells. Fig 5 clearly shows the simulated hemorrhagic stroke area within the reconstructed 2-D head model, where the stroke was located at (X = −40 mm, Y = 0 mm). Colour bar plots signal energy on a linear scale, normalised to the maximum in the 2-D head area.

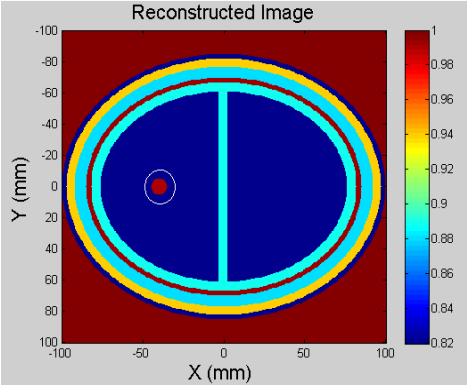

Fig 5 2-D reconstructed head image with hemorrhagic stroke area of 5 mm in diameter (circled in white)

5. Conclusion

This simulation paper has described a new image reconstruction algorithm for brain imaging and hemorrhagic stroke detection. Simulation result showed that small hemorrhagic stroke inside of a high dielectric contrast shield, comprising the skull and cerebral spinal fluid could be detected. No additional matching solution medium was necessary between the head model and the antenna array, only air, which greatly simplifies the practical implementation of such a system. The HMIA technique has potential benefits such as significant improvement of imaging results compare to other microwave imaging approaches, simplicity, safety and comfort compared to other screening methods, such as CT scanning.

6. Acknowledgment

The authors gratefully acknowledge the support of the Institute of Biomedical Technologies (IBTec) at the Auckland University of Technology (AUT), and the support of Callaghan Innovation, Auckland, New Zealand.

References

[1] Go, A. S., Mozaffarian, D., Roger, V. L., Benjamin, E. J., Berry, J. D., Borden, W. B., & Turner, M. B., Heart Disease and Stroke Statistics - 2013 Update A Report From the American Heart Association, *Circulation, Vol. 127, No. 1*, e6-e245, 2013.

[2] Mohammed, B. A. J., Abbosh, A. M., Ireland, D., & Bialkowski, M. E., Compact Wideband Antenna for Microwave Imaging of Brain, *Progress In Electromagnetics Research C, Vol. 27,* pp.27-39, 2012.

[3] Peyman, A., Holden, S. J., Watts, S., Perrott, R., & Gabriel, C., Dielectric properties of porcine cerebrospinal tissues at microwave frequencies: in vivo, in vitro and systematic variation with age, *Physics in medicine and biology, Vol. 52, No. 8,* pp.2229, 2007.

[4] Gabriel, S., Lau, R. W., & Gabriel, C., The dielectric properties of biological tissues: II. Measurements in the frequency range 10 Hz to 20 GHz, *Physics in medicine and biology, Vol. 41, No. 11*, pp.2251, 1996.

[5] Semenov, S. Y., & Corfield, D. R., Microwave tomography for brain imaging: Feasibility assessment for stroke detection, *International Journal of Antennas and Propagation*, 2008.

[6] Ireland, D., & Bialkowski, M., Feasibility study on microwave stroke detection using a realistic phantom and the FDTD method, *Microwave Conference Proceedings (APMC), 2010 Asia-Pacific*, pp.1360-1363, December, 2010.

[7] Trefna, H., & Persson, M. (2008, July). Antenna array design for brain monitoring, *Antennas and Propagation Society International Symposium*, pp.1-4, 2008.

[8] Harrington, R. F., Field computation by moment methods, *Wiley-IEEE Press*, 1993.

[9] Born, M., & Wolf, E. (1980). Principles of optics: electromagnetic theory of propagation, interference and diffraction of light. Chapter 10.4.2, pp. 510, *Pergamon Press, Sixth Edition*.

[10] Richmond, J., Scattering by a dielectric cylinder of arbitrary cross section shap, *IEEE Transactions on Antennas and Propagation*, *Vol. 13, No. 3*, pp.334-341, 1965.